Doctoral theses at NTNU, 2022:194

Gaute Fotland

Effects of Time Integration and Constraint Methods for Cable Simulations using ALE-ANCF Elements regarding Real-Time Analysis

Doctoral thesis

NTNU
Norwegian University of Science and Technology
Thesis for the Degree of Philosophiae Doctor
Faculty of Engineering
Department of Mechanical and Industrial Engineering

NTNU
Norwegian University of Science and Technology

Gaute Fotland

Effects of Time Integration and Constraint Methods for Cable Simulations using ALE-ANCF Elements regarding Real-Time Analysis

Thesis for the Degree of Philosophiae Doctor

Trondheim, June 2022

Norwegian University of Science and Technology
Faculty of Engineering
Department of Mechanical and Industrial Engineering

NTNU
Norwegian University of
Science and Technology

NTNU
Norwegian University of Science and Technology

Thesis for the Degree of Philosophiae Doctor

Faculty of Engineering
Department of Mechanical and Industrial Engineering

ISBN 978-82-326-6332-3 (printed ver.)
ISBN 978-82-326-6878-6 (electronic ver.)
ISSN 1503-8181 (printed ver.)
ISSN 2703-8084 (online ver.)

Doctoral theses at NTNU, 2022:194

Printed by NTNU Grafisk senter

To the living God

Summary

This thesis presents some of the requirements for developing a digital twin of an offshore crane. A digital twin will improve the control system for the crane with a real-time simulation. Furthermore, maintenance prediction could be improved, which again would reduce downtime. Through a systems engineering approach, it was found that a sufficient cable and pulley simulation formulation was vital for a digital twin. Governing aspects to select a formulation were found to be accuracy and real-time capabilities. The Absolute Nodal Coordinate Formulation (ANCF) in the framework of the Arbitrary Lagrangian-Eulerian (ALE) cable element was found to be a viable option. The ALE-ANCF cable element has the ability to exhibit large deformations, whilst allowing material to flow through the nodes without the nodes changing position.

The ALE-ANCF cable element was further assessed with two primary targets. Firstly, to investigate how the numerical time integrator affects the element. The two common integrators, the 4^{th} order Runge Kutta and the Generalized-α procedures were tested. A tool was developed to help select solution procedure based on the important aspects of a solver: *stability*, *accuracy*, and *efficiency*. Stability for a solver is important in order to achieve reliable results. To ensure stability for the 4^{th} order Runge Kutta procedure, a criterion to decide for the maximum time-step was developed, based on an effective element length and boundary conditions. The boundary conditions must ensure continuity for both displacement and rotation for the connected elements. For a real-time simulation, the efficiency of the solver is also critical. In general, the Generalized-α provides fast and accurate results as the high frequencies are dampened out and it is not hampered by requirements of the time-step size. The time-step size can be selected just by ensuring a sufficient number of time steps to capture the desired physical behavior of the model. Secondly, to investigate how the constraint methods used to create longer cable spans connecting cable elements affects the model. Through cases used for benchmarking, the Lagrange multipliers method, the penalty method, and linear coupling are all found to be viable constraint methods.

Finally, this thesis includes an analysis of the 4^{th} order Runge Kutta and Generalized-α for a lumped multi-element drill string model, formulated with Kane's method. The motivation was to develop a generic model for three dimensional directional wells, which can function as a virtual sensor for the drilling operation, capable of running real-time simulations.

Similar behavior as for the ALE-ANCF cable element was observed, where in general the Runge Kutta solution procedure is faster for smaller time-steps, but as the time-steps increase, the Generalized-α also provides fast solution times. Furthermore, Generalized-α dampens out the high frequencies introduced in the system from stiff penalty springs used to represent contact forces. Thus, a good representation of vibrations can be obtained. The statical behavior of the lumped mass model was verified by a FEM-model, and an ALE-ANCF cable element model. Mass proportional damping was thus implemented in the ALE-ANCF cable element for form finding.

Preface

This doctoral thesis has been submitted in partial fulfillment to the Norwegian University of Science and Technology (NTNU) for the degree of Philosophiae Doctor (PhD). The work has been carried out at the Department of Mechanical and Industrial Engineering (MTP) under the supervision of Associate Professor Bjørn Haugen, Professor Terje Rølvåg, and Professor Olav Egeland. The work with the PhD has been performed in the period of September 2017 to June 2022. The Norwegian Research Council supported the work through Center for Research-based Innovation (SFI) Offshore Mechatronics (OM) in Working Package (WP) 4.4, project number 237896.

Acknowledgments

I want to express my gratitude to Associate Professor Bjørn Haugen for being my supervisor. His continued support, guidance, and feedback have been truly invaluable to this work. Thanks to Professor Terje Rølvåg for giving me the opportunity to pursue a PhD degree, for sharing his ideas, and for being my supervisor at the start of this work. Thanks to my co-supervisor Professor Olav Egeland for ensuring the progress of the work.

I have appreciated my colleagues at the department, with many fruitful discussions originating by the coffee machine. The research would not have been complete without the collaborators, with special thanks to co-authors: Associate Professor Emeritus Cecilia Haskins, PhD Njål Kjærnes Tengesdal, and Associate Professor Christian Holden.

Furthermore, an especial thanks to my colleagues, which also was part of the best lunch group I could ever ask for: Håkon, Lise, Christian, Ali, Aksel, Tuan, and Yen. Thank you for keeping me sane through entertaining, non-scientific, and funny conversations.

I am grateful for all the proofreaders, who have improved the flow and readability of the thesis and the papers, with outstanding remarks from Thomas, Joakim, and Jarand.

A sincere thanks to my family, for the numerous 10-minute phone calls going home from the office, and to Mor and Far for believing in me over and over and over and over again.

Thanks to all my friends who have been cheering me on.

Thanks to my good friend and musician Arne Skorpe Sjøen, who through his work with Briotrio, Torfinn Thorsen – *Begynnelsen*, and his solo project has enriched my playlist.

Last but not least, I would like to thank my best friend, and the love of my life, Elisabeth. I am grateful that you have bought a house, fully renovating it, and made it a home for us, while I have been working with the thesis. I am excited to see what is in store for us as our next adventure.

Through these years working on the thesis I have held on to a sentence from the Norwegian national hymn “Gud signe vårt dyre fedreland” by Elias Blix:

Vil Gud ikkje vera Bygningsmann,
Me faafengt paa Huset byggja.

Contents

List of Figures

List of Tables

Abbreviations

ALE	=	Arbitrary Lagrangian–Eulerian
ANCF	=	Absolute Nodal Coordinate Formulation
DAE	=	Differential Algebraic Equations
DOF	=	Degree of Freedom
FEA	=	Finite Element Analysis
FEM	=	Finite Element Method
FFT	=	Fast Fourier Transform
G-α	=	Generalized-α
HHT	=	Hilber-Hughes-Taylor
LM	=	Lumped Model
MBS	=	Multibody Simulation
MOE	=	Measures of Effectiveness
MSD	=	Mass-Spring-Damper system
NCS	=	Norwegian Continental Shelf
ODE	=	Ordinary Differential Equation
RBM	=	Rigid Body Mode
RTF	=	Real-Time Factor
RK4	=	4^{th} order Runge Kutta
RMSE	=	Root Mean Square Error
ROV	=	Remotely Operated Vehicles
RTF	=	Real-Time Factor
TPM	=	Technical Performance Measures

Chapter 1

Introduction

1.1 Background and Motivation

With a coastal line of 2,532 km, Norway was well suited to become a maritime nation from the beginning. It is said that Norwegians are not only born with skies on their feet, but also salt water in their veins. Fishing have been, and still is, an important source of both food and income. The Vikings were known for building ships engineered with outstanding quality for its time, as they were fast, easy to maneuver, and could be sailed in shallow water. The ships were sailed for trading (and plundering) all over Europe, to Greenland and America in the west, and to Baghdad and Constantinople in the east.

In the late 60's early 70's the oil discovery started a new industrial era in Norway. The weather conditions with winter storms in the North Sea are harsh. This complicated the already demanding engineering challenges of locating and extracting the oil safely. Despite a rich naval legacy, offshore oil exploration and production was not known territory for the Norwegians, and a lot of groundwork had to be done to get to where we are today. The outcome has been many new developments, knowledge, and experience.

Salmon farming is another industry that has emerged in Norway since the 70's. The recent years there has been an exponential growth of the export of salmon, which has led to a demand for new locations for the farming sites. To comply with regulations from the Norwegian government limiting the number of fish per location, salmon farming companies are starting to use more exposed locations with larger ocean farms. Being livestock, there is the extra responsibility for the welfare of the fish. Escape of fish also has a great negative impact on the environment. The increasingly exposed locations also involves a greater risk for the personnel. The same challenges as with the oil industry, arise with demanding weather, wind, and currents, [1].

Offshore vessels with cranes play an important role for the industry today. They are used for lifting operations, such as installation of subsea templates, offshore wind turbine installation, and loading and unloading of equipment. The cost for an operation increase

with the complexity. For deep-water operations the installation and maintenance cost are higher, where waves, wind, and currents complicate these operations even more.

As in most industries the driving forces are cost and profit. The recent trend has been to use smaller vessels, with larger cranes mounted on deck, as a means for saving costs, [2]. Resulting ship motion makes the lifting operations more subjected to instability due to the environmental excitations. Crane instability can put severe restrictions on offshore crane operations and cause expensive downtime.

1.1.1 Challenges

For dynamic simulation of offshore vessels with cranes, the simulation of cable and pulleys in the crane were highlighted as important in Paper 1. Historically the simulations has been oversimplified, leading to a loss of dynamic behavior, reducing the accuracy of the results. A need for more advanced and accurate cable and pulley models are evident. The inherent dynamics affecting the behavior of cable-pulley systems were not accurately captured by established models. Research of cable and pulley simulation is not limited to cranes but also applies to a number of different simulation scenarios, such as elevators, ski lifts, power lines and draw works, as these all have cables.

Most crane operations are manually operated by a trained operator. The tasks could be challenging, where oscillations in the payload from ship motion must be suppressed by the operator, [3]. It takes a lot of practice to avoid overshooting the payload. A trend in the offshore industry is automatic systems to increase safety and operational time. The timing is good for development of a digital twin.

A digital twin of an offshore crane could support a wide range of applications. It would allow for safer lifting operations with less downtime based on anticipated failure modes, such as buckling in bars and actuators, material yielding and fatigue predictions, as well as an improved control system. Additionally, simulations would improve payload control and active damping, allowing for lifting operations in demanding weather conditions, and better maintenance schemes based on fatigue predictions. If the control system detects irregularities, the operator is notified. In dangerous situations, the control system could restrict continuation of the operation. For offshore crane operations, an important step forward would be to have a digital twin of the crane. The thesis addresses challenges related to simulation of the cable and pulley system, which is required as part of the realization of a digital twin. Important aspects of such a simulation is accuracy of the dynamics and the real-time capabilities. Thus, it is relevant to test different time integration methods. This is addressed in Paper 2.

Another important application for simulations for safer operations are simulation of drill strings. Several methods have been used to model this. In Paper 3, it is proposed to combine Kane's method with the Generalized-α (G-α) solver, which is described in this thesis. Such a simulation of a drill string would benefit from a real-time solver.

1.2 Publications

The following three international journal paper publications, listed chronologically, are included in the thesis:

Paper 1 [4], **Gaute Fotland**, Cecilia Haskins and Terje Rølvåg, "Trade Study to Select Best Alternative for Cable and Pulley Simulation for Cranes on Offshore Vessels," *Systems Engineering*, vol. 23, no. 2, pp. 177–188, 2020.

Paper 2 [5], **Gaute Fotland** and Bjørn Haugen, "Numerical Integration Algorithms and Constraint Formulations for an ALE-ANCF Cable Element," *Mechanism and Machine Theory*, vol. 170, Apr. 2022.

Paper 3 Njål K. Tengesdal, **Gaute Fotland**, Christian Holden, and Bjørn Haugen, "Modeling of Drill String Dynamics in Deviated Wells for Real-Time Simulation," Accepted in: *Simulation, SAGE*.

1.3 Contributions

The main contributions of the PhD project are given as follows:

Paper 1 In the first paper, requirements for a digital twin of an offshore crane is investigated. Several requirements are listed, whereas one of them is an improved cable and pulley simulation. This is the motivation for the investigation of possible cable formulations, to simulate a cable and pulley system. The Absolute Nodal Coordinate Formulation (ANCF) in the framework of the arbitrary Lagrangian-Eulerian (ALE) cable element was found to be a viable option. A functioning digital twin of an offshore crane could be applied to many different tasks, such as improved control systems as well as better maintenance schemes and extended operational time.

Paper 2 The second paper presents the ALE-ANCF cable element, suggested for cable and pulley simulation. The two key contributions from the paper were the aspects of numerical time integration solver and constraint methods for the selected element. Firstly, two different time integration procedures were tested, the 4^{th} order Runge Kutta (RK4) and the Generalized-α (G-α). To find a suitable solver for the formulation is important for the real-time aspect of a digital twin simulation. A tool to select the most suitable solver was presented. A criterion to find maximum time-step when using RK4 was also introduced. For simulation of large, elastic structures such as cranes, G-α is the most relevant time integration method. For a crane, where cables

are an integrated part of the structure, the element formulation also has to comply with the same time integration method. The relevant frequencies in such systems, including the lifting operations, are seen to be relatively low. Thus, the use of ALE-ANCF cable elements in combination with G-α, proves the feasibility for a digital twin application with real-time simulation. Common in literature, is the application of explicit time-integration methods for cable elements, being unfavorable when part of a larger finite element model structure. Secondly, different constraint methods, to create longer cable spans, were tested for the ALE-ANCF cable element. Lagrange Multipliers, the Penalty method and Linear coupling are all viable constraint methods.

Paper 3 The final paper adopts some of the motivation from Paper 2. A drill string model was formulated as a lumped mass model by Kane's method, and further generalized for an arbitrary 3-D wellbore configuration. It is investigated how the numerical time integrators 4^{th} order Runge Kutta and Generalized-α contribute to the stability, the accuracy, and the solution times. The real-time aspect is also of importance, as such a model could be used as a virtual sensor for drilling directional wells, and could be further developed into a digital twin. The statical behavior of the drill string was verified by a FEM-model.

1.4 Thesis Structure

The rest of thesis is structured as a paper-based thesis, and the following chapters are organized as follows. Chapter 2 includes relevant background theory for the material presented in the included papers. Furthermore, it presents models and simulations used in this thesis, with the accompanying findings. Chapter 3 describes the program created to run the simulations. Conclusions and suggestions for further work are given in Chapter 4. Finally, the papers are included in the Chapter Papers.

Chapter 2

Background Theory

2.1 Selection of Element Formulation

When exploring new complex systems, it is useful to structure the relevant information. This increases the possibility of making good decisions and simplifies problem solving. Systems engineering is a branch of science providing tools to handle this. It structures the information into useful road maps for decision making. To contextualize where cable and pulley are placed on offshore vessels were a first step, to better understand requirements for the simulation. For example, the dynamic behavior of a cable is of higher interest than the internal stride interaction when simulating crane behavior. Paper 1 used a context diagram as a tool to examine the systemic picture of what should and could be included to create a digital twin of an offshore crane. After all, the end goal of a digital twin would be to simulate the full crane system.

Paper 1 used the SPADE method, which is a systems engineering tool developed by Haskins in [6], and shown in Fig. 2.1. SPADE is an acronym constructed from the words: Stakeholders, Problem formulation, Alternatives, Decision making, and Evaluation. Evaluation is a continuous process and is therefore placed in the center of the figure. During the evaluation process, one updates the old findings with new and relevant information. This makes the SPADE methodology useful for dealing with problems where the destination is unknown. It is important to identify and involve the stakeholders, as they have relevant insight in how the product is and will be used. Therefore they are identified early in the design process. The problem formulation stage exposes deficiencies in existing technology. Based on these deficiencies, different solutions are compared in the alternatives stage. To evaluate and compare alternatives for an element formulation for cable and pulley simulation, the trade-off analysis tool, which is a systems engineering approach, was used [7]. In addition, this was combined with the subjective value method, [8], to structure and evaluate the candidates. The subjective value method weights the characteristics of each element formulation against each other to find the one that best suits the system as a whole, according to design

requirements.

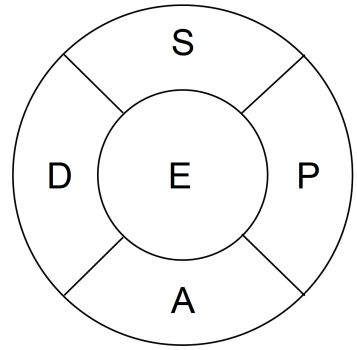

Figure 2.1: SPADE methodology/framework graphical representation, [6]

The stakeholder's viewpoint accumulated into two success criteria, Measures of Effectiveness (MOE), defined as the goal of the research in Paper 1.

- A cable and pulley simulation that improves the overall real-time simulation of a crane on an offshore vessel.
- A cable and pulley simulation that can be integrated with digital twin of a crane on an offshore vessel.

Technical Performance Measures (TPM) are key goals to be met, where the actual progress of technical achievement is monitored using periodic measures or tests. This will indicate how well a system is approaching its performance requirements, [9]. The technical performance measures for this project include:

- Less unplanned downtime: Due to better prediction of equipment failure, the crane can be maintained prior to breakdown.
- Less downtime: Maintenance is performed when required, instead of on a pre-determined schedule.
- Less maintenance cost: Only the worn-out parts are replaced, leading to a longer lifetime of crane and parts.
- Less waste: As the crane and the parts are in service for a longer period, there will be less waste.
- Fewer incidents: The number of industrial injuries concerning work with cranes on offshore vessels are reduced when using a digital twin. The digital twin has alarm systems for dangerous situations and has improved payload control.
- Faster operations: With better payload control, the lifting operations will be carried out more efficiently.

- Increased operational time: Due to a better control system, work can be done in harsher environments.

Most of these measures have a temporal quality, which means that the researcher must rely on historical data and data collected after the digital twin is implemented to assess the actual benefits of the digital twin, and then the simulation. However, some practical assertions regarding increased operational time and maintenance can be estimated.

Arbitrary Lagrangian–Eulerian (ALE) - Absolute Nodal Coordinate Formulation (ANCF), ALE-ANCF cable elements, have the highest score in the evaluation of different element formulation in Paper 1. For the last two decades, ANCF has gained attention for modelling of large-deformations and large-rotations in multibody dynamics, [10]. To handle large deformation is an important attribute to represent the dynamics of a cable. The ALE formulation combines the Lagrangian and the Eulerian formulations, as the name indicates. In the Lagrangian formulation, the nodes in the FEM mesh and the material are attached to each other. This is the common formulation to use for simulation of structures. In the Eulerian formulation, the nodes in the FEM mesh are fixed in space and the material can flow through it. This is the common formulation to use for simulation of fluids. ALE opens the possibility to have stationary nodes around the pulleys, as illustrated in Fig. 2.2. The advantage being that fewer elements are needed to represent the cable. The reason for this is that contact is numerically difficult to simulate, especially for the time steps when contact between elements occur during a simulation. When any random cable element can happen to be in contact with the pulley at some point of time, all the cable elements must be small. This results in large model files and time consuming simulations. For models with longer element, an explicit time integrator could be simpler and faster than an implicit time integrator. The possibility for longer cable spans could have been the motivation behind the selection of the *MatLab*-solver ODE-45, which is an explicit Runge-Kutta based solution procedure, for an elevator mechanism in [11]. With ALE, free cable elements can be larger, allowing fewer elements and faster simulations. Another advantage is that for the simulation of reeling, it is possible to add or remove excessive cable.

From previous work, cable modeling has been used for simulation of cranes, such as for tower cranes and container cranes, and payload oscillation control, [12] and [13]. Besides cranes, there are numerous fields of utilization for simulation of cables. A parachute was modeled in [14], a slender, deployable mesh antenna was simulated for benchmarking in [15], and a modern surgical robot with a cable-pulley system was modeled in [16].

ANCF have proven suitable for simulation of cables due to the favorable attributes with the ability for large-deformations and large-rotations in slender structures. Also ANCF elements have been applied to a wide variety of applications. Simulation of pantographs (overhead cables for electric trains) were done in [17] and [18]. Overhead power cables are modeled in [19]. For subsea applications, remotely operated vehicles (ROVs) are modeled with ANCF elements for the tether going to the surface in [20]. Parabolic leaf springs, commonly used for vehicle suspension, were analyzed with higher-order ANCF beam elements

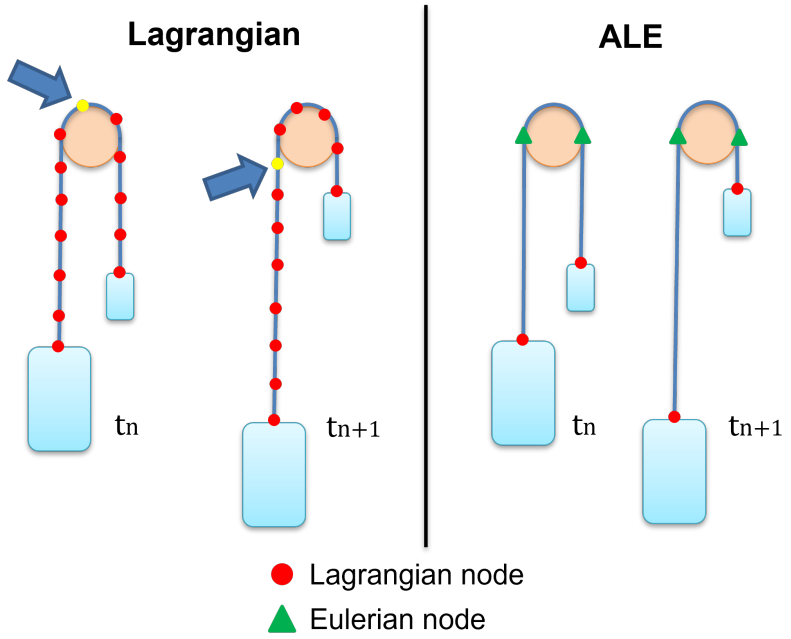

Figure 2.2: FEM model of an elevator mechanism with Lagrangian vs ALE formulation. The figure shows a cable pulled over a pulley with two masses attached, at two different time steps. A Lagrangian formulation requires many nodes to capture interaction between the cable and pulley; while an ALE formulation can have a high density of elements at the pulley, as they are stationary. This allows for fewer elements along the cable. The figure is adopted with modifications from [11].

to consider the complex geometry and the associated prestress in [21]. For ALE-ANCF cable element, an application typically of interest for the industry, is the prediction of global riser response due to slug flow [22].

The ANCF formulation was first introduced by Shabana in [10]. Nachbagauer and Gerstmayr have done extensive work to present a good overview of ANCF, [23], [24], and [25]. The ANCF is also developed for plates and shells, as proposed in [26]. Another application where the ANCF has been applied successfully is for topology optimization for flexible multibody systems. Sun et al. [27] has developed this method through several publications. In one of their latter publications also the ALE-ANCF method have been used for an optimization approach to simultaneously optimize the topology and geometrical sizes of a three-dimensional variable-length structure.

For modeling of pulleys and friction over the pulleys for the cable interaction, a contact formulation must be used. Several works have addressed this issue. For contact between cable segments, [28] and [29] should be consulted. Contact between the cable and the pulley is studied in [30] and [31], where the latter benchmark the simulation results with a laboratory

experiment.

One of the aspects pointed out as important design requirements for a cable simulation in Paper 1, was friction between the cable and pulley and between different cable segments. For the cable sliding through the pulleys, a different approach must be used to simulate friction over the pulley compared to the methods suggested for ANCF contact only. This is described for a linear ALE cable element of two nodes in [32], where the background for the development of the linear ALE cable element was to avoid the discontinuity that would take place in a pulley for the element proposed in [33]. Another proposal to address the unrealistic frictionless sliding over the pulley, was performed by a dynamic relaxation method for tensioned continuous cables [34]. A simple method for global response of a sliding cable system with friction, where the tension magnitude of each cable segment is obtained by an unknown sliding length vector, is developed. This results in additional nodal forces set by a sliding criterion modified by Fischer-Burmeister complementary functions, with a linear approach presented in [35], and a nonlinear in [36]. A further discussion of how pulleys, and thus friction, can be implemented for nonlinear ALE-ANCF cable elements are not conducted in the present work.

The work from Paper 1, found that the ALE-ANCF method was suitable for cable and pulley simulation. This formed the foundation for further interest in investigating different numerical time integration methods for the selected formulation. This is further presented in the following chapters of the thesis, based on Paper 2.

2.2 ALE-ANCF Cable Element Formulation

ANCF in the framework of ALE is investigated in this thesis. The element is defined based on work in [37], and is presented in the following section. For an ALE-ANCF cable element the mass is allowed to flow through the nodes in the element. The element is intended for slender geometries, with circular cross section. It follows the Euler-Bernoulli assumption for beams where the cross section is rigid and perpendicular to the deformed axis. The torsional stiffness and its related inertia is neglected. An illustration of the element is presented in Fig. 2.3. Here $\boldsymbol{r}$ is the position vector, $\boldsymbol{r}'$ is the slope vector, p is the material coordinate, and $\boldsymbol{f}$ is distributed load. s is the unit length of the element, eq. (2.5), and L_e is the element length, eq. (2.6). Note that the slope vector $\boldsymbol{r}'$ has both directional and "stretch"-like content. The vector has unit length if distance between the point $\boldsymbol{r}_1$ and $\boldsymbol{r}_2$ is the same as the "material" distance between p_1 and p_2. It's norm thus exhibits deformation gradient like behavior. The ALE method is commonly used for simulations of fluid flowing inside of pipes. In this case $\boldsymbol{r}$ would represent the pipe, the fluid p flows inside. Generalized coordinates refers to the parameters that uniquely describe the configuration of the system relative to some reference configuration. The generalized coordinates of the element are given in eq. (2.1), where the position vector and slope vector have components in x-, y- and z-direction, eq. (2.2). The slope vector is given by the derivative of the position vector eq. (2.3).

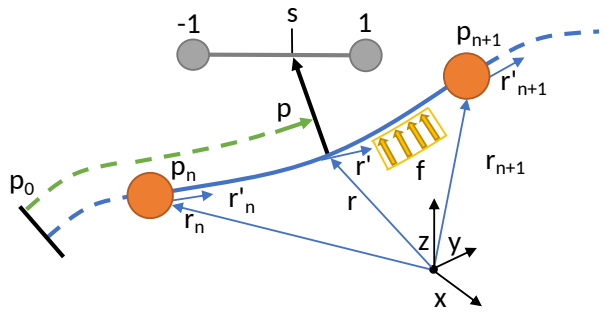

Figure 2.3: ANCF element in the framework of ALE, where mass can flow through, based on figure by Hong et.al. [37]. $\boldsymbol{r}$ is the position vector, $\boldsymbol{r}'$ is the slope, $\boldsymbol{f}$ is a distributed external load, and p is the material coordinate. The element is defined from node n to n+1, with the unitary element from -1 to 1.

$$\boldsymbol{q} = \begin{bmatrix} \boldsymbol{r}_1^T & \boldsymbol{r}_1'^T & \boldsymbol{r}_2^T & \boldsymbol{r}_2'^T & p_1 & p_2 \end{bmatrix}^T = \begin{bmatrix} \boldsymbol{q}_e^T & p_1 & p_2 \end{bmatrix}^T \tag{2.1}$$

$$\boldsymbol{r}_1 = \begin{bmatrix} r_{1x} & r_{1y} & r_{1z} \end{bmatrix}^T \tag{2.2}$$

$$\boldsymbol{r}' = \frac{\partial \boldsymbol{r}}{\partial p} \tag{2.3}$$

The shape function is constructed with the familiar C^1 continuous Hermite beam functions, as displayed in eq. (2.4); where s and L_e are found in eq. (2.5) and (2.6), and are plotted in Fig. 2.4.

$$\begin{aligned} N_1 &= \frac{1}{4}(s-1)^2(2+s), N_2 = \frac{L_e}{8}(s-1)^2(s+1) \\ N_3 &= \frac{1}{4}(s+1)^2(2-s), N_4 = \frac{L_e}{8}(s+1)^2(s-1) \end{aligned} \tag{2.4}$$

$$s = \frac{2p - p_1 - p_2}{p_2 - p_1} \tag{2.5}$$

$$L_e = p_2 - p_1 \tag{2.6}$$

The shape function is used to get the arbitrary point of the position and the slope of the element, see eq. (2.7) and (2.8). Also, the derivative of the slope is presented in eq. (2.9), as this is used for time integration methods in the thesis.

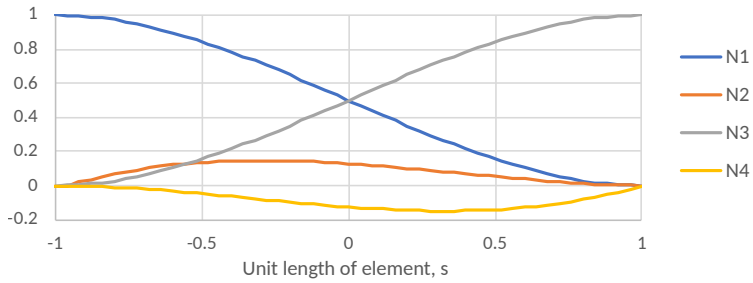

Figure 2.4: The plotted shape functions from eq. (2.4).

$$\boldsymbol{r} = N_1\boldsymbol{r}_1 + N_2\boldsymbol{r}'_1 + N_3\boldsymbol{r}_2 + N_4\boldsymbol{r}'_2 = \boldsymbol{N}_e\boldsymbol{q}_e \tag{2.7}$$

$$\boldsymbol{r}' = N'_1\boldsymbol{r}_1 + N'_2\boldsymbol{r}'_1 + N'_3\boldsymbol{r}_2 + N'_4\boldsymbol{r}'_2 = \boldsymbol{N}'_e\boldsymbol{q}_e \tag{2.8}$$

$$\boldsymbol{r}'' = N''_1\boldsymbol{r}_1 + N''_2\boldsymbol{r}'_1 + N''_3\boldsymbol{r}_2 + N''_4\boldsymbol{r}'_2 = \boldsymbol{N}''_e\boldsymbol{q}_e \tag{2.9}$$

For convenience the generalized coordinate $\boldsymbol{q}_e$ is constructed, where the material coordinates p_1 and p_2 are omitted, eq. (2.10), with the accompanying shape function in eq. (2.11). It is worth noting that the shape function in ALE is time dependent due to the mass flow.

$$\boldsymbol{q}_e = \begin{bmatrix}\boldsymbol{r}_1^T & \boldsymbol{r}_1'^T & \boldsymbol{r}_2^T & \boldsymbol{r}_2'^T\end{bmatrix}^T \tag{2.10}$$

$$\boldsymbol{N}_e = \begin{bmatrix}N_1\boldsymbol{I}_{3x3} & N_2\boldsymbol{I}_{3x3} & N_3\boldsymbol{I}_{3x3} & N_4\boldsymbol{I}_{3x3}\end{bmatrix} \tag{2.11}$$

The position of an arbitrary point with the time dependent variables indicated is thus given by.

$$\boldsymbol{r}(p,t) = \boldsymbol{N}_e(p, p_1(t), p_2(t))\boldsymbol{q}_e(t) \tag{2.12}$$

By time differentiation of eq. (2.7), the velocity and acceleration of the point is obtained. Due to the time varying shape function, this will also be differentiable with time. When applying the product rule and the chain rule it is recommended to substitute the variable s with the expression in eq. (2.5). This also makes the integration and derivation procedure for further calculations simplified. The velocity is given in eq. (2.13) and the acceleration in eq. (2.14), where $\dot{p}_1 = \frac{\partial p_1}{\partial t}$.

$$\dot{\boldsymbol{r}} = \frac{d\boldsymbol{r}}{dt} = \boldsymbol{N}_e\dot{\boldsymbol{q}}_e + \left(\frac{\partial \boldsymbol{N}_e}{\partial p_1}\dot{p}_1 + \frac{\partial \boldsymbol{N}_e}{\partial p_2}\dot{p}_2\right)\boldsymbol{q}_e = \boldsymbol{N}\dot{\boldsymbol{q}} \tag{2.13}$$

$$\begin{aligned}\ddot{\boldsymbol{r}} = \frac{d\dot{\boldsymbol{r}}}{dt} &= \boldsymbol{N}_e\ddot{\boldsymbol{q}}_e + \left(\frac{\partial \boldsymbol{N}_e}{\partial p_1}\ddot{p}_1 + \frac{\partial \boldsymbol{N}_e}{\partial p_2}\ddot{p}_2\right)\boldsymbol{q}_e + 2\left(\frac{\partial \boldsymbol{N}_e}{\partial p_1}\dot{p}_1 + \frac{\partial \boldsymbol{N}_e}{\partial p_2}\dot{p}_2\right)\dot{\boldsymbol{q}}_e + \\ &\quad \left(\frac{\partial^2 \boldsymbol{N}_e}{\partial p_1^2}\dot{p}_1^2 + 2\frac{\partial^2 \boldsymbol{N}_e}{\partial p_1 \partial p_2}\dot{p}_1\dot{p}_2 + \frac{\partial^2 \boldsymbol{N}_e}{\partial p_2^2}\dot{p}_2^2\right)\boldsymbol{q}_e \\ &= \boldsymbol{N}\ddot{\boldsymbol{q}} + \ddot{\boldsymbol{r}}_p\end{aligned} \tag{2.14}$$

For the convenience of further calculations $\boldsymbol{N}$ and $\ddot{\boldsymbol{r}}_p$ are used as substitutions in eq. (2.13) and (2.14). The two are written out in eq. (2.15) and (2.16), where $\ddot{\boldsymbol{r}}_p$ is the last part of $\ddot{\boldsymbol{r}}$ in eq. (2.14).

$$\boldsymbol{N} = \begin{bmatrix}\boldsymbol{N}_e & \frac{\partial \boldsymbol{N}_e}{\partial p_1}\boldsymbol{q}_e & \frac{\partial \boldsymbol{N}_e}{\partial p_2}\boldsymbol{q}_e\end{bmatrix} \tag{2.15}$$

$$\ddot{\boldsymbol{r}}_p = 2\left(\frac{\partial \boldsymbol{N}_e}{\partial p_1}\dot{p}_1 + \frac{\partial \boldsymbol{N}_e}{\partial p_2}\dot{p}_2\right)\dot{\boldsymbol{q}}_e + \left(\frac{\partial^2 \boldsymbol{N}_e}{\partial p_1^2}\dot{p}_1^2 + 2\frac{\partial^2 \boldsymbol{N}_e}{\partial p_1 \partial p_2}\dot{p}_1\dot{p}_2 + \frac{\partial^2 \boldsymbol{N}_e}{\partial p_2^2}\dot{p}_2^2\right)\boldsymbol{q}_e \tag{2.16}$$

The derivatives of the velocity and the acceleration presented in eq. (2.17) to (2.20) are included for convenience, as it is used for calculations for integration methods used in the thesis.

$$\dot{\boldsymbol{r}}' = \boldsymbol{N}_e'\dot{\boldsymbol{q}}_e + \left(\frac{\partial \boldsymbol{N}_e}{\partial p_1}\dot{p}_1 + \frac{\partial \boldsymbol{N}_e}{\partial p_2}\dot{p}_2\right)\boldsymbol{q}_e = \boldsymbol{N}'\dot{\boldsymbol{q}} \tag{2.17}$$

$$\dot{\boldsymbol{r}}'' = \boldsymbol{N}_e'\dot{\boldsymbol{q}}_e + \left(\frac{\partial \boldsymbol{N}_e}{\partial p_1}\dot{p}_1 + \frac{\partial \boldsymbol{N}_e}{\partial p_2}\dot{p}_2\right)\boldsymbol{q}_e = \boldsymbol{N}''\dot{\boldsymbol{q}} \tag{2.18}$$

$$\ddot{\boldsymbol{r}}' = \boldsymbol{N}'\ddot{\boldsymbol{q}} + \ddot{\boldsymbol{r}}_p' \tag{2.19}$$

$$\ddot{\boldsymbol{r}}_p' = 2\left(\frac{\partial \boldsymbol{N}_e'}{\partial p_1}\dot{p}_1 + \frac{\partial \boldsymbol{N}_e'}{\partial p_2}\dot{p}_2\right)\dot{\boldsymbol{q}}_e + \left(\frac{\partial^2 \boldsymbol{N}_e'}{\partial p_1^2}\dot{p}_1^2 + 2\frac{\partial^2 \boldsymbol{N}_e'}{\partial p_1 \partial p_2}\dot{p}_1\dot{p}_2 + \frac{\partial^2 \boldsymbol{N}_e'}{\partial p_2^2}\dot{p}_2^2\right)\boldsymbol{q}_e \tag{2.20}$$

The cubic shape element above can also be described with a linear shape function, [11]. This simplifies the calculations, as the slope is not included. For cases where the lateral vibrations could be neglected this could be a plausible solution. The generalized coordinates and shape function found in eq. (2.21) to (2.24) are then applied to the same equations as derived above.

$$\boldsymbol{q} = \begin{bmatrix}\boldsymbol{r}_1^T & \boldsymbol{r}_2^T & p_1 & p_2\end{bmatrix}^T \tag{2.21}$$

$$\boldsymbol{q}_e = \begin{bmatrix} \boldsymbol{r}_1^T & \boldsymbol{r}_2^T \end{bmatrix}^T \tag{2.22}$$

$$N_1^L = \frac{1-s}{2}, N_2^L = \frac{1+s}{2} \tag{2.23}$$

$$\boldsymbol{N}_e = \begin{bmatrix} N_1^L \boldsymbol{I}_{3x3} & N_2^L \boldsymbol{I}_{3x3} \end{bmatrix} \tag{2.24}$$

d'Alembert's principle is used to establish the equations of motion for the element with flowing mass, as the Lagrange equations cannot be applied directly [37]. It is more general than the Hamiltons principle, as it is not restricted to holonomic systems. In eq. (2.25) the general case of the principle with changing masses is stated. Here $\mathbf{F}_i$ is the sum of active forces applied to the i-th particle, $\dot{\mathbf{p}}_i$ is the time derivatives of the momenta of the system, and $\delta\mathbf{r}_i$ is its virtual displacements.

$$\sum_i (\mathbf{F}_i - \dot{\mathbf{p}}_i) \cdot \delta\mathbf{r}_i = 0 \tag{2.25}$$

The momentum of the mass is the product of its mass and velocity. The time derivatives of the momenta of the system are found in eq. (2.26). For a simulation of a cable or chain, the variation in cross section and density is neglected. Therefore the time derivative of the mass is canceled out.

$$\dot{\mathbf{p}}_i = m_i \mathbf{a}_i + \cancelto{0}{\dot{m}_i} \mathbf{v}_i \tag{2.26}$$

d'Alembert's equation then takes the form as in eq. (2.27). The equation requires the virtual displacement to obey the constraint conditions, or the sum of applied forces and inertia forces has to be equal.

$$\sum_i (\mathbf{F}_i - m_i \mathbf{a}_i) \cdot \delta\mathbf{r}_i = 0 \tag{2.27}$$

For dynamic problems with holonomic constraints, the governing equations are obtained by Hamilton's principle. In [38] an in dept derivation of how d'Alembert's principle can be written on the Hamilton form. This is valid since the derivative of the mass flow rate is canceled out, ref eq. (2.26). By dividing the forces in eq. (2.27), into elastic forces $\mathbf{F}_E$, and external forces $\mathbf{F}_f$, this system takes the form as in eq. (2.28). The mass in eq. (2.27) is discrete, while the mass is defined as the integral over the element depending on the cross section area and density over the length in eq. (2.28). The equation is also written from tensor form to matrix form.

$$\int_{p_1}^{p_2} \delta\boldsymbol{r}^T \left(\boldsymbol{F}_f + \boldsymbol{F}_E - \rho A \ddot{\boldsymbol{r}}\right) dp = 0 \tag{2.28}$$

The virtual displacements are given in eq. (2.29), with the virtual work formulated as forces in eq. (2.30) to (2.32).

$$\delta \boldsymbol{r} = \boldsymbol{N}_e \delta \boldsymbol{q}_e + \delta \boldsymbol{N}_e \boldsymbol{q}_e = \boldsymbol{N} \delta \boldsymbol{q} \tag{2.29}$$

$$\int_{p_1}^{p_2} \delta \boldsymbol{r}^T \boldsymbol{F}_f dp = \delta \boldsymbol{q}^T \int_{p_1}^{p_2} \boldsymbol{N}^T(p) \boldsymbol{f}(p,t) dp = \delta \boldsymbol{q}^T \frac{\partial p}{\partial s} \int_{-1}^{1} \boldsymbol{N}^T(s) \boldsymbol{f}(s,t) ds \tag{2.30}$$

$$\begin{aligned} &\int_{p_1}^{p_2} \delta \boldsymbol{r}^T \boldsymbol{F}_E dp = \\ &- \delta \boldsymbol{q}^T \frac{\partial p}{\partial s} \int_{-1}^{1} \left[\left(\frac{\partial \epsilon_0}{\partial \boldsymbol{q}} \right)^T EA(\epsilon_0 + c\dot{\epsilon}_0) + \left(\frac{\partial \kappa}{\partial \boldsymbol{q}} \right)^T EJ(\kappa + c\dot{\kappa}) \right] ds \end{aligned} \tag{2.31}$$

$$\int_{p_1}^{p_2} \delta \boldsymbol{r}^T \left(-\rho A \ddot{\boldsymbol{r}} \right) dp = -\delta \boldsymbol{q}^T \frac{\partial p}{\partial s} \int_{-1}^{1} \rho A \boldsymbol{N}^T \ddot{\boldsymbol{r}} ds \tag{2.32}$$

2.3 Governing Equations with Constraints

Constraints are used to model e.g. connections, joints and contact for a system. There are several methods to handle constraint. Three methods are now being presented, the Lagrange multiplier method, the penalty method, and the Augmented Lagrangian method. The latter is a combination of the two first methods. The methods are commonly described for the simplest case, where function minimization method is used to derive the governing equations, Ch. 7.2 in [39] and Ch. 6.3.8 in [40]. In addition nodes can be shared, which is the simplest method to constrain a model. This also reduces the number of DOFs in the system. This is equivalent by using a linear coupling, a master-slave technique, to constrain the nodes.

2.3.1 Lagrange Multiplier Method

The potential for the Lagrange multiplier method is given by W_L in eq. (2.33). This is the functional that is to be minimized, and the evaluated function is found in eq. (2.34). Here $\boldsymbol{\phi}$ represents the constraints and $\boldsymbol{\lambda}$ is the Lagrange multipliers. λ is a scaling factor, but it also provides a measure of the required internal forces to close the accompanying constraint. W is given in eq. (2.28). $\boldsymbol{R}$ is the residuals from $\frac{\partial W}{\partial \boldsymbol{q}}$. $\boldsymbol{G}$ is the differentiated constraints, where $\boldsymbol{G} = \frac{\partial \phi}{\partial \boldsymbol{q}}$.

$$W_L = W + \lambda_i \phi_i \equiv W + \phi^T \boldsymbol{\lambda} \tag{2.33}$$

$$\begin{cases} \frac{\partial W_L}{\partial \boldsymbol{q}} = \boldsymbol{R} + \boldsymbol{\lambda}^T \boldsymbol{G}(\boldsymbol{q}) = \boldsymbol{0} \\ \frac{\partial W_L}{\partial \boldsymbol{\lambda}} = \phi(\boldsymbol{q}) = \boldsymbol{0} \end{cases} \tag{2.34}$$

The governing equations are obtained and takes the common form for a mechanical system, as presented in eq. (2.40).

The reader should be aware that both $\boldsymbol{G}$ and $\boldsymbol{G}^T$ are common ways for $\frac{\partial \boldsymbol{\phi}}{\partial \boldsymbol{q}}$ to be defined. In this thesis the derivative of the constraint is defined as $\boldsymbol{G} = \frac{\partial \phi}{\partial \boldsymbol{q}}$, similar to [39], [40] and [41], while e.g. [42] uses the other definition.

2.3.2 Penalty Method

The potential for the Penalty Method is given by W_P in eq. (2.35), with the evaluated functional in eq. (2.36). W is given in eq. (2.28). $\boldsymbol{R}$ is the residuals from $\frac{\partial W}{\partial \boldsymbol{q}}$. The method has the advantage of not expanding the system, as it only introduces simple spring forces between the constraints with the quadratic penalty term, where $\boldsymbol{\phi}$ represents the constraints and k_{pen} is the penalty coefficient. The penalty springs are then constraints added to the system through the system constraint violation energy $1/2 \boldsymbol{\phi}^T \lceil \boldsymbol{k}_{pen} \rfloor \boldsymbol{\phi}$. The diagonal matrix $\lceil \boldsymbol{k}_{pen} \rfloor$ contains the individual penalty stiffnesses along the diagonal.

$$W_P = W + \frac{1}{2} k_{pen} \phi^T \phi \tag{2.35}$$

$$\frac{\partial W_P}{\partial \boldsymbol{q}} = \boldsymbol{R} + \lceil \boldsymbol{k}_{pen} \rfloor \boldsymbol{\phi}^T \boldsymbol{G} = \boldsymbol{0} \tag{2.36}$$

2.3.3 Augmented Lagrange Method

The potential for the augmented Lagrange method is given by W_{AL} in eq. (2.37), with the evaluated functional in eq. (2.38). Here $\boldsymbol{\phi}$ represents the constraints and $\boldsymbol{\lambda}$ is the Lagrange multipliers, k_{pen} is the penalty coefficient, k_{lag} is a scaling factor used to weight the Lagrange term against the penalty term internally. $\boldsymbol{R}$ is the residuals from $\frac{\partial W}{\partial \boldsymbol{q}}$.

$$W_{AL} = W + k_{lag} \phi^T \boldsymbol{\lambda} + \frac{1}{2} k_{pen} \phi^T \phi \tag{2.37}$$

$$\begin{cases} \frac{\partial W_{AL}}{\partial \boldsymbol{q}} = \boldsymbol{R} + k_{lag} \boldsymbol{\lambda}^T \boldsymbol{G}(\boldsymbol{q}) + \lceil \boldsymbol{k}_{pen} \rfloor \boldsymbol{G}^T \phi = \boldsymbol{0} \\ \frac{\partial W_{AL}}{\partial \boldsymbol{\lambda}} = \phi(\boldsymbol{q}) = \boldsymbol{0} \end{cases} \tag{2.38}$$

2.3.4 Mechanical System

The Lagrange multiplier method in eq. (2.34), forms the foundation for the common formulation known as a mechanical system, eq. (2.40). This is the governing equation used in e.g. [37]. The residual $\boldsymbol{R}$ is given by eq. (2.39).

$$\boldsymbol{R} = \boldsymbol{M}\ddot{\boldsymbol{q}} - \boldsymbol{Q}(\boldsymbol{q}, \dot{\boldsymbol{q}}, t) \tag{2.39}$$

$$\begin{cases} \boldsymbol{M}\ddot{\boldsymbol{q}} - \boldsymbol{Q}(\boldsymbol{q}, \dot{\boldsymbol{q}}, t) + \boldsymbol{G}^T\boldsymbol{\lambda} = \boldsymbol{0} \\ \boldsymbol{\phi}(\boldsymbol{q}, t) = \boldsymbol{0} \end{cases} \tag{2.40}$$

The system equation for the penalty method is the simplest; when performing the variation of the penalty stiffness, this contributes to the system dynamic equilibrium equation and takes the form as:

$$\boldsymbol{M}\ddot{\boldsymbol{q}} - \boldsymbol{Q}(\boldsymbol{q}, \dot{\boldsymbol{q}}, t) + \boldsymbol{G}^T\lceil\boldsymbol{k}_{pen}\rfloor\boldsymbol{\phi} = \boldsymbol{0} \tag{2.41}$$

For the expanded version, the augmented Lagrange method, both Lagrange multipliers and penalty constraints are included:

$$\begin{cases} \boldsymbol{M}\ddot{\boldsymbol{q}} - \boldsymbol{Q}(\boldsymbol{q}, \dot{\boldsymbol{q}}, t) + k_{lag}\boldsymbol{G}^T\boldsymbol{\lambda} + \boldsymbol{G}^T\lceil\boldsymbol{k}_{pen}\rfloor\boldsymbol{\phi} = \boldsymbol{0} \\ \boldsymbol{\phi}(\boldsymbol{q}, t) = \boldsymbol{0} \end{cases} \tag{2.42}$$

Writing out the forces derived from eq. (2.28) in the standard form of a mechanical system eq. (2.40), for a given time step, it takes the form of a function of generalized coordinates:

$$\begin{cases} \boldsymbol{M}_t\ddot{\boldsymbol{q}}_t + \boldsymbol{Q}_{pt} + \boldsymbol{Q}_{et} - \boldsymbol{Q}_{ft} + \boldsymbol{G}^T\boldsymbol{\lambda}_t = \boldsymbol{0} \\ \boldsymbol{\phi}_t(\boldsymbol{q}_t, t) = \boldsymbol{0} \end{cases} \tag{2.43}$$

where, $\boldsymbol{M}_{ele}$, is the mass matrix of the element in eq. (2.44). The total force vector is given in eq. (2.45), which consists of the following components: $\boldsymbol{Q}_p$, additional inertia forces, as a consequence of the material flow in eq. (2.46), according to eq. (2.16). For convenience, the elastic force $\boldsymbol{Q}_e$ is divided up into two parts, internal forces and damping forces, eq. (2.47). $\boldsymbol{Q}_{int}$ is the elastic internal forces in eq. (2.48), and $\boldsymbol{Q}_{damp}$ is the elastic damp forces in eq. (2.49).

There are three relevant cases. If incompressible liquid is to be simulated, $\boldsymbol{Q}_e$ is neglected, if a cable is simulated, the curvature term in $\boldsymbol{Q}_e$ is neglected, and if a beam is simulated, the full $\boldsymbol{Q}_e$ term is added. For the beam formulation, where the bending stiffness is included by curvature, J is the second moment of inertia and c is the damping coefficient. $\boldsymbol{Q}_f$ is the external forces, where $\boldsymbol{f}$ is a 3-D vector, distributing the external loads in the element in x-, y- and z-direction. As an example, the gravitational force in y-direction

would take the form $\boldsymbol{f} = \begin{bmatrix} 0 & \rho A g & 0 \end{bmatrix}^T$. It is worth noting that the external force $\boldsymbol{Q}_f$ has a negative sign in eq. (2.43). The forces are defined with p as variable, from p_1 to p_2, by eq. (2.51), with the integral boundaries set accordingly. ϕ represents the constraints in the system, with the accompanying λ.

$$\boldsymbol{M}_{ele} = \int_{p_1}^{p_2} \rho A \boldsymbol{N}^T \boldsymbol{N} dp \tag{2.44}$$

$$\boldsymbol{Q} = \boldsymbol{Q}_f - \boldsymbol{Q}_{int} - \boldsymbol{Q}_{damp} - \boldsymbol{Q}_p \tag{2.45}$$

$$\boldsymbol{Q}_p = \int_{p_1}^{p_2} \rho A \boldsymbol{N}^T \ddot{\boldsymbol{r}}_p dp \tag{2.46}$$

$$\boldsymbol{Q}_e = \boldsymbol{Q}_{int} + \boldsymbol{Q}_{damp} \tag{2.47}$$

$$\boldsymbol{Q}_{int} = \int_{p_1}^{p_2} \left(\frac{\partial \epsilon_0}{\partial \boldsymbol{q}}\right)^T EA\epsilon_0 + \left(\frac{\partial \kappa}{\partial \boldsymbol{q}}\right)^T EJ\kappa dp \tag{2.48}$$

$$\boldsymbol{Q}_{damp} = \int_{p_1}^{p_2} \left(\frac{\partial \epsilon_0}{\partial \boldsymbol{q}}\right)^T EAc\dot{\epsilon}_0 + \left(\frac{\partial \kappa}{\partial \boldsymbol{q}}\right)^T EJc\dot{\kappa} dp \tag{2.49}$$

$$\boldsymbol{Q}_f = \int_{p_1}^{p_2} \boldsymbol{N}^T \boldsymbol{f} dp \tag{2.50}$$

$$\frac{\partial p}{\partial s} = \frac{p_2 - p_1}{2} \tag{2.51}$$

For strain formulation the Green strain definition is used, eq. (2.52). This gives the strain rate as in eq. (2.53). The curvature is found according to eq. (2.55). For derivation of the differentiation of the curvature, see Sec. 2.4.3.

$$\epsilon_0 = \frac{1}{2}(\boldsymbol{r}'^T \boldsymbol{r}' - 1) \tag{2.52}$$

$$\dot{\epsilon}_0 = \frac{1}{2}(\dot{\boldsymbol{r}}'^T \boldsymbol{r}' + \boldsymbol{r}'^T \dot{\boldsymbol{r}}') \tag{2.53}$$

$$\frac{\partial \epsilon_0}{\partial \boldsymbol{q}} = \frac{1}{2}(\frac{\partial \boldsymbol{r}'^T}{\partial \boldsymbol{q}} \boldsymbol{r}' + \boldsymbol{r}'^T \frac{\partial \boldsymbol{r}'}{\partial \boldsymbol{q}}) \tag{2.54}$$

$$\kappa = \frac{\|\boldsymbol{r}' \times \boldsymbol{r}''\|}{\|\boldsymbol{r}'\|^3} \tag{2.55}$$

The standard form of the mechanical system is used for implementation and investigation of different numerical time integrators, eq. (2.40).

2.4 Numerical Time Integrators

A numerical time integrator has to be used to step through time when solving a mechanical system as in eq. (2.40). In this section the Generalized-α (G-α), and the 4$^{\text{th}}$ order Runge Kutta (RK4) method are presented. G-α is a generalization of the Newmark-β method presented in Sec. 2.4.1. A comparison of time integration methods for ALE-ANCF cable elements is not found in other literature, thus this study presents a systematic approach to compare the two different numerical time integrators. The time integrators are examined with the criteria *stability*, *accuracy*, and *efficiency*. Stability for a solver is important in order to at all times achieve results, and for the results to be reliable. The demand for accuracy of the results depends on what they are being used for. Thus, this will vary from case to case. For a real-time simulation, the efficiency of the solver is critical.

As G-α or Hilber-Hughes-Taylor (HHT) are methods commonly used as numerical time integration in software, it was of interest to investigate how ALE-ANCF behaved in combination with this method. RK4 is commonly used for control systems, fluid, and rigid body mechanism modeling, whereas G-α has been dominant in classical structural finite element software. ANCF elements has successfully been used together with G-α in thermo-mechanical coupled analysis, [43]. For a simulation of an ANCF membrane element for dynamic modeling of multilayer dielectric elastomer actuators, G-α was part of the solution step. The HHT-α method was used for an ANCF element to simulate the motion of a fluid, as the dam break, [44]. A recent study has implemented an ALE-ANCF variant, in combination with HHT-α to simulate a tether deployment and station-keeping phases of a tethered satellite system, [45]. The characteristics of the element allowed for complex dynamic properties such as large deformation, slack, and rebound. The two are therefore important to study in relation to ALE-ANCF cable elements since these elements are likely to be implemented in existing software where both algorithms are used beforehand.

The study of the different time integration methods was the foundation for Paper 2. In Paper 3, G-α was combined with Kane's method to check if it added stability to the simulation, and if it met the real-time requirements.

2.4.1 Newmark-β Integration

The Newmark-β method was proposed by N. M. Newmark in 1959 [46], and is a commonly used numerical time integrator. To impose this method, firstly the Differential Algebraic Equations (DAE) has to be linearized by the first variation of eq. (2.56), from the mechanical system in eq. (2.40). This leads to eq. (2.57), where $\Delta \boldsymbol{R}^q$ and $\Delta \boldsymbol{R}^\lambda$ are given in eq. (2.58). $\boldsymbol{R}^q$ refers to residuals when finding $\Delta \boldsymbol{q}$, and $\boldsymbol{R}^\lambda$ refers to residuals when finding $\Delta \boldsymbol{\lambda}$.

$$\begin{aligned} \boldsymbol{R}^q &= \boldsymbol{M}\ddot{\boldsymbol{q}} - \boldsymbol{Q} + \boldsymbol{G}^T\boldsymbol{\lambda} \\ \boldsymbol{R}^\lambda &= \boldsymbol{\phi} \end{aligned} \tag{2.56}$$

$$\begin{aligned} \boldsymbol{R}^q + \Delta \boldsymbol{R}^q &= 0 \\ \boldsymbol{R}^\lambda + \Delta \boldsymbol{R}^\lambda &= 0 \end{aligned} \tag{2.57}$$

$$\begin{aligned} \Delta \boldsymbol{R}^q &= \frac{\partial \boldsymbol{R}^q}{\partial \ddot{\boldsymbol{q}}} \Delta \ddot{\boldsymbol{q}} + \frac{\partial \boldsymbol{R}^q}{\partial \dot{\boldsymbol{q}}} \Delta \dot{\boldsymbol{q}} + \frac{\partial \boldsymbol{R}^q}{\partial \boldsymbol{q}} \Delta \boldsymbol{q} + \frac{\partial \boldsymbol{R}^q}{\partial t} \Delta t + \frac{\partial \boldsymbol{R}^q}{\partial \boldsymbol{\lambda}} \Delta \boldsymbol{\lambda} \\ \Delta \boldsymbol{R}^\lambda &= \frac{\partial \boldsymbol{R}^\lambda}{\partial \boldsymbol{q}} \Delta \boldsymbol{q} \end{aligned} \tag{2.58}$$

The differentials are calculated in eq. (2.59), where $\boldsymbol{K}_T$ and $\boldsymbol{C}_T$ represent the tangential stiffness matrix and the damping matrix.

$$\begin{aligned} \frac{\partial \boldsymbol{R}^q}{\partial \ddot{\boldsymbol{q}}} &= \boldsymbol{M} & \frac{\partial \boldsymbol{R}^q}{\partial \dot{\boldsymbol{q}}} &= \boldsymbol{C}_T = -\frac{\partial \boldsymbol{Q}}{\partial \dot{\boldsymbol{q}}} \\ \frac{\partial \boldsymbol{R}^q}{\partial \boldsymbol{q}} &= \boldsymbol{K}_T = \frac{\partial \boldsymbol{M} \ddot{\boldsymbol{q}}}{\partial \boldsymbol{q}} - \frac{\partial \boldsymbol{Q}}{\partial \boldsymbol{q}} + \frac{\partial \boldsymbol{G}^T}{\partial \boldsymbol{q}} \boldsymbol{\lambda} & \frac{\partial \boldsymbol{R}^q}{\partial t} &= \boldsymbol{0} \\ \frac{\partial \boldsymbol{R}^q}{\partial \boldsymbol{\lambda}} &= \boldsymbol{G}^T & \frac{\partial \boldsymbol{R}^\lambda}{\partial \boldsymbol{q}} &= \boldsymbol{G} \end{aligned} \tag{2.59}$$

The matrix system with nonlinear equations of motion is obtained:

$$\begin{bmatrix} \boldsymbol{M} & \boldsymbol{0} \\ \boldsymbol{0} & \boldsymbol{0} \end{bmatrix} \begin{bmatrix} \Delta \ddot{\boldsymbol{q}} \\ \Delta \ddot{\boldsymbol{\lambda}} \end{bmatrix} + \begin{bmatrix} \boldsymbol{C}_T & \boldsymbol{0} \\ \boldsymbol{0} & \boldsymbol{0} \end{bmatrix} \begin{bmatrix} \Delta \dot{\boldsymbol{q}} \\ \Delta \dot{\boldsymbol{\lambda}} \end{bmatrix} + \begin{bmatrix} \boldsymbol{K}_T & \boldsymbol{G}^T \\ \boldsymbol{G} & \boldsymbol{0} \end{bmatrix} \begin{bmatrix} \Delta \boldsymbol{q} \\ \Delta \boldsymbol{\lambda} \end{bmatrix} = \begin{bmatrix} -\boldsymbol{R}^q \\ -\boldsymbol{R}^\lambda \end{bmatrix} \tag{2.60}$$

When using the penalty method, the residuals, $\boldsymbol{R}^q$ and $\boldsymbol{R}^\lambda$, take a different form than for the Lagrange multiplier method. $\boldsymbol{R}^q$ is given in eq. (2.61), while $\boldsymbol{R}^\lambda$ is canceled. The tangential stiffness, $\boldsymbol{K}_T$ takes the form as in eq. (2.62).

$$\boldsymbol{R}^q = \boldsymbol{M} \ddot{\boldsymbol{q}} - \boldsymbol{Q} + \boldsymbol{G}^T \lceil \boldsymbol{k}_{pen} \rfloor \boldsymbol{\phi} \tag{2.61}$$

$$\frac{\partial \boldsymbol{R}^q}{\partial \boldsymbol{q}} = \boldsymbol{K}_T = \frac{\partial \boldsymbol{M} \ddot{\boldsymbol{q}}}{\partial \boldsymbol{q}} - \frac{\partial \boldsymbol{Q}}{\partial \boldsymbol{q}} + \lceil \boldsymbol{k}_{pen} \rfloor \left(\frac{\partial \boldsymbol{G}^T}{\partial \boldsymbol{q}} \boldsymbol{\phi} + \boldsymbol{G}^T \frac{\partial \boldsymbol{\phi}}{\partial \boldsymbol{q}} \right) \tag{2.62}$$

The Augmented Lagrange method becomes a combination of the penalty method and the Lagrange multiplier method, where $\boldsymbol{R}^q$, and $\boldsymbol{R}^\lambda$ is given in eq. (2.63). The tangential stiffness, $\boldsymbol{K}_T$ takes the form as in eq. (2.64).

$$\begin{aligned} \boldsymbol{R}^q &= \boldsymbol{M}\ddot{\boldsymbol{q}} - \boldsymbol{Q} + k_{lag}\boldsymbol{G}^T\boldsymbol{\lambda} + \lceil \boldsymbol{k}_{pen} \rfloor \boldsymbol{G}^T\boldsymbol{\phi} \\ \boldsymbol{R}^\lambda &= k_{lag}\boldsymbol{\phi} \end{aligned} \tag{2.63}$$

$$\frac{\partial \boldsymbol{R}^q}{\partial \boldsymbol{q}} = \boldsymbol{K}_T = \frac{\partial \boldsymbol{M}\ddot{\boldsymbol{q}}}{\partial \boldsymbol{q}} - \frac{\partial \boldsymbol{Q}}{\partial \boldsymbol{q}} + k_{lag}\frac{\partial \boldsymbol{G}^T}{\partial \boldsymbol{q}}\boldsymbol{\lambda} + \lceil \boldsymbol{k}_{pen} \rfloor \left(\frac{\partial \boldsymbol{G}^T}{\partial \boldsymbol{q}}\boldsymbol{\phi} + \boldsymbol{G}^T\frac{\partial \boldsymbol{\phi}}{\partial \boldsymbol{q}} \right) \tag{2.64}$$

Newmark-β integration suggests a procedure to rewrite the accelerations and velocities in eq. (2.60) in terms of displacement, [46]. The procedure is outlined in the following section, where the Newmark difference formulas are given by:

$$\boldsymbol{q}_{t+1} = \boldsymbol{q}_t + h\dot{\boldsymbol{q}}_t + \left(\frac{1}{2} - \beta \right) h^2\ddot{\boldsymbol{q}}_t + \beta h^2\ddot{\boldsymbol{q}}_{t+1} \tag{2.65}$$

$$\dot{\boldsymbol{q}}_{t+1} = \dot{\boldsymbol{q}}_t + (1-\gamma)h\ddot{\boldsymbol{q}}_t + \gamma h\ddot{\boldsymbol{q}}_{t+1} \tag{2.66}$$

Here h is the time-step size, and β and γ are user defined parameters. To obtain the average constant acceleration formula the parameters are set to, $\beta = \frac{1}{4}$ and $\gamma = \frac{1}{2}$. This option gives second order accuracy, and will also be unconditionally stable over the full frequency range. This choice is also the most commonly used in commercial analysis software.

The incremental form of displacement is given in eq. (2.67), and in combination with eq. (2.65) takes the form of eq. (2.68).

$$\boldsymbol{q}_{t+1} = \boldsymbol{q}_t + \Delta\boldsymbol{q}_t \tag{2.67}$$

$$\Delta\boldsymbol{q}_t = h\dot{\boldsymbol{q}}_t + \frac{1}{2}h^2\ddot{\boldsymbol{q}}_t + \beta h^2\Delta\ddot{\boldsymbol{q}}_t \tag{2.68}$$

The same goes for velocity, where the incremental form is given in eq. (2.69), and in combination with eq. (2.66) takes the form of eq. (2.70).

$$\dot{\boldsymbol{q}}_{t+1} = \dot{\boldsymbol{q}}_t + \Delta\dot{\boldsymbol{q}}_t \tag{2.69}$$

$$\Delta\dot{\boldsymbol{q}}_t = h\ddot{\boldsymbol{q}}_t + h\gamma\Delta\ddot{\boldsymbol{q}}_t \tag{2.70}$$

The incremental form of the acceleration is given by:

$$\Delta\ddot{\boldsymbol{q}}_t = \ddot{\boldsymbol{q}}_{t+1} - \ddot{\boldsymbol{q}}_t \tag{2.71}$$

When incrementing the solution, it is desired to solve the system with respect to the displacement increments, $\Delta\boldsymbol{q}$, by rearranging eq. (2.68). The incremental form of the acceleration is obtained, with $\Delta\boldsymbol{q}$ as the unknown in eq. (2.72).

$$\Delta\ddot{\boldsymbol{q}}_t = \frac{1}{\beta h^2}\Delta\boldsymbol{q}_t - \frac{1}{\beta h}\dot{\boldsymbol{q}}_t - \frac{1}{2\beta}\ddot{\boldsymbol{q}}_t = \frac{1}{\beta h^2}\Delta\boldsymbol{q}_t - \boldsymbol{a}_t \tag{2.72}$$

The incremental form of the velocity, eq. (2.73), is obtained by inserting eq. (2.72) into eq. (2.70).

$$\Delta\dot{\boldsymbol{q}}_t = \frac{\gamma}{\beta h}\Delta\boldsymbol{q}_t - \frac{\gamma}{\beta}\dot{\boldsymbol{q}}_t - h\left(\frac{\gamma}{2\beta} - 1\right)\ddot{\boldsymbol{q}}_t = \frac{\gamma}{\beta h}\Delta\boldsymbol{q}_t - \boldsymbol{d}_t \tag{2.73}$$

The velocity and acceleration incremental in the matrix system eq. (2.60), are substituted with eq. (2.72) and (2.73), and it takes the form as presented in eq. (2.74), where the incrementors are lambda and displacement.

$$\begin{aligned}\begin{bmatrix} \boldsymbol{M} & \boldsymbol{0} \\ \boldsymbol{0} & \boldsymbol{0} \end{bmatrix}\begin{bmatrix} \frac{1}{\beta h^2}\Delta\boldsymbol{q}_t - \boldsymbol{a}_t \\ \Delta\ddot{\boldsymbol{\lambda}} \end{bmatrix} + \begin{bmatrix} \boldsymbol{C}_T & \boldsymbol{0} \\ \boldsymbol{0} & \boldsymbol{0} \end{bmatrix}\begin{bmatrix} \frac{\gamma}{\beta h}\Delta\boldsymbol{q}_t - \boldsymbol{d}_t \\ \Delta\dot{\boldsymbol{\lambda}} \end{bmatrix} \\ + \begin{bmatrix} \boldsymbol{K}_T & \boldsymbol{G}^T \\ \boldsymbol{G} & \boldsymbol{0} \end{bmatrix}\begin{bmatrix} \Delta\boldsymbol{q} \\ \Delta\boldsymbol{\lambda} \end{bmatrix} = \begin{bmatrix} -\boldsymbol{R}^q \\ -\boldsymbol{R}^\lambda \end{bmatrix}\end{aligned} \tag{2.74}$$

By defining $\boldsymbol{S}_T$ according to eq. (2.75), the matrix system in eq. (2.74) can be compressed to eq. (2.76). To find the increments, the inverse of $\boldsymbol{S}_T$ is found and moved to the right hand side, eq. (2.77). The terms containing $\boldsymbol{a}_t$ and $\boldsymbol{d}_t$ are only used for the predictor step, not the corrector steps. That means it is only used for the first iteration each time step.

$$\boldsymbol{S}_T = \begin{bmatrix} \frac{1}{\beta h^2}\boldsymbol{M} + \frac{\gamma}{\beta h}\boldsymbol{C}_T + \boldsymbol{K}_T & \boldsymbol{G}^T \\ \boldsymbol{G} & \boldsymbol{0} \end{bmatrix} \tag{2.75}$$

$$\boldsymbol{S}_T\begin{bmatrix} \Delta\boldsymbol{q} \\ \Delta\boldsymbol{\lambda} \end{bmatrix} = \begin{bmatrix} -\boldsymbol{R}^q + \boldsymbol{M}\boldsymbol{a}_t + \boldsymbol{C}_T\boldsymbol{d}_t \\ -\boldsymbol{R}^\lambda \end{bmatrix} \tag{2.76}$$

$$\begin{bmatrix} \Delta\boldsymbol{q} \\ \Delta\boldsymbol{\lambda} \end{bmatrix} = \boldsymbol{S}_T^{-1}\begin{bmatrix} -\boldsymbol{R}^q + \boldsymbol{M}\boldsymbol{a}_t + \boldsymbol{C}_T\boldsymbol{d}_t \\ -\boldsymbol{R}^\lambda \end{bmatrix} \tag{2.77}$$

The energy based convergence criterion [47], that must be satisfied before continuing to the next time step is:

$$\epsilon_e = \sqrt{\left|\begin{bmatrix} \boldsymbol{R}^q & \boldsymbol{R}^\lambda \end{bmatrix}\begin{bmatrix} \Delta\boldsymbol{q} \\ \Delta\boldsymbol{\lambda} \end{bmatrix}\right|} \tag{2.78}$$

An error criterion based on energy is quite often more stable for simulations where both rotations and translations are part of the generalized coordinates. Energy based convergence criteria is also considered more robust with respect to soft versus stiff systems as well as unit changes (meters to millimeters for instance).

2.4.2 Generalized-α Integration

The Generalized-α by Chung and Hulbert from 1993 [48] is a generalization of the HHT-α algorithm by Hilber, Hughes, and Taylor from 1977 [49], and the WBZ-α algorithm by Wood, Bossak, and Zienkiewicz from 1980 [50]. The G-α method is intended to improve stability for Newmark-β integration by providing additional damping in the high-frequency range. The high frequency dissipation is introduced into the numerical solution by linear interpolation between the time steps. This means that if $\alpha = 0$, only the $t + 1$ time step is accounted for. α_m is used for the inertia forces, and α_f is used for elastic, damping and external forces. The effect of the numerical damping decreases as the time step decreases.

The selection of the parameters are done according to Chung and Hulbert [48]. For second-order ODEs, the proposed algorithmic parameters are given in eq. (2.79), (2.80) and (2.81), where $\rho_\infty \epsilon [0, 1]$. The method is unconditionally stable for the conditions presented, [48].

$$\alpha_m = \frac{2\rho_\infty - 1}{\rho_\infty + 1} \tag{2.79}$$

$$\alpha_f = \frac{\rho_\infty}{\rho_\infty + 1} \tag{2.80}$$

$$\beta = \frac{1}{4}\left(\gamma + \frac{1}{2}\right)^2 \tag{2.81}$$

γ is calculated according to eq. (2.82), and the stability region is met for eq. (2.83).

$$\gamma = \frac{1}{2} - \alpha_m + \alpha_f \tag{2.82}$$

The equations used to set the parameters are eq. (2.81) and (2.82), following the restrictions of eq. (2.83).

$$\alpha_m < \alpha_f < \frac{1}{2} \qquad \text{and} \qquad \gamma > \frac{1}{2} \tag{2.83}$$

A proposal to implement the method for mechanical systems was suggested in [51]. The method handles non-constant mass, which is required for an accurate solution for ALE-ANCF cable elements. Instead of a weighted formulation of the residual equation, as the common G-α method, the dynamic equilibrium is, at every time step, enforced. This is done by rewriting the Newmark formulas in eq. (2.65) and (2.66). The acceleration, $\ddot{\boldsymbol{q}}$, is replaced with the auxiliary variable $\boldsymbol{a}$, which is an acceleration-like variable (not the true acceleration), and takes the form as in eq. (2.84) and (2.85). The weighting is done by eq. (2.86).

$$\boldsymbol{q}_{t+1} = \boldsymbol{q}_t + h\dot{\boldsymbol{q}}_t + \left(\frac{1}{2} - \beta\right) h^2 \ddot{\boldsymbol{a}}_t + \beta h^2 \ddot{\boldsymbol{a}}_{t+1} \tag{2.84}$$

$$\dot{\boldsymbol{q}}_{t+1} = \dot{\boldsymbol{q}}_t + (1-\gamma)h\ddot{\boldsymbol{a}}_t + \gamma h\ddot{\boldsymbol{a}}_{t+1} \tag{2.85}$$

$$(1-\alpha_m)\boldsymbol{a}_{t+1} + \alpha_m \boldsymbol{a}_t = (1-\alpha_f)\ddot{\boldsymbol{q}}_{t+1} + \alpha_f \ddot{\boldsymbol{q}}_t \tag{2.86}$$

The solution procedure follows the algorithm in [51]. $\boldsymbol{S}_T$ takes the form as in eq. (2.87), where β' and γ' are defined in eq. (2.88) and (2.89). The mass $\boldsymbol{M}$, damping $\boldsymbol{C}_T$ and stiffness $\boldsymbol{K}_T$ follows the same derivation as in eq. (2.59). The error criterion in the algorithm is modified and updated with eq. (2.78), with a sufficiently small limit. For the first iteration each time step $\boldsymbol{a}_0 = \ddot{\boldsymbol{q}}_0$.

$$\boldsymbol{S}_T = \begin{bmatrix} \boldsymbol{M}\beta' + \boldsymbol{C}_T\gamma' + \boldsymbol{K}_T & \boldsymbol{G}^T \\ \boldsymbol{G} & \boldsymbol{0} \end{bmatrix} \tag{2.87}$$

$$\beta' = \frac{1-\alpha_m}{\beta h^2(1-\alpha_f)} \tag{2.88}$$

$$\gamma' = \frac{\gamma}{\beta h} \tag{2.89}$$

The solution procedure for the G-α used in the program is outlined in Fig. 2.5. The procedure is based on algorithm 1 in [51]. The procedure starts by initial configurations of the model where the cable elements are defined, constraints are set, and material parameters are set. In addition the parameters for the solver: α_m, α_f, critical error limit, time-step and end time are set. The first iteration is a predictor step, where the position and velocity is set. It then continues to the corrector iterations where the forces and residuals are computed. Based on this, the increments for position, velocity, acceleration, and Lagrange multipliers are obtained. Position, velocity, acceleration, and Lagrange multipliers are updated and corrected based on the increments. If the error residual is larger than the error criterion, the corrector iteration is repeated. If the error criterion is met, the model is updated and data stored, before it continues to the next time step. When the simulation has reached the maximum time, it ends.

The G-α procedure is tested as one of the numerical time integrators in both Paper 2 and Paper 3. In Paper 2 it takes the form as presented above. For Paper 3 it is presented in Sec. 2.9.2, where the governing equations have a slightly different form.

To further stabilize the solution procedure the preconditioning strategy proposed by [42] could be implemented. Preconditioning is simply a transformation of the matrices in the system making it more suitable for numerical solving methods, and less prone to numerical errors. The solution strategy takes the linear system from eq. (2.76) or (2.87), and redefines from eq. (2.90) to eq. (2.91). The new variables are defined in eq. (2.92) with the preconditioners in eq. (2.93). The subscript n indicates the size of free nodes, and m indicates the size of constraints.

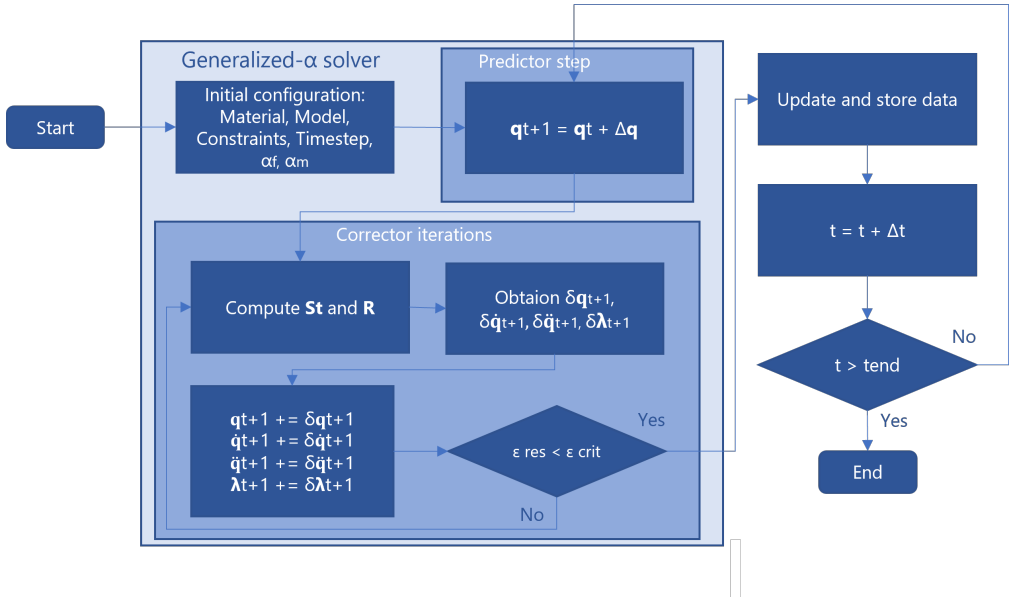

Figure 2.5: Outline of the solution procedure with numerical integration algorithm for the governing equations with the G-α method.

$$\boldsymbol{S}_T \Delta \boldsymbol{x} = \; -\boldsymbol{R} \tag{2.90}$$

$$\bar{\boldsymbol{S}}_T \Delta \bar{\boldsymbol{x}} = \; -\bar{\boldsymbol{R}} \tag{2.91}$$

$$\begin{aligned} \bar{\boldsymbol{S}}_T &= \boldsymbol{D}_L \boldsymbol{S}_T \boldsymbol{D}_R \\ \bar{\boldsymbol{R}} &= \boldsymbol{D}_L \boldsymbol{R} \\ \boldsymbol{x} &= \boldsymbol{D}_R \bar{\boldsymbol{x}} \end{aligned} \tag{2.92}$$

$$\begin{aligned} \boldsymbol{D}_R &= \begin{bmatrix} \boldsymbol{I}_n \beta h^2 & \boldsymbol{0} \\ \boldsymbol{0} & \boldsymbol{I}_m \end{bmatrix} \\ \boldsymbol{D}_L &= \begin{bmatrix} \boldsymbol{I}_n & \boldsymbol{0} \\ \boldsymbol{0} & \frac{1}{\beta h^2} \boldsymbol{I}_m \end{bmatrix} \end{aligned} \tag{2.93}$$

2.4.3 Differentiation of the Curvature, κ

As part of the G-α procedure, the system equations for a mechanical system has to be differentiated, eq. (2.42). The following section will present the step-by-step solution for the

differentiation of the curvature, κ. q_j and q_k represent the vector with generalized coordinates in eq. (2.1) written with index notation in separate axes, see Sec. 3.4.

Prior to the differentiation of the curvature, some background calculations are done. The magnitude of the slope vector is found by:

$$\left\|\boldsymbol{r'}\right\| = \sqrt{r_x^2 + r_y'^2 + r_z'^2} = \sqrt{\boldsymbol{r'}^T\boldsymbol{r'}} \tag{2.94}$$

Differentiation of the magnitude of the slope vector with exponent is found by:

$$\begin{aligned}\frac{\partial \left\|\boldsymbol{r'}\right\|^n}{\partial q_j} &= n\left\|\boldsymbol{r'}\right\|^{n-1}\frac{\partial \left\|\boldsymbol{r'}\right\|}{\partial q_j} = n\left\|\boldsymbol{r'}\right\|^{n-1}\frac{\partial\sqrt{\boldsymbol{r'}^T\boldsymbol{r'}}}{\partial q_j} \\ &= n\left\|\boldsymbol{r'}\right\|^{n-1}\frac{1}{2\sqrt{\boldsymbol{r'}^T\boldsymbol{r'}}}\frac{\partial \boldsymbol{r'}^2}{\partial q_j} = n\left\|\boldsymbol{r'}\right\|^{n-2}\frac{1}{2}2\boldsymbol{r'}^T\frac{\partial \boldsymbol{r'}}{\partial q_j} \\ &= n\left\|\boldsymbol{r'}\right\|^{n-2}\boldsymbol{r'}^T\frac{\partial \boldsymbol{r'}}{\partial q_j}\end{aligned} \tag{2.95}$$

The second derivative of the magnitude of the slope vector with exponent is found by the product rule and eq. (2.95), resulting in:

$$\begin{aligned}\frac{\partial^2 \left\|\boldsymbol{r'}\right\|^n}{\partial q^2} &= \frac{\partial}{\partial q_k}\left(n\left\|\boldsymbol{r'}\right\|^{(n-2)}\boldsymbol{r'}^T\frac{\partial \boldsymbol{r'}}{\partial q_j}\right) \\ &= n\left(\frac{\partial \left\|\boldsymbol{r'}\right\|^{(n-2)}}{\partial q_k}\boldsymbol{r'}^T\frac{\partial \boldsymbol{r'}}{\partial q_j} + \left\|\boldsymbol{r'}\right\|^{(n-2)}\frac{\partial \boldsymbol{r'}}{\partial q_k}\frac{\partial \boldsymbol{r'}}{\partial q_j} + \right. \\ &\quad \left.\left\|\boldsymbol{r'}\right\|^{(n-2)}\boldsymbol{r'}^T\frac{\partial^2 \boldsymbol{r'}}{\partial q_j \partial q_k}\right) \\ &= n\left(\left((n-2)\left\|\boldsymbol{r'}\right\|^{n-4}\boldsymbol{r'}^T\frac{\partial \boldsymbol{r'}}{\partial q_k}\right)\boldsymbol{r'}^T\frac{\partial \boldsymbol{r'}}{\partial q_j} + \right. \\ &\quad \left.\left\|\boldsymbol{r'}\right\|^{(n-2)}\frac{\partial \boldsymbol{r'}}{\partial q_k}\frac{\partial \boldsymbol{r'}}{\partial q_j} + \left\|\boldsymbol{r'}\right\|^{(n-2)}\boldsymbol{r'}^T\frac{\partial^2 \boldsymbol{r'}}{\partial q_j \partial q_k}\right)\end{aligned} \tag{2.96}$$

Differentiation of the cross product of the two vectors $\boldsymbol{A}(x)$ and $\boldsymbol{B}(x)$ is found by:

$$\begin{aligned}\frac{\partial}{\partial x}\left(\boldsymbol{A}\times\boldsymbol{B}\right) &= \frac{\partial}{\partial x}\begin{bmatrix} A_2B_3 - A_3B_2 \\ A_3B_1 - A_1B_3 \\ A_1B_2 - A_2B_1 \end{bmatrix} \\ &= \begin{bmatrix} \left(\frac{\partial A_2}{\partial x}B_3 + A_2\frac{\partial B_3}{\partial x}\right) - \left(\frac{\partial A_3}{\partial x}B_2 + A_3\frac{\partial B_2}{\partial x}\right) \\ \left(\frac{\partial A_3}{\partial x}B_1 + A_3\frac{\partial B_1}{\partial x}\right) - \left(\frac{\partial A_1}{\partial x}B_3 + A_1\frac{\partial B_3}{\partial x}\right) \\ \left(\frac{\partial A_1}{\partial x}B_2 + A_1\frac{\partial B_2}{\partial x}\right) - \left(\frac{\partial A_2}{\partial x}B_1 + A_2\frac{\partial B_1}{\partial x}\right) \end{bmatrix} \\ &= \frac{\partial \boldsymbol{A}}{\partial x}\times\boldsymbol{B} + \boldsymbol{A}\times\frac{\partial \boldsymbol{B}}{\partial x}\end{aligned} \tag{2.97}$$

From eq. (2.97) the differentiation of the cross product of $\boldsymbol{r}'$ and $\boldsymbol{r}''$ is found by:

$$\frac{\partial\left(\boldsymbol{r}'\times\boldsymbol{r}''\right)}{\partial q_j} = \frac{\partial \boldsymbol{r}'}{\partial q_j}\times\boldsymbol{r}'' + \boldsymbol{r}'\times\frac{\partial \boldsymbol{r}''}{\partial q_j} \tag{2.98}$$

Differentiation of magnitude is found in eq. (2.99), by combining (2.98) and (2.95).

$$\begin{aligned}\frac{\partial\left\|\boldsymbol{r}'\times\boldsymbol{r}''\right\|}{\partial q_j} &= \frac{\partial\sqrt{\left(\boldsymbol{r}'\times\boldsymbol{r}''\right)^T\left(\boldsymbol{r}'\times\boldsymbol{r}''\right)}}{\partial q_j} \\ &= \frac{\frac{\partial}{\partial q_j}\left(\left(\boldsymbol{r}'\times\boldsymbol{r}''\right)^T\left(\boldsymbol{r}'\times\boldsymbol{r}''\right)\right)}{2\sqrt{\left(\boldsymbol{r}'\times\boldsymbol{r}''\right)^T\left(\boldsymbol{r}'\times\boldsymbol{r}''\right)}} \\ &= \frac{\frac{\partial(\boldsymbol{r}'\times\boldsymbol{r}'')^T}{\partial q_j}\left(\boldsymbol{r}'\times\boldsymbol{r}''\right) + \left(\boldsymbol{r}'\times\boldsymbol{r}''\right)^T\frac{\partial(\boldsymbol{r}'\times\boldsymbol{r}'')}{\partial q_j}}{2\sqrt{\left(\boldsymbol{r}'\times\boldsymbol{r}''\right)^T\left(\boldsymbol{r}'\times\boldsymbol{r}''\right)}} \\ &= \frac{2\left(\boldsymbol{r}'\times\boldsymbol{r}''\right)^T\frac{\partial(\boldsymbol{r}'\times\boldsymbol{r}'')}{\partial q_j}}{2\left\|\boldsymbol{r}'\times\boldsymbol{r}''\right\|} \\ &= \frac{2\left(\boldsymbol{r}'\times\boldsymbol{r}''\right)^T\left(\frac{\partial \boldsymbol{r}'}{\partial q}\times\boldsymbol{r}'' + \boldsymbol{r}'\times\frac{\partial \boldsymbol{r}''}{\partial q_j}\right)}{2\left\|\boldsymbol{r}'\times\boldsymbol{r}''\right\|} \\ &= \frac{\left(\boldsymbol{r}'\times\boldsymbol{r}''\right)^T}{\left\|\boldsymbol{r}'\times\boldsymbol{r}''\right\|}\left(\frac{\partial \boldsymbol{r}'}{\partial q_j}\times\boldsymbol{r}'' + \boldsymbol{r}'\times\frac{\partial \boldsymbol{r}''}{\partial q_j}\right)\end{aligned} \tag{2.99}$$

Further expanding the expression, when combining eq. (2.98) and (2.99) with the quotient rule, eq. (2.100) is solved.

$$\begin{aligned}\frac{\partial}{\partial q}\left(\frac{(\boldsymbol{r}'\times\boldsymbol{r}'')^T}{\|\boldsymbol{r}'\times\boldsymbol{r}''\|}\right) &= \left(\frac{\frac{\partial(\boldsymbol{r}'\times\boldsymbol{r}'')^T}{\partial q}\|\boldsymbol{r}'\times\boldsymbol{r}''\| - (\boldsymbol{r}'\times\boldsymbol{r}'')^T\frac{\partial\|\boldsymbol{r}'\times\boldsymbol{r}''\|}{\partial q}}{\|\boldsymbol{r}'\times\boldsymbol{r}''\|^2}\right)\\ &= \frac{\left(\frac{\partial\boldsymbol{r}'}{\partial q}\times\boldsymbol{r}''+\boldsymbol{r}'\times\frac{\partial\boldsymbol{r}''}{\partial q}\right)^T\|\boldsymbol{r}'\times\boldsymbol{r}''\|}{\|\boldsymbol{r}'\times\boldsymbol{r}''\|^2} - \\ &\quad\frac{(\boldsymbol{r}'\times\boldsymbol{r}'')^T\frac{(\boldsymbol{r}'\times\boldsymbol{r}'')^T}{\|\boldsymbol{r}'\times\boldsymbol{r}''\|}\left(\frac{\partial\boldsymbol{r}'}{\partial q}\times\boldsymbol{r}''+\boldsymbol{r}'\times\frac{\partial\boldsymbol{r}''}{\partial q}\right)}{\|\boldsymbol{r}'\times\boldsymbol{r}''\|^2}\end{aligned} \tag{2.100}$$

The second derivative of the magnitude of cross product is found by using the product rule on eq. (2.99), where the quotient rule has to be used to solve this, in addition to eq. (2.98) and (2.100):

$$\begin{aligned}\frac{\partial^2\|\boldsymbol{r}'\times\boldsymbol{r}''\|}{\partial q^2} &= \frac{\partial}{\partial q_k}\left(\frac{(\boldsymbol{r}'\times\boldsymbol{r}'')^T}{\|\boldsymbol{r}'\times\boldsymbol{r}''\|}\left(\frac{\partial\boldsymbol{r}'}{\partial q_j}\times\boldsymbol{r}''+\boldsymbol{r}'\times\frac{\partial\boldsymbol{r}''}{\partial q_j}\right)\right)\\ &= \frac{\partial}{\partial q_k}\left(\frac{(\boldsymbol{r}'\times\boldsymbol{r}'')^T}{\|\boldsymbol{r}'\times\boldsymbol{r}''\|}\right)\left(\frac{\partial\boldsymbol{r}'}{\partial q_j}\times\boldsymbol{r}''+\boldsymbol{r}'\times\frac{\partial\boldsymbol{r}''}{\partial q_j}\right)+\\ &\quad\left(\frac{(\boldsymbol{r}'\times\boldsymbol{r}'')^T}{\|\boldsymbol{r}'\times\boldsymbol{r}''\|}\right)\frac{\partial}{\partial q_k}\left(\frac{\partial\boldsymbol{r}'}{\partial q_j}\times\boldsymbol{r}''+\boldsymbol{r}'\times\frac{\partial\boldsymbol{r}''}{\partial q_j}\right)\\ &= \left(\frac{\frac{\partial(\boldsymbol{r}'\times\boldsymbol{r}'')^T}{\partial q_k}\|\boldsymbol{r}'\times\boldsymbol{r}''\| - (\boldsymbol{r}'\times\boldsymbol{r}'')^T\frac{\partial\|\boldsymbol{r}'\times\boldsymbol{r}''\|}{\partial q_k}}{\|\boldsymbol{r}'\times\boldsymbol{r}''\|^2}\right)\left(\frac{\partial\boldsymbol{r}'}{\partial q_j}\times\boldsymbol{r}''+\boldsymbol{r}'\times\frac{\partial\boldsymbol{r}''}{\partial q_j}\right)+\\ &\quad\left(\frac{(\boldsymbol{r}'\times\boldsymbol{r}'')^T}{\|\boldsymbol{r}'\times\boldsymbol{r}''\|}\right)\left(\frac{\partial^2\boldsymbol{r}'}{\partial q_j\partial q_k}\times\boldsymbol{r}''+\frac{\partial\boldsymbol{r}'}{\partial q_j}\times\frac{\partial\boldsymbol{r}''}{\partial q_k}+\frac{\partial\boldsymbol{r}'}{\partial q_k}\times\frac{\partial\boldsymbol{r}''}{\partial q_j}+\boldsymbol{r}'\times\frac{\partial^2\boldsymbol{r}''}{\partial q_j\partial q_k}\right)\end{aligned} \tag{2.101}$$

The curvature is defined by eq. (2.55). The differentiation of position and velocity for the curvature, eq. (2.102) and (2.103), are found by the quotient rule in combination with eq. (2.95) and (2.99).

$$\begin{aligned}\frac{\partial\kappa}{\partial q} = \frac{\partial}{\partial q_j}\left(\frac{\|\boldsymbol{r}'\times\boldsymbol{r}''\|}{\|\boldsymbol{r}'\|^3}\right) &= \frac{\frac{\partial}{\partial q_j}\left(\|\boldsymbol{r}'\times\boldsymbol{r}''\|\right)\|\boldsymbol{r}'\|^3 - \|\boldsymbol{r}'\times\boldsymbol{r}''\|\frac{\partial}{\partial q_j}\left(\|\boldsymbol{r}'\|^3\right)}{\left(\|\boldsymbol{r}'\|^3\right)^2}\\ &= \frac{\left(\frac{(\boldsymbol{r}'\times\boldsymbol{r}'')^T}{\|\boldsymbol{r}'\times\boldsymbol{r}''\|}\left(\frac{\partial\boldsymbol{r}'}{\partial q_j}\times\boldsymbol{r}''+\boldsymbol{r}'\times\frac{\partial\boldsymbol{r}''}{\partial q_j}\right)\right)\|\boldsymbol{r}'\|^3 - \|\boldsymbol{r}'\times\boldsymbol{r}''\|\left(3\|\boldsymbol{r}'\|\frac{\partial\boldsymbol{r}'}{\partial q_j}^T\boldsymbol{r}'\right)}{\|\boldsymbol{r}'\|^6}\end{aligned} \tag{2.102}$$

$$\begin{aligned}\frac{\partial \kappa}{\partial \dot{q}} &= \frac{\partial}{\partial \dot{q}_j}\left(\frac{\|\boldsymbol{r}' \times \boldsymbol{r}''\|}{\|\boldsymbol{r}'\|^3}\right) = \frac{\frac{\partial}{\partial \dot{q}_j}\left(\|\boldsymbol{r}' \times \boldsymbol{r}''\|\right)\|\boldsymbol{r}'\|^3 - \|\boldsymbol{r}' \times \boldsymbol{r}''\|\frac{\partial}{\partial \dot{q}_j}\left(\|\boldsymbol{r}'\|^3\right)}{\left(\|\boldsymbol{r}'\|^3\right)^2} \\ &= \frac{\left(\frac{(\boldsymbol{r}'\times\boldsymbol{r}'')^T}{\|\boldsymbol{r}'\times\boldsymbol{r}''\|}\left(\frac{\partial \boldsymbol{r}'}{\partial \dot{q}_j}\times\boldsymbol{r}'' + \boldsymbol{r}'\times\frac{\partial \boldsymbol{r}''}{\partial \dot{q}_j}\right)\right)\|\boldsymbol{r}'\|^3 - \|\boldsymbol{r}'\times\boldsymbol{r}''\|\left(3\|\boldsymbol{r}'\|\frac{\partial \boldsymbol{r}'}{\partial \dot{q}_j}^T\boldsymbol{r}'\right)}{\|\boldsymbol{r}'\|^6}\end{aligned} \tag{2.103}$$

The double differentiation of position and velocity for the curvature, eq. (2.104) and (2.105), the quotient rule and product rule are used, in combination with eq. (2.95), (2.96), (2.99) and (2.101).

$$\begin{aligned}\frac{\partial^2 \kappa}{\partial q^2} &= \frac{\partial^2}{\partial q^2}\left(\frac{\|\boldsymbol{r}' \times \boldsymbol{r}''\|}{\|\boldsymbol{r}'\|^3}\right) \\ &= \frac{\partial}{\partial q_k}\left(\frac{\frac{\partial}{\partial q_j}\left(\|\boldsymbol{r}' \times \boldsymbol{r}''\|\right)\|\boldsymbol{r}'\|^3 - \|\boldsymbol{r}' \times \boldsymbol{r}''\|\frac{\partial}{\partial q_j}\left(\|\boldsymbol{r}'\|^3\right)}{\|\boldsymbol{r}'\|^6}\right) \\ &= \frac{\left(\frac{\partial^2}{\partial q^2}\left(\|\boldsymbol{r}' \times \boldsymbol{r}''\|\right)\|\boldsymbol{r}'\|^3 + \frac{\partial}{\partial q_j}\left(\|\boldsymbol{r}' \times \boldsymbol{r}''\|\right)\frac{\partial}{\partial q_k}\|\boldsymbol{r}'\|^3\right)}{\|\boldsymbol{r}'\|^6} - \\ &\quad \frac{\left(\frac{\partial}{\partial q_k}\|\boldsymbol{r}' \times \boldsymbol{r}''\|\frac{\partial}{\partial q_j}\left(\|\boldsymbol{r}'\|^3\right) + \|\boldsymbol{r}' \times \boldsymbol{r}''\|\frac{\partial^2}{\partial q^2}\left(\|\boldsymbol{r}'\|^3\right)\right)}{\|\boldsymbol{r}'\|^6} - \\ &\quad \frac{\left(\frac{\partial}{\partial q_j}\left(\|\boldsymbol{r}' \times \boldsymbol{r}''\|\right)\|\boldsymbol{r}'\|^3 - \|\boldsymbol{r}' \times \boldsymbol{r}''\|\frac{\partial}{\partial q_j}\left(\|\boldsymbol{r}'\|^3\right)\right)6\boldsymbol{r}'^T\frac{\partial \boldsymbol{r}'}{\partial q_k}}{\|\boldsymbol{r}'\|^8}\end{aligned} \tag{2.104}$$

$$\begin{aligned}\frac{\partial^2 \kappa}{\partial q \partial \dot{q}} &= \frac{\partial^2}{\partial q \partial \dot{q}}\left(\frac{\|\boldsymbol{r}' \times \boldsymbol{r}''\|}{\|\boldsymbol{r}'\|^3}\right) \\ &= \frac{\partial}{\partial \dot{q}_k}\left(\frac{\frac{\partial}{\partial q_j}\left(\|\boldsymbol{r}' \times \boldsymbol{r}''\|\right)\|\boldsymbol{r}'\|^3 - \|\boldsymbol{r}' \times \boldsymbol{r}''\|\frac{\partial}{\partial q_j}\left(\|\boldsymbol{r}'\|^3\right)}{\|\boldsymbol{r}'\|^6}\right) \\ &= \frac{\left(\frac{\partial^2}{\partial q^2}\left(\|\boldsymbol{r}' \times \boldsymbol{r}''\|\right)\|\boldsymbol{r}'\|^3 + \frac{\partial}{\partial q_j}\left(\|\boldsymbol{r}' \times \boldsymbol{r}''\|\right)\frac{\partial}{\partial \dot{q}_k}\|\boldsymbol{r}'\|^3\right)}{\|\boldsymbol{r}'\|^6} - \\ &\quad \frac{\left(\frac{\partial}{\partial \dot{q}_k}\|\boldsymbol{r}' \times \boldsymbol{r}''\|\frac{\partial}{\partial q_j}\left(\|\boldsymbol{r}'\|^3\right) + \|\boldsymbol{r}' \times \boldsymbol{r}''\|\frac{\partial^2}{\partial q \partial \dot{q}}\left(\|\boldsymbol{r}'\|^3\right)\right)}{\left(\|\boldsymbol{r}'\|\right)} - \\ &\quad \frac{\left(\frac{\partial}{\partial q_j}\left(\|\boldsymbol{r}' \times \boldsymbol{r}''\|\right)\|\boldsymbol{r}'\|^3 - \|\boldsymbol{r}' \times \boldsymbol{r}''\|\frac{\partial}{\partial q_j}\left(\|\boldsymbol{r}'\|^3\right)\right)6\boldsymbol{r}'^T\frac{\partial \boldsymbol{r}'}{\partial \dot{q}_k}}{\|\boldsymbol{r}'\|^8}\end{aligned} \tag{2.105}$$

Curvature rate, being the change in curvature over time, is presented:

$$\begin{aligned}
\dot{\kappa} &= \frac{d}{dt}\left(\frac{\|\boldsymbol{r}' \times \boldsymbol{r}''\|}{\|\boldsymbol{r}'\|^3}\right) \\
&= \frac{\frac{d}{dt}\left(\|\boldsymbol{r}' \times \boldsymbol{r}''\|\right)\|\boldsymbol{r}'\|^3 - \|\boldsymbol{r}' \times \boldsymbol{r}''\|\,\frac{d}{dt}\left(\|\boldsymbol{r}'\|^3\right)}{\left(\|\boldsymbol{r}'\|^3\right)^2} \\
&= \frac{\frac{(\boldsymbol{r}' \times \boldsymbol{r}'')^T}{\|\boldsymbol{r}' \times \boldsymbol{r}''\|}\left(\dot{\boldsymbol{r}}' \times \boldsymbol{r}'' + \boldsymbol{r}' \times \dot{\boldsymbol{r}}''\right)\|\boldsymbol{r}'\|^3 - \|\boldsymbol{r}' \times \boldsymbol{r}''\|\,3\,\|\boldsymbol{r}'\|\,\boldsymbol{r}'^T\dot{\boldsymbol{r}}'}{\|\boldsymbol{r}'\|^6}
\end{aligned} \tag{2.106}$$

The derivatives of position and velocity for the curvature rate, eq. (2.107) and (2.108), are found by the quotient rule in combination with eq. (2.98) and (2.100). Placeholders are used to make it easier to read.

$$
\begin{aligned}
\frac{\partial \dot{\kappa}}{\partial q} &= \frac{\partial}{\partial q}\left(\frac{\left(\frac{(\boldsymbol{r}'\times\boldsymbol{r}'')^T}{\|\boldsymbol{r}'\times\boldsymbol{r}''\|}\left(\dot{\boldsymbol{r}}'\times\boldsymbol{r}''+\boldsymbol{r}'\times\dot{\boldsymbol{r}}''\right)\|\boldsymbol{r}'\|^3\right)-\left(\|\boldsymbol{r}'\times\boldsymbol{r}''\|\,3\,\|\boldsymbol{r}'\|\,\boldsymbol{r}'^T\dot{\boldsymbol{r}}'\right)}{\|\boldsymbol{r}'\|^6}\right)\\
&= \frac{\partial}{\partial q}\left(\frac{A-B}{C}\right)\\
&= \frac{\left(\frac{\partial A}{\partial q}-\frac{\partial B}{\partial q}\right)C-(A-B)\frac{\partial C}{\partial q}}{C^2}\\
\frac{\partial A}{\partial q} &= \frac{\partial\left(\frac{(\boldsymbol{r}'\times\boldsymbol{r}'')^T}{\|\boldsymbol{r}'\times\boldsymbol{r}''\|}\left(\dot{\boldsymbol{r}}'\times\boldsymbol{r}''+\boldsymbol{r}'\times\dot{\boldsymbol{r}}''\right)\|\boldsymbol{r}'\|^3\right)}{\partial q}\\
&= \frac{\partial}{\partial q}\left(\frac{(\boldsymbol{r}'\times\boldsymbol{r}'')^T}{\|\boldsymbol{r}'\times\boldsymbol{r}''\|}\right)\left(\dot{\boldsymbol{r}}'\times\boldsymbol{r}''+\boldsymbol{r}'\times\dot{\boldsymbol{r}}''\right)\|\boldsymbol{r}'\|^3+\\
&\quad\left(\frac{(\boldsymbol{r}'\times\boldsymbol{r}'')^T}{\|\boldsymbol{r}'\times\boldsymbol{r}''\|}\right)\left(\frac{\partial}{\partial q}\left(\dot{\boldsymbol{r}}'\times\boldsymbol{r}''\right)+\frac{\partial}{\partial q}\left(\boldsymbol{r}'\times\dot{\boldsymbol{r}}''\right)\right)\|\boldsymbol{r}'\|^3+\\
&\quad\left(\frac{(\boldsymbol{r}'\times\boldsymbol{r}'')^T}{\|\boldsymbol{r}'\times\boldsymbol{r}''\|}\right)\left(\dot{\boldsymbol{r}}'\times\boldsymbol{r}''+\boldsymbol{r}'\times\dot{\boldsymbol{r}}''\right)3\,\|\boldsymbol{r}'\|\,\boldsymbol{r}'^T\frac{\partial\boldsymbol{r}'}{\partial q}\\
\frac{\partial B}{\partial q} &= \frac{\partial\left(\|\boldsymbol{r}'\times\boldsymbol{r}''\|\,3\,\|\boldsymbol{r}'\|\,\boldsymbol{r}'^T\dot{\boldsymbol{r}}'\right)}{\partial q}\\
&= 3\left(\frac{\partial}{\partial q}\left(\|\boldsymbol{r}'\times\boldsymbol{r}''\|\right)\|\boldsymbol{r}'\|\,\boldsymbol{r}'^T\dot{\boldsymbol{r}}'+\|\boldsymbol{r}'\times\boldsymbol{r}''\|\frac{\partial}{\partial q}\left(\|\boldsymbol{r}'\|\right)\boldsymbol{r}'^T\dot{\boldsymbol{r}}'\right)+\\
&\quad 3\left(\|\boldsymbol{r}'\times\boldsymbol{r}''\|\,\|\boldsymbol{r}'\|\frac{\partial\boldsymbol{r}'}{\partial q}^T\dot{\boldsymbol{r}}'+\|\boldsymbol{r}'\times\boldsymbol{r}''\|\,\|\boldsymbol{r}'\|\,\boldsymbol{r}'^T\frac{\partial\dot{\boldsymbol{r}}'}{\partial q}\right)\\
\frac{\partial C}{\partial q} &= \frac{\partial\left(\|\boldsymbol{r}'\|^6\right)}{\partial q}\\
&= 6\,\|\boldsymbol{r}'\|^4\,\boldsymbol{r}'\frac{\partial\boldsymbol{r}'}{\partial q}
\end{aligned}
\tag{2.107}
$$

$$
\begin{aligned}
\frac{\partial \dot{\kappa}}{\partial \dot{q}} &= \frac{\partial}{\partial \dot{q}} \left(\frac{\left(\frac{(\boldsymbol{r}' \times \boldsymbol{r}'')^T}{\|\boldsymbol{r}' \times \boldsymbol{r}''\|} \left(\dot{\boldsymbol{r}}' \times \boldsymbol{r}'' + \boldsymbol{r}' \times \dot{\boldsymbol{r}}'' \right) \|\boldsymbol{r}'\|^3 \right) - \left(\|\boldsymbol{r}' \times \boldsymbol{r}''\| \, 3 \, \|\boldsymbol{r}'\| \, \boldsymbol{r}'^T \dot{\boldsymbol{r}}' \right)}{\|\boldsymbol{r}'\|^6} \right) \\
&= \frac{\partial}{\partial \dot{q}} \left(\frac{A - B}{C} \right) \\
&= \frac{\left(\frac{\partial A}{\partial \dot{q}} - \frac{\partial B}{\partial \dot{q}} \right) C - (A - B) \frac{\partial C}{\partial \dot{q}}}{C^2} \\
\frac{\partial A}{\partial \dot{q}} &= \frac{\partial \left(\frac{(\boldsymbol{r}' \times \boldsymbol{r}'')^T}{\|\boldsymbol{r}' \times \boldsymbol{r}''\|} \left(\dot{\boldsymbol{r}}' \times \boldsymbol{r}'' + \boldsymbol{r}' \times \dot{\boldsymbol{r}}'' \right) \|\boldsymbol{r}'\|^3 \right)}{\partial \dot{q}} \\
&= \frac{\partial}{\partial \dot{q}} \left(\frac{(\boldsymbol{r}' \times \boldsymbol{r}'')^T}{\|\boldsymbol{r}' \times \boldsymbol{r}''\|} \right) \left(\dot{\boldsymbol{r}}' \times \boldsymbol{r}'' + \boldsymbol{r}' \times \dot{\boldsymbol{r}}'' \right) \|\boldsymbol{r}'\|^3 + \\
&\quad \left(\frac{(\boldsymbol{r}' \times \boldsymbol{r}'')^T}{\|\boldsymbol{r}' \times \boldsymbol{r}''\|} \right) \left(\frac{\partial}{\partial \dot{q}} \left(\dot{\boldsymbol{r}}' \times \boldsymbol{r}'' \right) + \frac{\partial}{\partial \dot{q}} \left(\boldsymbol{r}' \times \dot{\boldsymbol{r}}'' \right) \right) \|\boldsymbol{r}'\|^3 + \\
&\quad \left(\frac{(\boldsymbol{r}' \times \boldsymbol{r}'')^T}{\|\boldsymbol{r}' \times \boldsymbol{r}''\|} \right) \left(\dot{\boldsymbol{r}}' \times \boldsymbol{r}'' + \boldsymbol{r}' \times \dot{\boldsymbol{r}}'' \right) 3 \, \|\boldsymbol{r}'\| \, \boldsymbol{r}'^T \frac{\partial \boldsymbol{r}'}{\partial \dot{q}} \\
\frac{\partial B}{\partial \dot{q}} &= \frac{\partial \left(\|\boldsymbol{r}' \times \boldsymbol{r}''\| \, 3 \, \|\boldsymbol{r}'\| \, \boldsymbol{r}'^T \dot{\boldsymbol{r}}' \right)}{\partial \dot{q}} \\
&= 3 \left(\frac{\partial}{\partial \dot{q}} \left(\|\boldsymbol{r}' \times \boldsymbol{r}''\| \right) \|\boldsymbol{r}'\| \, \boldsymbol{r}'^T \dot{\boldsymbol{r}}' + \|\boldsymbol{r}' \times \boldsymbol{r}''\| \, \frac{\partial}{\partial \dot{q}} \left(\|\boldsymbol{r}'\| \right) \boldsymbol{r}'^T \dot{\boldsymbol{r}}' \right) + \\
&\quad 3 \left(\|\boldsymbol{r}' \times \boldsymbol{r}''\| \, \|\boldsymbol{r}'\| \, \frac{\partial \boldsymbol{r}'}{\partial \dot{q}}^T \dot{\boldsymbol{r}}' + \|\boldsymbol{r}' \times \boldsymbol{r}''\| \, \|\boldsymbol{r}'\| \, \boldsymbol{r}'^T \frac{\partial \dot{\boldsymbol{r}}'}{\partial \dot{q}} \right) \\
\frac{\partial C}{\partial \dot{q}} &= \frac{\partial \left(\|\boldsymbol{r}'\|^6 \right)}{\partial \dot{q}} \\
&= 6 \, \|\boldsymbol{r}'\|^4 \, \boldsymbol{r}' \frac{\partial \boldsymbol{r}'}{\partial \dot{q}}
\end{aligned}
\tag{2.108}
$$

2.4.4 Runge Kutta - RK4

RK4 has often been used in similar studies, and is thus an evident candidate for a numerical study with respect to explicit versus implicit time-integration. The Runge-Kutta methods originated more than 100 years ago from the famous paper by C. Runge [52]. A very readable treatise on the history of the Runge-Kutta methods was written by J.C. Butcher [53]. Butcher is also the originator for the famous Butcher tables for presenting the Runge-Kutta factors.

RK4 is an explicit time integrator, which means that the state at the next time-step can be calculated based solely on variables at previous time-steps and thus requires no equation solving. Based on the state-space formulation, eq. (2.109), with the state vector, $\boldsymbol{x}$, defined in eq. (2.110). $\boldsymbol{A}$ is the dynamic matrix, $\boldsymbol{g}(\boldsymbol{x})$ contains all the nonlinear terms, $\boldsymbol{B}$ is the input matrix, and $\boldsymbol{u}$ is the input to the system. External forces are the input to the system, given for the relevant time steps. $\boldsymbol{Q}$ is nonlinear and contains external forces, internal forces, damping forces and additional inertia forces, eq. (2.45). For this system the stiffness and damping are nonlinear, and therefore become a part of the restoring forces $\boldsymbol{g}(\boldsymbol{x})$. The unconstrained mechanical system from (2.40), presented in eq. (2.111), can be expressed on a lower difference order if the number of unknowns are doubled. The second order DAE takes the form of a first order DAE as presented in eq. (2.112). This is the starting point for the integrator using a first order form of the system.

$$\dot{\boldsymbol{x}} = \boldsymbol{A}\boldsymbol{x} + \boldsymbol{g}(\boldsymbol{x}) + \boldsymbol{B}\boldsymbol{u} \tag{2.109}$$

$$\boldsymbol{x} = \begin{bmatrix} \boldsymbol{q} \\ \dot{\boldsymbol{q}} \end{bmatrix} \tag{2.110}$$

$$\boldsymbol{M}\ddot{\boldsymbol{q}} = \boldsymbol{Q}(\boldsymbol{q}, \dot{\boldsymbol{q}}, t) = \boldsymbol{Q}_f - \boldsymbol{Q}_{int} - \boldsymbol{Q}_{damp} - \boldsymbol{Q}_p \tag{2.111}$$

$$\begin{aligned} &\frac{d}{dt}\begin{bmatrix} \boldsymbol{q} \\ \dot{\boldsymbol{q}} \end{bmatrix} \\ &= \begin{bmatrix} \boldsymbol{0} & \boldsymbol{I} \\ \boldsymbol{0} & \boldsymbol{0} \end{bmatrix}\begin{bmatrix} \boldsymbol{q} \\ \dot{\boldsymbol{q}} \end{bmatrix} + \begin{bmatrix} \boldsymbol{0} \\ -\boldsymbol{M}^{-1}(\boldsymbol{Q}_{int} + \boldsymbol{Q}_{damp} + \boldsymbol{Q}_p) \end{bmatrix} + \begin{bmatrix} \boldsymbol{0} \\ \boldsymbol{M}^{-1} \end{bmatrix}\boldsymbol{Q}_f \end{aligned} \tag{2.112}$$

For the solver used in this thesis, the time increments are constant. The solver advances, $\boldsymbol{x}$, of the general non-homogeneous first order ordinary differential equations in eq. (2.113) with a time-step, h. The goal is to find the state of the system at $\boldsymbol{x}(t+h)$. This is done by taking the known external forces as input. The initial conditions are given as $\boldsymbol{x}(0) = \boldsymbol{x}_0$. The solution procedure for RK4 calculates $\dot{\boldsymbol{x}}$ four times each time increment, eq. (2.114). The four derivatives are used in eq. (2.115) to construct $\boldsymbol{x}$ for the next time step. For further advancement in time, the procedure is repeated.

$$\dot{\boldsymbol{x}}(t) = f(t, \boldsymbol{x}(t), \boldsymbol{u}(t)), \qquad \boldsymbol{x}(0) = \boldsymbol{x}_0 \tag{2.113}$$

$$\dot{\boldsymbol{x}}_1 = f(t, \boldsymbol{x}(t), \boldsymbol{u}(t)) \tag{2.114a}$$
$$\dot{\boldsymbol{x}}_2 = f\left(t + \frac{h}{2}, \boldsymbol{x}(t) + \dot{\boldsymbol{x}}_1 \frac{h}{2}, \boldsymbol{u}\left(t + \frac{h}{2}\right)\right) \tag{2.114b}$$
$$\dot{\boldsymbol{x}}_3 = f\left(t + \frac{h}{2}, \boldsymbol{x}(t) + \dot{\boldsymbol{x}}_2 \frac{h}{2}, \boldsymbol{u}\left(t + \frac{h}{2}\right)\right) \tag{2.114c}$$
$$\dot{\boldsymbol{x}}_4 = f\left(t + h, \boldsymbol{x}(t) + \dot{\boldsymbol{x}}_3 h, \boldsymbol{u}\left(t + h\right)\right) \tag{2.114d}$$

$$\boldsymbol{x}(t + h) = \boldsymbol{x}(t) + (\dot{\boldsymbol{x}}_1 + 2(\dot{\boldsymbol{x}}_2 + \dot{\boldsymbol{x}}_3) + \dot{\boldsymbol{x}}_4)\frac{h}{6} \tag{2.115}$$

2.4.5 Runge Kutta for Constrained Systems

The problem of solving a mechanical system by Runge Kutta is studied in several works, and different approaches have been attempted, with [54], [55] and [56] as examples. Recommended books on the topic are [57] and [41]. One of the main problems using a RK solution procedure is that the mechanical system is a second order Differential Algebraic Equation (DAE) that must be reduced to a lower order. As part of the reduction, the constraint equation must be differentiated. The undesired risk with this procedure is that the accuracy in the constraints could be lost, which again causes drift in the results. The method implemented in this thesis is instead based on, [56], which starts with a Lagrangian formulation of the equations of motion describing the dynamics of a constrained multibody system, as in eq. (2.116). $\boldsymbol{v}$, represents the generalized velocities, and $\boldsymbol{\phi}$ is the constraints.

$$\dot{\boldsymbol{q}} = \boldsymbol{v} \tag{2.116a}$$
$$\boldsymbol{M}(\boldsymbol{q})\dot{\boldsymbol{v}} = \boldsymbol{Q}(\boldsymbol{q}, \boldsymbol{v}) - \boldsymbol{G}^T(\boldsymbol{q})\boldsymbol{\lambda} \tag{2.116b}$$
$$\boldsymbol{0} = \boldsymbol{\phi}(\boldsymbol{q}) \tag{2.116c}$$

A step-by-step solution to the second order differentiation of the algebraic position constraint is given by:

$$\boldsymbol{\phi} = \mathbf{0} \tag{2.117a}$$

$$\dot{\boldsymbol{\phi}} = \frac{d\boldsymbol{\phi}}{dt} = \frac{\partial \boldsymbol{\phi}}{\partial \boldsymbol{q}} \frac{\partial \boldsymbol{q}}{\partial t} + \cancelto{0}{\frac{\partial \boldsymbol{\phi}}{\partial t}} = \boldsymbol{G}\dot{\boldsymbol{q}} = \mathbf{0} \tag{2.117b}$$

$$\ddot{\boldsymbol{\phi}} = \frac{d^2\boldsymbol{\phi}}{dt^2} = \frac{d}{dt}\left(\boldsymbol{G}\dot{\boldsymbol{q}}\right) = \boldsymbol{G}\frac{d\dot{\boldsymbol{q}}}{dt} + \dot{\boldsymbol{q}}^T \frac{d\boldsymbol{G}}{dt} = \boldsymbol{G}\ddot{\boldsymbol{q}} + \dot{\boldsymbol{q}}^T \frac{\partial \boldsymbol{G}}{\partial \boldsymbol{q}} \frac{\partial \boldsymbol{q}}{\partial t} + \cancelto{0}{\frac{\partial \boldsymbol{G}}{\partial t}} \tag{2.117c}$$

$$= \boldsymbol{G}\ddot{\boldsymbol{q}} + \dot{\boldsymbol{q}}^T \frac{\partial \boldsymbol{G}}{\partial \boldsymbol{q}} \dot{\boldsymbol{q}} = \mathbf{0}$$

$$\boldsymbol{G}\ddot{\boldsymbol{q}} = -\dot{\boldsymbol{q}}^T \boldsymbol{G}_{,\boldsymbol{q}} \dot{\boldsymbol{q}} \tag{2.117d}$$

The solution procedure for $\dot{\boldsymbol{q}}^T \boldsymbol{G}_{,\boldsymbol{q}} \dot{\boldsymbol{q}}$ in eq. (2.117) is clearer when using index notation. The equation now takes the form:

$$C_i = \dot{q}_j G_{ij,q_k} \dot{q}_k \tag{2.118}$$

$\dot{q}_j$ and $\dot{q}_k$ represent the velocities of the generalized coordinates from eq. (2.1) in separate axes. According to $G_{ij} = \frac{\partial \phi_i}{\partial q_j}$, i is the number of constraints. This results in the vector C_i with size i.

Inserting the differentiation of the constraints from eq. (2.117d) into the mechanical system, it can be written in the following form:

$$\begin{bmatrix} \boldsymbol{M} & \boldsymbol{G}^T \\ \boldsymbol{G} & 0 \end{bmatrix} \begin{bmatrix} \ddot{\boldsymbol{q}} \\ \boldsymbol{\lambda} \end{bmatrix} = \begin{bmatrix} \boldsymbol{Q} \\ -\dot{\boldsymbol{q}}^T \boldsymbol{G}_{,\boldsymbol{q}} \dot{\boldsymbol{q}} \end{bmatrix} \tag{2.119}$$

where $\boldsymbol{Q}$ is defined according to eq. (2.45).

This gives the solution for the acceleration:

$$\ddot{\boldsymbol{q}} = \boldsymbol{M}^{-1}(\boldsymbol{Q} - \boldsymbol{G}^T \boldsymbol{\lambda}) \tag{2.120}$$

An expression for $\boldsymbol{\lambda}$ is found by taking eq. (2.120) and substituting it back into eq. (2.117d), to get:

$$\boldsymbol{G}\ddot{\boldsymbol{q}} = -\dot{\boldsymbol{q}}^T \boldsymbol{G}_{,\boldsymbol{q}} \dot{\boldsymbol{q}} \tag{2.121a}$$

$$\boldsymbol{G}\left(\boldsymbol{M}^{-1}\boldsymbol{Q} - \boldsymbol{M}^{-1}\boldsymbol{G}^T\boldsymbol{\lambda}\right) = -\dot{\boldsymbol{q}}^T \boldsymbol{G}_{,\boldsymbol{q}} \dot{\boldsymbol{q}} \tag{2.121b}$$

$$\boldsymbol{G}\boldsymbol{M}^{-1}\boldsymbol{G}^T\boldsymbol{\lambda} = \boldsymbol{G}\boldsymbol{M}^{-1}\boldsymbol{Q} + \dot{\boldsymbol{q}}^T \boldsymbol{G}_{,\boldsymbol{q}} \dot{\boldsymbol{q}} \tag{2.121c}$$

$$\boldsymbol{\lambda} = \left(\boldsymbol{G}\boldsymbol{M}^{-1}\boldsymbol{G}^T\right)^{-1}\left(\boldsymbol{G}\boldsymbol{M}^{-1}\boldsymbol{Q} + \dot{\boldsymbol{q}}^T \boldsymbol{G}_{,\boldsymbol{q}} \dot{\boldsymbol{q}}\right) \tag{2.121d}$$

By inserting eq. (2.121d) into the mechanical system, a first order formulation is obtained as an expression for the acceleration, eq. (2.122). It is important to note that the two

are not to be considered equal, as the constraint is a derivative. This is what makes the solution subjected to drifting.

$$\ddot{\boldsymbol{q}} = \boldsymbol{M}^{-1}\boldsymbol{Q} - \boldsymbol{M}^{-1}\boldsymbol{G}^T\left(\boldsymbol{G}\boldsymbol{M}^{-1}\boldsymbol{G}^T\right)^{-1}\left(\boldsymbol{G}\boldsymbol{M}^{-1}\boldsymbol{Q} + \dot{\boldsymbol{q}}^T\boldsymbol{G}_{,\boldsymbol{q}}\dot{\boldsymbol{q}}\right) \tag{2.122}$$

This leads to the state-space formulation used for solving by RK4 in this thesis:

$$\begin{aligned}\frac{d}{dt}\begin{bmatrix}\boldsymbol{q}\\ \dot{\boldsymbol{q}}\end{bmatrix} &= \begin{bmatrix}\boldsymbol{0} & \boldsymbol{I}\\ \boldsymbol{0} & \boldsymbol{0}\end{bmatrix}\begin{bmatrix}\boldsymbol{q}\\ \dot{\boldsymbol{q}}\end{bmatrix}\\ &+ \begin{bmatrix}\boldsymbol{0}\\ -\boldsymbol{M}^{-1}\left(\boldsymbol{Q}_{int} + \boldsymbol{Q}_{damp} + \boldsymbol{Q}_p + \boldsymbol{G}^T\left(\boldsymbol{G}\boldsymbol{M}^{-1}\boldsymbol{G}^T\right)^{-1}\left(\boldsymbol{G}\boldsymbol{M}^{-1}\boldsymbol{Q} + \dot{\boldsymbol{q}}^T\boldsymbol{G}_{,\boldsymbol{q}}\,\dot{\boldsymbol{q}}\right)\right)\end{bmatrix}\\ &+ \begin{bmatrix}\boldsymbol{0}\\ \boldsymbol{M}^{-1}\end{bmatrix}\boldsymbol{Q}_f\end{aligned} \tag{2.123}$$

The RK4 solver from eq. (2.113) to (2.115) is used to propagate eq. (2.123), providing a temporary generalized coordinate vector $\tilde{\boldsymbol{q}}$. $\tilde{\boldsymbol{q}}$ is further stabilized to a new temporary generalized coordinate vector $\hat{\boldsymbol{q}}$ through the stabilization step in eq. (2.124). A final stabilization step to get the generalized coordinate vector $\boldsymbol{q}$ is performed in eq. (2.125), before continuing to the next time step. To achieve a more robust solver the double stabilization step is recommended, [56].

$$\begin{bmatrix}\hat{\boldsymbol{q}}_{t+1}\\ \hat{\dot{\boldsymbol{q}}}_{t+1}\end{bmatrix} = \begin{bmatrix}\tilde{\boldsymbol{q}}_{t+1}\\ \tilde{\dot{\boldsymbol{q}}}_{t+1}\end{bmatrix} - \boldsymbol{F}(\tilde{\boldsymbol{q}}_{t+1}, \tilde{\dot{\boldsymbol{q}}}_{t+1})\boldsymbol{s}(\tilde{\boldsymbol{q}}_{t+1}, \tilde{\dot{\boldsymbol{q}}}_{t+1}) \tag{2.124}$$

$$\begin{bmatrix}\boldsymbol{q}_{t+1}\\ \dot{\boldsymbol{q}}_{t+1}\end{bmatrix} = \begin{bmatrix}\hat{\boldsymbol{q}}_{t+1}\\ \hat{\dot{\boldsymbol{q}}}_{t+1}\end{bmatrix} - \boldsymbol{F}(\tilde{\boldsymbol{q}}_{t+1}, \tilde{\dot{\boldsymbol{q}}}_{t+1})\boldsymbol{s}(\hat{\boldsymbol{q}}_{t+1}, \hat{\dot{\boldsymbol{q}}}_{t+1}) \tag{2.125}$$

Where $\boldsymbol{s}$ and $\boldsymbol{F}$ are defined in eq. (2.126) and (2.127), with an alternative simpler definition of $\boldsymbol{F}$ in eq. (2.128), [56].

$$\boldsymbol{s} = \begin{bmatrix}\boldsymbol{\Phi}\\ \boldsymbol{G}\dot{\boldsymbol{q}}\end{bmatrix} \tag{2.126}$$

$$\boldsymbol{F} = \boldsymbol{M}^{-1}\boldsymbol{G}^T\boldsymbol{G}(\boldsymbol{M}^{-1}\boldsymbol{G}^T)^{-1}\begin{bmatrix}\boldsymbol{I} & \boldsymbol{0}\\ \boldsymbol{0} & \boldsymbol{I}\end{bmatrix} \tag{2.127}$$

$$\boldsymbol{F} = \boldsymbol{G}^T(\boldsymbol{G}\boldsymbol{G}^T)^{-1}\begin{bmatrix}\boldsymbol{I} & \boldsymbol{0}\\ \boldsymbol{0} & \boldsymbol{I}\end{bmatrix} \tag{2.128}$$

2.5 Case 1: Cable - Cantilever Bar and RK4 Maximum Time-Step

Different attributes of the ALE-ANCF cable element can be highlighted by a cable modeled as a cantilever bar, with one free and one fixed end. The model can be used to find the maximum stable time-step for an ALE-ANCF cable element model when using the RK4 time integrator. Furthermore, the axial frequencies, the 1st and 2nd axial vibration mode for the ALE-ANCF cable element can be verified.

To predict the maximum stable time-step for the RK4 time integrator, it was investigated if the theoretical time-step for a Mass-Spring-Damper system (MSD), could be used to describe the behavior of the ALE-ANCF cable element.

The single degree of freedom problem, damped free vibration, shown in Fig. 2.6, takes the form as:

$$m\ddot{u} + c\dot{u} + ku = 0 \tag{2.129}$$

where m is the mass, k is the spring stiffness, c is the damping factor, and u is the displacement.

Assuming the solution on the form:

$$u = u_0 e^{\lambda t}, \qquad \dot{u} = u_0 \lambda e^{\lambda t}, \qquad \ddot{u} = u_0 \lambda^2 e^{\lambda t} \tag{2.130}$$

and inserting in the free vibration eq. (2.129) gives us:

$$\left(m\lambda^2 + c\lambda + k\right) u_0 e^{\lambda t} = 0 \tag{2.131}$$

where eigenvalue λ consists of a real and an imaginary part.

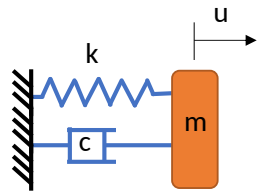

Figure 2.6: A simple 1-D Mass-Spring-Damper system.

Starting with the free vibration eq. (2.129), and assuming the solution on the form of eq. (2.130), gives us eq. (2.131). The eigenvalue λ consists of a real and an imaginary part.

$$m\ddot{u} + c\dot{u} + ku = 0 \tag{2.132}$$

$$u = u_0 e^{\lambda t}, \qquad \dot{u} = u_0 \lambda e^{\lambda t}, \qquad \ddot{u} = u_0 \lambda^2 e^{\lambda t} \tag{2.133}$$

$$\left(m\lambda^2 + c\lambda + k\right) u_0 e^{\lambda t} = 0 \tag{2.134}$$

When introducing undamped eigenfrequency ω_0, critical damping c_c and relative damping ratio ξ, the eigenvalue can be written as:

$$\lambda = \omega_0 \left(-\xi \pm i\sqrt{1-\xi^2}\right) \tag{2.135}$$

where $\omega_0 = \sqrt{\frac{k}{m}}$, $\xi = \frac{c}{c_c}$, and $c_c = 2\sqrt{km} = 2m\omega_0$

For the undamped system only the imaginary part remains, and we have the non-trivial solution leading to:

$$m\lambda^2 + k = 0 \quad \Rightarrow \quad \lambda = i\sqrt{\frac{k}{m}} = i\omega_0 \quad \Rightarrow \quad \lambda h = \omega_0 i h \tag{2.136}$$

The stability region for RK4 can be drawn from several sources, such as Figure 2.1 in [57, p. 17], and in this thesis presented in Fig. 2.7. For the undamped problem the stable area for the solver is described by $\lambda h \leq 2.8i$. Combining the stable area with eq. (2.136), the maximum stable time-step h is restricted by:

$$h \leq \frac{2.8}{\omega_0}, \quad \text{where} \quad \omega_0 = \sqrt{\frac{k}{m}} \tag{2.137}$$

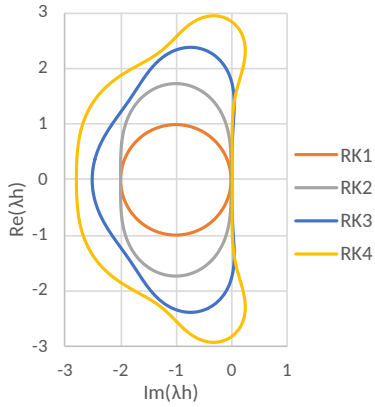

Figure 2.7: Stability region for the Runge Kutta orders RK1, RK2, RK3 and RK4 with imaginary and real λh on the axes.

The eigenfrequency ω in eq. (2.135) is given in radians per second. The frequency is the number of cycles per unit of time, given as $Hz = \frac{1}{s}$, is presented in eq. (2.138). The period is time for a single oscillation, as presented in eq. (2.139).

$$f = \frac{\omega}{2\pi} \tag{2.138}$$

$$T = \frac{1}{f} \tag{2.139}$$

The oscillator described by eq. (2.140) is plotted for four values of the relative damping ratio ξ in Fig. 2.8. Also the accompanying $e^{-\lambda t}$ are plotted, which shows the diminishing oscillation. In the equation, a is the initial amplitude, λ is the decay rate (damping coefficient), and ϕ the phase angle. When $\xi = 1$, the oscillator is critically damped, and no oscillation takes place. If $\xi < 1$ the oscillator is under damped, and some oscillation takes place. The oscillator is undamped if $\xi = 0$. With $\xi > 1$ the oscillator is over damped, and the system moves slowly, like syrup, towards equilibrium.

$$x = e^{-\lambda t} a \cos[\omega t - \phi] \tag{2.140}$$

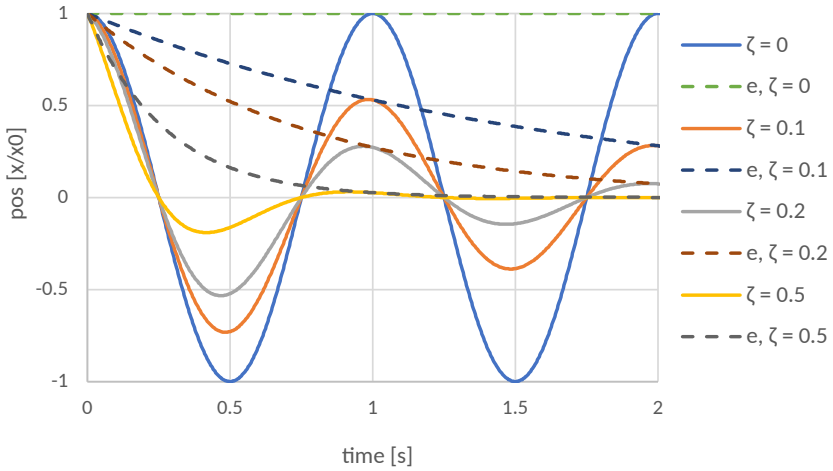

Figure 2.8: Effect of damping ratio on an oscillator.

The damping coefficient will predict the system behavior according to Fig. 2.8. Damping is introduced in the system by the damping force in eq. (2.49). To find how this affects the system, the critical damping coefficient could be found as in eq. (2.135). To calculate the critical damping coefficient, a simple method is to find the largest values in the diagonals from $\boldsymbol{K}_T$, $\boldsymbol{C}_T$, and $\boldsymbol{M}$ in eq. (2.75) when solving the system by the G-α method. The value from $\boldsymbol{C}_T$ are used as the actual damping, and the values from $\boldsymbol{K}_T$ and $\boldsymbol{M}$ are used to find the critical damping.

2.5.1 Highest Frequency of a Meshed Cable

For a discretized cable subjected to axial vibrations, which is modeled with linear bar elements, the highest frequency of the mesh is given by the vibration mode where every other node is moving in the same direction. All the nodes then have the same amplitude, as shown in Fig. 2.9.

Due to symmetry, as the nodes move opposite of each other, the system is simplified by a fixed spring with a mass m, stiffness k, and displacement u. The mass and stiffness for a half linear bar element is given in eq. (2.141), and defines the highest frequency for a MSD. The mass and stiffness of half a linear bar element, as shown in Fig. 2.9, becomes:

$$m = \frac{1}{2}\rho A L_e, \qquad k = \frac{EA}{\frac{L_e}{2}} = \frac{2EA}{L_e} \tag{2.141}$$

When inserting the cable properties for half the linear bar element in eq. (2.137), an alternative expression for eigenfrequency is achieved, eq. (2.142). S is the speed of sound traveling through the given material.

$$\omega_0 = \sqrt{\frac{k}{m}} = \frac{2}{L_e}\sqrt{\frac{E}{\rho}} = \frac{2}{L_e}S \quad \text{where} \quad S = \sqrt{\frac{E}{\rho}} \tag{2.142}$$

This leads to an expression based on element length to be used as a criterion for maximum time-step for a stable RK4 solver, eq. (2.143). The maximum stable time-step in RK4 is limited by the highest frequency in the mesh, which commonly is the axial frequency of the shortest element.

$$h \leq \frac{2.8}{\omega_0} = 2.8\frac{L_e}{2S} \tag{2.143}$$

Note that this expression is based on a *linear* variation of the displacements along the element length L_e. We will later see that the ALE-ANCF cable element can represent a higher variation of the displacements along L_e, and the expression will then have to be modified.

The highest axial frequencies results from an undamped MSD and ALE-ANCF cable element are presented and compared in Fig. 2.10. The cable was modeled with $\rho A = 1$, $L = 1$ and $EA = 1000$, with a varying number of elements with evenly spaced nodes. The cable was pinned in one end, hanging in a gravity field working in the axial direction. It is clearly evident that MSD has significantly lower highest frequency than ANCF-ALE cable elements, thus MSD is not sufficient to predict the maximum time-step for RK4 directly. Another method to predict a general criterion for maximum time-step for a stable RK4 solver is therefore of interest. To establish such an expression for the highest frequency within a mesh based on the shortest ALE-ANCF cable element, a free 1-D axial element is investigated, Fig. 2.11a. The DOFs for the model are $r_{1x}, r'_{1x}, r_{2x}, r'_{2x}$.

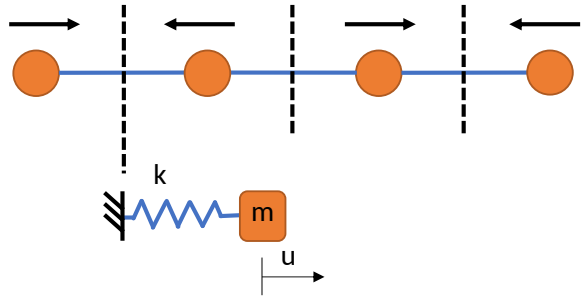

Figure 2.9: A meshed cable where the smallest element is simplified to a Mass-Spring system due to symmetry. Vertical lines indicates zero displacement.

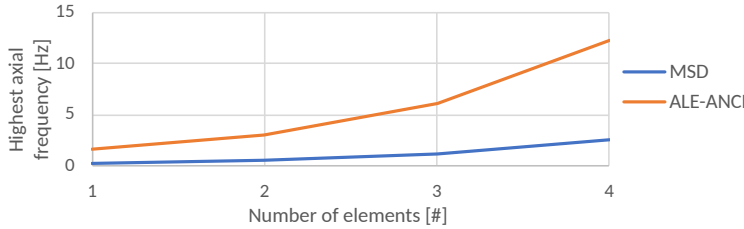

Figure 2.10: The highest axial frequency for MSD and ALE-ANCF cable swinging freely with gravity in the axial direction. The number of elements are varying with constant cable length. The ratio between the highest frequencies verifies the effective length in Table 2.1.

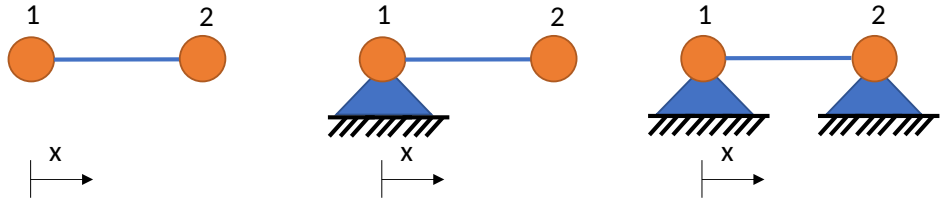

(a) Free-Free **(b)** Pinned-Free **(c)** Pinned-Pinned

Figure 2.11: Single element 1-D problem with different boundary conditions.

For an undamped system with multiple degrees of freedom, eq. (2.144) can be used to find the eigenfrequencies. Here, $\boldsymbol{K}$ is the stiffness matrix for the element, $\boldsymbol{M}$ is the mass matrix for the element, ω is the eigenvalues given as angular velocity and $\boldsymbol{v}$ is the eigenvector. The element in Fig. 2.11a is not constrained in the x-direction, thus there will be one "0-frequency" Rigid Body Mode (RBM) and three "deformational" modes with positive eigenvalues.

$$\left(\boldsymbol{K} - \omega_i^2 \boldsymbol{M}\right) \boldsymbol{v}_i = \boldsymbol{0} \tag{2.144}$$

In eq. (2.144) ω_i and $\boldsymbol{v}_i$ are corresponding eigenvalue and eigenvector. This eigenvector can

be determined by an eigenvalue analysis, and will be the highest possible frequency in the system. The eigenvector can serve as a step towards getting a criterion to find the maximum time-step, eq. (2.146).

$$\text{Free-Free Linear bar element:} \quad \boldsymbol{v}_{max} = \begin{bmatrix} r_{1x} \\ r_{2x} \end{bmatrix} = \begin{bmatrix} 1.0L_e \\ -1.0L_e \end{bmatrix} \tag{2.145}$$

$$\text{Free-Free ALE-ANCF element:} \quad \boldsymbol{v}_{max} = \begin{bmatrix} r_{1x} \\ r'_{1x} \\ r_{2x} \\ r'_{2x} \end{bmatrix} = \begin{bmatrix} -0.06L_e \\ 0.71 \\ 0.06L_e \\ 0.71 \end{bmatrix} \tag{2.146}$$

$$\text{Pinned-Free ALE-ANCF element:} \quad \boldsymbol{v}_{max} = \begin{bmatrix} r'_{1x} \\ r_{2x} \\ r'_{2x} \end{bmatrix} = \begin{bmatrix} 0.38 \\ 0.10L_e \\ 0.92 \end{bmatrix} \tag{2.147}$$

$$\text{Pinned-Pinned ALE-ANCF element:} \quad \boldsymbol{v}_{max} = \begin{bmatrix} r'_{1x} \\ r'_{2x} \end{bmatrix} = \begin{bmatrix} 0.71 \\ 0.71 \end{bmatrix} \tag{2.148}$$

When rearranging and pre-multiplying eq. (2.144) with $\boldsymbol{v}_{max}^T$, the familiar Rayleigh quotient for maximum squared eigenfrequency is established:

$$\frac{\boldsymbol{v}_{max}^T \boldsymbol{K} \boldsymbol{v}_{max}}{\boldsymbol{v}_{max}^T \boldsymbol{M} \boldsymbol{v}_{max}} = \omega_{max}^2 \tag{2.149}$$

In combination with the stable time-step region for RK4 in eq. (2.137), a criterion for the maximum time-step is given in eq. (2.150); where $\boldsymbol{v}_{max}$ is given by eq. (2.146) to (2.148).

$$h \leq \frac{2.8}{\omega_{max}} = \frac{2.8}{\sqrt{\frac{\boldsymbol{v}_{max}^T \boldsymbol{K} \boldsymbol{v}_{max}}{\boldsymbol{v}_{max}^T \boldsymbol{M} \boldsymbol{v}_{max}}}} \tag{2.150}$$

The element shape is found by $\boldsymbol{N}_e \boldsymbol{v}_{max}$, with the shape function from eq. (2.11) and the eigenvectors from eq. (2.146) to (2.148). For an element with length $L_e = 1$ and configurations as in Fig. 2.11, the results are presented in Fig. 2.12.

For a cable modeled by several elements, a propagatable element displacement with a repeatable pattern has to be found. A requirement is then that the displacement and slope are continuous. This is not the case for the highest frequency in the Free-Free configuration, where there is discontinuity, see Fig. 2.12. None of the modes for the Free-Free configuration are found to be propagatable, see Table 2.1. The $\boldsymbol{v}_{f/f,3}$ Fig. 2.14 is seemingly equal to $\boldsymbol{v}_{+/-,1}$ Fig. 2.18, but turns out to have a minor rotation at the end resulting in discontinuity as illustrated in Fig. 2.13. Thus, this configuration is not directly relevant for a meshed cable.

When ALE-ANCF cable elements are connected in a cable, the shared nodes enforces equal displacement and slope. This is satisfied in the Pinned-Pinned configuration, as in

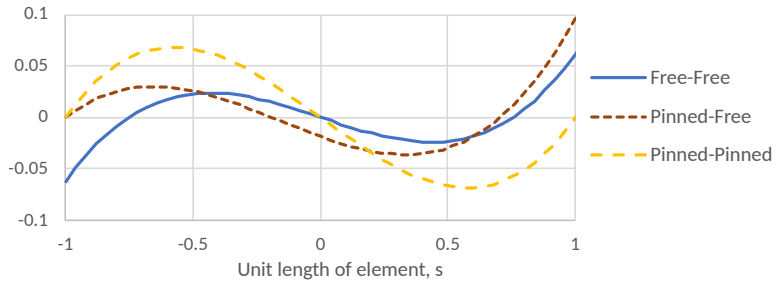

Figure 2.12: The highest vibration modes for an element of length $L_e = 1$ with the three different boundary conditions presented in Fig. 2.11 introduced by eq. (2.146), (2.147), and (2.148).

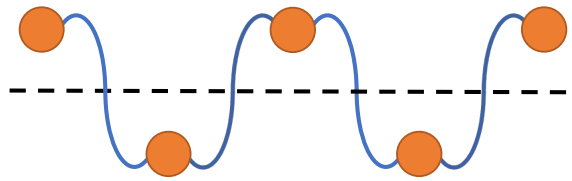

Figure 2.13: Free-free discontinuity without constraints.

Fig. 2.11c. The highest frequency then has a mode shaped similar to a sine wave, as the Pinned-Pinned in Fig. 2.12. For a cable pinned in both ends, this will be highest frequency in the system.

The end element of the mesh does not have to be propagatable for a cable with a free end globally. Only the first node of the end element must be restrained to have a continuous displacement and slope. The Pinned-Free configuration in Fig. 2.12 is continuous in one end and discontinuous in the other. The shape of this element has more than a sine wave over the element length, and thus has the highest frequency in an otherwise propagatable mesh. This will be the governing element if present in the cable model, provided that the elements are modeled with equal length.

Table 2.1 compares the highest eigenfrequencies, and thus the maximum stable time-step h_{max}, for the elements in Fig. 2.11 when they are modeled by MSD and ALE-ANCF cable elements respectively. The eigenvectors are given by eq. (2.145), (2.146), (2.147), and (2.148). The effective length in the table is independent of material data and element length. The corresponding element shapes are found in Fig. 2.14 to 2.16.

The MSD cannot directly be used to predict the maximum time-step for RK4, but if eq. (2.143) is updated with effective length to eq. (2.151), the higher frequencies are accounted for. The effective length must be set according to the relevant boundary conditions, as suggested in Table 2.1. A strategy to predict the maximum time-step for RK4 with ALE-ANCF cable elements, according to a MSD, has thus been developed.

Configuration	Prop mesh	$\omega_{max}[rad/s]$	L_{eff}/L_e [-]	h_{max} [s]
$MSD_{f/f}$	Yes	63.3	1.00	44.3E-3
$\boldsymbol{v}_{f/f,1}$	No	412.5	0.15	6.8E-3
$\boldsymbol{v}_{f/f,2}$	RBM	0	0	0
$\boldsymbol{v}_{f/f,3}$	No	99.37	0.64	28.2E-3
$\boldsymbol{v}_{f/f,4}$	No	244.9	0.26	11.4E-3
$\boldsymbol{v}_{p/f,1}$	Yes, end	330.4	0.19	8.5E-3
$\boldsymbol{v}_{p/f,2}$	Yes, end	152.9	0.41	18.3E-3
$\boldsymbol{v}_{p/f,3}$	Yes, end	49.7	1.27	56.3E-3
$\boldsymbol{v}_{p/p,1}$	Yes	244.9	0.31	13.7E-3
$\boldsymbol{v}_{p/p,2}$	Yes	100.0	0.63	20.8E-3
$\boldsymbol{v}_{+/-,1}$	Yes	99.4	0.64	28.2E-3
$\boldsymbol{v}_{+/-,2}$	Yes	99.9	0.63	28.0E-3
$\boldsymbol{v}_{+/+,1}$	RBM	0	0	0
$\boldsymbol{v}_{+/+,2}$	Yes	204.9	0.31	13.7E-3

Table 2.1: Maximum time-steps h_{max} and equivalent effective element lengths L_{eff} for single element models of Fig. 2.11 (RBM: Rigid Body Mode).

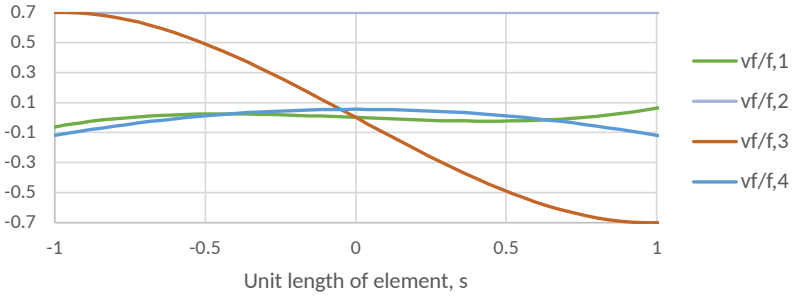

Figure 2.14: The four vibration modes for an element of length $L_e = 1$ corresponding to configuration Fig. 2.11a.

$$h \leq \frac{2.8}{\frac{2}{L_{eff}}\sqrt{\frac{E}{\rho}}} = 2.8\frac{L_{eff}}{2S} \tag{2.151}$$

For both the Free-Free and the Pinned-Free configuration in Fig. 2.12, the element is both in tension and compression internally.

For the Free-Free configuration, the element is in tension before $s = -0.77$ and after $s = 0.77$, and in compression between these. The points at $s = -0.77$, $s = 0$, and $s = 0.77$ can be considered pinned, as they are zero displacement points for the vibration mode.

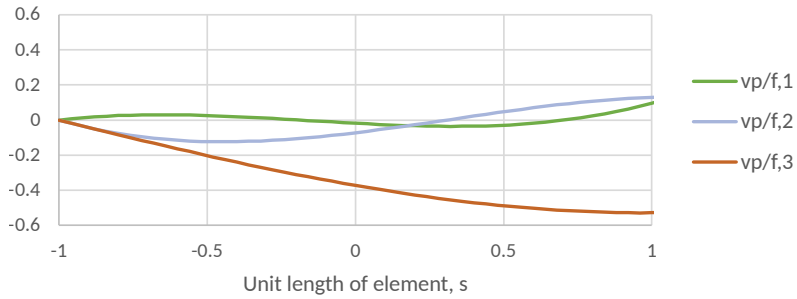

Figure 2.15: The three vibration modes for an element of length $L_e = 1$ corresponding to configuration Fig. 2.11b

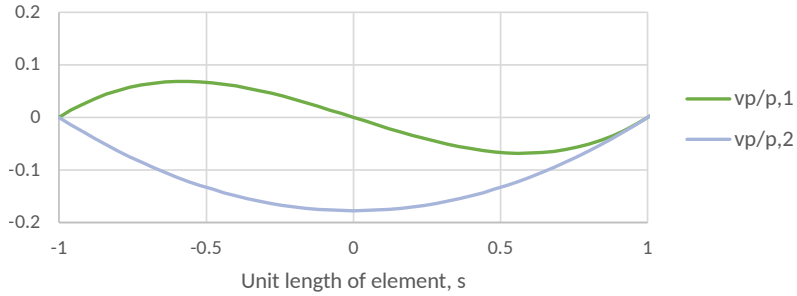

Figure 2.16: The two vibration modes for an element of length $L_e = 1$ corresponding to configuration Fig. 2.11c

Applying the same procedure to the ALE-ANCF cable element as for the Mass-Spring in Fig. 2.9; by dividing the cable element into "sub-elements" and introducing masses in $s = 0.5$ and $s = 1.0$ would lead to zero displacement at $s = 0.77$. The shortest element would then be $L_e = 0.23$, and the findings in Table 2.1 are supported, as it is reasonable to assume that the difference in effective length is due to the non-linear displacement.

An alternative method to enforce continuity in the mesh is to predetermine a mesh pattern. For a linear bar element, the highest frequency in a continuous mesh is given by a repeated pattern of +1, -1, as given in eq. (2.145) and illustrated in Fig. 2.17.

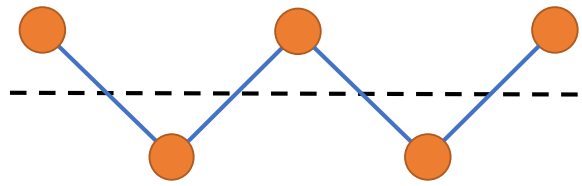

Figure 2.17: The highest frequency for a propagatable mesh pattern in a bar.

A similar approach as for the bar element can be used for an ALE-ANCF cable element.

To ensure a propagatable mesh, an enforced pattern can be introduced by repeatable eigenvectors, eq. (2.152) and (2.153). With a $+/-$ pattern, both r_x and r'_x must have opposite sign at each end. $\boldsymbol{v}_{+/-}$ then takes the form as in eq. (2.152). For the ALE-ANCF cable element, also an enforced $+/+$ pattern will provide a propagatable mode, eq. (2.153).

$$\boldsymbol{v}_{+/-} = \begin{bmatrix} r_{1x} \\ r'_{1x} \\ r_{2x} \\ r'_{2x} \end{bmatrix} = \begin{bmatrix} r_{1x} \\ r'_{1x} \\ -r_{1x} \\ -r'_{1x} \end{bmatrix} = \begin{bmatrix} 1 & 0 \\ 0 & 1 \\ -1 & 0 \\ 0 & -1 \end{bmatrix} \begin{bmatrix} r_{1x} \\ r'_{1x} \end{bmatrix} = \boldsymbol{A}_{+/-} \begin{bmatrix} r_{1x} \\ r'_{1x} \end{bmatrix} \tag{2.152}$$

$$\boldsymbol{v}_{+/+} = \begin{bmatrix} r_{1x} \\ r'_{1x} \\ r_{2x} \\ r'_{2x} \end{bmatrix} = \begin{bmatrix} r_{1x} \\ r'_{1x} \\ r_{1x} \\ r'_{1x} \end{bmatrix} = \begin{bmatrix} 1 & 0 \\ 0 & 1 \\ 1 & 0 \\ 0 & 1 \end{bmatrix} \begin{bmatrix} r_{1x} \\ r'_{1x} \end{bmatrix} = \boldsymbol{A}_{+/+} \begin{bmatrix} r_{1x} \\ r'_{1x} \end{bmatrix} \tag{2.153}$$

The system can now be reduced from 4 to 2 DOFs by the use of $\boldsymbol{A}_{+/-}$ and $\boldsymbol{A}_{+/+}$, and the stiffness matrix and the mass matrix take the form $\widetilde{\boldsymbol{K}} = \boldsymbol{A}^T \boldsymbol{K} \boldsymbol{A}$ and $\widetilde{\boldsymbol{M}} = \boldsymbol{A}^T \boldsymbol{M} \boldsymbol{A}$. This is further used in the method presented for eq. (2.149), to obtain the eigenfrequencies.

The four vibration modes for an element with predetermined patterns is presented in Fig. 2.18. The $+/-$ pattern leads to a half sine wave over the element length, where $\boldsymbol{v}_{+/-,1}$ has zero rotation and $\boldsymbol{v}_{+/-,2}$ has zero displacement. The $+/+$ pattern can have the same r_x at each node, which gives rigid body mode for $\boldsymbol{v}_{+/+,1}$, while $\boldsymbol{v}_{+/+,2}$ is equal to the Pinned-Pinned configuration in Fig. 2.12 with zero rotation. The latter is given as Propagatable Free-Free in Table 2.1.

This method ensures a propagatable displacement. As the end element does not have to be repeatable, the method could fail to predict the maximum frequency, as it lacks a representation of the free end configuration. A weakness with this approach is that the Pinned - Free configuration is excluded by the predetermined pattern.

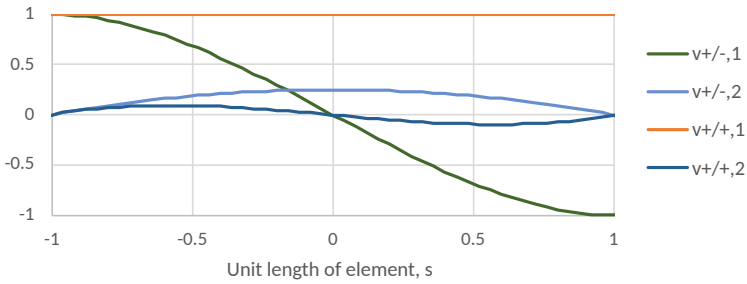

Figure 2.18: The four vibration modes for an element of length $L_e = 1$ with predetermined pattern.

An illustration of the governing frequency of an ALE-ANCF cable element is given in Fig. 2.19. The continuous mesh is represented as jigsaw puzzles, where there are five available pieces. The pieces from A to E are arranged in descending order for highest maximum frequency. Piece A and B is not propagatable, and can thus not be used in the mesh. Piece C is not propagatable, but can be used on the end of the puzzle, and the highest eigenfrequency in the puzzle is now governed by C. Alternatively the puzzle can be extended by new D pieces, which leaves the highest frequency unchanged, until it is ended by piece E, which does not alter the highest frequency.

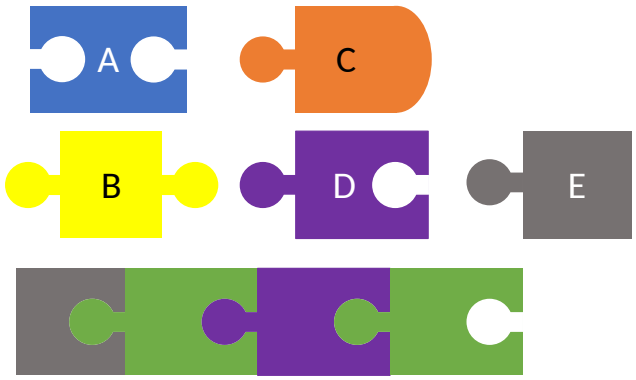

Figure 2.19: Jigsaw puzzle illustration of the highest frequency for a continuous and propagatable mesh patter.

A hammer test was performed in Paper 2 to verify the criterion for the critical time-step for an ALE-ANCF cable element solved with RK4. The test procedure is to initially have an external force hit the end node, then allow the elements to swing freely, as if just hit by a hammer. This is presented for a two-element cable in Fig. 2.20, and has 5 DOFs, $r_{0x}^{'}, r_{1x}, r_{1x}^{'}, r_{2x}, r_{2x}^{'}$. By the use of Fast Fourier Transform (FFT) analysis, the frequencies in a cantilever bar of ALE-ANCF cable elements were found.

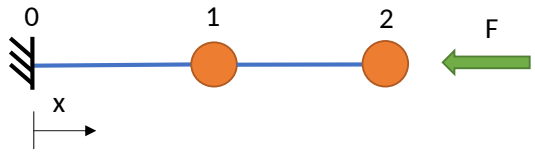

Figure 2.20: Two-element cantilever bar undergoing the hammer test.

For practical simulation applications, the frequencies are subjected to change over a time domain. Thus, FFT is appropriate to find what eigenfrequencies is present, and to detect frequencies causing instability in the algorithm. Time integration is the primary focus of the present study, the eigenfrequency analysis is a consequence, thus the FFT is more relevant method than linearization of the equations and then calculate the eigenvalues.

As an example, the procedure for a two-element hammer test, with the material data $\rho A = 1$, $L_e = 0.5$ and $EA = 1$ is presented. The response in the axial force is presented in Fig. 2.21, where it becomes evident that the smaller time-steps include higher frequencies. To trigger the highest frequencies from a hammer test, the time-steps must be small enough to represent them. The force is plotted instead of displacement, as it is easier to observe the high frequency when the slope is part of the force expression. The FFT is presented in Fig. 2.22, and is based on 100 sec series of the node displacement. Here, the 5 eigenfrequencies are visible for the smallest time-step, with the highest frequency at $3.1Hz$. The highest frequency is plugged into eq. (2.137) to find the maximum time-step. The maximum time-step for a stable RK4 solver is congruent with the suggested criterion and verified by the FFT maximum time-step.

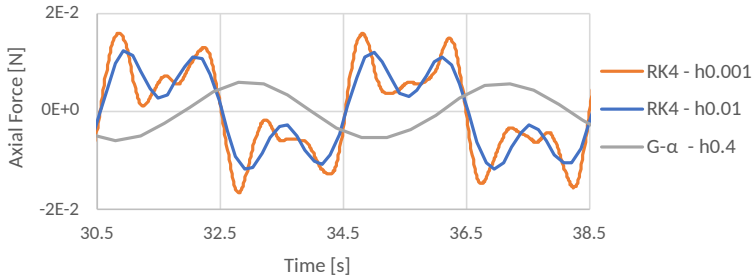

Figure 2.21: The axial force from cable segment 2 from the two-element hammer test, for RK4 with time-step h=0.001 sec, h=0.01sec, and G-α with time-step h=0.4.

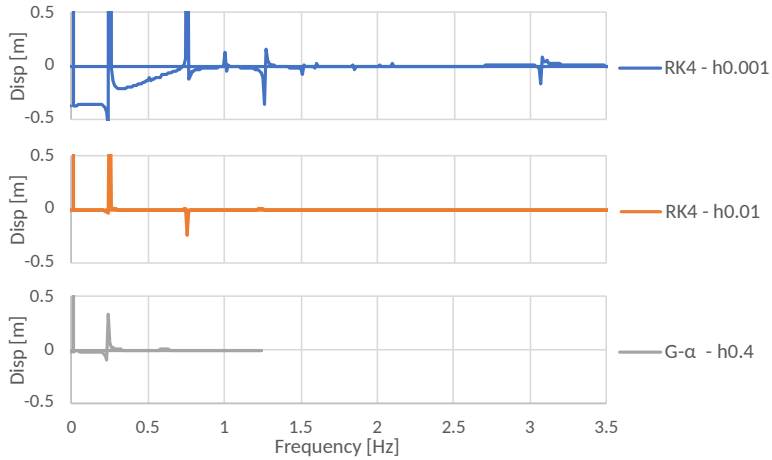

Figure 2.22: Frequencies detected from FFT of displacement in node for RK4 with time-step h=0.001 sec, h=0.01sec, and G-α with time-step h=0.4.

When using the maximum time-step, the number of time steps per highest frequency is

just above 2, Fig. 2.21. For a decent representation of an oscillation it is recommended to have at least 10 time steps. This means that it is not required for RK4 to represent the highest frequencies accurately for it to be a stable solver. When running a FFT of a simulation with the maximum time-step, only the lower frequencies are captured, Fig. 2.22. If the time-step is larger than the criterion for maximum time-step, the simulation will diverge and fail as fictitious energy is added to the system.

As an alternative to RK4, G-α can be used as the numerical integration method. This method is not limited by the axial frequency. The time-steps can therefore be significantly larger than for RK4. For the two-element hammer test, the 1st vibration mode is 0.25 Hz, which equals a period of 4 sec. To have 10 time steps for each period, $h = 0.4s$. In Fig. 2.21 G-α represents the 1$^{\text{st}}$ axial vibration mode, which is confirmed in Fig. 2.22. This results in a relative error in the result and phase, which is further discussed in Sec. 2.8.

The hammer test was also carried out in a configuration of the elements where the node positions where fixed, and the flow variables were free. The slope DOFs were free, since they are associated with the strain. The 5 DOFs for the system were $r'_{0x}, p_1, r'_{1x}, p_2, r'_{2x}$. Instead of a force acting on the end node, a prescribed displacement was used on the fixed node to trigger the oscillations. Free flowing DOFs resulted in the same frequencies in the cable as with free position DOFs.

In practical terms, the consequence of a small element limiting the maximum time-step for a simulation is exemplified by a vessel with a crane rolling in the waves, Fig. 2.23. If the goal is to simulate how the payload in the crane is affected by the waves, the period of the waves, which is the time for one oscillation, is the frequency of interest. As a rule of thumb, it is good to have at least 10 time-steps each period, for a decent representation of the wave. The advantage of the G-α method is unconditionally stable if the criterion is met. Thus, the limiting factor for the time-step size is the accuracy. The accuracy is good as long as the number of time-steps for the desired frequencies are sufficient, Fig. 2.23.

In contrast, the critical time-step for RK4 is limited by the smallest element in the model, Fig. 2.23. For a model, such as the vessel with a crane, the smaller elements in e.g. the crane can really limit the critical time-step. Even though the resolution for the sea waves are high, and also higher frequencies could be represented, it might not be of interest for the overall simulation. The total solution time could be significantly faster for the G-α method compared to RK4.

2.5.2 Nonlinear Stiffness Effects due to Green Strain

To investigate how the axial stiffness influences the MSD and ALE-ANCF cable element, the cantilever bar was configured with a gravity field working in the axial direction, modeling a cable hanging in a gravity field. The cable was modeled with 1 element, $\rho A = 1$, $L = 1$, where different axial stiffnesses were tested, Fig. 2.24. The plot shows the ratio between the 1$^{\text{st}}$ vibration mode for MSD and an ALE-ANCF cable, based on FFT analysis. The trend in the plot is independent of the number of elements in the cable. It becomes

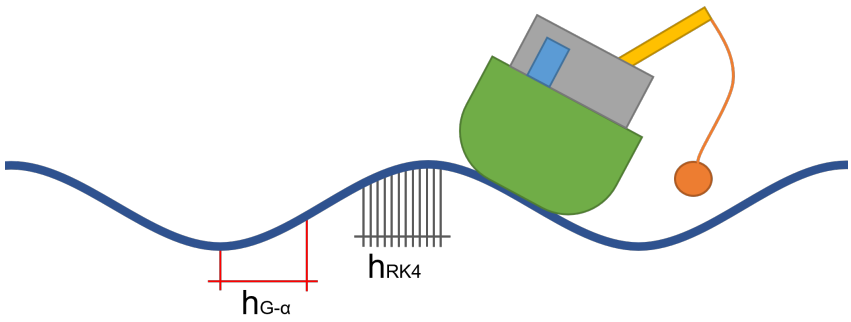

Figure 2.23: Vessel with a crane rolling in the waves, where the time-step for G-α and RK4 are indicated.

evident that the axial frequency in MSD is only 79% of the ALE-ANCF cable for the stable area. To validate the results for axial frequency, the results were compared to an exact solution of axial vibration problems for elastic bars, [58]. The results for an ALE-ANCF cable matched perfectly. Thus, it can be concluded that a single element MSD is an insufficient simplification for an exact frequency representation. The MSD has a massless spring, only with a point mass at the end, while the cable is a continuous mass. The lumped mass instead of a distributed mass is believed to be one of the main issues.

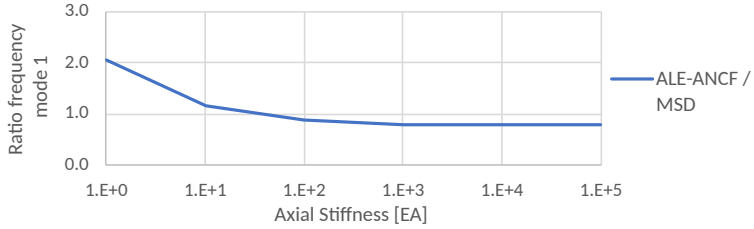

Figure 2.24: Ratio between the 1st axial vibration mode for MSD and an ALE-ANCF cable, swinging freely with gravity in axial direction.

Furthermore, from Fig. 2.24 a divergence in the frequency below an axial stiffness of $EA = 1000$ is observed. For a hanging cable in a gravity field with $EA = 1$, the frequency is over 2 times higher for the ALE-ANCF cable than the MSD. This was found to be due to the Green strain definition used in the ALE-ANCF cable element, eq. (2.52). It became evident that the resulting nonlinear strain-displacement definition made the axial frequency too high. Therefore, the engineering strain definition, eq. (2.154) and (2.155), was tested instead of Green strain.

$$\epsilon_{eng} = \frac{\Delta \boldsymbol{r}}{\Delta p} - 1 = \frac{\boldsymbol{r}_2 - \boldsymbol{r}_1}{p_2 - p_1} - 1 \tag{2.154}$$

$$\frac{\partial \epsilon_{eng}}{\partial \boldsymbol{q}} = \frac{\partial \left(\frac{\boldsymbol{r}_2 - \boldsymbol{r}_1}{p_2 - p_1} \right)}{\partial \boldsymbol{q}} \tag{2.155}$$

This resulted in a consistent relationship between frequencies of ALE-ANCF cable and the MSD, as the mass and stiffness changed.

A very large strain will affect the accuracy of the results. For a cable hanging in a gravity field using the Green strain definition, it is recommended to use the following relationship between mass and stiffness, eq. (2.156).

$$\rho A L < \frac{EA}{1000} \tag{2.156}$$

An ALE-ANCF cable element with length 1, from $p_1 = 0$ to $p_1 = 1$, pinned in node 1, $r_1 = 0$, and varying node 2 from $r_2 = 0.5$ to $r_2 = 1.5$, is found in Fig. 2.25. It can be observed that engineering strain has a linear behavior, while Green strain has a cubic behavior. This is what causes the difference when using Green strain instead of engineering strain. In the event of simulating a cable in a crane, this is far outside the maximum strain of 2%, [59]. In this strain area the difference between Green strain and engineering strain is negligible, Fig. 2.25.

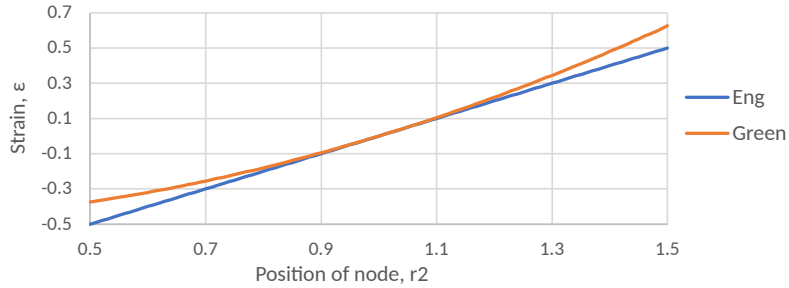

Figure 2.25: Engineering strain vs Green strain in an ALE-ANCF cable element.

2.6 Case 2: Constrained Cable - Cantilever Beam

An important quality for an ALE-ANCF cable element is to be connected with neighboring elements, to create longer cable spans. This will achieve possibilities for advanced geometrical shapes. Different constraint methods are tested to connect the ALE-ANCF cable elements. In Case 1, the elements are connected by shared nodes, which is the simplest method as it reduces the number of DOFs in the system. This is equivalent to using the master-slave technique with linear coupling, to constrain the nodes. The constraint procedures tested in Case 2 are the penalty method and the Lagrange multiplier method. Constraints, ϕ, are used to connect the cable elements together. The constraint methods are applied to position

DOFs, slope DOFs and flow DOFs from eq. (2.1), as presented in eq. (2.157), where the superscript e indicates the element number. This is done for two neighboring cable spans in x-, y- and z-direction, creating one constraint for each direction.

$$\boldsymbol{\phi} = \begin{bmatrix} \boldsymbol{r}_2^e - \boldsymbol{r}_1^{e+1} \\ \boldsymbol{r}'^e_2 - \boldsymbol{r}'^{e+1}_1 \\ p_2^e - p_1^{e+1} \end{bmatrix} = \mathbf{0} \tag{2.157}$$

In Case 2 the same cantilever beam model as in Case 1, Fig. 2.20, is used, where the elements have separate nodes connected by constraints instead of shared nodes.

For the penalty method, the penalty springs are user defined. To select an adequate stiffness the square root rule can be useful eq. (2.158), [60, p. 9-5]. The largest stiffness in the system prior to adding the penalty springs is then found and given in the order of 10^k. b is the working machine precision. The unit of $\boldsymbol{k}_{pen}$ is defined by $\frac{EA}{L}$.

$$\lceil \boldsymbol{k}_{pen} \rfloor = 10^k \sqrt{10^b} \tag{2.158}$$

In this case the highest stiffness in the cable was found to be 4.8. For the set-up used, $b \approx 16$. According to the square root rule, the best penalty spring stiffness equals $\lceil \boldsymbol{k}_{pen} \rfloor = 10^9$. When solving the constrained system with the G-α method, the penalty method provides the same frequency as in Case 1. If a stiffer penalty spring is used, $\lceil \boldsymbol{k}_{pen} \rfloor = 10^{12}$, the results are the same but the number of iterations each time-step starts to increase. This is in accordance with the square root rule, eq. (2.158).

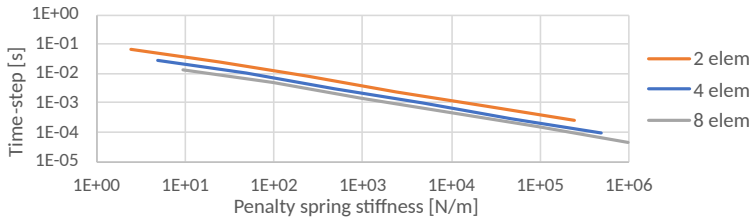

Figure 2.26: Critical time-step plotted against penalty spring stiffness in cantilever beam.

The plot in Fig. 2.26 shows how the penalty spring stiffness impacts the maximum time-step for the of the cantilever beam. The penalty spring is a multiplication of the highest stiffness. With penalty springs added in the system, the stiffness increases, which also increases the frequencies. This results in a significant reduction in the maximum time-step for a stable RK4 solver. If the penalty spring stiffness is set with similar stiffness as the system stiffness, RK4 can run with a slightly reduced time-step, but the accuracy is poor as the constraints are too loose to properly connect the nodes. From the plot, a clear trend of how the penalty spring decrease the time-step can be observed. RK4 is a less than ideal method to use in combination with the penalty spring and will therefore not be used in combination with penalty constraints for the remainder of this paper.

When using the Lagrange Multiplier method to constrain the system, additional equations are introduced into the system matrix. For RK4, the method presented in Sec. 2.4.5 is used. The constraint method provides the same frequency and maximum time-step as found in Case 1.

The accuracy of the G-α is found to be unaffected by the choice of constraint method.

2.7 Case 3: Garden Hose

To validate the accuracy of the constraint methods in combination with the numerical time integrators, a cantilevered garden hose with water flowing out at the free end is simulated. The garden hose makes a good case as it is an advanced model with several aspects of interest for benchmarking the solution procedure, such as large deformations and material flow. Water flows as the material, p, in the elements, causing frequency flutter in the hose. Two separate elements, placed on top of each other, represent the water and the hose. The overlaying elements share position DOFs and slope DOFs; and are connected with constraints. The flow nodes are fixed for the hose elements and prescribed for the water elements. The garden hose is held fixed at one end, and can thus be represented as a cantilever beam under gravity, Fig. 2.27. The case is based on work by [37], with the material parameters given in Table 2.2.

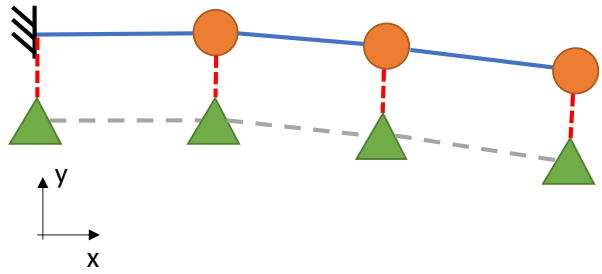

Figure 2.27: A model of the garden hose; the red circular nodes indicate the hose, the green triangular nodes indicate the water with flow. The hose and the water is connected with constraints.

To test how the ALE-ANCF cable element behaves in bending with constraints, the model is first configured with flow speed below critical flutter speed. To find the statics solution, damping is added to the system to stabilize it. From the results in Fig. 2.28, the garden hose starts to straighten out as the water flow increases.

The lateral displacement in the hose end is presented for a simulation with $35m/s$ water flow in Fig. 2.29. The flutter is steady after initiation. In Fig. 2.30 the position and velocity for the hose end is plotted for water flows of $15m/s$, $25m/s$ and $35m/s$. The results are in good agreement with [37].

	Hose Element	Water Element
L_e $[m]$	0.05	0.05
Num elem $[\#]$	10	10
EA $[N]$	10.0	0.0
EJ $[N/m^2]$	0.00108	0.0
ρA $[kg/m]$	0.0031316	0.0007854
cDamp $[Ns/m]$	0.0031316	0
Flow $[m/s]$	0	Prescribed

Table 2.2: The material parameters used in Case 3.

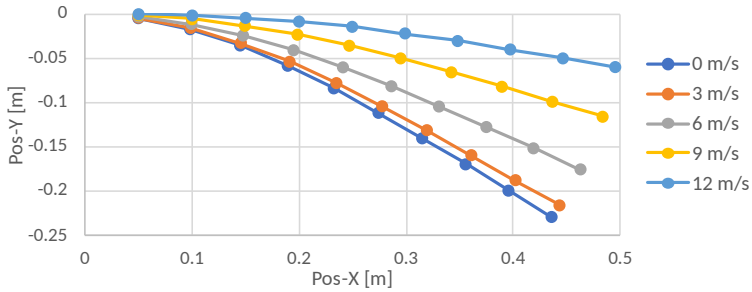

Figure 2.28: Statics solution for garden hose with a water flow of $0m/s$, $3m/s$, $6m/s$, $9m/s$ and $12m/s$.

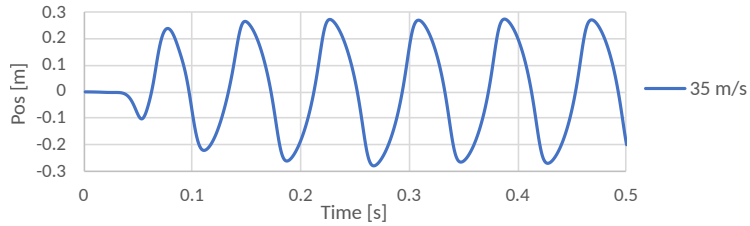

Figure 2.29: Lateral displacement in the garden hose end plotted against time, with a water flow of $35m/s$.

To connect the water elements with the hose elements in the simulation linear coupling, penalty springs and the Lagrange multipliers were tested. For RK4, the maximum time-step for one hose element is found to be $h = 0.000245s$, according to the criterion described in Case 1. This agrees with simulation for the garden hose when using linear couplings or Lagrange multipliers, as this is the limit where the results starts to diverge.

The time-step requirement for the G-α method is to capture the movement of the garden hose. It is recommended to have 10 time-steps each oscillation. If the time-steps are too large to capture the behavior of the system, the solver has difficulty converging and provides poor results.

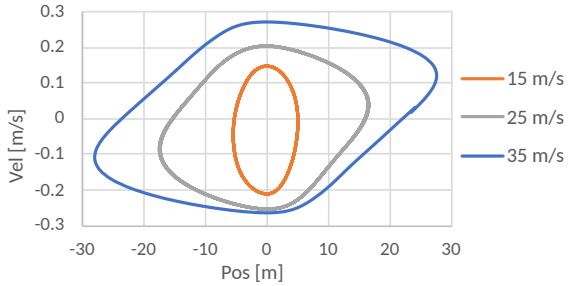

Figure 2.30: Lateral position and lateral velocity of the hose end for water flows of $15m/s$, $25m/s$ and $35m/s$.

2.7.1 Material Flow Direction

One of the special attributes of the ALE-ANCF cable element presented in Sec. 2.1, is the possibility for mass flowing through the nodes. In Paper 2, one of the cases simulates water flowing out of a garden hose.

To visualize how the material flow is used and defined for the simulation, the definition of the direction of the water flow is illustrated in Fig. 2.31. The water is represented by the number from 1 to 12, each representing a unit of water. The water is found in the tank reservoir, in the garden hose represented by the green flow nodes, or in the puddle after being splashed out of the garden hose. The water flow is constant. The red nodes represent the position nodes for the garden hose. The green flow nodes are connected to the red position nodes with constraints. At $t = 0$ the crane is opened. At $t = 1$ the water flows from the tank, through the hose and out in the puddle. The flow speed is negative, $\dot{p} < 0$, as seen by the decreasing number in the flow nodes.

The example with water flowing in a garden hose is equivalent with a cable being reeled. The cable comes from a lower node with a negative material flow, $\dot{p} < 0$, and opposite, it comes from a higher node if the flow variable is positive, $\dot{p} > 0$.

2.8 Solution Times

The various choices for constraint formulations and time integration algorithms will affect the overall solution time, both regarding accuracy and efficiency.

In general, the explicit RK4 algorithm has a maximum time-step based on the highest eigenfrequency in the system. If the actual loading and response has a significantly lower frequency, this often results in a very inefficient solution algorithm.

In general, the G-α algorithm does not have the same stability restriction, and the necessary time-step is guided more by accuracy considerations. The G-α thus allows a much more straight-forward tailoring of efficiency vs accuracy of the simulation.

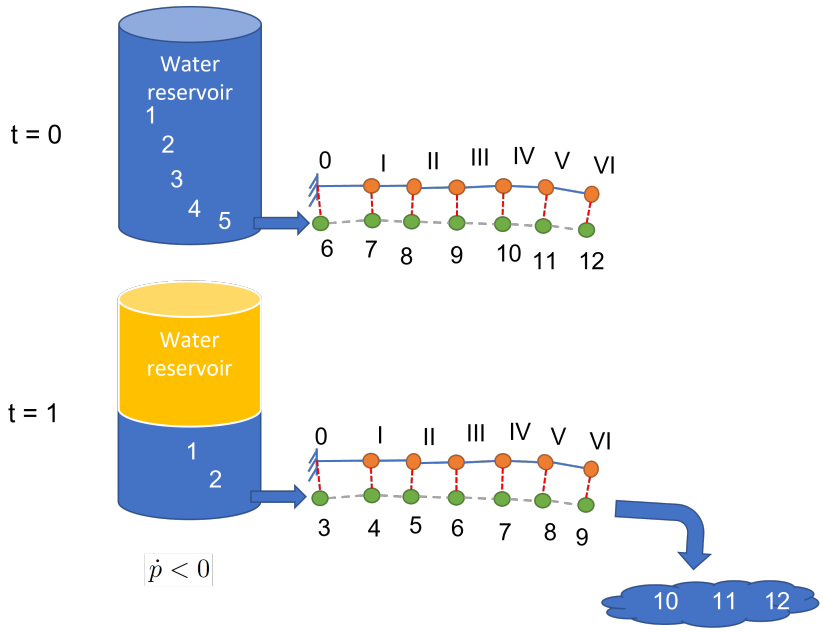

Figure 2.31: Illustration of water flow direction in a garden hose from a reservoir tank.

Fig. 2.32 shows a comparison of relative solution time for RK4 and G-α for the cantilever beam in Case 1 and 2, with 1, 2, 4 and 8 elements. The relative solution time is found by normalizing the CPU time against the CPU time for 1 element RK4. RK4 is solved with the maximum time-step. RK4 is also solved with Lagrange multipliers connecting the nodes. The G-α method is solved with the same time-step size as the maximum for RK4, and for the required time-step to have 10 time steps each oscillation for 1st and 2nd vibration mode, (indicated as mode 2 and mode 1 in the plot). G-α is also solved with the Lagrange multiplier method and penalty method. For the 1 element configuration, no elements are connected, thus no constraints are used. This configuration only has the 1st axial vibration mode.

Calculating one time step for RK4 is faster than one time step for the G-α solver, as can be seen in Fig. 2.32. When solving the cantilever beam with 1 and 2 elements, RK4 is more efficient than G-α. With more than 2 elements, G-α becomes faster when only the 1st vibration mode is represented, and from 8 elements when also the 2nd vibration mode is represented. The constraint method chosen for G-α generally does not affect the solution time significantly; but there is a tendency for shared nodes to be slightly faster than the Lagrange multiplier method, which again is marginally faster than the penalty method.

From Case 3, the solution time for the garden hose with a $35m/s$ water flow is compared for RK4 and G-α, Fig. 2.33. The total solution time for the G-α solver is almost 5 times faster than RK4. RK4 with Lagrange multipliers is slower than with linear couplings. RK4

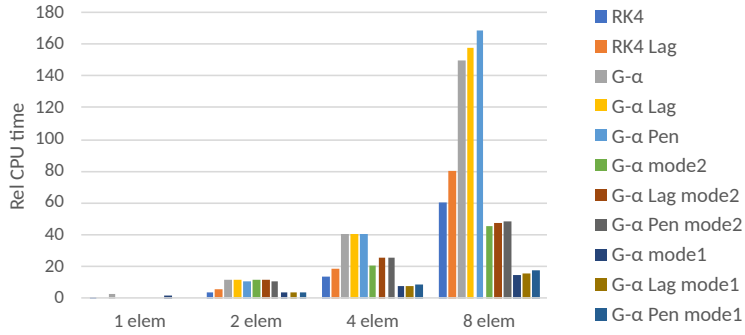

Figure 2.32: Solution time comparison for RK4 and G-α with different constraint methods for Case 1 and 2.

is an inefficient solver due to the short elements. This is a simulation scenario where the advantage of G-α is evident.

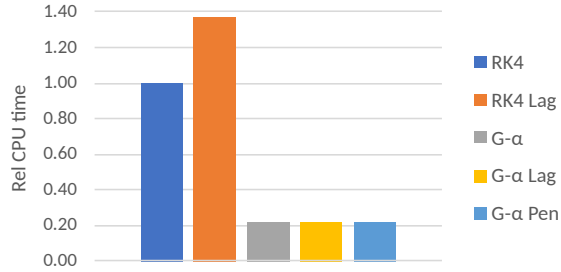

Figure 2.33: Solution times comparison for RK4 and G-α with different constraint methods for Case 3, $35m/s$.

The solution time for a simulation is affected by several factors, where the most apparent is the software/programming language used for implementation along with the computing power used to run the simulation. A useful tool to help select the best solution procedure for a real-time simulation is a plot with accuracy plotted against relative CPU time. The relative CPU time is a relevant measure since the relation between the simulations is expected to be similar independent of software and computing power. Three different plots are made: error in position, error in axial force, and error in phase.

For a bar hanging in a gravity field, as presented in Case 1, the error in amplitude of the displacement, amplitude of the axial force, and phase of the displacement are plotted against the relative CPU time, Fig. 2.34, 2.35, and 2.36 respectively. The error is found by normalizing against the RK4 run with 8 elements. The relative CPU time is found by normalizing against the RK4 run with 1 element.

In Fig. 2.34 the amplitude of the displacement is taken from the free end node of the cantilever bar. With a time-step capturing the oscillation in the bar, the error is very small

also for G-α. RK4 is accurate for all the runs, while G-α overshoots a little before it stabilizes. G-α is faster than RK4 from 2 elements and onwards, and the advantage increases by reduction in the element length. For RK4, the maximum time-step is limited by the highest frequency in the mesh, and the accuracy is therefore mainly controlled by the number of elements in the mesh.

In Fig. 2.35 the amplitude of the axial force is taken from the pinned first node of the cantilever bar. The plot shows that the solution converges with increasing number of elements. It also shows that the convergence is slower than for displacement, which is expected as the force is a derived measure. For G-α both time-step size and the number of elements have an impact on the accuracy.

In Fig. 2.36, the phase of the displacement is taken from the free end node of the cantilever bar. The error is very small as the CPU time increases. The phase error for G-α is high at large time-steps. At lower time-steps G-α provides accurate results and is competitive against RK4.

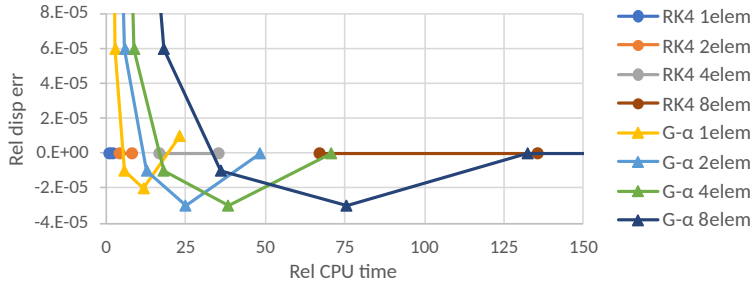

Figure 2.34: Error plot for relative displacement plotted against relative computation time for RK4 and G-α with different constraint methods.

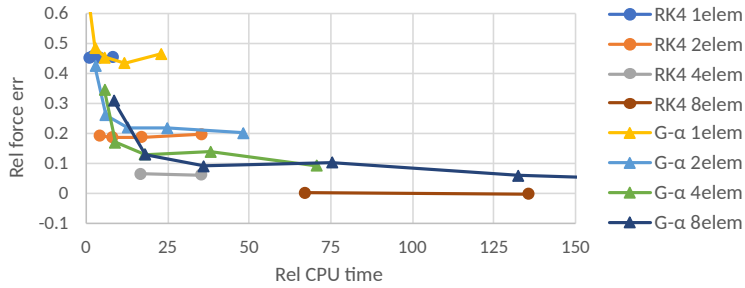

Figure 2.35: Error plot for relative force plotted against relative computation time for RK4 and G-α with different constraint methods.

To apply the insight from the plots, it is important for the user to know what the desired output from the simulation is, as there is a difference in accuracy between for example axial force and displacement.

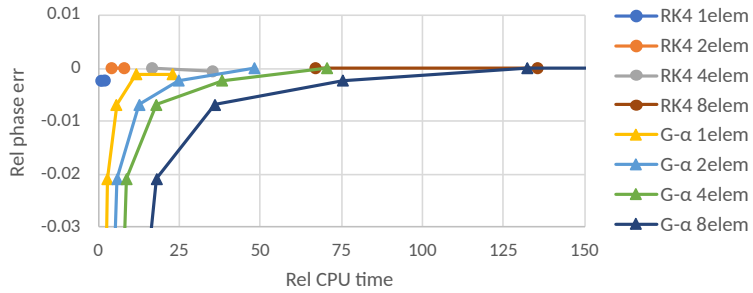

Figure 2.36: Error plot for relative phase plotted against relative computation time for RK4 and G-α with different constraint methods.

2.9 Analysis of Numerical Integration for Directional Well Drilling Strings for Real-Time Simulation

2.9.1 Introduction

Troll is one of the greatest offshore oil fields on the Norwegian Continental Shelf (NCS), containing immense amounts of oil and gas resources, even after over 20 years in production. The hydrocarbon containing reservoir height is classified as thin (22-25 m in height). To make it economically justifiable to start production of the field, development of long horizontal drilling had to be done. The two first horizontal wells for the Troll field were 500 m and 800 m, and were drilled in 1989 and 1990, [61].

Deviated oil and gas wells are drilled with an angle from the straight vertical geometry. A highly deviated well can be defined by a well with inclination above $60°$ for most of their length, [62]. To maximize the productiveness of the reservoir, several direction changes and a $90°$ inclination can be maintained for long distances. Challenges arises when drilling such well geometries with substantial friction between the drill string and the wellbore wall during both rotation and translatory motion, [63]. Other challenges are related to hole-cleaning of cuttings, and formation what is referred to as a key seat. A key seat is a channel similar to the diameter of the drill pipe where larger sections such as joints, drill collars, stabilizers, and bits can be pulled into and get stuck. For oil and gas fields on NCS, such as Troll and Oseberg field, [64], advanced directional drilling methods have been applied.

It is critical to maintain control of the entire process drilling operation to ensure a safe drilling operation, for both people and the environment. Real-time data combined with control systems for the drilling operation could allow for improved safety, time saving, improved wellbore quality, and extended reservoir sections, [65]. The relevance of an efficient simulation model, to run alongside the drilling process, is thus established for a directional drilling application. The virtual model will enable prediction of the transient behavior. Monitoring of the pressure profile in the wellbore is important for well-stability. Surge (running the drill string down in the well) and swab (retrieving the drill string) pressures affects the

down hole pressure, and should be kept under control to prevent instabilities.

Paper 3 explores the possibility for simple and efficient drill string models running real-time, describing motion in all axes in unconventional wells, being important for predicting transient behavior during drilling analysis. The model and its properties are proposed to act as a virtual sensor for drilling directional wells, and could be further developed into a digital twin. Furthermore, a lumped parameter formulation of a drill string is generalized to an arbitrary 3-D wellbore configuration. The wellbore is represented by a parametric curve in space with the drill string motions being a perturbation of the nominal curve. A FEM model typically becomes computationally inefficient due to the complexity, whereas the lumped model is significantly simpler. Kane's method are used to formulate the equations of motion in coordinate form, based on Newton-Euler formulation. A simpler expression of the equations of motion are obtained by the use of Kane's method in comparison to Lagrange's equations, [66]. With a minimal set of ODEs the method is suitable for real-time simulation [67].

Paper 3 gives a comparison of the RK4 and the G-α solver when simulating drilling systems. Like with the ALE-ANCF cable element, the lumped model is tested with both Runge Kutta methods and the G-α solver. The behavior of the ALE-ANCF cable element was also compared to the lumped model as a drill string in a deviated well was modeled in a case study.

2.9.2 Governing Equations

The governing equations of motion for the lumped mass drill string system, written as the conventional second-order ODE.

$$\mathbf{M}(\boldsymbol{q})\ddot{\boldsymbol{q}} + \mathbf{C}(\boldsymbol{q}, \dot{\boldsymbol{q}})\dot{\boldsymbol{q}} + \mathbf{D}(\boldsymbol{q}, \dot{\boldsymbol{q}})\dot{\boldsymbol{q}} + \mathbf{K}\boldsymbol{q} = \boldsymbol{\tau}(\boldsymbol{q}, \dot{\boldsymbol{q}}, t) \tag{2.159}$$

The system inertia matrix, Coriolis matrix, and system damping matrix are defined as:

$$\mathbf{M} = \sum_{i}^{n} \mathbf{J}_i^\top \boldsymbol{\mathcal{M}}_i \mathbf{J}_i \in \mathbb{R}^{n_q \times n_q} \tag{2.160}$$

$$\mathbf{C}(\boldsymbol{q}, \dot{\boldsymbol{q}}) = \sum_{i}^{n} \mathbf{J}_i^\top \boldsymbol{\mathcal{M}}_i \dot{\mathbf{J}}_i \in \mathbb{R}^{n_q \times n_q} \tag{2.161}$$

$$\mathbf{D}(\dot{\boldsymbol{q}}) = \sum_{i}^{n} \mathbf{J}_i^\top \boldsymbol{\mathcal{D}}(\dot{\boldsymbol{q}})_i \mathbf{J}_i \in \mathbb{R}^{n_q \times n_q} \tag{2.162}$$

The generalized forces and torques are given by:

$$\boldsymbol{\tau} = \boldsymbol{\tau}_a + \boldsymbol{\tau}_g + \boldsymbol{\tau}_e + \boldsymbol{\tau}_c \tag{2.163}$$

$$\begin{aligned}\boldsymbol{\tau}_a &= \sum_i^n \mathbf{J}_i^\top \boldsymbol{\mathcal{F}}_i^a, \quad \boldsymbol{\tau}_g = \sum_i^n \mathbf{J}_i^\top \boldsymbol{\mathcal{F}}_i^g, \\ \boldsymbol{\tau}_c &= \sum_i^n \mathbf{J}_i^\top \boldsymbol{\mathcal{F}}_i^c, \quad \boldsymbol{\tau}_e = \sum_i^n \mathbf{J}_i^\top \boldsymbol{\mathcal{F}}_i^e\end{aligned} \tag{2.164}$$

where $\boldsymbol{\tau}_a$ is the applied forces and torques, $\boldsymbol{\tau}_g$ is the external gravitational forces, $\boldsymbol{\tau}_c$ is the generalized contact forces and torques, and $\boldsymbol{\tau}_e$ represent the generalized tension forces. $\mathbf{J}_i$ is the link Jacobian. For a complete derivation of the lumped mass drill string system, see Paper 3.

2.9.3 Numerical Time Integrator

The residuals are given by eq. (2.165), which is similar to what is presented in Sec. 2.3.4, and the numerical time integration follows the same procedure as in Sec. 2.4. The G-α integrator used for Lumped Model (LM), in conformity with ALE-ANCF cable elements, also follows the procedure outlined in [51].

$$\boldsymbol{R}^q = \boldsymbol{M}(\boldsymbol{q})\ddot{\boldsymbol{q}} + \boldsymbol{C}(\boldsymbol{q},\dot{\boldsymbol{q}})\dot{\boldsymbol{q}} + \boldsymbol{D}(\dot{\boldsymbol{q}})\dot{\boldsymbol{q}} + \boldsymbol{K}(\boldsymbol{q})\boldsymbol{q} - \boldsymbol{\tau}(\boldsymbol{q},\dot{\boldsymbol{q}},t) \tag{2.165}$$

For G-α, when calculating $\boldsymbol{S}_T$ in eq. (2.87), the following in eq. (2.166) are valid. The Coriolis matrix and system damping matrix is combined for the tangential-damping matrix.

$$\begin{aligned}\frac{\partial \boldsymbol{R}^q}{\partial \ddot{\boldsymbol{q}}} &= \boldsymbol{M} \\ \frac{\partial \boldsymbol{R}^q}{\partial \dot{\boldsymbol{q}}} &= \boldsymbol{C}_T = \frac{\partial \mathbf{D}\dot{\boldsymbol{q}}}{\partial \dot{\boldsymbol{q}}} + \frac{\partial \mathbf{C}\dot{\boldsymbol{q}}}{\partial \dot{\boldsymbol{q}}} - \frac{\boldsymbol{\tau}}{\partial \dot{\boldsymbol{q}}} \\ \frac{\partial \boldsymbol{R}^q}{\partial \boldsymbol{q}} &= \boldsymbol{K}_T = \frac{\partial \boldsymbol{M}\ddot{\boldsymbol{q}}}{\partial \boldsymbol{q}} + \frac{\partial \mathbf{K}\boldsymbol{q}}{\partial \boldsymbol{q}} - \frac{\boldsymbol{\tau}}{\partial \boldsymbol{q}}\end{aligned} \tag{2.166}$$

The G-α solutions procedure is presented in Algorithm 1. When contact occurs the formation stiffness is typically larger than the structural stiffness. The tangent-stiffness and damping matrix for G-α can become ill-conditioned with a low number of lumped elements, due to the large contact stiffness, with a large spread in the matrix values.

2.9.4 Cases - Drill String

Two of the cases in Paper 3 were used to validate the lumped mass model. The cases were based on a drill string, which in normal conditions is stretched because of the internal weight, influence of gravity, and buoyancy due to the mud in the annulus.

Algorithm 1 Numerical integration of eq. (2.159) with G-α.

1: Initialization: Set eccentricity and compute $\boldsymbol{\mathcal{M}}_i$, from drill-string structural parameters.
2: Define velocities of the COG for each body i, and calculate the projection Jacobian $\mathbf{J}_i$.
3: Project all i matrices and perform the summation to form $\mathbf{M}$, $\mathbf{K}$.
4: In G_α, derive tangent-stiffness $\mathbf{K}_T$ and damping matrices $\mathbf{C}_T$.
5: Provide $\boldsymbol{q}_{t=0}, \dot{\boldsymbol{q}}_{t=0}, \ddot{\boldsymbol{q}}_{t=0}$.
6: **while** Simulation: $t > 0, t \neq t_f$ **do**
7: Calculate drill string inputs, $u_h(v_b, u_{\text{heave}}), T_d(\varphi_s)$
8: Compute generalized forces and torques, $\boldsymbol{\tau}(t, \boldsymbol{q}, \dot{\boldsymbol{q}}, u_h, T_d)$.
9: Iterate t_{n+1} displacements, velocities, and accelerations according to Algorithm 1 in [51], until convergence.
10: **end while**

For a deviated wellbore configuration, such as the J-well, the drill-string model in (2.159) is deformed by gravity in both lateral and longitudinal-direction, where both the axial stiffness and the bending stiffness of the pipe affects the configuration. The goal for the simulation is to verify that it obtains its form of the pipe at rest for the given material data presented in Table 2.3. It is assumed that the drill string is hanging in its dry-weight down in the wellbore, without buoyancy effects. To verify the static solution of the axial and bending forces, the two effects are isolated in separate tests, a vertical and a horizontal configuration.

FEM models were used for the benchmarking. The FEM models were created in `Abaqus`, being an acknowledged commercial software for FEA. The models were created with 2D beam elements, where both a linear and a nonlinear solution was found. For configuration B and C, the nonlinear solution would not converge with a static solver and had to be solved with a dynamic explicit solver.

Furthermore, the cases were also used to verify the accuracy of the ALE-ANCF cable element, and to find the number of elements required to obtain satisfactory representation of the deformation in the drill string. To use ALE-ANCF cable elements for form finding by the use of a dynamic solver, additional damping had to be included. This was done by the use of mass proportional damping. The damping procedure is presented in the following section. The last part was not included in any of the papers, only in the following sections of the thesis.

2.9.4.1 Mass Proportional Damping for the ALE-ANCF Cable Element

For a system built with linear elements, a static solution should be obtainable, even though the system might provide incorrect results. To improve accuracy of the system, nonlinear elements must be used. Furthermore, if for example the goal of the simulation is form finding, then a nonlinear static solution could have difficulties with convergence, and a dynamic solver must be used. Therefore, mass proportional damping was implemented to improve convergence for dynamic solvers in combination with ALE-ANCF cable elements.

Table 2.3: Drill string material and force parameters.

	Description	Value	Unit
E	Young's modulus	$200{\cdot}10^9$	Pa
G	Shear modulus	$79{\cdot}10^9$	Pa
ρ_s	Material density, steel	7850	$[\mathrm{kg}\cdot\mathrm{m}^{-3}]$
L	Unstretched length	1000	$[\mathrm{m}]$
L_p	Length pipe	880	$[\mathrm{m}]$
L_c	Length collar	120	$[\mathrm{m}]$
$d^o_{i,\mathrm{p}}$	Drill pipe OD	0.127	m
$d^i_{i,\mathrm{p}}$	Drill pipe ID	0.1086	m
$d^o_{i,\mathrm{c}}$	Drill collar OD	0.165	m
$d^i_{i,\mathrm{c}}$	Drill collar ID	0.0572	m
I^x_{p}	2nd moment of inertia	$0.0594{\cdot}10^{-4}$	m^4
I^x_{c}	2nd moment of inertia	$0.3595{\cdot}10^{-4}$	m^4
g	Gravity	9.81	$[\mathrm{m/s}^2]$
f_{eA}	Force at end	0	[kN]
g_A	Gravity	9.81e-6	$[\mathrm{m/s}^2]$
f_{eB}	Force at end	0	[kN]
g_B	Gravity	9.81e-4	$[\mathrm{m/s}^2]$
f_{eC}	Force at end	1500	[kN]
g_C	Gravity	9.81	$[\mathrm{m/s}^2]$

To find a static solution with a dynamic solver, additional damping was implemented so that the simulation would settle down. A common method to implement damping in a system is the Rayleigh-damping, [68]:

$$\boldsymbol{C} = \alpha_1 \boldsymbol{M} + \alpha_2 \boldsymbol{K} \tag{2.167}$$

Rayleigh-damping is a proportional damping, where the damping is assumed to be a linear combination of the mass and stiffness matrices. The coefficients have the dimensions $\alpha_1 = [\frac{1}{s}]$ and $\alpha_2 = [s]$, giving the time unit in seconds.

From the total force vector eq. (2.45), the contribution to damping comes from eq. (2.49), which is associated with the axial stiffness and bending stiffness.

It is therefore suggested to expand eq. (2.45) with a damping force associated with the mass. This will provide damping more in line with Rayleigh-damping to the system in eq. (2.40). The added damping force is presented in eq. (2.168). Also eq. (2.169) is added as a contribution in $\boldsymbol{C}_T$ in eq. (2.59).

$$\boldsymbol{Q}_m = -\int_{p_1}^{p_2} \alpha_1 \rho A \boldsymbol{N}^T \boldsymbol{N} \dot{\boldsymbol{q}} dp = -\alpha_1 \boldsymbol{M} \dot{\boldsymbol{q}} \tag{2.168}$$

$$\frac{\partial \boldsymbol{Q}_m}{\partial \dot{\boldsymbol{q}}} = -\alpha_1 \boldsymbol{M} \tag{2.169}$$

The systems response is highly affected by the mass proportional damping, α_1. Increasing the mass proportional damping will result in a more and more diagonal damping matrix, which is good for the stability of the solver, but the accuracy is affected negatively. The effect can be observed as "syrup" motions in the system.

2.9.4.2 Case - Free-Hanging Vertical Solution

The vertical case is a cable hanging in gravity. The stretch are presented as displacements from the unstretched configuration, Fig. 2.37. From the FEM results, the total elongation of the drill string is $38cm$. The ALE-ANCF solution was modeled with both element segments of $40m$ and a model with 1 element for the pipe section and one element for the collar section. The ALE-ANCF results solution agree with the FEM results, thus, to get the axial elongation it is satisfactory with only one element for the pipe section and one element for the collar section. For the LMs, convergence is observed as the number of masses increase.

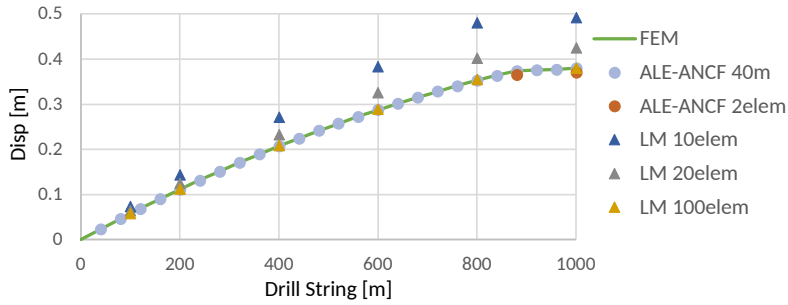

Figure 2.37: Vertical drill string in gravity. Changes in node position are indicated as displacements from unstretched configuration.

2.9.4.3 Case - Convergence to a Horizontal Drill Solution

To verify the forces due to bending and axial tension, simply supported beam in horizontal orientation affected by gravity is modeled. It is presented as a drill string in Fig. 2.38.

For the LM to represent a pinned boundary condition at the bit end, a static force in horizontal direction has to be applied at the bit end. The force equals the horizontal reaction force at the bit end for the FEM model. Undesirable horizontal displacement is restricted by this force. For a linear analysis, the horizontal force does not affect the vertical bending deformation. This can be observed in Fig. 2.40, where FEM linear has no horizontal displacement even without constraints. The lack of coupling between bending and axial tension

leads to a faulty representation of the deformed shape. The LM also includes springs in vertical and out of plane direction at the bit end, to represent the pinned boundary condition.

Three different configurations are presented with different values of the gravity and axial force, A, B, and C.

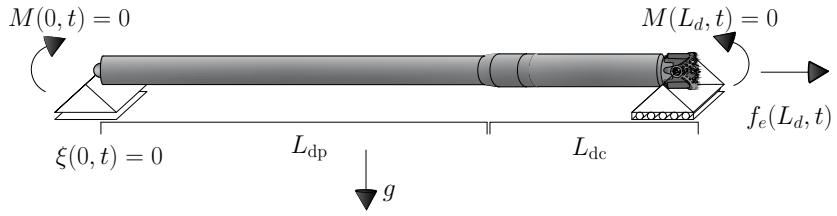

Figure 2.38: Drill string presented as a simply supported beam. The collar is free to move in horizontal direction. For configuration C, an external force f_e is acting on the bore head. There are no bending moment, M, at the ends.

For configuration A, the loading condition with reduced gravity to $g_A = 9.81e-6m/s$ and zero horizontal force, the linear and nonlinear FEM has coinciding results, Fig. 2.39. For this configuration the bending stiffness is governing for the shape of the drill string. With elements that are $240m$ long, a decent representation of the drill string is obtained. With an increase of elements, to elements that are $80m$ long, ALE-ANCF and FEM has coinciding results. The LM also has similar results to the FEM results.

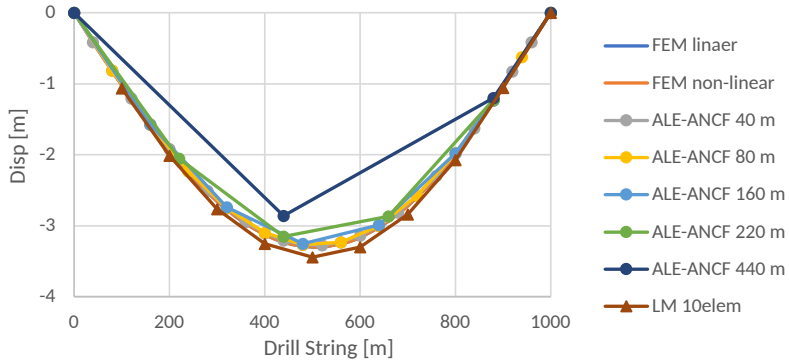

Figure 2.39: Drill string configuration A.

As the gravity increases to $g_B = 9.81e-4m/s$, the linear analysis start to deviate from the nonlinear analysis, Fig. 2.40. With zero horizontal force, the nonlinear analysis also shows the contraction of the drill string with a negative horizontal displacement, due to strong coupling to the axial tension. With elements that are $440m$ long, the convergence is much worse compared to configuration A. With an increase of elements, to elements that are $80m$ long, ALE-ANCF and FEM has coinciding results. The LM also has similar results to the FEM results.

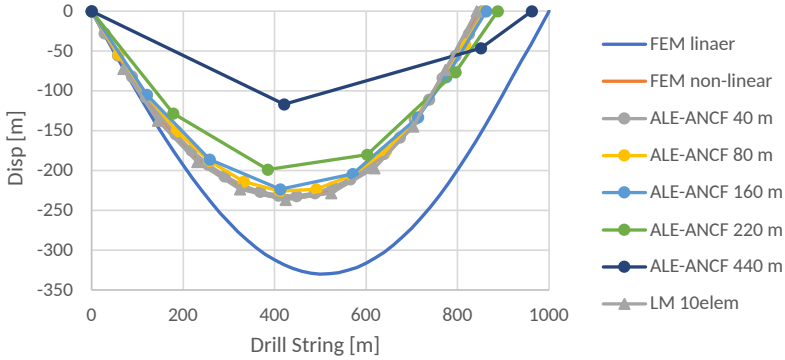

Figure 2.40: Drill string configuration B

With full gravity $g_C = 9.81m/s$, the implementation includes a horizontal force of $f_{eC} = 1500kN$ at the bit end, Fig. 2.41. This is similar to a beam with pinned boundary conditions in both ends. The required number of elements are equal as for configuration A. The results from ALE-ANCF are still in agreement with FEM results. The linear FEM results are in the order or $1e6m$, meaning that the method is inadequate for a realistic representation of the drill string, and are therefore not considered relevant. The FEM nonlinear solutions must be solved with a dynamic solver. The LM converge as the number of elements are increased from 10 to 20.

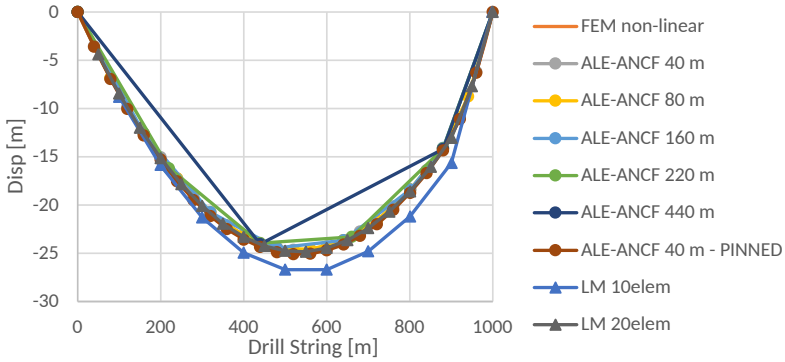

Figure 2.41: Drill string configuration C.

Both LM and ALE-ANCF cable elements demonstrates an ability for a close match with the FEM results for the bending case.

For LM significant effects such as complex geometrical stiffening effects are neglected, and the displacements is an effect of the external and restoring forces. As when simulating an actual drill-string, it is confined in the borehole such that the lateral movement is limited, and the curvature is relatively low. The length-to-diameter ratio of each element is large. For calculation of actual stress and strain of a drill-string segment, geometrical stiffening

effects must be included. FEM models would then be a better suited option, whereas the purpose of the LM is to be a simplified and efficient model.

In Fig. 2.42, the effect of mass proportional damping is demonstrated. The plot shows the vertical displacement of the node at $440m$ (one of the center nodes), for the $1000m$ long drill string, with configuration C. The blue line shows a simulation with G-α as numerical integrator. A decrease is observed in the plot due to numerical damping. In the orange line the mass proportional damping is introduced as $\alpha_1 = 0.1$. Already from the first oscillation the cable is significantly damped, and fully damped by 10 oscillations, due to the mass proportional damping.

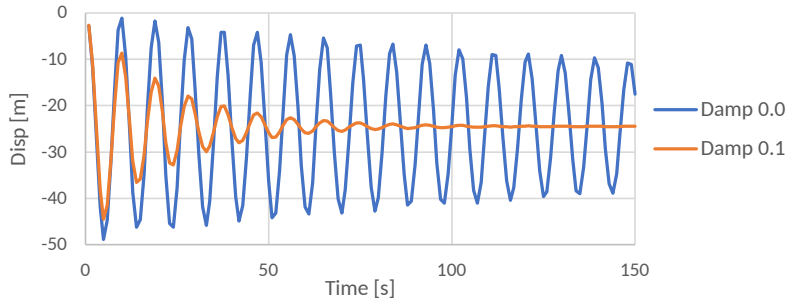

Figure 2.42: Drill string configuration C, with vertical displacement from node 3 at $440m$ with $\alpha_1 = 0.0$ and $\alpha_1 = 0.1$

From the cases above it is found that ALE-ANCF can be used for form finding when mass proportional damping is introduced. The results are then in agreement with FEM results. The required number of elements for the ALE-ANCF cable are relatively low for an accurate representation.

2.9.5 Critical Time-step

From Sec. 2.5, the critical time-step for RK4 is limited by the highest frequency in the system. The same derivation holds when used for the LM. For convenience, eq. (2.137) is repeated and updated in eq. (2.170).

$$h \leq \frac{2.8}{\omega_{max}}, \quad \text{where} \quad \omega_{max} = \sqrt{\frac{k_{\text{co}}}{\min([m_1, \ldots, m_n])}} \tag{2.170}$$

m is now represented by the minimum of all the individual drill string element masses, denoted by $\min(\cdot)$. A penalty spring method is used to represent contact forces between the wall and the drill string, where the formation stiffness is given by k_{co}. For simulation of a drill string, the highest eigenfrequency occur as transverse vibrations during contact between the wall and the drill string. For a free hanging form of the drill string, the formation

of penalty springs will not occur. Free hanging conditions are generally not the case for practical applications. In general the drill string will be in contact with the wellbore wall.

Nonlinear models including contact and stick-slip behavior demand a relatively low time-step for a stable solver. Contact forces are modeled by stiff penalty springs. The high stiffness cause high frequencies, which cause instability and poor representation of vibrations in the drill string if it is not damped. G-α is thus a viable option, as it dampens out high frequencies.

2.9.6 Solution Times

A simulation study was performed to investigate the performance of the RK4 and G-α for the LM. The model parameters are given in Table 2.3, with the wellbore configuration and initial element position shown in Fig. 2.43. The fixed base frame is defined with the orthogonal unit vectors, $\vec{a}_i$, with positive $\vec{a}_3$ axis pointing downwards. For the model set-up it was assumed that the traveling block velocity could be manipulated. The drill string was set stationary in the rig floor slips, so that the drill string follows the sea heave motion. The block position was set by a periodic function, with simple wave characteristics. The periodic function used to define the block position, u_h, is given by eq. (2.171). As the simulation start, the initial configuration of the drill string is subjected to gravity and contact forces from resting on the wellbore wall. For reference the base-case is set as RK4 with the smallest time-step, $h = 10^{-4}$. The measure used for comparison is given by the square of the error, e_n, in eq. (2.172), where $\vec{p}$ is the bit position, for the solvers $S \in \{\mathrm{G}_{\alpha 1}, \ldots, \mathrm{G}_{\alpha 5}, \mathrm{RK4}_1, \ldots, \mathrm{RK4}_5\}$, and for the time-steps $h \in \{10^{-4}, 10^{-3}, 10^{-2}, 2 \cdot 10^{-2}, 10^{-1}\}$.

$$u_h = \sin\left(\frac{2\pi(t-5)}{20} + \frac{(t-5)^2}{400}\right) \tag{2.171}$$

$$e_n = (||\vec{p}^{\,\mathrm{RK4}_1}_{n,b_n}|| - ||\vec{p}^{\,S}_{n,b_n}||) \tag{2.172}$$

The upper plot in Fig. 2.44 show the squared input for the traveling block, and the norm of the bit velocity for $\mathrm{RK4}_1$ and G-α_1, $||\vec{v}^{\,c}_{nb_n}||$. Here $\vec{v}^{\,c}$ is the linear velocity of the mass center, where b indicate the local frame for the nth element i.e. the bit. A magnified window of the stiction phase between 18 to 21 sec is presented. It can be observed that G-α is more stable in this area with no oscillations.

To quantify the accumulated error from eq. (2.172) in a simulation, the Root Mean Square Error (RMSE) is used and calculated according to eq. (2.173), where N is the total number of time steps in the simulation, and $e^2_{n,i}$ is the square of the error for the nth element i.e. the bit. The unit is given as displacement. From Table 2.5 and the bottom plot in Fig. 2.44, the RMSEs are in the range om centimeters or millimeters, which is good compared to the total length of the drill string. As the time-step for G-α increases, the accuracy decreases. This is the behavior as observed with ALE-ANCF cable elements. To capture the highest

Table 2.4: Model parameters with $n = 12$ for the J-well studies. The structural parameters are given in Table 2.3. *-marked applies for the model in rotation and lifting.

	Description	Value	Unit
ρ_m	Density, mud	1840	$\mathrm{kg\,m^{-3}}$
L_{dc}	Length BHA	240	m
L_{vr}	Vertical reach	3200	m
L_{hr}	Horizontal reach	1000	m
d_w	Borehole diameter	0.2032	m
ϵ_1,ϵ_2	BHA eccentricity*	0, 10^{-4}	m
μ_k	Kinetic friction factor	0.2	-
μ_s	Static friction factor	0.3	-
k_c	Formation stiffness	10^9 $(d^o_{i,.}/d^o_{i,\mathrm{dc}})$	$\mathrm{N\,m^{-1}}$
d_c	Formation damping	$5{\cdot}10^6$ $(d^o_{i,.}/d^o_{i,\mathrm{dc}})$	$\mathrm{N\,s\,m^{-1}}$
v_{tr}	Slip velocity threshold	10^{-5}	$\mathrm{m\,s^{-1}}$
C_a	Added mass coeff.	1	-
C_d	Drag force coeff.	1	-
c^r_i	Damping coeff.	20	$\mathrm{N\,m\,s\,rad^{-1}}$
$c^f_{2,i}$	Damping coeff.	10	$\mathrm{N\,s\,m^{-1}}$
$c^c_{f,i}$	Viscous friction coeff.	1.5	$\mathrm{N\,m\,s\,rad^{-1}}$
p_∞	G_α	0.1	-
h	Simulation time-step	0.001	s

frequencies in the drill string, the same principle as presented in Fig. 2.23 holds, where large time-steps will not capture the high frequencies.

$$\mathrm{RMSE} = \sqrt{\frac{1}{N}\sum_{1}^{N} e^2_{n,i}} \tag{2.173}$$

To investigate the solution times, and thus the real-time capacity, for the simulation, a Real-Time Factor (RTF) was introduced in eq. (2.174). The actual time for the simulation is normalized against the final time of the simulation. If it takes 1 sec to simulating a drill string for 10 seconds, RTF equals 0.1. As the time-step is increased in Table 2.5, the advantage of being unconditionally stable is manifested for G-α. For RK4 $h = 0.02$ and 0.1 sec did not converge, as maximum time-step size is exceeded, the solver becomes numerically unstable.

$$\mathrm{RTF} = \frac{\mathrm{time}_{\mathrm{actual}}}{\mathrm{time}_{\mathrm{final}}} \tag{2.174}$$

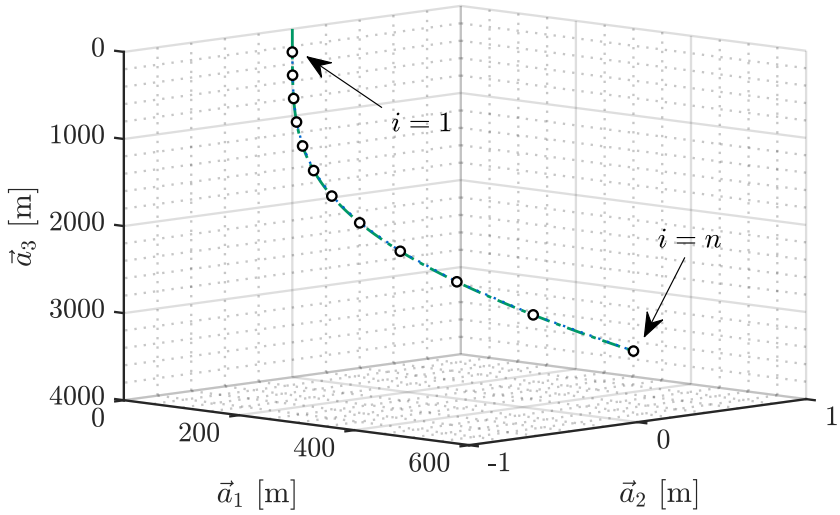

Figure 2.43: Wellbore configuration with model element position indicated by circles.

Table 2.5: RTF and RMSE for the drill string simulation case.

h	Solver	RTF	RMSE
0.0001	RK4	23.8	0
0.0001	G-α	36	$3.65{\cdot}10^{-2}$
0.001	RK4	2.29	$5.18{\cdot}10^{-4}$
0.001	G-α	19.9	$6.1{\cdot}10^{-3}$
0.01	RK4	0.226	$3.43{\cdot}10^{-3}$
0.01	G-α	3.06	$9.03{\cdot}10^{-3}$
0.02	G-α	2.06	$1.51{\cdot}10^{-2}$
0.1	G-α	0.475	$6.45{\cdot}10^{-2}$

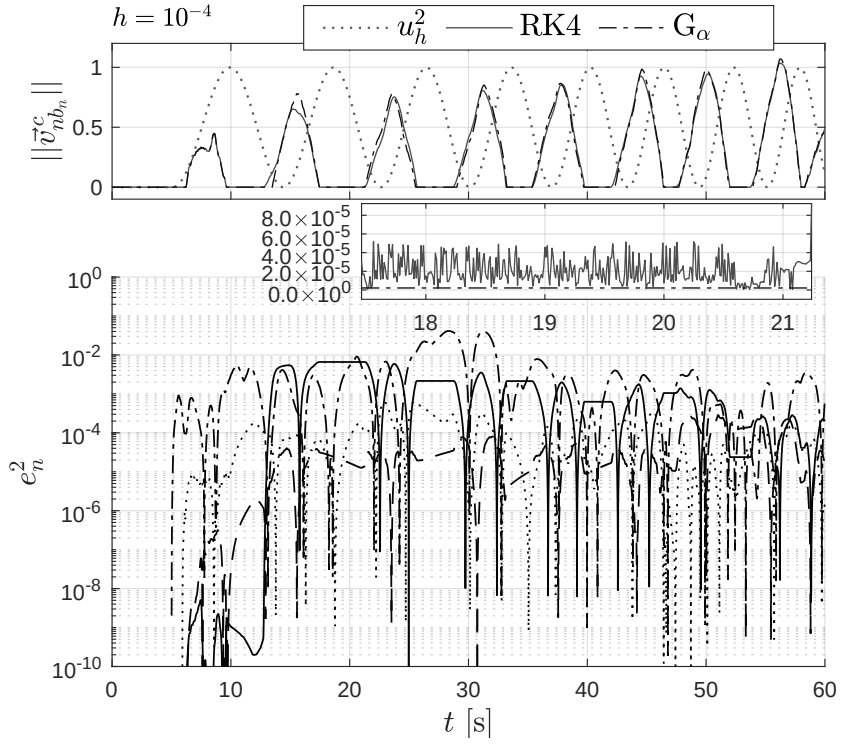

Figure 2.44: Comparing e_n^2 for $h \in \{10^{-4}, 10^{-3}, 10^{-2}, 10^{-1}\}$, with G-$\alpha$ and for RK4_1 as base-case in heave motion. For the lower-most plot the y-axis is in log scale, and solid line denotes $h = 10^{-4}$, dashed line $h = 10^{-3}$, dotted line $h = 10^{-2}$ and dash-dotted line $h = 10^{-1}$, respectively. A magnified window from 18 sec to 21 sec is displayed as the middle plot.

Chapter 3

Program

A `Python` program was created for testing and benchmarking of the ALE-ANCF cable formulation presented in this work. `Python` was chosen due to the many predefined libraries for e.g. plotting and matrix handling. It is a popular open-source programming language, where the users have easy access to examples, guides and help online. This makes it a convenient programming language for prototyping programs of the sort presented in this work. An introduction to the program follows, with an outline of different functionality.

3.1 Setup of the Program

The model in the simulation is initiated by a setup-file in `YAML`-format. An example of such a setup-file can be found in Appendix A, where the syntax is presented. `YAML` is a human-readable serialization language, [69]. It is often used for configuration-files, where the parameters and initial settings for a computer program are defined. In this program the initial values such as initial node placement, material flow, boundary condition, forces, and material parameters are defined. The user defined parameters are presented in the sections below. Having a separate model-file offers for the ability to run different models without changing the solver-files. The advantage of defining the model in a separate `YAML`-file is the flexibility for building and running the simulation in a different software. The node, material and force definitions are independent of the solver software.

3.1.1 Material Parameters

The material parameters are given in *CableModelMaterial*. The different parameters being set are *CableStiffness*, *CableMass* with the unit $\frac{kg}{m}$, *CableDamping* and *Gravity*. The gravity is defined in x-, y-, and z-direction. All the parameters are given in SI-units for the present work.

3.1.2 Nodes

The model is defined by nodes and elements. Two type of nodes are implemented. The *Node7Dof* is used for cubic elements, where the position eq. (2.2), and the slope eq. (2.3), are defined in x-, y-, and z-direction. The 7$^{\text{th}}$ degree of freedom (DOF) is the material node, p. The node can be viewed as eq. (2.1) where only the part with subscripts 1 is included. The other node is *Node4Dof* used for linear elements. It equals *Node7Dof* without the slope, $\boldsymbol{r}'$ from eq. (2.3).

The DOFs in the nodes can be set to free, prescribed, or fixed, controlling the boundary conditions in the elements. Reeling of cable is implemented by prescribing the material flow in a node by a function acting as a winch. The function sets the material position p with the accompanying material flow velocity $\dot{p}$ and material flow acceleration $\ddot{p}$ based on a flow velocity input for a time span. In a similar manner this can be done to position DOFs to prescribe the node position, $\boldsymbol{r}$, and accompanying velocity and acceleration, in x-, y-, and z-direction.

3.1.3 Cable Elements

The ALE-ANCF cable elements are implemented in the program by *CableALEelement*. The element requires the two end nodes in the form *Node7Dof* as input. Alternatively the element with linear shape function can be used, *CableALEelementLin*. The element requires the two end nodes in the form *Node4Dof* as input.

3.1.4 One Node Spring Elements

One node spring elements are axial springs associated to a node, *OneNodeSpring*. The 1$^{\text{st}}$ node is the initial position, and 2$^{\text{nd}}$ node is the axial spring associated node. The spring force is calculated based on the displacement between the 1$^{\text{st}}$ and the 2$^{\text{nd}}$ node, and the spring stiffness. The input requirements are the associated nodes given as a list, spring stiffness, k_{sp}, and damping coefficient, c_{sp}. The spring force affects the internal forces, $\boldsymbol{Q}_e$, eq. (2.47), and is related to position, $\boldsymbol{r}$. The spring force is introduced by eq. (3.1). The contribution in the stiffness matrix then becomes as presented in eq. (3.2).

$$\boldsymbol{Q}_{spring} = k_{sp}(\boldsymbol{r}_n - \boldsymbol{r}_{n,0}) \tag{3.1}$$

$$\frac{\partial \boldsymbol{Q}_{spring}}{\partial \boldsymbol{q}} = k_{sp}\boldsymbol{I}_{3x3} \tag{3.2}$$

An example of where springs are convenient is as roof springs in the elevator case presented in [11]. Instead of using the one node spring, a separate ALE-ANCF cable element with an adequate stiffness, and without material flow, could have been used as roof spring.

The *OneNodeSpring* can also include a damper. The damping force is included in $\boldsymbol{Q}_e$, eq. (2.47), as introduced in eq. (3.3). The contribution in the damping matrix then becomes, eq. (3.4).

$$\boldsymbol{Q}_{springDamp} = c_{sp}\dot{\boldsymbol{r}}_n \tag{3.3}$$

$$\frac{\partial \boldsymbol{Q}_{springDamp}}{\partial \dot{\boldsymbol{q}}} = c_{sp}\boldsymbol{I}_{3x3} \tag{3.4}$$

3.1.5 Point Force and Gravity

Point force can be added to individual nodes in the model by the use of *PointForce*. The required inputs are the nodes the force is associated with given as a list, and how large the force is in x-, y-, and z-direction, given in newton. The point force affects the external forces in $\boldsymbol{Q}_f$, eq. (2.50). It is related to the position, $\boldsymbol{r}$, as the material flow is independent of how the cable is attached to other bodies in the model.

For implementation of gravity, the gravity acceleration is set in *CableModelMaterial*, where it affects all the masses in the model.

3.1.6 Point Mass

Point masses, *PointMass*, are used to add individual masses to the model. The masses are affected by the gravity, if gravity is included in *CableModelMaterial*. The required inputs are which node the mass is associated with given as a list, and mass weight (kg). The point masses are added into the mass matrix of the system for the relevant nodes related to position, $\boldsymbol{r}$, as an attached mass is independent of the flowing material.

3.1.7 Mass Proportional Damping

Mass proportional damping is presented in Sec. 2.9.4.1. This is implemented in the program by setting the parameter *massDamp*, in the initialization.

3.1.8 Constraints

The constraints are derived in Sec. 2.3 and specifically for this program in Sec. 3.7. The constraints can be applied to the position DOFs, tangential slope DOFs or material flow DOFs. If a constraint is applied to position DOFs or tangential DOFs, an individual constraint will be generated in each free direction. The constraints can be imposed by three different methods, the Lagrange multiplier method, the penalty method, or linear couplings. The required inputs are the two nodes being constrained, what DOFs, and what type of constraint method being used. For the penalty method, the penalty spring stiffness must be specified. For the

linear coupling method, the weighting between the master nodes must be defined if more than one.

When modeling a cable containing several cable elements, the nodes can be shared, since $\boldsymbol{r}$, $\boldsymbol{r}'$, and p have to be equal for the end nodes in neighboring cables. This is more effective, as it generates fewer DOFs in the system matrix compared to having separate nodes connected with constraints.

3.1.9 Time Integrator

There are several options for time integrators implemented in the program. The different types are Newmark, G-α and RK4. α_m and α_f must be set for the G-α solver. *eps_energy* is the error criterion, which is included for the iterative integrators. *maxIter* sets the maximum number of iterations before it kills the simulation. *time_step* sets the size of each time step. *time_end* sets how long the simulation goes before finishing.

3.2 Visualization

To obtain accurate results from a simulation is worthless unless they are interpreted correctly. The results must be presented in a way so that the decision makers understand them. Visualization of results is a powerful method to communicate them. It is also a powerful tool to help the user to interpret the results, and to better understand what is happening during a simulation. It can e.g be used to detect critical time steps or critical parts of the model in a simulation. Visualization of the results is an interactive process for the user, where changes to the model can be made according to the results presented.

In this work the software `ParaView` is used to animate the simulations. `ParaView` is an open-source software, which provides the user full control over the visualization procedure, [70]. A screenshot from the software is found in Fig. 3.1. The screenshot is taken of the animation from the flutter in the garden hose in Sec. 2.7. It is useful to see how the garden hose is deformed during a simulation. `ParaView` can be used to visualize e.g. deformations and axial forces, which can be given a color score to indicate how different parts of the model are affected. The animation is done in this work by outputting a vtk-file each time step, which can be interpreted by `ParaView`, to create an animation.

3.3 Matrix Differentiation

Differentiation of a vector by a vector results in a matrix, eq. (3.5). Similarly a matrix differentiated by a scalar results in a matrix, eq. (3.6).

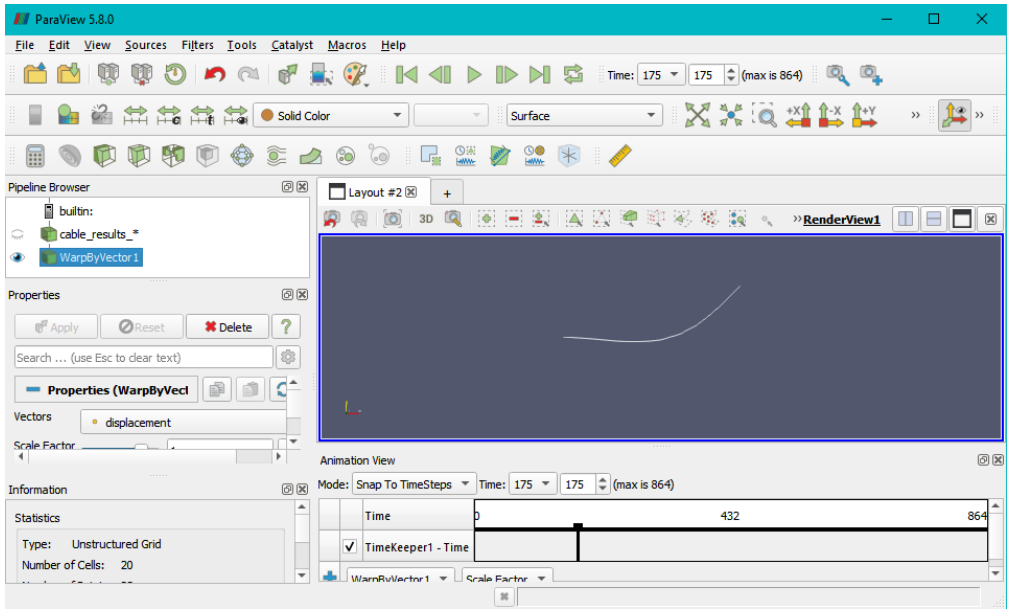

Figure 3.1: `ParaView`, a commercial software used to animate the fluttering garden hose in Sec. 2.7.

$$\frac{\partial \boldsymbol{y}}{\partial \boldsymbol{x}} = \begin{bmatrix} \frac{\partial y_1}{\partial x_1} & \frac{\partial y_1}{\partial x_2} & \frac{\partial y_1}{\partial x_3} & \cdots & \frac{\partial y_1}{\partial x_n} \\ \frac{\partial y_2}{\partial x_1} & \frac{\partial y_2}{\partial x_2} & \frac{\partial y_2}{\partial x_3} & \cdots & \frac{\partial y_2}{\partial x_n} \\ \vdots & \vdots & \vdots & \ddots & \vdots \\ \frac{\partial y_m}{\partial x_1} & \frac{\partial y_m}{\partial x_2} & \frac{\partial y_m}{\partial x_3} & \cdots & \frac{\partial y_m}{\partial x_n} \end{bmatrix} \tag{3.5}$$

$$\frac{\partial \boldsymbol{A}}{\partial g} = \begin{bmatrix} \frac{\partial A_{11}}{\partial g} & \frac{\partial A_{12}}{\partial g} & \frac{\partial A_{13}}{\partial g} & \cdots & \frac{\partial A_{1n}}{\partial g} \\ \frac{\partial A_{21}}{\partial g} & \frac{\partial A_{22}}{\partial g} & \frac{\partial A_{23}}{\partial g} & \cdots & \frac{\partial A_{2n}}{\partial g} \\ \vdots & \vdots & \vdots & \ddots & \vdots \\ \frac{\partial A_{m1}}{\partial g} & \frac{\partial A_{m2}}{\partial g} & \frac{\partial A_{m3}}{\partial g} & \cdots & \frac{\partial A_{mn}}{\partial g} \end{bmatrix} \tag{3.6}$$

As part of the solution procedure for G-α, for instance $\left(\frac{\partial \boldsymbol{Q}_p}{\partial \boldsymbol{q}}\right)$ has to be calculated, eq. (2.59). According to eq. (3.5), the output is a matrix, since both $\boldsymbol{Q}_p$ and $\boldsymbol{q}$ are vectors. By the use of the product rule, the solutions can be found by the steps outlined in eq. (3.7). Since the integral limits are differentiable, the Leibniz rule has been applied, leading to the two additional terms after the integral. It is recommended to use p as the variable, instead of s, eq. (2.5), since s is a function of p, $s(p)$.

$$\frac{\partial \boldsymbol{Q}_p}{\partial \boldsymbol{q}} = \frac{\partial}{\partial \boldsymbol{q}} \left(\int_{p_1}^{p_2} \rho A \boldsymbol{N}^T \ddot{\boldsymbol{r}}_p dp \right) = \rho A \left(\int_{p_1}^{p_2} \frac{\partial \boldsymbol{N}^T}{\partial \boldsymbol{q}} \ddot{\boldsymbol{r}}_p + \boldsymbol{N}^T \frac{\partial \ddot{\boldsymbol{r}}_p}{\partial \boldsymbol{q}} dp \right) - \frac{\partial p_1}{\partial \boldsymbol{q}} \rho A \boldsymbol{N}^T \ddot{\boldsymbol{r}}_p + \frac{\partial p_2}{\partial \boldsymbol{q}} \rho A \boldsymbol{N}^T \ddot{\boldsymbol{r}}_p \tag{3.7}$$

Both $\frac{\partial \boldsymbol{N}^T}{\partial \boldsymbol{q}}$ and $\frac{\partial \ddot{\boldsymbol{r}}_p}{\partial \boldsymbol{q}}$ are matrices differentiated by vectors. This is handled by differentiating the vector by the rows in the matrix. The procedure is repeated for every column in the matrix. The resulting matrices from the differentiation are summed. An illustration of the procedure is presented in Fig. 3.2. In the `Python`-library `NumPy`, the differentiation of a matrix by a vector can simply be handled with broadcasting by introducing N-dimensional arrays, Sec. 3.4.

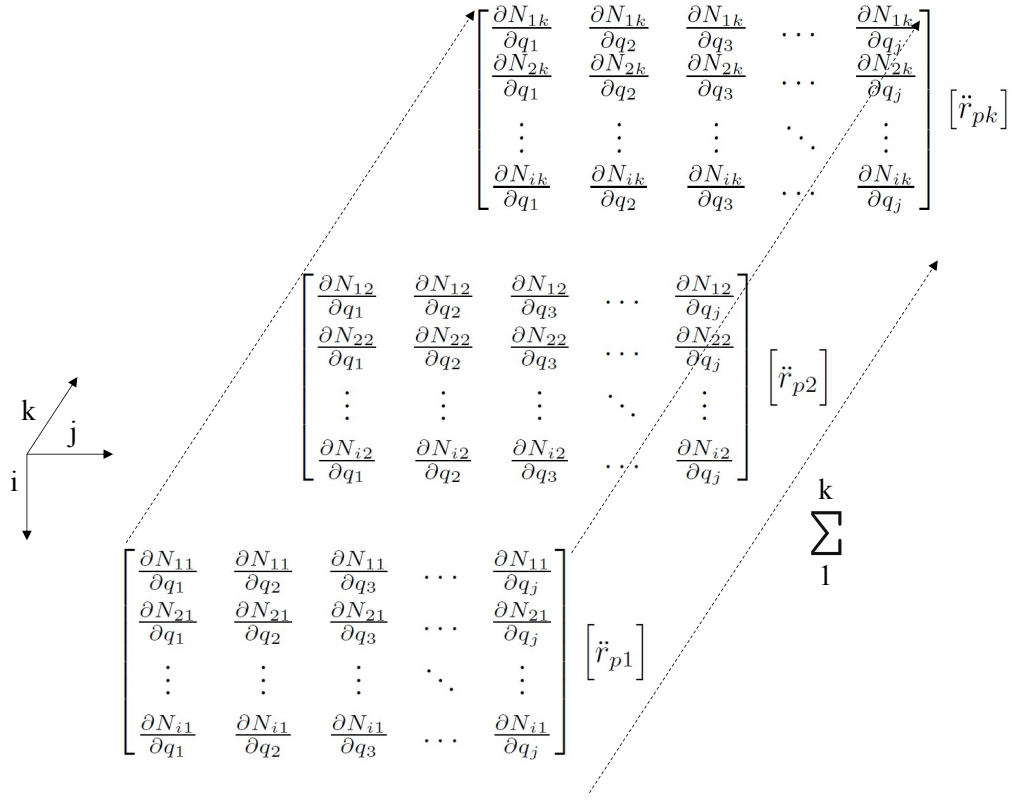

Figure 3.2: Illustration of matrix differentiated by vector.

3.4 Broadcasting

Broadcasting refers to how e.g. the `Python`-library `NumPy` handles several axes or dimensions in arithmetic operations. This is done by dividing an array into a finite number of dimensions, N-dimensions. A conceptual visualization of broadcasting is found in Fig. 3.3. In this illustration, 1-D, 2-D, and 3-D matrices has a regular coordinate system, where each object has an individual index in the i-, j-, k-direction, as commonly used. For higher dimensions, the 3-D dimension becomes a sub-dimension cube. The cubes form a new system in a 3-D room in the l-, m-, n-direction. This repeats itself for the finite number of dimensions, and each individual object still has an individual index. This method is convenient for matrix operations.

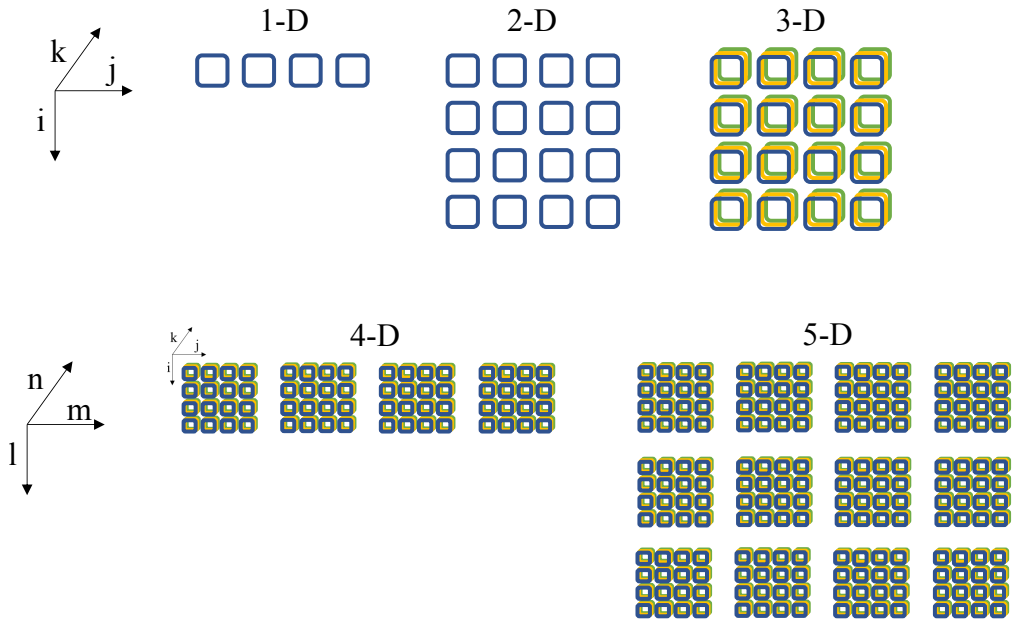

Figure 3.3: A conceptual visualization of an N-dimensional arrays, used in e.g. the `Python`-library `NumPy`.

As an example how broadcasting is used in the program, the computation procedure for eq. (3.7) in Sec. 3.3 is presented. The equation is rewritten to index form in eq. (3.8), where i, j, and k present one axis each. The syntax for the program presented in Fig. 3.4, where x contains 5 integration points for Gauss-integration, see Sec. 3.6, integrated from p_1 to p_2. The output is a 14 by 14 matrix.

$$\frac{\partial Q_{pi}}{\partial q_j} = \sum_{k=1}^{3} \left((\rho A \left(\int_{p_1}^{p_2} \frac{\partial N_{ik}}{\partial q_j} \ddot{r}_{pk} + N_{ik} \frac{\partial \ddot{r}_{pk}}{\partial q_j} dp \right) - \frac{\partial p_1}{\partial q_j} \rho A N_{ik} \ddot{r}_{pk} + \frac{\partial p_2}{\partial q_j} \rho A N_{ik} \ddot{r}_{pk} \right) \tag{3.8}$$

```
def Qp_dq(self):

    def func(x):
        Ndq_rpdd = np.zeros((14,14,np.size(x)))

        for p in range(np.size(x)): # x is the vector containing the integration points
                                    # p is the integration point number
                                    # Index order    [k,    i,    j], summary of axis k
            Ndq_rpdd[:,:,p] += np.sum( Ndq(x[p])     [:,    :,    :] *
                                       rpdd(x[p])    [:, None, None] +
                                       N(x[p])       [:,    :, None] *
                                       rpdd_dq(x[p]) [:, None,    :] , axis=0)
        return Ndq_rpdd

    integrand = integrate.fixed_quad(func,p1,p2,n=5)[0]  # Gauss Integration

    integrand[:,12] -= np.sum(N(p1)[:,:] * rpdd(p1) , axis=0)
    integrand[:,13] += np.sum(N(p2)[:,:] * rpdd(p2) , axis=0)

    return rhoA * integrand
```

Figure 3.4: Example of the syntax in the program using broadcasting to compute eq. (3.8).

It is worth noting that for axis that is not present in a vector or matrix, a "None", is added as a placeholder. This is done to control which axis being multiplied prior to summation. Broadcasting is a relatively efficient way of handling matrix operations, as presented in following section, Sec. 3.5.2.

3.5 Solution Time for Matrix Operations

3.5.1 Introduction

Different solution techniques were tested to find the more efficient solution procedure for matrix operations in the program. The libraries tested were `NumPy`, `SymPy` and `NumExpr`. The intent of the testing was not meant for benchmarking of `Python`-libraries, rather as useful insight for development of the program. As numerous test runs have been carried out during development of the program, the run time each simulation is relevant. The program is intended to be rewritten in a more efficient and appropriate language for more advanced MBS with ALE-ANCF cable elements, when prototyping is finished.

3.5.2 Test

One of the more time consuming operations during a time-step for the G-α method was to solve $\frac{\partial \boldsymbol{M}\ddot{\boldsymbol{q}}}{\partial \boldsymbol{q}}$. Therefore, this was used for a simple benchmarking of preferred solution routines for matrix operations in the program.

`NumPy` was used with two different solution procedures. The first was done by looping through every position in the matrix with one for-loop for each axis.

The other procedure used in `NumPy` was broadcasting. Broadcasting severely reduced the number of operations each time step compared to the for-loop procedure.

`Sympy` was solving the expression with symbols analytically. The result were stored in a separate file. When solving the expression, the symbols were replaced with the relevant values.

`NumExpr` is a package that compiles the code. The solution procedure was similar to the broadcasting. `NumExpr` is created for fast solving of large arrays.

3.5.3 Results

The relative CPU time for the four solution procedures tested for matrix operations are presented in Table 3.1. The CPU time is normalized against the time for broadcasting. Compiled code and broadcasting has similar capacity for this operation. For-looping is significantly slower. Analytical solution is slower and more cumbersome to work with.

Table 3.1: Speed test for matrix operations with different solutions procedure, where relative CPU time is presented.

Method	Package	Rel CPU
For-loop	`NumPy`	14317
Analytical	`SymPy`	45
Broadcasting	`NumPy`	1
Compiled	`NumPy`	1

3.5.4 Conclusion

Broadcasting in `NumPy` is a simple and efficient way to handle matrix operations. For the size of the matrices dealt with in this script, it is as efficient as using `NumExpr`. Therefore, the `NumPy` package with broadcasting is used extensively for matrix operations in the program created as part of this thesis.

3.6 Gaussian Quadrature

For numerical integration, the Gaussian quadrature method is used in the program. The method is briefly outlined below. For a more in depth presentation of numerical integration

methods, several books have good presentations of this topic, such as Ch. 6 in [71].

The integral presented in eq. (3.9) is divided up into a finite number of integration points, n_{int}. The polynomials in the integral are exact for the degree of $2n_{int} - 1$. Where ξ_l are the integration points, and w_l are the weights ascribed to the integration points.

$$\int_{-1}^{1} g(\xi)d\xi = \sum_{l=1}^{n_{int}} g(\xi_l)w_l \tag{3.9}$$

When solving the Gauss quadrature with an integral from a to b, the equation is rewritten to:

$$\int_{a}^{b} g(x)dx \approx \frac{b-a}{2} \sum_{l=1}^{n_{int}} g(\frac{b-a}{2}\xi_l + \frac{b+a}{2})w_l \tag{3.10}$$

3.7 Constraints in the Cable System

When creating a model for simulation, there are three different types of constraints implemented. The first is to constrain the position DOFs, $\boldsymbol{r}$, of two neighboring cable spans, eq. (3.11), see Fig. 2.3. This is done in x-, y-, and z-direction individually, creating one constraint for each direction, eq. (3.12), where the superscript e indicates the element number. If the initial position between two constrained nodes differ, this is handled as a desired distance, and will be kept constant between the two. The constant distance is added to the constraint as a constant value, creating the zero reference for the constraint. The differential of eq. (3.11) is found in eq. (3.13), where each row represent x-, y-, and z-direction accordingly. The second differential of $\boldsymbol{\phi}$, is given in eq. (3.14), where each constraint has one matrix each. This becomes a 3-D zero matrix. This procedure is used in Sec. 2.6.

$$\boldsymbol{\phi} = \left[\boldsymbol{r}_2^e - \boldsymbol{r}_1^{e+1}\right] \tag{3.11}$$

$$\boldsymbol{\phi} = \begin{bmatrix} r_x^e - r_x^{e+1} \\ r_y^e - r_y^{e+1} \\ r_z^e - r_z^{e+1} \end{bmatrix} \tag{3.12}$$

$$\boldsymbol{G} = \frac{\partial \boldsymbol{\phi}}{\partial \boldsymbol{q}} = \begin{bmatrix} 1 & 0 & 0 & 0 & 0 & 0 & -1 & 0 & 0 & 0 & 0 & 0 & 0 & 0 \\ 0 & 1 & 0 & 0 & 0 & 0 & 0 & -1 & 0 & 0 & 0 & 0 & 0 & 0 \\ 0 & 0 & 1 & 0 & 0 & 0 & 0 & 0 & -1 & 0 & 0 & 0 & 0 & 0 \end{bmatrix} \tag{3.13}$$

$$\frac{\partial \boldsymbol{G}}{\partial \boldsymbol{q}} = 0_{3,14,14} \tag{3.14}$$

The generalized coordinates used for calculating the differential of the constraints are given in eq. (2.1). The subscript indicate which node end of the cable element, while the

superscript e indicates the cable element, where $e+1$ is the connected cable element. This definition of $\boldsymbol{q}$ is very useful, as it includes the relevant ends of the cable spans being constrained.

$$\boldsymbol{q} = \begin{bmatrix} \boldsymbol{r}_2^e & \boldsymbol{r}_2'^e & \boldsymbol{r}_1^{e+1} & \boldsymbol{r}_1'^{e+1} & p_2^e & p_1^{e+1} \end{bmatrix} \tag{3.15}$$

The second constraint is to constrain the material coordinate, p, of two connected cable spans, eq. (3.16), see Fig. 2.3. If the initial position between two constrained node positions differ, material is added between p_2^e and p_1^{e+1} according to Frobenius norm. The differential of eq. (3.16) is found in eq. (3.17) The second differential of $\boldsymbol{\phi}$ becomes a zero matrix.

$$\boldsymbol{\phi} = \begin{bmatrix} p_2^e - p_1^{e+1} \end{bmatrix} \tag{3.16}$$

$$\boldsymbol{G} = \frac{\partial \phi}{\partial \boldsymbol{q}} = \begin{bmatrix} 0 & 0 & 0 & 0 & 0 & 0 & 0 & 0 & 0 & 0 & 0 & 0 & 1 & -1 \end{bmatrix} \tag{3.17}$$

The third constraint is to constrain the tangential slope DOFs, $\boldsymbol{r}'$, of two connected cable spans, eq. (3.18), see Fig. 2.3. As with the position type constraint, this is done in x-, y-, and z-direction, creating one constraint for each direction. The differential of eq. (3.18) is found in eq. (3.19), where each row represent x-, y-, and z-direction accordingly.

$$\boldsymbol{\phi} = \begin{bmatrix} \boldsymbol{r}_2'^e - \boldsymbol{r}_1'^{e+1} \end{bmatrix} \tag{3.18}$$

$$\boldsymbol{G} = \frac{\partial \boldsymbol{\phi}}{\partial \boldsymbol{q}} = \begin{bmatrix} 0 & 0 & 0 & 1 & 0 & 0 & 0 & 0 & 0 & -1 & 0 & 0 & 0 & 0 \\ 0 & 0 & 0 & 0 & 1 & 0 & 0 & 0 & 0 & 0 & -1 & 0 & 0 & 0 \\ 0 & 0 & 0 & 0 & 0 & 1 & 0 & 0 & 0 & 0 & 0 & -1 & 0 & 0 \end{bmatrix} \tag{3.19}$$

The three constraint types that are implemented are both holonomic and conservative. Holonomic constraint depends only on the coordinates and time; whereas nonholonomic constraints are dependent of path, and is described by parameters subjected to the differentials of the constraints. A general discussion of how to implement nonholonomic constraints is done by [38].

Chapter 4

Conclusions and Further Work

4.1 Conclusions

The overall conclusions of this work are summarized in this section:

- The SPADE model has been used as a framework towards the creation of a digital twin of cranes on offshore vessels. A digital twin of an offshore crane would allow for safer lifting operation with less downtime, improved fatigue prediction, and better maintenance planning. Also, a better simulation model would improve the control system and monitoring, which again would allow for safer lifting operations, by e.g. detection and alarming of critical loading conditions and improved payload control. There are several challenges related to achieving a satisfactory functioning digital twin. Through different cases, it was evident that simulations lacked a sufficiently robust numerical formulation for cable and pulley representation. A satisfactory cable and pulley simulation is essential for an operational FEA, used for a real-time monitoring.
- A trade study to select best alternative for cable and pulley simulation for cranes on offshore vessels were performed with the systems engineering approach known as subjective value method. The ALE-ANCF cable element had the highest score as it is very suitable for real-time simulations since few elements are needed, and the nodes can be stationary at contact areas with the pulley. It also has good dynamic representation of the cable, and can include contact as well as time varying length. A satisfactory cable and pulley simulation is essential for an operational FEA, used for a real-time digital twin.
- The axial frequencies from ALE-ANCF cable element for 1^{st} and 2^{nd} vibration mode are in complete agreement with the axial frequency found in [58]. The frequency is independent of how the element is constrained with free position DOF and fixed flow DOF, or fixed position DOF and free flow DOF. A simplification of the cable to a single degree of freedom MSD does not provide an accurate axial frequency.

- The MSD element length cannot directly be used to predict the maximum time-step for RK4, as higher frequencies are present in the ALE-ANCF cable elements. A criterion to predict the maximum time-step for RK4 is created based on an easy to calculate *effective* (or *equivalent*) length as a fraction of the shortest element length in the mesh as well as the boundary conditions. The criterion is verified through eigenvalue analysis as well as numerical hammer test and FFT.
- With high demands on the solution time to obtain real-time simulations, the selection of solver is important. The literature lacks a recommendation of which solver to choose for ALE-ANCF cable elements. Therefore, the present study presents a systematic approach to compare RK4 and G-α. RK4 is used in similar studies, and G-α is commonly used in classical structural mechanics software, making them good candidates for a numerical study with respect to explicit versus implicit time-integration. The systematic approach examines with the criteria *stability*, *accuracy*, and *efficiency*. It is found that RK4 is a good choice when simulating models with few elements and long cable spans. The stability limit for RK4 gets worse as the number of elements increase, despite the real frequency response in the system being the same. When performing simulations with equal time-steps, RK4 is about 3 times faster than G-α. For external loads requiring small time-steps, or where high frequencies in the system are of interest, RK4 is the most efficient solver. For loads with lower frequencies than the stability limit for RK4, G-α is better. G-α provides fast and accurate results as the high frequencies are dampened out and it is not hampered by requirements on the time-step size. The time-step size can be selected just by ensuring a sufficient number of time steps to capture the desired physical behavior of the model. Thus, G-α is found to often be the best alternative for most practical applications. Adams, [72], also concludes that the CPU time increase with element stiffness for a ANCF element for an explicit solver, while it has little effect on the implicit solver.
- To achieve possibilities for advanced geometrical shapes, the ALE-ANCF cable element has to be connected with neighboring elements. In relation to the time integration methods, coupling methods are examined. The penalty method, Lagrange multiplier method and linear coupling are the methods used for connecting ALE-ANCF cable elements. For a system constrained by the penalty method, the penalty springs increase the stiffness in the system causing higher frequencies, which again reduces the maximum time-step for RK4. When using the Lagrange multiplier method with RK4, the solution is vulnerable to drifting as the constraints are differentiated as part of the solution procedure. To connect elements using constraints; the Lagrange multiplier method, penalty method or linear coupling are all valid methods providing similar results and solution times for the case with G-α.
- A lumped model to simulate a drill string in an arbitrary wellbore is presented, where the equations of motion are defined by the use of Kane's method. From comparison with FEA for a static horizontal and static vertical configuration of the drill string,

the lumped model conforms with FEA. With increasing number of elements, the solution converges. For ALE-ANCF cable elements, mass proportional damping was introduced, in means to stabilize the dynamic simulation. ALE-ANCF cable elements efficiently converged to the same solution as lumped model; thus, mass proportional damping was successfully used in combination with ALE-ANCF cable elements.

- The lumped model is solved with both RK4 and G-α as numerical time integrators, where both efficiency and error propagation are compared. The same tendency as for ALE-ANCF cable elements is observed. RK4 is faster for smaller time-steps. As the time-step is increased, RK4 reaches a maximum time-step, where the simulation start to diverge. For G-α larger time-steps are possible, and thus this can also provide high simulation speed. Even though the accuracy is reduced as time-steps are increased, it could still provide satisfactory results. The lumped model is suitable for real-time implementation with solution times below real-time. The model is thus useful for monitoring down hole dynamics of drill strings in drilling operations.
- A brief summary of findings comparing RK4 and G-α are presented in Table 4.1.

4.2 Further Work

The methods suggested in this paper could be developed by the following research points:

- This work is based on programs which can be considered prototypes. For both the ALE-ANCF cable element and the lumped model, further improvement of the solver should be a focus area. To improve solution time, adaptive time-step algorithms could be considered. Implementation in a more suitable software with compiled code is also believed to make a huge impact on simulation speed.
- To further improve the calculation speed for ALE-ANCF cable element, a low order element with engineering strain and linear shape function could be tested. Limitations due to neglecting nonlinear characteristics must be identified, where i.e. bending stiffness and flow force from inertia of the material flow through the cable could be defined according to the angle between neighboring elements.
- To move towards a control system of an offshore crane, with an ALE-ANCF cable element used to model the wire, the laboratory knuckle boom crane presented in Paper 1 should be simulated for benchmarking. A model already exists in a commercial software with sensor input as a functionality. The crane are then to be instrumented, to enable sensor data input into the simulation, where forces from the ALE-ANCF cable element could be imported from an external solver. To have a fully functioning digital twin, commercial software could be used for processing of sensor data, calculation, simulation, and visualization. A heave compensation case could be tested and compared to existing experiment data for the laboratory knuckle boom crane, to check if ALE-ANCF cable elements improve the simulation quality. This will be a

G-α

Pro	Con
• Allows large time-steps when loading and response is low-frequency • No step-size restriction, unconditionally stable. • Provides damping to modes that are high frequency relative to the time-step. • Time-step requirement unaffected by penalty method constraints.	• Each time-step is numerically expensive. • Require iterations for optimal accuracy for nonlinear problems, especially with large time-steps.

RK4

Pro	Con
• Numerical low cost for each time-step. • Numerically efficient with high frequency loading. • Highly predictable computation times	• Has maximum time-step associated with smallest element in the model • Unnecessary number of time-steps for low frequency loading and response • Penalty method constraints affects maximum time-step negatively.

Table 4.1: Characteristic Pros and Cons of the G-α and RK4 algorithms

trial by fire for how the solver handles slack cables, and real-time analysis with G-α. Furthermore, it will highlight the usefulness of this research for the industry.

- Several cases could be evaluated for benchmarking both to further improve the functionality of the code, and investigate the possibilities of ALE-ANCF cable elements:
  - Diabolo: A diabolo is a juggling toy. The interesting part is the string, where the diabolo spins and are thrown from. The string could be modeled as ALE-ANCF cable elements with contact along the string. The numerical solution procedure will be put to a test as the string goes in and out of contact with the diabolo.

- Prestressed concrete: Concrete is a material that has very good compression qualities, and very poor stress qualities as it easily fractures. A common method to prevent concrete to fracture is to either pretension or posttension the concrete. Pretension is done by pretension steel wires prior to pouring the concrete. As the concrete is hardened, the anchors for the steel wires are released, causing the steel wire to compress the concrete. For posttensioning, the concrete is poured over plastic or steel sleeves with steel wires inside. As the concrete is hardened, the steel wire can be tensioned. Elegant, slender concrete structures, such as bridges and vast roofs, commonly use the posttensioning technique. ALE-ANCF cable elements are believed to be well suited for modeling the steel wire, both due to the ability for large-deformations and large-rotations, and material flow through the nodes allowing for simple tensioning of the deformed steel wire.
- Siphoning beads: Siphoning beads, chain fountain, or Mould effect, is a phenomenon where a chain of beads rises higher and higher over the edge of a container, as it falls over the edge of the container. ALE-ANCF cable elements could be suitable to simulate this phenomenon, as the mass flowing through the elements cause inertia forces.

References

[1] I. M. Holmen, I. B. Utne, and S. Haugen, "Risk assessments in the Norwegian aquaculture industry: Status and improved practice," *Aquacultural Engineering*, vol. 83, pp. 65–75, Nov. 2018.

[2] G. O. Tysse and O. Egeland, "Dynamic Interaction of a Heavy Crane and a Ship in Wave Motion," vol. 39, pp. 45–60, Jan. 2018.

[3] F. Rauscher, S. Nann, and O. Sawodny, "Motion Control of an Overhead Crane Using a Wireless Hook Mounted IMU," in *2018 Annual American Control Conference (ACC)*, pp. 5677–5682, June 2018.

[4] G. Fotland, C. Haskins, and T. Rølvåg, "Trade Study to Select Best Alternative for Cable and Pulley Simulation for Cranes on Offshore Vessels," *Systems Engineering*, vol. 23, no. 2, pp. 177–188, 2020.

[5] G. Fotland and B. Haugen, "Numerical integration algorithms and constraint formulations for an ALE-ANCF cable element," *Mechanism and Machine Theory*, vol. 170, p. 104659, Apr. 2022.

[6] C. Haskins, *Systems Engineering Analyzed, Synthesized, and Applied to Sustainable Industrial Park Development (Doctoral Dissertation)*. No. 2008:175. ISBN: 978-82-471-1028-7, Tapir Akademisk Forlag, May 2008.

[7] B. S. Blanchard and W. J. Fabrycky, *Systems Engineering and Analysis*. Prentice-Hall International Series in Industrial and Systems Engineering, Upper Saddle River, NJ: Pearson Prentice Hall, fourth ed., 2006.

[8] A. Kossiakoff, W. N. Sweet, S. J. Seymour, and S. M. Biemer, *Systems Engineering Principles and Practice*. John Wiley & Sons, Apr. 2011.

[9] P. R. Garvey and C. Chien-Ching, "An Index to Measure and Monitor a System-of-Systems' Performance Risk," *Defense AR Journal; Fort Belvoir*, vol. 13, no. 1, pp. 404–418, 2006.

[10] A. A. Shabana, "Definition of the Slopes and the Finite Element Absolute Nodal Coordinate Formulation," *Multibody System Dynamics*, vol. 1, pp. 339–348, Sept. 1997.

[11] J. L. Escalona, "An arbitrary Lagrangian–Eulerian discretization method for modeling and simulation of reeving systems in multibody dynamics," *Mechanism and Machine Theory*, vol. 112, pp. 1–21, 2017.

[12] F. Ju and Y. S. Choo, "Super element approach to cable passing through multiple pulleys," *International Journal of Solids and Structures*, vol. 42, pp. 3533–3547, June 2005.

[13] A. Arena, A. Casalotti, W. Lacarbonara, and M. P. Cartmell, "Dynamics of container cranes: Three-dimensional modeling, full-scale experiments, and identification," *International Journal of Mechanical Sciences*, vol. 93, pp. 8–21, Apr. 2015.

[14] B. Zhou, M. L. Accorsi, and J. W. Leonard, "Finite element formulation for modeling sliding cable elements," *Computers & Structures*, vol. 82, pp. 271–280, Jan. 2004.

[15] Y. Peng, Z. Zhao, M. Zhou, J. He, J. Yang, and Y. Xiao, "Flexible Multibody Model and the Dynamics of the Deployment of Mesh Antennas," *Journal of Guidance, Control, and Dynamics*, vol. 40, pp. 1499–1510, June 2017.

[16] R. Xue, B. Ren, Z. Yan, and Z. Du, "A cable-pulley system modeling based position compensation control for a laparoscope surgical robot," *Mechanism and Machine Theory*, vol. 118, pp. 283–299, Dec. 2017.

[17] J.-H. Seo, H. Sugiyama, and A. A. Shabana, "Three-Dimensional Large Deformation Analysis of the Multibody Pantograph/Catenary Systems," *Nonlinear Dynamics*, vol. 42, pp. 199–215, Oct. 2005.

[18] S. Kulkarni, C. M. Pappalardo, and A. A. Shabana, "Pantograph/Catenary Contact Formulations," *Journal of Vibration and Acoustics*, vol. 139, Nov. 2016.

[19] B. Zemljarič, "Analyses of the overhead-line cable stringing and sagging on hilly terrain with an absolute nodal coordinate formulation," *Electric Power Systems Research*, vol. 140, pp. 296–302, 2016.

[20] T. Z. Htun, H. Suzuki, and D. García-Vallejo, "Dynamic modeling of a radially multilayered tether cable for a remotely-operated underwater vehicle (ROV) based on the absolute nodal coordinate formulation (ANCF)," *Mechanism and Machine Theory*, vol. 153, p. 103961, Nov. 2020.

[21] T. Wang, B. Tinsley, M. D. Patel, and A. A. Shabana, "Nonlinear dynamic analysis of parabolic leaf springs using ANCF geometry and data acquisition," *Nonlinear Dynamics*, vol. 93, pp. 2487–2515, Sept. 2018.

[22] D. Liu, S. Ai, L. Sun, J. Wei, and N. He, "Numerical modelling of offshore risers conveying slug flow under the ALE–ANCF framework," *Ocean Engineering*, vol. 235, p. 109415, Sept. 2021.

[23] K. Nachbagauer, "State of the Art of ANCF Elements Regarding Geometric Description, Interpolation Strategies, Definition of Elastic Forces, Validation and the Locking Phenomenon in Comparison with Proposed Beam Finite Elements," *Archives of Computational Methods in Engineering*, vol. 21, pp. 293–319, Sept. 2014.

[24] J. Gerstmayr, H. Sugiyama, and A. Mikkola, "Review on the Absolute Nodal Coordinate Formulation for Large Deformation Analysis of Multibody Systems," *Journal of Computational and Nonlinear Dynamics*, vol. 8, pp. 1–12, July 2013.

[25] J. Gerstmayr, A. Humer, P. Gruber, and K. Nachbagauer, "The Absolute Nodal Coordinate Formulation," in *Structure-Preserving Integrators in Nonlinear Structural Dynamics and Flexible Multibody Dynamics*, CISM International Centre for Mechanical Sciences, pp. 159–200, Springer, Cham, 2016.

[26] A. M. Mikkola and A. A. Shabana, "A Non-Incremental Finite Element Procedure for the Analysis of Large Deformation of Plates and Shells in Mechanical System Applications," *Multibody System Dynamics*, vol. 9, pp. 283–309, Apr. 2003.

[27] J. Sun, Q. Tian, H. Hu, and N. Pedersen, "Simultaneous topology and size optimization of a 3D variable-length structure described by the ALE–ANCF," *Mechanism and Machine Theory*, vol. 129, pp. 80–105, 2018.

[28] Q. Wang, Q. Tian, and H. Hu, "Dynamic simulation of frictional contacts of thin beams duing lage overall motions via absolute nodal coodinate fomulation," *Nonlinear Dynamics*, vol. 77, pp. 1411–1425, Sept. 2014.

[29] Q. Wang, Q. Tian, and H. Hu, "Dynamic simulation of frictional multi-zone contacts of thin beams," *Nonlinear Dynamics*, vol. 83, pp. 1919–1937, Mar. 2016.

[30] S. Takehara, M. Kawarada, and K. Hase, "Dynamic Contact between a Wire Rope and a Pulley Using Absolute Nodal Coordinate Formulation," *Machines*, vol. 4, p. 4, Jan. 2016.

[31] R. Bulín, M. Hajžman, and P. Polach, "Nonlinear Dynamics of a Cable–Pulley System Using the Absolute Nodal Coordinate Formulation," *Mechanics Research Communications*, vol. 82, pp. 21–28, June 2017.

[32] Y. Peng, Y. Wei, and M. Zhou, "Efficient modeling of cable-pulley system with friction based on arbitrary-Lagrangian-Eulerian approach," *Applied Mathematics and Mechanics (English Edition)*, vol. 38, no. 12, pp. 1785–1802, 2017.

[33] D. Hong and G. Ren, "A modeling of sliding joint on one-dimensional flexible medium," *Multibody System Dynamics*, vol. 26, pp. 91–106, June 2011.

[34] N. Bel Hadj Ali, A. C. Sychterz, and I. F. C. Smith, "A dynamic-relaxation formulation for analysis of cable structures with sliding-induced friction," *International Journal of Solids and Structures*, vol. 126–127, pp. 240–251, Nov. 2017.

[35] Z. Kan, H. Peng, and B. Chen, "A simple linear complementarity approach for sliding cable modeling considering friction," *Mechanical Systems and Signal Processing*, vol. 130, pp. 293–314, Sept. 2019.

[36] Z. Kan, F. Li, H. Peng, B. Chen, and X. Song, "Sliding cable modeling: A nonlinear complementarity function based framework," *Mechanical Systems and Signal Processing*, vol. 146, p. 107021, Jan. 2021.

[37] D. Hong, J. Tang, and G. Ren, "Dynamic modeling of mass-flowing linear medium with large amplitude displacement and rotation," *Journal of Fluids and Structures*, vol. 27, no. 8, pp. 1137–1148, 2011.

[38] M. R. Flannery, "The enigma of nonholonomic constraints," *American Journal of Physics*, vol. 73, pp. 265–272, Feb. 2005.

[39] M. Géradin and A. Cardona, *Flexible Multibody Dynamics : A Finite Element Approach*. Chichester: Wiley, 2001.

[40] T. Belytschko, K. I. Elkhodary, B. Moran, and W. K. Liu, *Nonlinear Finite Elements for Continua and Structures*. Hoboken, New Jersey: Wiley, second ed., 2014.

[41] E. Eich-Soellner and C. Führer, *Numerical Methods in Multibody Dynamics*. European Consortium for Mathematics in Industry, Wiesbaden: Vieweg+Teubner Verlag, 1998.

[42] C. L. Bottasso, D. Dopico, and L. Trainelli, "On the optimal scaling of index three DAEs in multibody dynamics," *Multibody System Dynamics*, vol. 19, pp. 3–20, Feb. 2008.

[43] Y.-Q. Cui, Z.-Q. Yu, and P. Lan, "A novel method of thermo-mechanical coupled analysis based on the unified description," *Mechanism and Machine Theory*, vol. 134, pp. 376–392, Apr. 2019.

[44] E. Grossi and A. A. Shabana, "Verification of a Total Lagrangian ANCF Solution Procedure for Fluid–Structure Interaction Problems," *Journal of Verification, Validation and Uncertainty Quantification*, vol. 2, Feb. 2018.

[45] Y. Zhang, X. Jiang, Z.-f. Bai, J.-w. Guo, and C. Wei, "Dynamics and rebound behavior analysis of flexible tethered satellite system in deployment and station-keeping phases," *Defence Technology*, Apr. 2021.

[46] N. M. Newmark, "A Method of Computation for Structural Dynamics," *Journal of the Engineering Mechanics Division*, vol. 85, no. 3, pp. 67–94, 1959.

[47] T. Belytschko and D. F. Schoeberle, "On the Unconditional Stability of an Implicit Algorithm for Nonlinear Structural Dynamics," *Journal of Applied Mechanics*, vol. 42, pp. 865–869, Dec. 1975.

[48] J. Chung and G. M. Hulbert, "A Time Integration Algorithm for Structural Dynamics With Improved Numerical Dissipation: The Generalized-α Method," *Journal of Applied Mechanics*, vol. 60, no. 2, pp. 371–375, 1993.

[49] H. M. Hilber, T. J. R. Hughes, and R. L. Taylor, "Improved numerical dissipation for time integration algorithms in structural dynamics," *Earthquake Engineering & Structural Dynamics*, vol. 5, no. 3, pp. 283–292, 1977.

[50] W. L. Wood, M. Bossak, and O. C. Zienkiewicz, "An alpha modification of Newmark's method," *International Journal for Numerical Methods in Engineering*, vol. 15, no. 10, pp. 1562–1566, 1980.

[51] M. Arnold and O. Brüls, "Convergence of the generalized-α scheme for constrained mechanical systems," *Multibody System Dynamics*, vol. 85, pp. 187–202, 2007.

[52] C. Runge, "Ueber die numerische Auflösung von Differentialgleichungen," *Mathematische Annalen*, vol. 46, no. 2, pp. 167–178, 1895.

[53] J. C. Butcher, "A history of Runge-Kutta methods," *Applied Numerical Mathematics*, vol. 20, no. 3, pp. 247–260, 1996.

[54] D. Negrut, E. J. Haug, and H. C. German, "An Implicit Runge–Kutta Method for Integration of Differential Algebraic Equations of Multibody Dynamics," *Multibody System Dynamics*, vol. 9, pp. 121–142, 2003.

[55] U. M. Ascher, H. Chin, and S. Reich, "Stabilization of DAEs and invariant manifolds," *Numerische Mathematik*, vol. 67, no. 2, pp. 131–149, 1994.

[56] U. M. Ascher, H. Chin, L. R. Petzold, and S. Reich, "Stabilization of Constrained Mechanical Systems with DAEs and Invariant Manifolds," *Mechanics of Structures and Machines*, vol. 23, no. 2, pp. 135–157, 1995.

[57] E. Hairer and G. Wanner, *Solving Ordinary Differential Equations II. Stiff and Differential-Algebraic Problems*. Springer Series in Computational Mathematics, Berlin, Heidelberg: Springer Berlin Heidelberg, 1996.

[58] H. Ma, "Exact solutions of axial vibration problems of elastic bars," *International Journal for Numerical Methods in Engineering*, vol. 75, no. 2, pp. 241–252, 2008.

[59] "Certex Finland, Company homepage: https://www.certex.fi/en, Accessed: 2020-10-22," Oct. 2020.

[60] C. A. Felippa, "Introduction to Finite Element Methods - ASEN 5007, Lecture Notes," *University of Colorado*, pp. 1–791.

[61] N. Henriksen and D. Storegjerde, "Cost Effective Horizontal Drilling in the Troll Field Through use of State of the Art Technology and Optimal Operations," in *SPE/IADC Drilling Conference*, pp. 57–68, OnePetro, Mar. 1997.

[62] T. A. Inglis, "Highly Deviated and Horizontal Wells," in *Directional Drilling* (T. A. Inglis, ed.), Petroleum Engineering and Development Studies, pp. 196–211, Dordrecht: Springer Netherlands, 1987.

[63] T. V. Aarrestad, "Torque and Drag-Two Factors in Extended-Reach Drilling," *Journal of Petroleum Technology*, vol. 46, pp. 800–803, Sept. 1994.

[64] S. Andresen, S. Hovda, and T. L. Olsen, "Experience With Drilling C-26A, A World Record Extended Reach Horizontal Well in the Oseberg Field, North Sea.," in *SPE Annual Technical Conference and Exhibition*, OnePetro, Oct. 1995.

[65] R. Foster and R. Macmillan, "High Speed Telemetry on Wired Drill Pipe, History, and Impact on Drilling Process," in *Offshore Technology Conference*, OnePetro, Apr. 2018.

[66] T. R. Kane and D. A. Levinson, "Formulation of Equations of Motion for Complex Spacecraft," *Journal of Guidance and Control*, vol. 3, no. 2, pp. 99–112, 1980.

[67] O. Egeland and J. T. Gravdahl, *Modeling and Simulation for Automatic Control*. Trondheim: Marine Cybernetics, 2002.

[68] S. Adhikari, *Damping Models for Structural Vibration*. PhD thesis, University of Cambridge, Cambridge, 2001.

[69] "YAML, URL: https://en.wikipedia.org/w/index.php?title=YAML&oldid=980312066, Accessed: 2020-09-25," *Wikipedia*, Sept. 2020.

[70] "ParaView - Python, URL: https://www.paraview.org/python/, Accessed 2020-10-06.."

[71] K. Bell, *An Engineering Approach to Finite Element Analysis of Linear Structural Mechanics Problems*. Trondheim: Akademika Publ, first ed., 2013.

[72] B. Hussein, D. Negrut, and A. A. Shabana, "Use of the Implicit HHT-I3 and the Explicit ADAMS Methods with the Absolute Nodal Coordinate Formulation," 2007.

Papers

Paper 1

Trade Study to Select Best Alternative for Cable and Pulley Simulation for Cranes on Offshore Vessels

Received: 14 January 2019 | Revised: 15 May 2019 | Accepted: 4 June 2019

DOI: 10.1002/sys.21503

REGULAR PAPER

WILEY

Trade study to select best alternative for cable and pulley simulation for cranes on offshore vessels

Gaute Fotland | **Cecilia Haskins** | **Terje Rølvåg**

Department of Mechanical and Industrial Engineering, Norwegian University of Science and Technology, Trondheim, Norway

Correspondence
Gaute Fotland, Department of Mechanical and Industrial Engineering, Norwegian University of Science and Technology, Trondheim 7034, Norway.
Email: gaute.fotland@ntnu.no

Funding information
Norwegian Research Council, Grant/Award Number: 237896

Abstract

Cranes on offshore vessels are subjected to crane dynamics, structural couplings to the vessel, and environmental influence by waves and currents. The recent trend has been to use larger cranes on smaller vessels, which makes the lifting operation more complex and potentially dangerous. The use of digital twins (DTs) is emerging as one way to enable safer operations, real-time simulation, and maintenance prediction. On offshore vessels, a DT can monitor the lifting operation to create a safer work environment. The SPADE model has been used as a framework toward the creation of a DT of cranes on offshore vessels. Several cases involving simulation of cranes revealed the lack of an adequate simulation of cable and pulleys suitable for use in a DT. The simulation is important for accurate results and for implementation in control systems. A trade study was performed to determine a numerical method adequate for cable and pulley simulation. The trade study identified the absolute nodal coordinate formulation in the framework of arbitrary Lagrangian–Eulerian as a promising numerical formulation.

KEYWORDS
cable, crane, digital twin, FEM, MBS, pulley, simulation

1 | INTRODUCTION

Offshore vessels with cranes are used for operations, such as installation of subsea templates, offshore wind turbine installation, and loading and unloading of equipment. Wind, waves, and currents complicate these operations. The recent trend has been to use smaller vessels, with larger cranes, as a means for saving costs. This makes the lifting operation more subject to instability due to the environmental excitations. A digital twin (DT) of an offshore crane supports a wide range of applications. It would allow for safer lifting operations with less downtime based on anticipated failure modes, such as buckling in bars and actuators, material yielding and fatigue predictions, as well as an improved control system. The DT simulations improve payload control allowing for lifting operations in demanding weather conditions, and better maintenance schemes based on fatigue predictions. If the control system detects irregularities, the operator is notified. In dangerous situations, the control system could restrict continuation of the operation. A DT could be used to estimate the weight of the payload, instead of using a scale, and the project manager could use data from the DT as basis for risk analysis when planning lifting operations.

A step toward creating a DT of a crane on offshore vessels is to improve the simulations. The Norwegian oil and gas industry relies heavily on offshore vessels with cranes, and the Research Council of Norway is currently funding this research through an innovation grant (SFI). This paper investigates the requirements for improved simulations as part of this research. The structure of this paper is as follows: first, the paper presents a context diagram of crane dynamics for a better understanding of physics and dynamics, with the theoretical background for simulation. Then, stakeholders are identified to investigate different interests in the research. The main body of the paper then reports on requests for crane simulation according to cases and previous research. Here, it is observed that cable and pulley simulation lacks sufficient accuracy, and a better simulation of cable and pulleys is needed for a DT. Based on design requirements, a trade study is performed to investigate alternatives for different numerical methods for dynamic simulations of cable and pulleys to embed in a DT, where the real-time aspect is important. The paper concludes with a suggested cable and pulley simulation and further work. The paper follows the SPADE methodology as proposed by Haskins.[1]

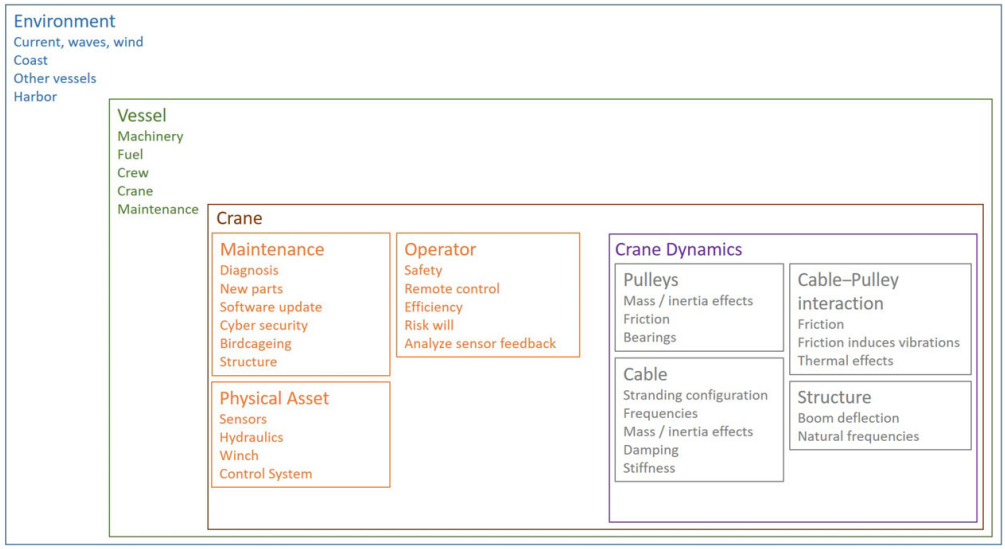

FIGURE 1 Context diagram for the crane dynamics of cable and pulleys

2 | BACKGROUND

Schluse and Rossmann[2] list several domains where the term "digital twin" is used differently for industrial practices: manufacturing flexibility, product design, maintenance, increased lifetime, testing, structural monitoring, performance efficiency, quality, and automation. A DT can be used, not only for engineering and manufacturing, but also operations and service. According to Boschert and Rosen,[3] this implies that the DT could become a part of the real system, with actionable interactions. For the remainder of this paper, DT is defined as a digital copy of a physical asset, collecting real-time data from the asset and deriving information not being measured directly in the hardware.

The context diagram is a helpful tool to examine the systemic picture of what must be included to create a DT of an offshore crane, see Figure 1. The goal of a DT is to be able to simulate the whole crane system. The primary context for the DT is crane dynamics, which is an attribute of the crane, both the physical asset and its maintenance and operation. These in turn are mounted on a vessel that operates in maritime environments, including both open water and harbor operations. The way these elements interact during a lifting operation is described here.

The winch on the crane is an essential part of the lifting mechanism. The crane operator is responsible for safe lifting operations, and therefore could be willing to work in harsher environments with a better control system. The control system includes heave and sway compensation and detection of critical loading conditions. The heave compensation maintains the payload motionless with regard to the seabed or other vessels. The anti-sway prevents the payload from swinging. For lifting operations involving other vessels, the vessels will be in different swing phases. Tordal et al[4] has proposed a method for vessel to vessel operations, where a motion reference unit is placed in each vessel allowing for an accurate and reliable relative motion estimate. Critical loading conditions causing severe instability and rolling in the vessel should be detected and handled by the control system.

The context diagram highlights that crane dynamics are influenced by the cable and pulleys. The control system would benefit from simulations running in the DT that provide additional input data, such as the time delays caused by the hydraulics of the crane. This includes other factors of crane dynamics, such as ways the boom deflects, pulleys, bearings, inertia effects, friction, and damping. The frequency on the bearings could be influential when it comes to decoupling the crane for simulation, without significant loss of accuracy. The inherent dynamics and friction effects in a crane may cause out of phase tension oscillations in the cables, which again leads to control system instabilities. The frequencies or vibrations in the cable are relevant inputs for the control system. The frequencies are influenced by the loading conditions and the length of the cable. Cables can withstand large axial loads in comparison to bending, compression, and torsional loads. For lifting operation with long cable spans, the elongation of the cable cannot be neglected. The cable pulley interaction is important, where contact and friction have to be defined.

Likewise, maintenance is a critical factor for the crane to be operational and is important when planning, to minimize downtime. A functioning DT requires the physical crane to be equipped with weather-resistant sensors, placed where they are shielded from the environment.

A multibody system (MBS) consists of several submodels, which make up the system being simulated, see Figure 2. The different parts have a computer aided design (CAD) model, which could be used as a rigid body, or meshed with finite elements for elastic behavior. Mechanism modeling uses joints to connect the parts for interaction. Control system modeling is used for actuators, such as the hydraulic cylinders

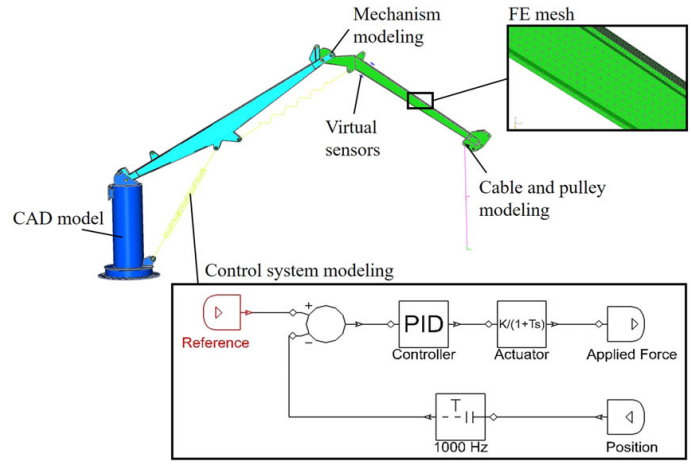

FIGURE 2 A CAD model of the crane system with different submodeling elements indicated

and the virtual sensors. The 1D flow chart presents an example of a control system, where real or virtual sensors can be the position input. The applied force will be set according to deviation in measurement and reference value. Cable and pulley modeling is usually simplified to an axial spring.

Finite element analysis (FEA) as applied in engineering is a computational tool for performing engineering analysis typically for design and optimization. It can be used both for static and dynamic simulations, where dynamic simulations step through a given time interval. An important difference between an engineering simulation and a DT is that a simulation cannot foresee future scenarios and changing circumstances. The DT on the other hand takes in real-time sensor data and updates the simulation, as it steps through time. This gives the engineer a much better insight into what is happening, and this real-time aspect requires fast calculations. Therefore, the purpose of FEA in an operational mode is as an estimator, instead of design and optimization. FEA are numerical methods, or formulations, where the finite element method (FEM) is one of them. FEM is commonly used for failure assessment, fracture, and crash simulation. Hong et al[5] remark that FEM is more relevant for crane simulation than other numerical methods, such as rigid body simulation, since it accounts for the flex in the crane boom during heavy lifting. FEM works by dividing the CAD model into many small pieces called elements, see Figure 2. The elements have material and geometrical properties. Then, forces and boundary conditions are included in the model. Mathematical equations describe the behavior of the elements, and how they interact with each other during the simulation. There are numerous element types, specialized for different simulation tasks.

A simple example of a DT is found in Figure 3. In this illustration, the physical sensor data (PSD) from the physical crane are stored in a state vector, which contains stroke length of actuators, turn angle, reference strain for verification and calibration, and applied load from the payload at the crane tip.

$$PSD(t) = [\Delta L1, \Delta L2, \Delta\Theta, \epsilon_{ref}, \epsilon_{temp}, mg]$$

The state vector is time dependent. The dotted arrow indicates how the state vector is transferred to the server cloud. The digital crane model retrieves the $PSD(t)$ from the cloud, for calculations. Based on the input from the physical crane, the inverse method can be used to extrapolate forces and strains to virtual sensors in the digital model. While the physical actuators are measuring stroke length, the reaction forces can be found in the digital actuators.

The strain history can be found for any part of the crane, by virtual sensors. This is relevant for detecting fatigue failure. It is important to cross check and recalibrate the DT to avoid divergence from the physical crane over time. The virtual strains are verified by comparison with reference strains from strain gauges placed at hot spots. For offshore cranes, the strain gauges have to be carefully placed and shielded from the harsh environment. Drifting in strain gauges is inevitable, for example, where the temperature is fluctuating. A strain gauge is placed at an untensioned part of the crane, as a reference for temperature. Filtering sensor noise is important to handle drifting in sensors. When starting the DT, both the DT and the physical crane should be in a preset zero position. Direction and size of forces are relevant for detecting stability issues and critical loading conditions. The digital model can have an infinite number of states, free of charge. The outputs from the digital crane, digital sensor data (DSD), are stored in the state vector and sent to the cloud.

$$DSD(t) = [F1, F2, M, \epsilon 1, \epsilon 2, \epsilon 3, \epsilon 4]$$

The data in the cloud could be used further for visualization and presentation of results. The weather and wave forecast are additional data relevant to store in the server cloud, for risk analysis of the job.

In the video posted by Raftery,[6] a DT is demonstrated by a simple beam with a sensor at the top end, which allows for the whole stress distribution in the beam to be calculated. Different colors indicate the stress level in the beam. The stress is a consequence of the force applied by the hand. The inverse method refers to the numerical equations in a simulation, where the input data are a measured value,

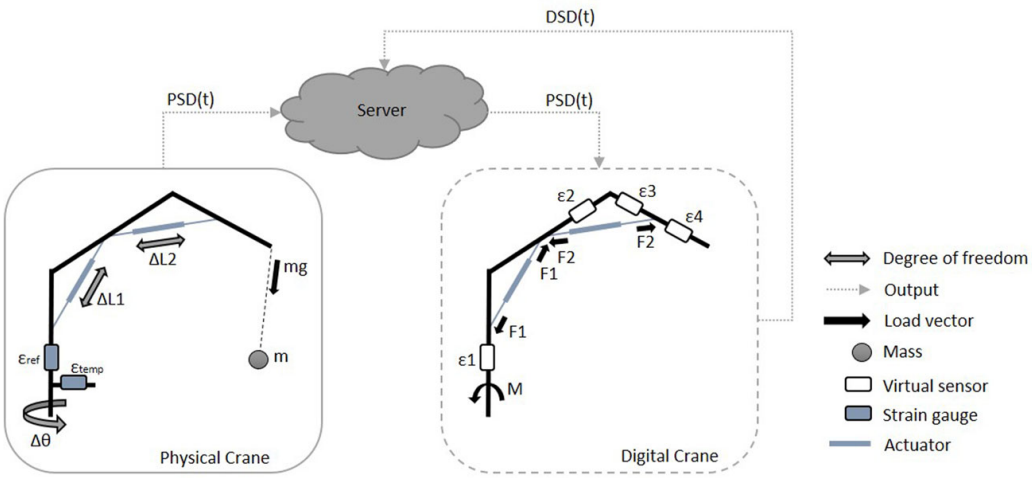

FIGURE 3 Sensors on the physical crane send real-time collected data to the DT. By the inverse method, the DT distributes the inputs to virtual sensors

and the DT behaves accordingly. There are several ways to do the inverse calculations, and there is a need for inverse methods that accurately calculate distributed displacements, frequencies, or loading conditions, to predict the structural integrity. Solvers must be accurate and time efficient, as the time of the simulation has to be less than the physical time for a real-time DT. Further discussion of inverse methods is outside the scope of this paper. The fact that physical sensors are expensive while virtual sensors are free of charge, as well as the real-time aspect, helps the DT gain momentum. Challenges related to what sensors to use, where to install them, and how to process and filter the data from the sensors will not be addressed in this paper.

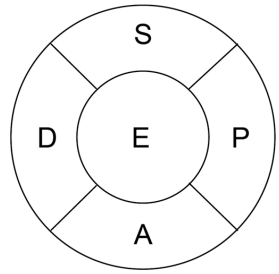

FIGURE 4 "SPADE methodology/framework graphical representation"[1]

3 | RESEARCH METHOD

When exploring new complex systems, it is useful to structure the relevant information. This increases the possibility of making good decisions, exposing gaps, problem solving, and making progress with confidence. Systems engineering (SE) provides tools to handle this. Creating a reliable and robust DT of an offshore crane is new technology. This makes SE tools highly relevant and useful for such a development project.

The SPADE methodology was introduced by Haskins,[1] see Figure 4, and was used as the research method in this paper. SPADE is an acronym constructed from the words: stakeholders, problem formulation, alternatives, decision making, and evaluation. Evaluation is a continuous process and is therefore placed in the center of the figure. During the evaluation process, one updates the old findings with new and relevant information. This makes the SPADE methodology useful for dealing with problems where the destination is unknown. It also helps to give relevant answers according to what the stakeholders actually desire for a DT of an offshore crane, as the stakeholders are identified early in the design process. During the evaluation process, a consultation with the stakeholders can be done to discuss preliminary proposals. New stakeholders can also be included during the evaluation process. The problem formulation stage exposes deficiencies in existing technology for the creation of a DT of an offshore crane. Based on these deficiencies, different solutions are compared in the alternatives stage. To evaluate and compare alternatives for a numerical formulation for cable and pulley simulation, the tradeoff analysis tool based on Blanchard and Fabrycky[7] was used, see Figure 5. For the "Evaluation of the design requirement" step in the trade of analysis, a table based on the subjective value method was used according to Kossiakoff et al.[8] The subjective value method weights the characteristics of each formulation against each other to find the one that best suits the system as a whole, according to design requirements. The score assigned was based on papers describing the features. Extensive testing of all the alternatives for cable and pulley simulation would be inadequate due to time limitations, making the trade study a more suitable process. Making a qualified decision based on available information allows the project to move forward with a steady pace. Decision making is the final stage in the SPADE methodology, where the best alternative for a DT is chosen.

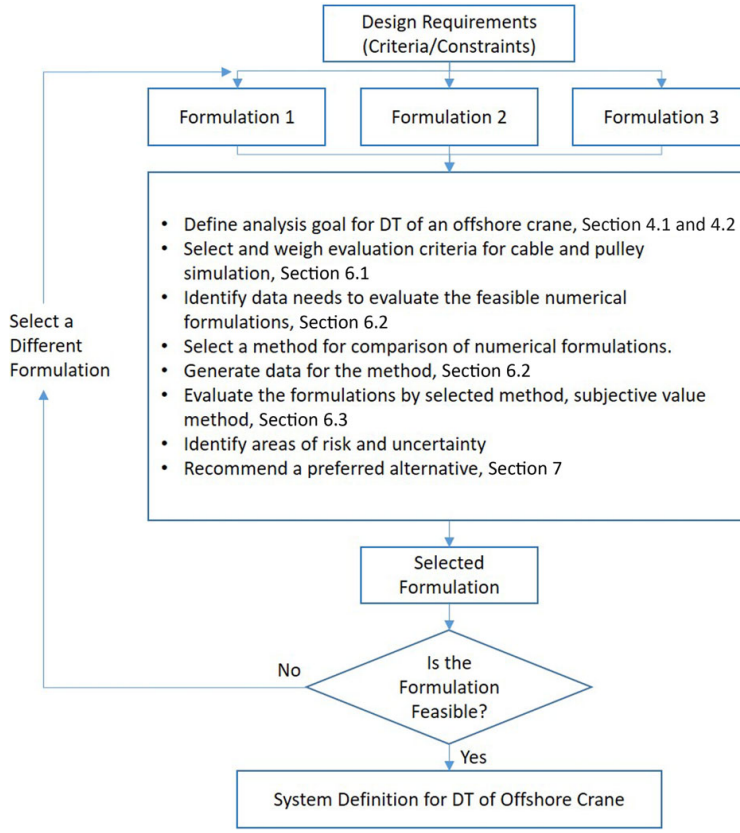

FIGURE 5 Trade-off analysis process, based on Blanchard and Fabrycky[7]

4 | IDENTIFICATION OF SYSTEM STAKEHOLDERS AND NEEDS

Grieves and Vickers[9] cite siloing, (lack of) knowledge of the physical world, and the number of possible states that a system can take as the main challenges for a DT. Siloing refers to lack of communication between the different groups working on the same project. The issue of siloing is addressed by identifying the stakeholders and involving them in the project. A stakeholder is defined by Freeman[10] as "any group or individual who can affect or is affected by the achievement of the organization's objectives."[10] (p. 46)

As previously mentioned, SFI Offshore Mechatronics functions as a bridge for knowledge flow between academia and industry. The project goal is to strengthen competitiveness and innovation capacity in Norway. This research is part of a project with a stated vision to create "advanced offshore mechatronic systems for autonomous operation and condition monitoring of topside drilling systems under the control of land-based operation centers, to ensure safe and efficient operation in deeper water and in harsh environments." The project has the following partners:

Academic Partners:

- Aalborg University
- NORCE (Research Institute)
- NTNU (Trondheim and Aalesund)
- RWTH Aachen
- University of Agder

Industry Partners:

- ABB
- Bosch Rexroth
- Cameron
- Egde Consulting
- GCE NODE (Cluster)
- Klüber Lubrication
- Lundin Norway
- MacGregor
- MHWirth
- National Oilwell Varco
- Skeie Technology
- Stepchange

Partners meet regularly, and industry partners make themselves available to academic researchers. Figure 6 summarizes the needs of the stakeholders for this research.

- SFI crane producer partners are interested in making safe and reliable products. Improved simulations of cranes as well as real-time feedback would help them to understand how forces acts on the

Stakeholders		
Group:	**Who:**	**Needs:**
Primary	The Research Council of Norway	Strengthen competitiveness and innovation capacity in Norway
	SFI Partner Crane producers	Improved simulations
Secondary	Vessel manufacturers	Flexible solutions
	Vessel owners	Ships capable of multiple operations
	Operators of cranes	Safer lifting operations
Tertiary	Software companies	Improving their capability for solving more intricate problems
	Producers of sensors	How their equipment is used
	Other industries	New technology they could benefit from

FIGURE 6 Stakeholders for a DT of a crane on offshore vessels

crane during operation. This would be valuable insight for technical upgrades, which are usually based on what the vessel manufacturers and owners request for the products.

- Vessel manufactures are interested in installing the most suitable crane for the vessels. They are also interested in flexible solutions, which provide a competitive advantage.
- Vessel owners want vessels capable of multiple operations, because laid-up vessels are very costly. This also implies using the right equipment for the job, with the lowest cost. Improved simulation allows for better planning of the operation, as well as better planning of maintenance work.
- Operators of cranes want reliable controls and safer lifting operations. Increased automation and improved control systems, where real-time feedback is important, means that the operations become easier with improved payload control, vessel to vessel transfers, and heave compensation.
- Software companies specializing in simulation and analysis of problems concerning failure assessment, fracture, and fatigue are interested in improving and expanding their capability to provide accurate and fast calculations for solving intricate problems.
- Producers of sensors and monitoring equipment for physical assets are interested in the ways their equipment is used by the industry and how the data collected are applied in simulations.
- Other industries could benefit from new technology developed for offshore cranes. Elevators, draw works, power-lines, and robotics are examples of applications with similar challenges involving cable and pulley simulation.

4.1 | Measures of effectiveness

When the problem has been formulated, then criteria are put in correct term as measures of effectiveness (MOE). MOE represent the viewpoint of stakeholders and Sproles[11] argues that it assists in making the right choices based on the stakeholders' needs. This establishes the success criteria to recognize when the end goal is reached. MOE for this project:

- A cable and pulley simulation that improves the overall real-time simulation of a crane on an offshore vessel.
- A cable and pulley simulation that can be integrated with DT of a crane on an offshore vessel.

4.2 | Technical performance measures

Technical performance measures (TPMs) are key goals to be met, where the actual progress of technical achievement is monitored using periodic measures or tests. As noted by Garvey and Chien-Ching,[12] this will indicate how well a system is approaching its performance requirements. The TPMs for this project include:

- Less unplanned downtime: Due to better prediction of equipment failure, the crane can be maintained prior to breakdown.
- Less downtime: Maintenance is performed when required, instead of on a predetermined schedule.
- Less maintenance cost: Only the worn-out parts are replaced, leading to a longer lifetime of crane and parts.
- Less waste: As the crane and the parts are in service for a longer period, there will be less waste.
- Fewer incidents: The number of industrial injuries concerning work with cranes on offshore vessels is reduced when using a DT. The DT has alarm systems for dangerous situations and has improved payload control.
- Faster operations: With better payload control, the lifting operations will be carried out more efficiently.
- Increased operational time: Due to a better control system, work can be done in harsher environments.

Most of these measures have a temporal quality, which means that the researcher must rely on historical data and data collected after the DT is implemented to assess the actual benefits of the DT, and then the simulation. However, some practical assertions regarding increased operational time and maintenance can be estimated.

5 | PROBLEM FORMULATION

Over the past 40 years, there have been several studies concerning simulation of offshore cranes, where, for example, Strengehagen and Gran[13] investigated the dynamic response and fatigue life of offshore

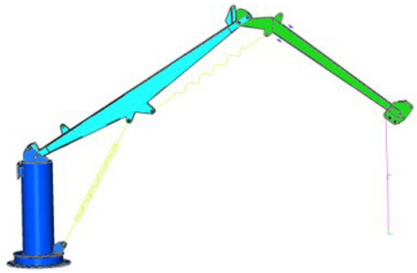

FIGURE 7 Laboratory crane 1 is a knuckle boom crane built in one of the laboratories at NTNU, with a detailed FEM model of the crane

cranes over 30 years ago. They stated "Limitations in the method for this application are mainly that the method is linear and that all elements are taking compression as well as tension. Both limitations are mostly concerned with the ropes."[13] (p. 520). Compression forces in ropes and cables will only cause them to fold, not take up any significant force. Langen et al[14] published work concerning the dynamic behavior of an offshore crane. Their goal was design verification against overload and fatigue. The cables in the simulation were represented as axial springs. Ku and Roh[15] and Hong et al[5] are more recent studies concerning offshore cranes. The first investigates the safety of installation of offshore wind turbines by floating cranes. This is done by simulation with wind, hydrostatic, and dynamic forces acting on the crane. The second predicts dynamic loads on a crane on an offshore support vessel. It argues for the importance of using a flexible body model, rather than a rigid body, as the boom flexes. Research addressing coupling motions between crane and vessel, ways external forces act on the crane structure, ways the boom flexes, and the location of hot spots for stress, is well documented. The matter of simulating MBS assembled with cable and pulleys, such as cranes, has been simplified over time, hence the need for more advanced and accurate cable and pulley simulation has emerged. Moseid[16] started this work by introducing several challenges related to two-dimensional finite element- based modeling of cable and pulley systems, such as inherent dynamics and friction effects. This project seeks to develop a cable and pulley simulation capable of real-time structural monitoring and improved payload control for cranes on offshore vessels.

The fact that cable and pulley simulation is needed is also evident in the following cases from Fedem Technology and NTNU sources, presented in the next sections, where there are different types of cranes investigated, and the objectives of the simulations vary. They have in common that they would benefit from an improved cable and pulley simulation. The cases exposed the need for an improved cable and pulley simulation and will function as benchmarks for further research.

5.1 | Laboratory crane 1 - knuckle boom crane

A knuckle boom crane for testing is built in a laboratory at NTNU, see Figure 7. The crane is accessible for running experiments and benchmarking. It is instrumented with strain gauges for data collection when running experiments, as well as a detailed FEM model. The

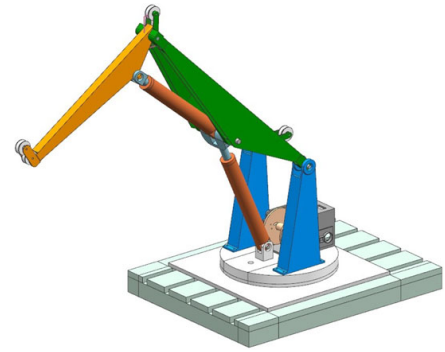

FIGURE 8 Laboratory crane 2 is a knuckle boom crane for testing in a wave pool

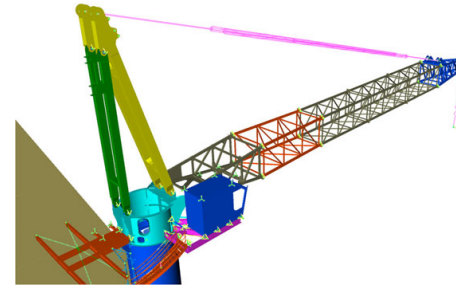

FIGURE 9 Tower crane installed on the oil rig Johan Sverdrup

FEM model does not include an advanced cable and pulley simulation, where stiffness or varying cable length is included. The goal with the crane is to detect error conditions during lifting operations, structural integrity calculations, fatigue life prediction, and stability monitoring. Insight gained here could be used for condition-based maintenance.

5.2 | Laboratory crane 2 - knuckle boom crane

A knuckle boom crane for testing in a wave pool is located in a laboratory at NTNU, see Figure 8. This allows for testing how the vessel movements affect the lifting operation, and what response this will have in the crane and the payload. The hydrodynamics must be included in the simulation. Studies conducted with this crane can help uncover and assess critical conditions for when the system becomes unstable. The main factors influencing stability are critical payloads, wave and wind conditions, and active damping.

5.3 | Johan Sverdrup - tower crane

Structural vibrations in the tower cranes on the recently deployed oil rig Johan Sverdrup have been investigated, see Figure 9. The FEM model of the oil rig is very detailed. FEM accounts for internal deformations in the crane, which is a reason to use it for analysis of structural flexibility. The crane is a complicated system with delays related to boom flex, hydraulics, and tension in the cable. Since the

frequency in the cable changes with varying length, mass, and stiffness in the cable, an improved cable and pulley simulation could make the overall results more accurate for this case.

6 | ALTERNATIVES FROM TRADE STUDY

To identify the best alternative feasible as a numerical formulation for cable and pulley simulation, a trade-off analysis based on Blanchard and Fabrycky[7] has been performed, see Figure 5. The main intention for this project is to improve the overall behavior of a crane. To include internal effects in the cable, such as interaction between the strides, demand additional computing power. This could jeopardize the real-time aspect for a DT, where dynamics are of main interest. For offshore cranes, the demands for dynamics are set higher than for onshore cranes with less platform movement. A pulley rotates from friction when the cable moves over it. If the friction is too low, the cable will slide over the pulley instead of rotating it. When the winch stops pulling the cable, the rotational inertia in the sheaves could cause the cable to move. To simulate these effects, the numerical formulation must include contact and friction. Accidents during lifting operations can have severe consequences. A risk analysis is therefore critical prior to lifting operations. The equipment used must be trusted. If an operational FEA is going to be used as an estimator for controlling the crane, it must be proven reliable and stable. This implies that the formulation must handle different simulation scenarios. If the control system fails, the crane could suddenly drop the payload, jerk the payload, or stop running. Tested formulations known to be stable and robust should be used to prevent this. Design requirements for a numerical formulation of a cable and pulley simulation follow in the next section.

6.1 | Design requirements

1. The simulation method should be compatible with FEM, as FEM is commonly used for simulations of crane systems.
2. The simulation method should include dynamics in the cable, where mass, damping, stiffness, and inertia effects are included. This is important for prediction of reaction forces and position of a cable in motion.
3. The simulation method should include contact and friction between cable and pulley, and between different cable segments.
4. The simulation method should perform with acceptable computational speed, to accommodate the real-time aspect of a DT.
5. The simulation method should compute varying cable length over time, with mass updated accordingly. This is important for correct axial stiffness for applications, where the cable is lowered or elevated.
6. The simulation method should result in reliable numerical formulation with documentation as evidence of extensive testing.

6.2 | Alternatives for cable and pulley simulation

Based on the MOE, stakeholders, and design requirements, alternatives for cable and pulley simulation are identified and briefly described in the following sections.

6.2.1 | Spring

In FEA, a cable has commonly been represented as an axial spring.[14,17] This is derived from Hooke's law, $F = -kx$, where F is the force, k is the spring characteristic, and x is the axial displacement. For more advanced behavior, the spring characteristic can be tabulated dependent on the cable length. This formulation neglects mass and inertia forces, only axial stiffness is included in the cable dynamics. The normal forces on the pulleys are not considered. The approach results in fast calculations, and can provide sufficient results for certain simulations. The formulation is reliable, as it is simple and has been extensively tested.

6.2.2 | Isogeometric analysis

Raknes et al[18] use isogeometric analysis (IGA) to describe large deformations in a 3D cable. Ribs of an umbrella and bow and arrow are numerical examples tested. Thai et al[19] published a paper concerning static application of cables with IGA. The textbook by Cottrell et al describes IGA, and in chapter 3 it is presented how IGA relates to FEM. Instead of generating a mesh, IGA do calculations directly on the CAD geometry. It is possible to have IGA and FEM interact, but it would be challenging in more advanced models where nodes in the mesh and CAD geometry do not necessarily coexist and merge. IGA still suffers from some numerical challenges, and the major drawback is that it struggles to handle contact analysis.[21] The use of IGA would involve a risk, as the numerical formulation is less mature than FEM, and possess possible complications when combining it with FEA.

6.2.3 | The bar finite element for cable

The bar finite element[22] is based on a principle to split the bar element into perfectly straight and homogeneous elements. The elements have elastic properties without rotational degrees of freedom (DOF). Through a coupling between consecutive bar elements, bending stiffness is included. This leads to forces on the extremities of these two elements when a curvature occurs on the modelled cable. A large number of elements are required for an exact representation of the cable. The formulation includes drag forces from water, and has been tested for simulation of fish cages and fishing gear.

6.2.4 | A parametric super element

Ju and Choo[23] present a super element numerical formulation for a cable passing through several pulleys. The method can represent complex geometric paths for a long cable. A tower crane has been analyzed by this formulation. Static simulations are the primary target for this formulation; therefore, it neglects the dynamic behavior of the pulley.

6.2.5 | The floating frame of reference formulation

Floating frame of reference formulation (FFRF) was the most widely used formulation for simulation of flexible MBS.[24] In FFRF, there are two sets of coordinates used to describe the configuration of the deformable bodies; the rigid is described in the global coordinate system, while the local deformation is described in a local coordinate

system. To compensate for the distance between the global and local coordinate system, centrifugal and Coriolis terms must be considered. This leads to a nonconstant mass matrix. The inertia forces become complex expressions, while the elastic forces are simple. FFRF is suitable for small-deformation and large-rotation analysis. Chamorro et al[25] use FFRF for simulation of railway tracks, which have similar geometry as a cable. Only the variable-domain finite element (VFE) variant of the FFRF, as presented in, for example, Horie et al,[26] is good for MBS.[27] The VFE cannot account for large deformations and large overall motion with variable-length bodies due to the inherent nature of FFRF.

6.2.6 | Geometrical nonlinear beam formulation

Jonker and Meijaard[28] proposed the geometrically nonlinear beam formulation (GNBF) for large deflection problems in analysis of flexible MBS. Timoshenko beam theory serves as the foundation for the deformation modes in the formulation. The beam is shear deformable. A cable is a very slender geometry, where shear forces could imperil the simulation of cables for errors. The GNBF is compared to several methods, including the discrete deformation mode by Bathe and Bolourchi,[29] geometrically exact formulations by Romero,[30] natural coordinate formulation by Avello et al,[31] and a corotational formulation by Crisfield,[32] against which GNBF shows good results. Compared to absolute nodal coordinate formulation (ANCF), see Section 6.2.7, it is more accurate and less computationally demanding. Romero[30] points out that a geometrically exact formulation requires a special time stepping method. This makes the geometrically exact formulation more complicated to implement than ANCF.

6.2.7 | The absolute nodal coordinate formulation

For the last two decades, the ANCF has gained attention for modeling of large-deformations and large-rotations in multibody dynamics, with simulation of tires and belt drives as examples.[33] Shabana[34] was the first to propose this element. In contrast to FFRF, ANCF has a constant mass matrix, and no centrifugal and Coriolis forces. This makes it relatively easy for the ANCF to solve accelerations, and continuity of the deformation gradient for dynamic simulations. ANCF elements use nodal displacements and slopes as DOF instead of rotational parameters as in FFRF. Dibold et al[35] found that ANCF is less complicated and converges faster than FFRF in large deformations, especially with an increasing number of elements. Within the framework of ANCF, there are several element formulations, including special cable elements. A good overview of important features and applications of ANCF is given in Gerstmayr et al[36] and Nachbagauer.[37] Nachbagauer addresses the differences between different ANCF elements. She ends up proposing what she sees as the most beneficial 3D ANCF element to use. Gerstmayr et al[38] present ANCF elements with and without torsional stiffness, shear, and cross section deformation. Bulin et al[39] presented a cable-pulley system, where the cable was an ANCF element, and contact forces caused the pulley to rotate. A quadrosphere cable mechanism was simulated with this formulation with promising results.[40] There are different approaches to simulate contact between the cable and the pulley. Westin and Irani[41] developed a method for 2D cases with a large dynamic variation in the wrap angle and cable tension. It is common to use Hertz as the contact formulation, while Takehara et al[42] use Quinn method. Wang et al[43] studied the contact between cables, and narrowed it down to a cable with continuous contact zone.[44] Both studies used a master-slave technique.

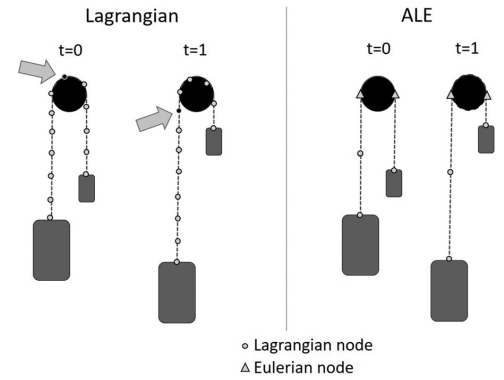

FIGURE 10 FEM model of an elevator mechanism with Lagrangian versus ALE formulation. The figure shows a cable pulled over a pulley with two masses attached, at two different time steps. A Lagrangian formulation requires many nodes to capture interaction between the cable and pulley; while an ALE formulation can have a high density of elements at the pulley, as they are stationary. This allows for fewer elements along the cable. The figure is based on figure by Escalona[48]

6.2.8 | Arbitrary Lagrangian–Eulerian - ANCF

The arbitrary Lagrangian–Eulerian (ALE) formulation combines the Lagrangian and the Eulerian formulations, as the name suggests. In the Lagrangian formulation, the nodes in the FEM mesh and the material are attached to each other. This is the common formulation to use for simulation of structures. In the Eulerian formulation, the nodes in the FEM mesh are fixed in space and the material can flow through it. This is the common formulation to use for simulation of fluids. Hong and Ren[45] proposed the ANCF in the framework of ALE, where the material could flow through the ANCF elements. Without the ALE formulation, the element would behave as a ≪regular≫ ANCF element. ALE opened possibility to have stationary nodes around the pulleys, as illustrated in Figure 10. The advantage being that fewer elements are needed to represent the cable. The reason for this is that contact is numerically difficult to simulate, especially for the timesteps when contact between elements occur during a simulation. When any random cable element can happen to be in contact with the pulley at some point of time, all the cable elements must be small. With ALE, free cable elements can be larger, allowing for fewer elements and faster simulations. Another advantage is that for the simulation of reeling, it is possible to add or remove excessive cable. Based on Hong and Ren,[45] Peng et al[46] came up with an ALE formulation for cable and pulley simulation handling variable cable length. A deployable mesh antenna was simulated for benchmarking.[47]

Design Requirements							
Formulations:	1. FEM Compatible	2. Dynamics	3. Contact	4. Calculation Speed	5. Time Varying Length	6. Reliability	SUM Results
Spring	5	1	1	5	3	4	19
IGA	1	4	2	0	0	2	9
The Bar Finite Element for Cable	5	3	2	4	0	2	16
A Parametric Super Element	5	1	1	4	1	1	13
FFRF	5	3	3	3	2	2	18
GNBF	5	3	0	4	0	2	14
ANCF	5	4	3	3	3	3	21
ALE-ANCF	5	4	4	4	5	4	26
Coupling Motion between Cable and Pulley	5	4	4	4	4	1	22

FIGURE 11 The alternatives for cable and pulley simulation evaluated according to the subjective value method, based on Kossiakoff et al,[8] where 0 = not known, 1 = poor, 2 = fair, 3 = satisfactory, 4 = good, and 5 = superior

Escalona[48] discusses 1D, 2D, and 3D ALE formulation with and without transverse deformation and twist. The ALE formulation is suitable for real-time simulations, due to efficient calculations.

6.2.9 | Coupling motion between cable and pulley

Qi et al[49] and Wang et al[50] point out that few studies propose a good formulation of coupling between cable and movable pulleys. Pulleys play an important role, with tensioning of the cable, and the flow of the cable relies on the rotation of the pulley. A numerical formulation for dynamic analysis of flexible cables with time-varying length and coupling motions between cable and pulleys was proposed. The contact segment of the cable moves together with the contact point on the pulley, with a shape constraint spatial description. Cubic spline interpolation is used to discretize the cable, which, can be regarded as an axially moving 1D-flow medium. The simulation includes tensile strain, inertia, and gravitational forces of the cable and pulleys. The bending stiffness and torsional stiffness are neglected in this formulation, as flexible cables are easy to bend and twist. The papers present examples of simulations of cable-pulley lifting systems of movable and fixed pulleys, with good results when compared to simulations done in the ADAMS software. There have not been other studies verifying the formulation.

6.3 | Evaluation of alternatives

It is not straightforward to decide upon the best alternative for a numerical formulation to use for cable and pulley simulation. There are many aspects to take into consideration, such as calculation time, dynamics, and contact formulations. An analysis based on the subjective value method according to Kossiakoff et al[8] is presented in Figure 11. This was used for cross-referencing design requirements and options for evaluation of the different formulation candidates. Each of the criteria was weighted equally with the scoring from: 0 = not known, 1 = poor, 2 = fair, 3 = satisfactory, 4 = good, and 5 = superior.

Based on the alternatives of numerical formulations for cable and pulley simulation evaluated in this paper, the spring element is commonly used, but is lacking both a good dynamic representation and contact formulation. IGA is premature, as it is not FEM compatible, and the formulation is not extensively tested, although it might be relevant in the future. ANCF converges faster than FFRF.[35] ALE-ANCF has the highest score. It can represent contact between cable and pulley with stationary nodes, it allows for models with fewer elements and fast calculations. This makes it suitable for real-time DTs. ALE-ANCF also allows for varying cable length. The coupling motion between cable and pulley is a promising method, with the second highest score. The method has a low score on reliability, as only one research group has publications on it. Even though the formulation seems promising, it should be used with care until further testing has been done.

7 | CONCLUSIONS

Decision making is the fourth element of SPADE. A trade study was performed to investigate alternatives for cable and pulley simulations. The numerical method ALE-ANCF had the highest score in the evaluation by the subjective value method. This method is very suitable for real-time simulations since few elements are needed, and the nodes can be stationary at contact areas with the pulley. It also has good dynamic representation of the cable, and can include contact as well as time varying length. ALE-ANCF is the recommended formulation to implement in a DT of an offshore crane.

DT applications in SE tend to focus on manufacturing, whereas this paper has focused on maintenance and real-time operations of an offshore crane. Requirements to create a DT of an offshore crane for safer lifting operations with less downtime have been addressed. Improved fatigue predictions allow for less downtime due to better planning of maintenance. An improved control system makes the lifting operations safer with detection and alarming of critical loading conditions and improved payload control. It also leads to less downtime as lifting operations can take place in harsher environments. There are several challenges related to achieving a satisfactory functioning DT. Through different cases, it was evident that simulations lacked a sufficiently

robust numerical formulation for cable and pulley representation. A satisfactory cable and pulley simulation is essential for an operational FEA, used for a real-time DT.

SE has proven to be a useful approach for the creation of a DT, because it provides a ready-made framework with tools to expose deficiencies, establish design requirements, and find alternatives. For structuring complex systems, this is invaluable. Since the creation of DT of offshore cranes has never been done before, SE is highly relevant.

8 | FURTHER WORK

This paper documents the process of choosing a numerical formulation method. It remains now to move to the next phases as follows:

- To verify the selected formulation for cable and pulley simulation, a DT of the laboratory knuckle boom crane should be made for benchmarking. This will verify if the selected alternative is feasible. Testing will also reveal further requirements for having a fully functioning DT of an offshore crane.
- A DT requires software for processing of sensor data, calculations, simulations, and visualization. There is a large selection of software available, where some are specialized for certain tasks, while others are generalized. Further work involves the investigation of software alternatives to use for a DT of an offshore crane.

ACKNOWLEDGMENTS

The research presented in this paper has received funding from the Research Council of Norway, SFI Offshore Mechatronics, project number 237896. Thanks to Industry Partners for sharing their needs for the DT, and to the anonymous reviewers whose suggestions helped improve this paper.

ORCID

Gaute Fotland https://orcid.org/0000-0001-9949-6867
Cecilia Haskins https://orcid.org/0000-0002-2506-8808
Terje Rølvåg https://orcid.org/0000-0003-0677-3154

REFERENCES

1. Haskins C. *Systems Engineering Analyzed, Synthesized, and Applied to Sustainable Industrial Park Development* [doctoral dissertation]. Tapir Akademisk Forlag; 2008:175.
2. Schluse M, Rossmann J. From simulation to experimentable digital twins: simulation-based development and operation of complex technical systems. In: *2016 IEEE International Symposium on Systems Engineering (ISSE)*; 2016:1–6.
3. Boschert S, Rosen R. Digital twin—the simulation aspect. In: Bradley D, ed. *Mechatronic Futures*. Cham: Springer; 2016:59–74.
4. Tørdal SS, Hovland G. Ship-to-ship state observer using sensor fusion and the extended Kalman filter. *J Offshore Mech Arctic Eng*. 2019;141:041603.
5. Hong JW, Roh MI, Ham SH, Ha S. Dynamic simulation of subsea equipment installation using an offshore support vessel based on flexible multibody system dynamics. *J Marine Sci Technol*. 2016;24:807–821.
6. Raftery T. SAP's 2017 Digital twin solution demo [video file]. https://www.youtube.com/watch?v=ssPx4MvPPXM; 2017. Accessed September 14, 2018.
7. Blanchard BS, Fabrycky WJ. *Systems Engineering and Analysis*. 4th ed. Prentice-Hall International Series in Industrial and Systems Engineering. Upper Saddle River, NJ: Pearson Prentice Hall; 2006.
8. Kossiakoff A, Sweet WN, Seymour SJ, Biemer SM. *Systems Engineering Principles and Practice*. John Wiley & Sons; 2011.
9. Grieves M, Vickers J. Digital twin: mitigating unpredictable, undesirable emergent behavior in complex systems. In: Kahlen FJ, Flumerfelt S and Alves A, eds. *Transdisciplinary Perspectives on Complex Systems*. Cham: Springer; 2017:85–113.
10. Freeman RE. *Strategic Management: A Stakeholder Approach*. Pitman Series in Business and Public Policy. Boston, MA: Pitman; 1984.
11. Sproles N. Coming to grips with measures of effectiveness. *Syst Eng*. 2000;3:50–58.
12. Garvey PR, Chien-Ching C. An index to measure and monitor a system-of-systems' performance risk. *Defense AR J*. 2006;13:404–418.
13. Strengehagen J, Gran S. Supply boat motion, dynamic response and fatigue of offshore cranes. In: *Offshore Technology Conference*; 1980.
14. Langen I, Than TK, Birkeland O, Rølvåg T. *Simulation of Dynamic Behaviour of a FPSO Crane*. Stavanger University College; 2000:18.
15. Ku N, Roh MI. Dynamic response simulation of an offshore wind turbine suspended by a floating crane. *Ships Offshore Struct*. 2015;10:621–634.
16. Moseid JA. *Mathematical Modelling of Cable and Pulley Systems* [master's thesis]. Norwegian University of Science and Technology. NTNU Open; 2017.
17. Arena A, Casalotti A, Lacarbonara W, Cartmell MP. Dynamics of container cranes: three-dimensional modeling, full-scale experiments, and identification. *Int J Mech Sci*. 2015;93:8–21.
18. Raknes SB, Deng X, Bazilevs Y, Benson DJ, Mathisen KM, Kvamsdal T. Isogeometric rotation-free bending-stabilized cables: statics, dynamics, bending strips and coupling with shells. *Comp Methods Appl Mech Eng*. 2013;263:127–143.
19. Thai S, Kim NI, Lee J. Isogeometric cable elements based on B-spline curves. *Meccanica*. 2017;52:1219–1237.
20. Cottrell JA, Hughes TJR, Bazilevs Y. NURBS as a Basis for Analysis: Linear Problems. In: *Isogeometric Analysis*. John Wiley & Sons, Ltd; 2009: 69–107.
21. Cardoso RPR, Adetoro OB. On contact modelling in isogeometric analysis. *Eur J Comput Mech*. 2017;26:443–472.
22. Priour D. The bar finite element for cable. In: *A Finite Element Method for Netting*. SpringerBriefs in Environmental Science. Dordrecht: Springer; 2013:71–86.
23. Ju F, Choo YS. Super element approach to cable passing through multiple pulleys. *Int J Solids Struct*. 2005;42:3533–3547.
24. Shabana AA. Flexible multibody dynamics: review of past and recent developments. *Multibody Syst Dyn*. 1997;1:189–222.
25. Chamorro R, Escalona JL, González M. An approach for modeling long flexible bodies with application to railroad dynamics. *Multibody Syst Dyn*. 2011;26:135–152.
26. Horie Y, Takehara S, Terumichi Y, Sogabe K. Numerical approach for the analysis of flexible beam motion with time-varying length and large displacement using component mode synthesis. In: *The 21th Workshop on JAXA Astrodynamics and Flight Mechanics*; 2011.
27. Sun J, Tian Q, Hu H, Pedersen NL. Topology optimization of a flexible multibody system with variable-length bodies described by ALE–ANCF. *Nonlinear Dyn*. 2018;93:413–441.
28. Jonker JB, Meijaard JP. A geometrically non-linear formulation of a three-dimensional beam element for solving large deflection multibody system problems. *Int J Non-Linear Mech*. 2013;53:63–74.
29. Bathe KJ, Bolourchi S. Large displacement analysis of three-dimensional beam structures. *Int J Numer Methods Eng*. 1979;14:961–986.

30. Romero I. A comparison of finite elements for nonlinear beams: the absolute nodal coordinate and geometrically exact formulations. *Multibody Syst Dyn*. 2008;20:51–68.
31. Avello A, de Jalón JG, Bayo E. Dynamics of flexible multibody systems using Cartesian co-ordinates and large displacement theory. *Int J Numer Methods Eng*. 1991;32:1543–1563.
32. Crisfield MA. A consistent co-rotational formulation for non-linear, three-dimensional, beam-elements. *Comp Methods Appl Mechan Eng*. 1990;81:131–150.
33. Shabana AA. *Computational Continuum Mechanics*. John Wiley & Sons; 2018.
34. Shabana AA. Definition of the slopes and the finite element absolute nodal coordinate formulation. *Multibody Syst Dyn*. 1997;1:339–348.
35. Dibold M, Gerstmayr J, Irschik H. A detailed comparison of the absolute nodal coordinate and the floating frame of reference formulation in deformable multibody systems. *J Comput Nonlinear Dyn*. 2009;4:021006.
36. Gerstmayr J, Sugiyama H, Mikkola A. Review on the absolute nodal coordinate formulation for large deformation analysis of multibody systems. *J Comput Nonlinear Dyn*. 2013;8:1–12.
37. Nachbagauer K. State of the art of ANCF elements regarding geometric description, interpolation strategies, definition of elastic forces, validation and the locking phenomenon in comparison with proposed beam finite elements. *Arch Comput Methods Eng*. 2014;21:293–319.
38. Gerstmayr J, Humer A, Gruber P, Nachbagauer K. The absolute nodal coordinate formulation. In: Betsch P, ed. *Structure-Preserving Integrators in Nonlinear Structural Dynamics and Flexible Multibody Dynamics*. CISM International Centre for Mechanical Sciences. Cham: Springer; 2016:159–200.
39. Bulín R, Hajžman M, Polach P. Nonlinear dynamics of a cable–pulley system using the absolute nodal coordinate formulation. *Mechan Res Commun*. 2017;82:21–28.
40. Bulín R, Hajžman M, Polach P. Complex modelling and dynamical analysis of parallel cable mechanisms. In: Carvalho JCM, Martins D, Simoni R, Simas H, eds. *Multibody Mechatronic Systems*. vol. 54. Cham: Springer International Publishing; 2018:193–202.
41. Westin C, Irani RA. Cable–pulley interaction with dynamic wrap angle using the absolute nodal coordinate formulation. In: *4th International Conference of Control, Dynamic Systems, and Robotics (CDSR'17)*; 2017:133.
42. Takehara S, Kawarada M, Hase K. Dynamic contact between a wire rope and a pulley using absolute nodal coordinate formulation. *Machines*. 2016;4:4.
43. Wang Q, Tian Q, Hu H. Dynamic simulation of frictional contacts of thin beams during large overall motions via absolute nodal coordinate formulation. *Nonlinear Dyn*. 2014;77:1411–1425.
44. Wang Q, Tian Q, Hu H. Dynamic simulation of frictional multi-zone contacts of thin beams. *Nonlinear Dyn*. 2016;83:1919–1937.
45. Hong D, Ren G. A modeling of sliding joint on one-dimensional flexible medium. *Multibody Syst Dyn*. 2011;26:91–106.
46. Peng Y, Wei Y, Zhou M. Efficient modeling of cable-pulley system with friction based on arbitrary-Lagrangian–Eulerian approach. *Appl Math Mech*. 2017;38:1785–1802.
47. Peng Y, Zhao Z, Zhou M, He J, Yang J, Xiao Y. Flexible multibody model and the dynamics of the deployment of mesh antennas. *J Guidance Control Dyn*. 2017;40:1499–1510.
48. Escalona JL. An arbitrary Lagrangian–Eulerian discretization method for modeling and simulation of reeving systems in multibody dynamics. *Mech Mach Theory*. 2017;112:1–21.
49. Qi Z, Wang J, Wang G. An efficient model for dynamic analysis and simulation of cable-pulley systems with time-varying cable lengths. *Mech Mach Theory*. 2017;116:383–403.
50. Wang J, Qi Z, Wang G. Hybrid modeling for dynamic analysis of cable-pulley systems with time-varying length cable and its application. *J Sound Vibrat*. 2017;406:277–294.

AUTHOR BIOGRAPHIES

Gaute Fotland completed his MSc in Mechanical Engineering at NTNU in 2017 within the field of Engineering Design and Material, where he delivered his Master's Thesis: "Material and Fatigue Life Investigation of a Lead Alloy used as Sheathing in Subsea Power Cables." As part of the thesis, FEA was used to decide for the most suitable test specimen geometries, prior to testing of the lead sheathing in the laboratory. Fotland joined SFI Offshore Mechatronics for a PhD within optimizing cable and pulley systems for cranes in FEA.

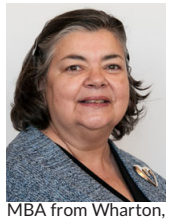

Cecilia Haskins is an associate professor, consultant, and author. Her 35-year professional career includes positions with large and small firms, commercial and government projects, specializing in project management and systems engineering. Her educational background includes an MBA from Wharton, University of Pennsylvania and a PhD in systems engineering from NTNU. She possesses a unique ability to understand issues with an insider's view of both the business and technology domains. Currently, she teaches systems engineering and project management courses at both the graduate and undergraduate levels. She has been recognized as a Certified Systems Engineering Professional since 2004.

Terje Rølvåg was born in Mo i Rana on October 16, 1963. Rølvåg holds an MSc and a PhD within finite element dynamics of elastic mechanisms and control from NTH. His publications are mainly within nonlinear finite element dynamics and active damping of elastic mechanisms. He has been central in developing FEDEM, a finite element-based modeling, and simulation tool with multidisciplinary capabilities (see http://www.fedem.com http://www.fedem.com). He has also established several engineering companies and optimized products for the automotive, offshore, and aerospace industries. Rølvåg's research interests cover computer science applied for engineering applications focusing on simulation of behavior and strength of electromechanical products.

How to cite this article: Fotland G, Haskins C, Rølvåg T. Trade study to select best alternative for cable and pulley simulation for cranes on offshore vessels. *Systems Engineering*. 2019;1–12. https://doi.org/10.1002/sys.21503

Paper 2

Numerical Integration Algorithms and Constraint Formulations for an ALE-ANCF Cable Element

Mechanism and Machine Theory 170 (2022) 104659

Contents lists available at ScienceDirect

Mechanism and Machine Theory

journal homepage: www.elsevier.com/locate/mechmt

Research paper

Numerical integration algorithms and constraint formulations for an ALE-ANCF cable element

Gaute Fotland *, Bjørn Haugen

Norwegian University of Science and Technology (NTNU), Department of Mechanical and Industrial Engineering (MTP), Norway

ARTICLE INFO

Keywords:
Runge–Kutta (RK4)
Generalized-α
Numerical integration
ALE-ANCF cable element

ABSTRACT

In this study, the Absolute Nodal Coordinate Formulation (ANCF) is examined in the framework of the Arbitrary Lagrangian–Eulerian (ALE) formulation for cable simulation. The objective is to determine the stability, efficiency, and accuracy in different frequency domains for two different numerical time integration methods. The methods being compared are the Runge–Kutta method RK4, and the Generalized-α method. For simulations where the lower frequency domain is of interest, the Generalized-α method is stable, accurate and can be used with large time-steps; while where the high frequency domains is of interest, the RK4 procedure can be a more efficient method.

The penalty method, the Lagrange multiplier method and linear coupling are tested as constraint methods for connecting ALE-ANCF cable elements. For RK4, the penalty constraint method highly affects the maximum time-step, which again affects the total solution time. For the Generalized-α method, the constraint methods all provide accurate results, and they have similar solution time. ALE-ANCF cable elements can be connected by different constraint techniques without impeding the ability to exhibit large deformations.

1. Introduction

1.1. Background

Simulation in offshore crane engineering and digital twin applications enables both ultimate load prediction and fatigue load prediction, supporting condition-based maintenance. The importance of such tools is increasing as the recent trend has been to use smaller vessels with larger cranes in order to save costs. This makes the lifting operation subject to greater instability due to the environmental excitations. Finite Element Analysis (FEA) provides strain and stress time histories from lifting operation and wave and wind induced motions. This data can be used for fatigue life and operational time prediction. Multibody Simulation (MBS), where Finite Element Method (FEM) models are connected by joints, can embed crane boom flexibility and crane dynamic effects. In addition, integrated control systems can enable real time digital twin applications such as improved payload control and active damping. Cable and pulleys contribute to nonlinear effects due to inertia, damping and stiffness variations during crane operations.

1.2. Formulation of the problem of interest for this investigation

To obtain real time simulations for a crane and its wire, the solution time for the solver is of essence where high standards are required. Thus the numerical time integrator must be selected accordingly. The Absolute Nodal Coordinate Formulation (ANCF)

* Corresponding author.
E-mail address: gaute.fotland@ntnu.no (G. Fotland).

https://doi.org/10.1016/j.mechmachtheory.2021.104659
Received 24 September 2021; Received in revised form 1 November 2021; Accepted 15 November 2021

Abbreviations

ALE	Arbitrary Lagrangian–Eulerian
ANCF	Absolute Nodal Coordinate Formulation
DAE	Differential Algebraic Equations
DOF	Degree of Freedom
FEA	Finite Element Analysis
FEM	Finite Element Method
FFT	Fast Fourier Transform
G-α	Generalized-α
MBS	Multibody Simulation
MSD	Mass–Spring–Damper system
ODE	Ordinary Differential Equation
RBM	Rigid Body Mode
RK4	Runge–Kutta 4th Order

in the framework of the Arbitrary Lagrangian–Eulerian (ALE) formulation is identified as the most suitable numerical formulation for cable and pulley simulation [1]. The ANCF elements have the ability to exhibit large deformations, while the ALE formulation allows material to flow through the element nodes, without the nodes changing position. Therefore, only a small number of elements are needed to describe long cable spans. In Lagrangian FEM, the element length must remain small since any element can happen to be in contact with the pulley during a simulation. An ALE-ANCF cable element was used for modeling a reeving system in [2]. The study used the numerical time integrator ODE-45 in *MatLab* for the reeving systems, which is an explicit Runge–Kutta based solution procedure. As a step towards improved simulations of offshore cranes, the purpose of this study is therefore to investigate different numerical integration algorithms and constraint methods for an ALE-ANCF cable element.

1.3. Literature survey

From previous work, cable modeling has been used for simulation of cranes, such as for tower cranes and container cranes, and payload oscillation control, [3,4]. Besides cranes, there are numerous fields of utilization for simulation of cables. A parachute was modeled in [5], a slender, deployable mesh antenna was simulated for benchmarking in [6], and, a modern surgical robot with a cable-pulley system was modeled in [7].

ANCF have proven suitable for simulation of cables due to the favorable attributes with the ability for large-deformations and large-rotations in slender structures. Also ANCF elements have been applied to a wide variety of applications. Simulation of pantographs, which is the overhead cables for trams, was simulated in [8,9]. Overhead power cables are modeled in [10]. For subsea applications, remotely operated vehicles (ROVs) are modeled with ANCF elements for the tether going to the surface in [11]. Parabolic leaf springs, commonly used for vehicle suspension, were analyzed with higher-order ANCF beam elements to consider the complex geometry and the associated prestress in [12]. For ALE-ANCF cable element, an application typically of interest for the industry, is the prediction of global riser response due to slug flow in [13].

The ANCF formulation was first introduced by Shabana in [14]. Nachbagauer and Gerstmayr have done extensive work to present a good overview of ANCF, [15,16], and [17]. The ANCF is also developed for plates and shells, as proposed in [18]. Other applications where the ANCF have been applied successfully is for topology optimization for flexible multibody systems. Sun et al. has developed this method through several publications, where also the ALE-ANCF have been used in an optimization approach to simultaneously optimize the topology and geometrical sizes of a three-dimensional variable-length structure, [19]. This paper follows in large parts the ALE-ANCF cable element presented in [20].

For modeling of pulleys, and friction over the pulleys for the cable interaction, a contact formulation must be used. Several work has addressed this issue. For contact between cable segments, [21,22] should be consulted. Contact between the cable and the pulley is studied in [23,24], where the latter benchmark the simulation results with a laboratory experiment. One of the aspects pointed out as important design requirements for a cable simulation in [1] was friction between the cable and pulley and between different cable segments. For the cable sliding through the pulleys, a different approach must be used to simulate friction over the pulley compared to the methods suggested for ANCF contact only. This is described for a linear ALE cable element of two nodes in [25], where the background for the development of the linear ALE cable element was to avoid the discontinuity that would take place in a pulley for the element proposed in [26]. Another proposal to address the unrealistic frictionless sliding over the pulley, was performed by a dynamic relaxation method for tensioned continuous cables [27]. A simple method for global response of a sliding cable system with friction, where the tension magnitude of each cable segment is obtained by an unknown sliding length vector, is developed. This results in additional nodal forces set by a sliding criterion modified by Fischer–Burmeister complementary functions. A linear approach is presented in [28], and a nonlinear in [29]. A further discussion of how pulleys, and thus friction, can be implemented for nonlinear ALE-ANCF cable elements are not conducted in the present work.

The 4th order Runge–Kutta (RK4) has often been used in similar studies, and is thus an evident candidate for a numerical study with respect to explicit versus implicit time-integration. The Runge–Kutta methods has their origin more than 100 years ago from the famous paper by C. Runge [30]. A very readable treatise on the history of the Runge–Kutta methods was written by J.C. Butcher [31], who is also the originator for the famous Butcher tables for presenting the Runge–Kutta factors.

The Generalized-α (G-α) by Chung and Hulbert from 1993 [32] is a generalization of the HHT-α algorithm by Hilber, Hughes, and Taylor from 1977 [33], and the WBZ-α algorithm by Wood, Bossak, and Zienkiewicz from 1980 [34].

ANCF elements has successfully been used together with G-α in thermo-mechanical coupled analysis, [35]. For a simulation of an ANCF membrane element for dynamic modeling of multilayer dielectric elastomer actuators, G-α was part of the solution step. The HHT-α method was used for an ANCF element to simulate the motion of a fluid, as the dam break, [36]. A recent study have implemented an ALE-ANCF variant, in combination with HHT-α to simulate a tether deployment and station-keeping phases of a tethered satellite system, [37]. The characteristics of the element allowed for complex dynamic properties such as large deformation, slack, and rebound.

1.4. Scope and contribution of this study

This study presents a systematic approach to compare the two different numerical time integrators; the 4th order Runge–Kutta method (RK4) and the Generalized-α (G-α) for the ALE-ANCF cable element. Such a comparison is not found in other literature. RK4 is commonly used for control systems, fluid, and rigid body mechanism modeling, whereas G-α has been dominant in classical structural finite element software. The two are therefore important to study in relation to ALE-ANCF cable elements since these elements are likely to be implemented in existing software where both algorithms are used beforehand. Furthermore, a commercial software using the G-α integration is a likely recipient of this implementation of the ALE-ANCF cable element. A comparison of RK4 and G-α would reveal if the software is suitable for using the ALE-ANCF cable element.

The systematic approach examines two different numerical time integrators with the criteria *stability*, *accuracy*, and *efficiency*. Stability for a solver is important in order to at all times achieve results, and for the results to be reliable. The demand for accuracy of the results depends on what they are being used for. Thus, this will vary from case to case. For a real time simulation, the efficiency of the solver is critical. This study creates a tool that helps choose a numerical time integrator, as well as the proper parameters for it, providing a combination of *stability*, *accuracy* and *efficiency* for the simulation.

An important quality for an ALE-ANCF cable element is to be connected with neighboring elements, to create longer cable spans. This will achieve possibilities for advanced geometrical shapes. Coupling between ALE-ANCF cable elements and "regular" Euler–Bernoulli beam elements was used to simulate flutter in a pipe due to water flow, [20]. This case has been adopted in this paper in order to benchmark different constraint methods for coupling ALE-ANCF cable elements. In relation to the time integration methods, the systemic approach examines the effect of coupling method according to the *stability*, *accuracy* and *efficiency*. The penalty method, Lagrange multiplier method and linear coupling are the methods used for connecting ALE-ANCF cable elements.

For simulation of large, elastic structures such as cranes, G-α is the most relevant time integration method. For a crane, where cables are an integrated part of the structure, the element formulation also has to go together with the same time integration method. The relevant frequencies in such systems, including the lifting operations, are relatively low. The main contribution of this paper is the use of ALE-ANCF cable elements in combination with G-α, to prove the feasibility for a digital twin application with real time simulation. Other papers have typically used explicit time integration methods for cable elements, which is especially unfavorable being part of a larger structure.

1.5. Organization of the paper

The paper is organized as follows: Section 2 presents the ALE-ANCF cable element. Section 3 presents the solution procedure for RK4, RK4 with constraints, and G-α for a mechanical system. Section 4 finds the axial frequency of an ALE-ANCF cable element, and further use it as a criterion to obtain the maximum time-step for the RK4 solution procedure. Section 5 investigates the effects of constraints on the system. Section 6 test the ALE-ANCF cable element on an advanced case, to verify both the integration method and the constraints on a demanding simulation. Section 7 present results showing effects of various combinations of algorithm and constraint formulation on *stability*, *accuracy* and *efficiency*. Section 8 present conclusive remarks and possibilities for further work.

2. ALE-ANCF cable element

In the following section, a brief introduction to the element is given. The formulation used in the present work follows in large parts the formulation proposed in [20]. The ALE-ANCF cable element is an element where the material can flow through the element. It is created for slender geometries with large deformations and circular cross sections. It follows the Euler–Bernoulli assumption for beams, where the cross section is rigid and perpendicular to the deformed axis. The torsional stiffness and its related inertia are ignored. In Fig. 1, the ALE-ANCF cable element is presented, where $\boldsymbol{r}$ is the position vector, $\boldsymbol{r}'$ is the slope vector, p is the material coordinate, and $\boldsymbol{f}$ is distributed load. The general coordinates in the element are defined by $\boldsymbol{q}$, where node position, slope and material position are given, Eq. (1). The position vector and slope vector have components in x-, y- and z-direction. $\boldsymbol{q}_e$ contains the general coordinates, where the mass flow is omitted. $\boldsymbol{N}_e$, Eq. (2), is the matrix containing the shape functions, Eq. (3), which is time dependent in ALE due to the mass flow. The shape function of Eq. (3) are the familiar C^1 continuous Hermite beam functions, and are plotted in Fig. 2. s is the unit length of the element, Eq. (4), and L_e is the element length, Eq. (5). The position, $\boldsymbol{r}$, and the

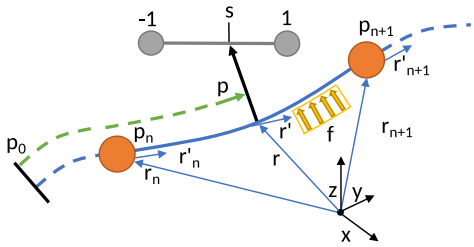

Fig. 1. ANCF element in the framework of ALE, where mass can flow through, based on figure by Hong et al. [20]. $\boldsymbol{r}$ is the position vector, $\boldsymbol{r}'$ is the slope, $\boldsymbol{f}$ is a distributed external load, and p is the material coordinate. The element is defined from node n to n+1, with the unitary element from −1 to 1.

slope, $\boldsymbol{r}'$ of an arbitrary point are given by Eqs. (6) and (7). Note that the slope vector $\boldsymbol{r}'$ has both directional and "stretch"-like content. The vector has unit length if distance between the point $\boldsymbol{r}_1$ and $\boldsymbol{r}_2$ is the same as the "material" distance between p_1 and p_2. Its norm thus exhibits deformation gradient like behavior.

$$\boldsymbol{q} = \begin{bmatrix} \boldsymbol{r}_1^T & \boldsymbol{r}_1'^T & \boldsymbol{r}_2^T & \boldsymbol{r}_2'^T & p_1 & p_2 \end{bmatrix}^T = \begin{bmatrix} \boldsymbol{q}_e^T & p_1 & p_2 \end{bmatrix}^T \tag{1}$$

$$\boldsymbol{N}_e = \begin{bmatrix} N_1 \boldsymbol{I}_{3x3} & N_2 \boldsymbol{I}_{3x3} & N_3 \boldsymbol{I}_{3x3} & N_4 \boldsymbol{I}_{3x3} \end{bmatrix} \tag{2}$$

$$\begin{aligned} N_1 &= \frac{1}{4}(s-1)^2(2+s),\ N_2 = \frac{L_e}{8}(s-1)^2(s+1) \\ N_3 &= \frac{1}{4}(s+1)^2(2-s),\ N_4 = \frac{L_e}{8}(s+1)^2(s-1) \end{aligned} \tag{3}$$

$$s = \frac{2p - p_1 - p_2}{p_2 - p_1} \tag{4}$$

$$L_e = p_2 - p_1 \tag{5}$$

$$\boldsymbol{r}(p,t) = \boldsymbol{N}_e(p, p_1(t), p_2(t))\boldsymbol{q}_e(t) \tag{6}$$

$$\boldsymbol{r}' = \frac{\partial \boldsymbol{r}}{\partial p} \tag{7}$$

The velocity and acceleration of the position, $\boldsymbol{r}$, are obtained by time derivatives:

$$\dot{\boldsymbol{r}} = \frac{d\boldsymbol{r}}{dt} = \boldsymbol{N}_e\dot{\boldsymbol{q}}_e + \left(\frac{\partial \boldsymbol{N}_e}{\partial p_1}\dot{p}_1 + \frac{\partial \boldsymbol{N}_e}{\partial p_2}\dot{p}_2\right)\boldsymbol{q}_e = \boldsymbol{N}\dot{\boldsymbol{q}} \tag{8}$$

$$\begin{aligned} \ddot{\boldsymbol{r}} = \frac{d\dot{\boldsymbol{r}}}{dt} &= \boldsymbol{N}_e\ddot{\boldsymbol{q}}_e + \left(\frac{\partial \boldsymbol{N}_e}{\partial p_1}\ddot{p}_1 + \frac{\partial \boldsymbol{N}_e}{\partial p_2}\ddot{p}_2\right)\boldsymbol{q}_e + 2\left(\frac{\partial \boldsymbol{N}_e}{\partial p_1}\dot{p}_1 + \frac{\partial \boldsymbol{N}_e}{\partial p_2}\dot{p}_2\right)\dot{\boldsymbol{q}}_e + \left(\frac{\partial^2 \boldsymbol{N}_e}{\partial p_1^2}\dot{p}_1^2 + 2\frac{\partial^2 \boldsymbol{N}_e}{\partial p_1 \partial p_2}\dot{p}_1\dot{p}_2 + \frac{\partial^2 \boldsymbol{N}_e}{\partial p_2^2}\dot{p}_2^2\right)\boldsymbol{q}_e \\ &= \boldsymbol{N}\ddot{\boldsymbol{q}} + \ddot{\boldsymbol{r}}_p \end{aligned} \tag{9}$$

For the convenience of further calculations $\boldsymbol{N}$ and $\ddot{\boldsymbol{r}}_p$ are used as substitutions in Eqs. (8) and (9). The two are defined as:

$$\boldsymbol{N} = \begin{bmatrix} \boldsymbol{N}_e & \frac{\partial \boldsymbol{N}_e}{\partial p_1}\boldsymbol{q}_e & \frac{\partial \boldsymbol{N}_e}{\partial p_2}\boldsymbol{q}_e \end{bmatrix} \tag{10}$$

$$\ddot{\boldsymbol{r}}_p = 2\left(\frac{\partial \boldsymbol{N}_e}{\partial p_1}\dot{p}_1 + \frac{\partial \boldsymbol{N}_e}{\partial p_2}\dot{p}_2\right)\dot{\boldsymbol{q}}_e + \left(\frac{\partial^2 \boldsymbol{N}_e}{\partial p_1^2}\dot{p}_1^2 + 2\frac{\partial^2 \boldsymbol{N}_e}{\partial p_1 \partial p_2}\dot{p}_1\dot{p}_2 + \frac{\partial^2 \boldsymbol{N}_e}{\partial p_2^2}\dot{p}_2^2\right)\boldsymbol{q}_e \tag{11}$$

where $\ddot{\boldsymbol{r}}_p$ equals the last part of Eq. (9).

d'Alembert's principle can be used to develop the governing equations for a system modeled by ALE-ANCF cable elements [20]. The system takes the form of a standard mechanical system as presented as:

$$\begin{cases} \boldsymbol{M}\ddot{\boldsymbol{q}} - \boldsymbol{Q}(\boldsymbol{q}, \dot{\boldsymbol{q}}, t) + \left(\frac{\partial \boldsymbol{\phi}}{\partial \boldsymbol{q}}\right)^T \lambda = \boldsymbol{0} \\ \boldsymbol{\phi}(\boldsymbol{q}, t) = \boldsymbol{0} \end{cases} \tag{12}$$

where $\boldsymbol{M}$ is the mass matrix, $\boldsymbol{Q}$ is the force matrix, $\boldsymbol{\phi}$ is the constraint vector, λ is the Lagrange multiplier vector, and $\boldsymbol{q}$, $\dot{\boldsymbol{q}}$ and $\ddot{\boldsymbol{q}}$, are the position, velocity and acceleration vectors. These need to be solved by a numerical integration algorithm.

The mass matrix $\boldsymbol{M}$ is the sum of the element contributions $\boldsymbol{M}_{ele}$, where ρ is the mass density and A is the cross section area:

$$\boldsymbol{M}_{ele} = \int_{p_1}^{p_2} \rho A \boldsymbol{N}^T \boldsymbol{N} dp \tag{13}$$

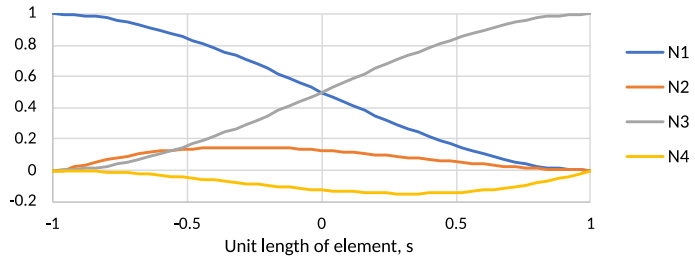

Fig. 2. The plotted shape functions from Eq. (3).

Total force vector $\boldsymbol{Q}$ consists of external forces $\boldsymbol{Q}_f$, internal forces $\boldsymbol{Q}_{int}$, damping forces $\boldsymbol{Q}_{damp}$, and additional "flow" forces $\boldsymbol{Q}_p$, according to [20]. Viewed as acting on the nodes, these forces contribute as:

$$\boldsymbol{Q} = \boldsymbol{Q}_f - \boldsymbol{Q}_{int} - \boldsymbol{Q}_{damp} - \boldsymbol{Q}_p \tag{14}$$

Additional inertia forces:

$$\boldsymbol{Q}_p = \int_{p_1}^{p_2} \rho A \boldsymbol{N}^T \ddot{\boldsymbol{r}}_p dp \tag{15}$$

Internal forces where ϵ_0 is the strain, EA is the axial stiffness, EJ is the bending stiffness, and κ is the curvature:

$$\boldsymbol{Q}_{int} = \int_{p_1}^{p_2} \left(\frac{\partial \epsilon_0}{\partial \boldsymbol{q}}\right)^T EA\epsilon_0 + \left(\frac{\partial \kappa}{\partial \boldsymbol{q}}\right)^T EJ\kappa dp \tag{16}$$

Damping forces (internal), where c is the damping coefficient, $\dot{\epsilon}$ is the strain rate, and $\dot{\kappa}$ is the curvature change rate:

$$\boldsymbol{Q}_{damp} = \int_{p_1}^{p_2} \left(\frac{\partial \epsilon_0}{\partial \boldsymbol{q}}\right)^T EAc\dot{\epsilon}_0 + \left(\frac{\partial \kappa}{\partial \boldsymbol{q}}\right)^T EJc\dot{\kappa} dp \tag{17}$$

External forces:

$$\boldsymbol{Q}_f = \int_{p_1}^{p_2} \boldsymbol{N}^T \boldsymbol{f} dp \tag{18}$$

Green strain:

$$\epsilon_0 = \frac{1}{2}(\boldsymbol{r}'^T \boldsymbol{r}' - 1) \tag{19}$$

Curvature:

$$\kappa = \frac{\|\boldsymbol{r}' \times \boldsymbol{r}''\|}{\|\boldsymbol{r}'\|^3} \tag{20}$$

The penalty method is an alternative method to handle constraints in the system, [38, p. 9–3]. The constraints are then added to the system through the system constraint violation energy $1/2\ \boldsymbol{\phi}^T \lceil \boldsymbol{k}_{pen} \rfloor \boldsymbol{\phi}$. The diagonal matrix $\lceil \boldsymbol{k}_{pen} \rfloor$ contains the individual penalty stiffnesses along the diagonal. When performing the variation of the penalty stiffness, this contributes to the system dynamic equilibrium equation and takes the form:

$$\boldsymbol{M}\ddot{\boldsymbol{q}} - \boldsymbol{Q}(\boldsymbol{q}, \dot{\boldsymbol{q}}, t) + \boldsymbol{G}^T \lceil \boldsymbol{k}_{pen} \rfloor \boldsymbol{\phi} = \boldsymbol{0} \tag{21}$$

where $\boldsymbol{G} = \partial \boldsymbol{\phi} / \partial \boldsymbol{q}$.

3. Solution procedure

To model the system behavior over time, numerical time integrators must be used in the system equations. In this section, different time integrators will be presented.

3.1. Runge–Kutta 4th order (RK4)

RK4 is an explicit time integrator, which means that the state at the next time-step can be calculated based solely on variables at previous time-steps and thus requires no equation solving. The state–space formulation is presented in Eq. (22), with the state vector, $\boldsymbol{x}$, defined in Eq. (23). $\boldsymbol{A}$ is the dynamic matrix, $\boldsymbol{g}$ contains all the nonlinear term, $\boldsymbol{B}$ is the input matrix, and $\boldsymbol{u}$ is the input to the system. External forces are the input to the system, given for the relevant time steps. $\boldsymbol{Q}$ is nonlinear and contains external forces, internal forces, damping forces and additional inertia forces, Eq. (14). For this system the stiffness and damping are nonlinear, and

therefore becomes a part of the restoring forces $\boldsymbol{g}(\boldsymbol{x})$. The unconstrained mechanical system from Eq. (12) can be written as Eq. (24), where $\boldsymbol{I}$ is the identity matrix. This is the starting point for the integrator using a first order form of the system.

$$\dot{\boldsymbol{x}} = \boldsymbol{A}\boldsymbol{x} + \boldsymbol{g}(\boldsymbol{x}) + \boldsymbol{B}\boldsymbol{u} \tag{22}$$

$$\boldsymbol{x} = \begin{bmatrix} \boldsymbol{q} \\ \dot{\boldsymbol{q}} \end{bmatrix} \tag{23}$$

$$\frac{d}{dt}\begin{bmatrix} \boldsymbol{q} \\ \dot{\boldsymbol{q}} \end{bmatrix} = \begin{bmatrix} \boldsymbol{0} & \boldsymbol{I} \\ \boldsymbol{0} & \boldsymbol{0} \end{bmatrix}\begin{bmatrix} \boldsymbol{q} \\ \dot{\boldsymbol{q}} \end{bmatrix} + \begin{bmatrix} \boldsymbol{0} \\ -\boldsymbol{M}^{-1}(\boldsymbol{Q}_{int} + \boldsymbol{Q}_{damp} + \boldsymbol{Q}_p) \end{bmatrix} + \begin{bmatrix} \boldsymbol{0} \\ \boldsymbol{M}^{-1} \end{bmatrix}\boldsymbol{Q}_f \tag{24}$$

For the solver used in this work, the time increments are constant. The solver advances, $\boldsymbol{x}$, of the general non-homogeneous first order ordinary differential equations in Eq. (25) with a time-step, h. The goal is to find the state of the system at $\boldsymbol{x}(t+h)$. The initial conditions are given as $\boldsymbol{x}(0) = \boldsymbol{x}_0$. The solution procedure for RK4 calculates $\dot{\boldsymbol{x}}$ four times each time increment, Eq. (26). The four derivatives are used in Eq. (27) to construct $\boldsymbol{x}$ for the next time step. For further advancement in time, the procedure is repeated.

$$\dot{\boldsymbol{x}}(t) = f(t, \boldsymbol{x}(t), \boldsymbol{u}(t)), \qquad \boldsymbol{x}(0) = \boldsymbol{x}_0 \tag{25}$$

$$\dot{\boldsymbol{x}}_1 = f(t, \boldsymbol{x}(t), \boldsymbol{u}(t)) \tag{26a}$$

$$\dot{\boldsymbol{x}}_2 = f\left(t + \frac{h}{2}, \boldsymbol{x}(t) + \dot{\boldsymbol{x}}_1\frac{h}{2}, \boldsymbol{u}\left(t + \frac{h}{2}\right)\right) \tag{26b}$$

$$\dot{\boldsymbol{x}}_3 = f\left(t + \frac{h}{2}, \boldsymbol{x}(t) + \dot{\boldsymbol{x}}_2\frac{h}{2}, \boldsymbol{u}\left(t + \frac{h}{2}\right)\right) \tag{26c}$$

$$\dot{\boldsymbol{x}}_4 = f\left(t + h, \boldsymbol{x}(t) + \dot{\boldsymbol{x}}_3 h, \boldsymbol{u}\left(t + h\right)\right) \tag{26d}$$

$$\boldsymbol{x}(t+h) = \boldsymbol{x}(t) + (\dot{\boldsymbol{x}}_1 + 2(\dot{\boldsymbol{x}}_2 + \dot{\boldsymbol{x}}_3) + \dot{\boldsymbol{x}}_4)\frac{h}{6} \tag{27}$$

3.2. RK4 with constraints

Solving a mechanical system with constraints by Runge–Kutta is studied in several works i.e. [39–41]. One of the main problems using a RK solution procedure is that the mechanical system is a second order Differential Algebraic Equation (DAE) that must be reduced to a lower order. As part of the reduction, the constraint equation must be differentiated. A step-by-step solution to the second order differentiation of the algebraic position constraint is given in Eq. ((28)). The undesired risk with this procedure is that the accuracy in the constraints could be lost, which again causes drift in the results. The method implemented in this work is instead based on the discretization of the stabilized ODE formulation, [41].

$$\boldsymbol{\phi} = \boldsymbol{0} \tag{28a}$$

$$\dot{\boldsymbol{\phi}} = \frac{d\boldsymbol{\phi}}{dt} = \frac{\partial\boldsymbol{\phi}}{\partial\boldsymbol{q}}\frac{\partial\boldsymbol{q}}{\partial t} + \cancelto{0}{\frac{\partial\boldsymbol{\phi}}{\partial t}} = \boldsymbol{G}\dot{\boldsymbol{q}} = \boldsymbol{0} \tag{28b}$$

$$\begin{aligned} \ddot{\boldsymbol{\phi}} &= \frac{d^2\boldsymbol{\phi}}{dt^2} = \frac{d}{dt}(\boldsymbol{G}\dot{\boldsymbol{q}}) = \boldsymbol{G}\frac{d\dot{\boldsymbol{q}}}{dt} + \dot{\boldsymbol{q}}^T\frac{d\boldsymbol{G}}{dt} = \boldsymbol{G}\ddot{\boldsymbol{q}} + \dot{\boldsymbol{q}}^T\frac{\partial\boldsymbol{G}}{\partial\boldsymbol{q}}\frac{\partial\boldsymbol{q}}{\partial t} + \cancelto{0}{\frac{\partial\boldsymbol{G}}{\partial t}} \\ &= \boldsymbol{G}\ddot{\boldsymbol{q}} + \dot{\boldsymbol{q}}^T\frac{\partial\boldsymbol{G}}{\partial\boldsymbol{q}}\dot{\boldsymbol{q}} = \boldsymbol{0} \end{aligned} \tag{28c}$$

$$\boldsymbol{G}\ddot{\boldsymbol{q}} = -\dot{\boldsymbol{q}}^T\boldsymbol{G}_{,\boldsymbol{q}}\dot{\boldsymbol{q}} \tag{28d}$$

The solution procedure for $\dot{\boldsymbol{q}}^T\boldsymbol{G}_{,\boldsymbol{q}}\dot{\boldsymbol{q}}$ in Eq. (28) is clearer when using index notation. The equation now takes the form:

$$C_i = \dot{q}_j G_{ij,q_k}\dot{q}_k \tag{29}$$

$\dot{q}_j$ and $\dot{q}_k$ represent the velocities of the generalized coordinates from Eq. (1) in separate axes. According to $G_{ij} = \frac{\partial\phi_i}{\partial q_j}$, i is the number of constraints. This results in the vector C_i with size i.

Inserting the differentiation of the constraints from Eq. (28d) into the mechanical system, it can be written in the following form:

$$\begin{bmatrix} \boldsymbol{M} & \boldsymbol{G}^T \\ \boldsymbol{G} & 0 \end{bmatrix}\begin{bmatrix} \ddot{\boldsymbol{q}} \\ \lambda \end{bmatrix} = \begin{bmatrix} \boldsymbol{Q} \\ -\dot{\boldsymbol{q}}^T\boldsymbol{G}_{,\boldsymbol{q}}\dot{\boldsymbol{q}} \end{bmatrix} \tag{30}$$

where $\boldsymbol{Q}$ is defined according to Eq. (14).

This gives the solution for the acceleration, Eq. (31).

$$\ddot{\boldsymbol{q}} = \boldsymbol{M}^{-1}(\boldsymbol{Q} - \boldsymbol{G}^T\lambda) \tag{31}$$

An expression for λ is found by taking Eq. (31) and substituting it back into Eq. (28d), to get Eq. (32).

$$\boldsymbol{G}\ddot{\boldsymbol{q}} = -\dot{\boldsymbol{q}}^T \boldsymbol{G}_{,q}\dot{\boldsymbol{q}} \tag{32a}$$

$$\boldsymbol{G}\left(\boldsymbol{M}^{-1}\boldsymbol{Q} - \boldsymbol{M}^{-1}\boldsymbol{G}^T\lambda\right) = -\dot{\boldsymbol{q}}^T \boldsymbol{G}_{,q}\dot{\boldsymbol{q}} \tag{32b}$$

$$\boldsymbol{G}\boldsymbol{M}^{-1}\boldsymbol{G}^T\lambda = \boldsymbol{G}\boldsymbol{M}^{-1}\boldsymbol{Q} + \dot{\boldsymbol{q}}^T \boldsymbol{G}_{,q}\dot{\boldsymbol{q}} \tag{32c}$$

$$\lambda = \left(\boldsymbol{G}\boldsymbol{M}^{-1}\boldsymbol{G}^T\right)^{-1}\left(\boldsymbol{G}\boldsymbol{M}^{-1}\boldsymbol{Q} + \dot{\boldsymbol{q}}^T \boldsymbol{G}_{,q}\dot{\boldsymbol{q}}\right) \tag{32d}$$

By inserting Eq. (32d) into the mechanical system, a first order formulation is obtained as an expression for the acceleration, Eq. (33). It is important to note that the two are not to be considered equal, as the constraint is a derivative. This is what makes the solution subjected to drifting.

$$\ddot{\boldsymbol{q}} = \boldsymbol{M}^{-1}\boldsymbol{Q} - \boldsymbol{M}^{-1}\boldsymbol{G}^T\left(\boldsymbol{G}\boldsymbol{M}^{-1}\boldsymbol{G}^T\right)^{-1}\left(\boldsymbol{G}\boldsymbol{M}^{-1}\boldsymbol{Q} + \dot{\boldsymbol{q}}^T \boldsymbol{G}_{,q}\dot{\boldsymbol{q}}\right) \tag{33}$$

This leads to the state–space formulation used for solving by RK4 in this work:

$$\frac{d}{dt}\begin{bmatrix} \boldsymbol{q} \\ \dot{\boldsymbol{q}} \end{bmatrix} = \begin{bmatrix} \boldsymbol{0} & \boldsymbol{I} \\ \boldsymbol{0} & \boldsymbol{0} \end{bmatrix}\begin{bmatrix} \boldsymbol{q} \\ \dot{\boldsymbol{q}} \end{bmatrix} + \begin{bmatrix} \boldsymbol{0} \\ \boldsymbol{M}^{-1}\left(\boldsymbol{Q} - \boldsymbol{G}^T\left(\boldsymbol{G}\boldsymbol{M}^{-1}\boldsymbol{G}^T\right)^{-1}\left(\boldsymbol{G}\boldsymbol{M}^{-1}\boldsymbol{Q} + \dot{\boldsymbol{q}}^T\boldsymbol{G}_{,q}\dot{\boldsymbol{q}}\right)\right) \end{bmatrix} \tag{34}$$

The RK4 solver from Eq. (25) to (27) is used to propagate Eq. (34), providing a temporary generalized coordinate vector $\tilde{\boldsymbol{q}}$. $\tilde{\boldsymbol{q}}$ is further stabilized to a new temporary generalized coordinate vector $\hat{\boldsymbol{q}}$ through the stabilization step in Eq. (35). A final stabilization step to get the generalized coordinate vector $\boldsymbol{q}$ is performed in Eq. (36), before continuing to the next time step. To get a more robust solver the double stabilization step is recommended, [41].

$$\begin{bmatrix} \hat{\boldsymbol{q}}_{t+1} \\ \hat{\dot{\boldsymbol{q}}}_{t+1} \end{bmatrix} = \begin{bmatrix} \tilde{\boldsymbol{q}}_{t+1} \\ \tilde{\dot{\boldsymbol{q}}}_{t+1} \end{bmatrix} - \boldsymbol{F}(\tilde{\boldsymbol{q}}_{t+1}, \tilde{\dot{\boldsymbol{q}}}_{t+1})\boldsymbol{s}(\tilde{\boldsymbol{q}}_{t+1}, \tilde{\dot{\boldsymbol{q}}}_{t+1}) \tag{35}$$

$$\begin{bmatrix} \boldsymbol{q}_{t+1} \\ \dot{\boldsymbol{q}}_{t+1} \end{bmatrix} = \begin{bmatrix} \hat{\boldsymbol{q}}_{t+1} \\ \hat{\dot{\boldsymbol{q}}}_{t+1} \end{bmatrix} - \boldsymbol{F}(\tilde{\boldsymbol{q}}_{t+1}, \tilde{\dot{\boldsymbol{q}}}_{t+1})\boldsymbol{s}(\hat{\boldsymbol{q}}_{t+1}, \hat{\dot{\boldsymbol{q}}}_{t+1}) \tag{36}$$

where $\boldsymbol{s}$ and $\boldsymbol{F}$ are defined as follows:

$$\boldsymbol{s} = \begin{bmatrix} \boldsymbol{\Phi} \\ \boldsymbol{G}\dot{\boldsymbol{q}} \end{bmatrix} \tag{37}$$

$$\boldsymbol{F} = \boldsymbol{M}^{-1}\boldsymbol{G}^T\boldsymbol{G}(\boldsymbol{M}^{-1}\boldsymbol{G}^T)^{-1}\begin{bmatrix} \boldsymbol{I} & \boldsymbol{0} \\ \boldsymbol{0} & \boldsymbol{I} \end{bmatrix} \tag{38}$$

3.3. Newmark-β integration

The Newmark-β method was proposed by N. M. Newmark in 1959 [42], and is a commonly used numerical time integrator. To impose this method, firstly the DAE of the mechanical system Eq. (12) must be linearized by the first variation of Eq. (39). This leads to Eq. (40), where $\Delta\boldsymbol{R}^q$ and $\Delta\boldsymbol{R}^\lambda$ are given in Eq. (41). $\boldsymbol{R}^q$ refers to residuals when finding $\Delta\boldsymbol{q}$, and $\boldsymbol{R}^\lambda$ refers to residuals when finding $\Delta\lambda$.

$$\begin{aligned} \boldsymbol{R}^q &= \boldsymbol{M}\ddot{\boldsymbol{q}} - \boldsymbol{Q} + \boldsymbol{G}^T\lambda \\ \boldsymbol{R}^\lambda &= \boldsymbol{\phi} \end{aligned} \tag{39}$$

$$\begin{aligned} \boldsymbol{R}^q + \Delta\boldsymbol{R}^q &= 0 \\ \boldsymbol{R}^\lambda + \Delta\boldsymbol{R}^\lambda &= 0 \end{aligned} \tag{40}$$

$$\begin{aligned} \Delta\boldsymbol{R}^q &= \frac{\partial\boldsymbol{R}^q}{\partial\ddot{\boldsymbol{q}}}\Delta\ddot{\boldsymbol{q}} + \frac{\partial\boldsymbol{R}^q}{\partial\dot{\boldsymbol{q}}}\Delta\dot{\boldsymbol{q}} + \frac{\partial\boldsymbol{R}^q}{\partial\boldsymbol{q}}\Delta\boldsymbol{q} + \frac{\partial\boldsymbol{R}^q}{\partial t}\Delta t + \frac{\partial\boldsymbol{R}^q}{\partial\lambda}\Delta\lambda \\ \Delta\boldsymbol{R}^\lambda &= \frac{\partial\boldsymbol{R}^\lambda}{\partial\boldsymbol{q}}\Delta\boldsymbol{q} \end{aligned} \tag{41}$$

The differentials are calculated in Eq. (42), where $\boldsymbol{K}_T$ and $\boldsymbol{C}_T$ represent the tangential stiffness matrix and the damping matrix.

$$\begin{aligned} \frac{\partial\boldsymbol{R}^q}{\partial\ddot{\boldsymbol{q}}} &= \boldsymbol{M} & \frac{\partial\boldsymbol{R}^q}{\partial\dot{\boldsymbol{q}}} &= \boldsymbol{C}_T = -\frac{\partial\boldsymbol{Q}}{\partial\dot{\boldsymbol{q}}} \\ \frac{\partial\boldsymbol{R}^q}{\partial\boldsymbol{q}} &= \boldsymbol{K}_T = \frac{\partial\boldsymbol{M}\ddot{\boldsymbol{q}}}{\partial\boldsymbol{q}} - \frac{\partial\boldsymbol{Q}}{\partial\boldsymbol{q}} + \frac{\partial\boldsymbol{G}^T}{\partial\boldsymbol{q}}\lambda & \frac{\partial\boldsymbol{R}^q}{\partial t} &= 0 \\ \frac{\partial\boldsymbol{R}^q}{\partial\lambda} &= \boldsymbol{G}^T & \frac{\partial\boldsymbol{R}^\lambda}{\partial\boldsymbol{q}} &= \boldsymbol{G} \end{aligned} \tag{42}$$

The matrix system with nonlinear equations of motion is obtained:

$$\begin{bmatrix} \boldsymbol{M} & \boldsymbol{0} \\ \boldsymbol{0} & \boldsymbol{0} \end{bmatrix}\begin{bmatrix} \Delta\ddot{\boldsymbol{q}} \\ \Delta\ddot{\lambda} \end{bmatrix} + \begin{bmatrix} \boldsymbol{C}_T & \boldsymbol{0} \\ \boldsymbol{0} & \boldsymbol{0} \end{bmatrix}\begin{bmatrix} \Delta\dot{\boldsymbol{q}} \\ \Delta\dot{\lambda} \end{bmatrix} + \begin{bmatrix} \boldsymbol{K}_T & \boldsymbol{G}^T \\ \boldsymbol{G} & \boldsymbol{0} \end{bmatrix}\begin{bmatrix} \Delta\boldsymbol{q} \\ \Delta\lambda \end{bmatrix} = \begin{bmatrix} -\boldsymbol{R}^q \\ -\boldsymbol{R}^\lambda \end{bmatrix} \tag{43}$$

When using the penalty method, the residuals, $\boldsymbol{R}^q$ and $\boldsymbol{R}^\lambda$, take a different form than for the Lagrange multiplier method. $\boldsymbol{R}^q$, is given in Eq. (44), while $\boldsymbol{R}^\lambda$ is canceled. The tangential stiffness, $\boldsymbol{K}_T$ takes the form as in Eq. (45).

$$\boldsymbol{R}^q = \boldsymbol{M}\ddot{\boldsymbol{q}} - \boldsymbol{Q} + \boldsymbol{G}^T \lceil \boldsymbol{k}_{pen} \rfloor \boldsymbol{\phi} \tag{44}$$

$$\frac{\partial \boldsymbol{R}^q}{\partial \boldsymbol{q}} = \boldsymbol{K}_T = \frac{\partial \boldsymbol{M}\ddot{\boldsymbol{q}}}{\partial \boldsymbol{q}} - \frac{\partial \boldsymbol{Q}}{\partial \boldsymbol{q}} + \lceil \boldsymbol{k}_{pen} \rfloor \left(\frac{\partial \boldsymbol{G}^T}{\partial \boldsymbol{q}} \boldsymbol{\phi} + \boldsymbol{G}^T \frac{\partial \boldsymbol{\phi}}{\partial \boldsymbol{q}} \right) \tag{45}$$

Newmark-β integration suggests a procedure to rewrite the accelerations and velocities in Eq. (43) in terms of displacement, [42]. The procedure is outlined in the following section, where the Newmark difference formulas are given in Eqs. (46) and (47).

$$\boldsymbol{q}_{t+1} = \boldsymbol{q}_t + h\dot{\boldsymbol{q}}_t + \left(\frac{1}{2} - \beta \right) h^2 \ddot{\boldsymbol{q}}_t + \beta h^2 \ddot{\boldsymbol{q}}_{t+1} \tag{46}$$

$$\dot{\boldsymbol{q}}_{t+1} = \dot{\boldsymbol{q}}_t + (1-\gamma) h\ddot{\boldsymbol{q}}_t + \gamma h \ddot{\boldsymbol{q}}_{t+1} \tag{47}$$

Here h is the time-step size, and β and γ are user defined parameters. To obtain the average constant acceleration formula the parameters are set to, $\beta = \frac{1}{4}$ and $\gamma = \frac{1}{2}$. This option gives second order accuracy, and will also be unconditionally stable over the full frequency range. This choice is also the most commonly used in commercial analysis software.

The incremental form of displacement is given in Eq. (48), and in combination with Eq. (46) takes the form of Eq. (49).

$$\boldsymbol{q}_{t+1} = \boldsymbol{q}_t + \Delta \boldsymbol{q}_t \tag{48}$$

$$\Delta \boldsymbol{q}_t = h\dot{\boldsymbol{q}}_t + \frac{1}{2} h^2 \ddot{\boldsymbol{q}}_t + \beta h^2 \Delta \ddot{\boldsymbol{q}}_t \tag{49}$$

The same goes for velocity, where the incremental form is given in Eq. (50), and in combination with Eq. (47) takes the form of Eq. (51).

$$\dot{\boldsymbol{q}}_{t+1} = \dot{\boldsymbol{q}}_t + \Delta \dot{\boldsymbol{q}}_t \tag{50}$$

$$\Delta \dot{\boldsymbol{q}}_t = h\ddot{\boldsymbol{q}}_t + h\gamma \Delta \ddot{\boldsymbol{q}}_t \tag{51}$$

The incremental form of the acceleration is given by:

$$\Delta \ddot{\boldsymbol{q}}_t = \ddot{\boldsymbol{q}}_{t+1} - \ddot{\boldsymbol{q}}_t \tag{52}$$

When incrementing the solution, it is desired to solve the system with respect to the displacement increments, $\Delta \boldsymbol{q}$, by rearranging Eq. (49). The incrementation form of the acceleration is obtained, with $\Delta \boldsymbol{q}$ as the unknown in Eq. (53).

$$\Delta \ddot{\boldsymbol{q}}_t = \frac{1}{\beta h^2} \Delta \boldsymbol{q}_t - \frac{1}{\beta h} \dot{\boldsymbol{q}}_t - \frac{1}{2\beta} \ddot{\boldsymbol{q}}_t = \frac{1}{\beta h^2} \Delta \boldsymbol{q}_t - \boldsymbol{a}_t \tag{53}$$

The incrementation form of the velocity, Eq. (54), is obtained by inserting Eq. (53) into Eq. (51).

$$\Delta \dot{\boldsymbol{q}}_t = \frac{\gamma}{\beta h} \Delta \boldsymbol{q}_t - \frac{\gamma}{\beta} \dot{\boldsymbol{q}}_t - h \left(\frac{\gamma}{2\beta} - 1 \right) \ddot{\boldsymbol{q}}_t = \frac{\gamma}{\beta h} \Delta \boldsymbol{q}_t - \boldsymbol{d}_t \tag{54}$$

The velocity and acceleration incrementation in the matrix system Eq. (43), are substituted with Eqs. (53) and (54), and it takes the form as presented in Eq. (55), where the incrementors are lambda and displacement.

$$\begin{bmatrix} \boldsymbol{M} & \boldsymbol{0} \\ \boldsymbol{0} & \boldsymbol{0} \end{bmatrix} \begin{bmatrix} \frac{1}{\beta h^2} \Delta \boldsymbol{q}_t - \boldsymbol{a}_t \\ \Delta \ddot{\boldsymbol{\lambda}} \end{bmatrix} + \begin{bmatrix} \boldsymbol{C}_T & \boldsymbol{0} \\ \boldsymbol{0} & \boldsymbol{0} \end{bmatrix} \begin{bmatrix} \frac{\gamma}{\beta h} \Delta \boldsymbol{q}_t - \boldsymbol{d}_t \\ \Delta \dot{\boldsymbol{\lambda}} \end{bmatrix} + \begin{bmatrix} \boldsymbol{K}_T & \boldsymbol{G}^T \\ \boldsymbol{G} & \boldsymbol{0} \end{bmatrix} \begin{bmatrix} \Delta \boldsymbol{q} \\ \Delta \boldsymbol{\lambda} \end{bmatrix} = \begin{bmatrix} -\boldsymbol{R}^q \\ -\boldsymbol{R}^\lambda \end{bmatrix} \tag{55}$$

By defining $\boldsymbol{S}_T$ according to Eq. (56), the matrix system in Eq. (55) can be compressed to Eq. (57). To find the increments, the inverse of $\boldsymbol{S}_T$ is found and moved to the right hand side, Eq. (58). The terms containing $\boldsymbol{a}_t$ and $\boldsymbol{d}_t$ are only used for the predictor step, not the corrector steps. That means it is only used for the first iteration each time step.

$$\boldsymbol{S}_T = \begin{bmatrix} \frac{1}{\beta h^2} \boldsymbol{M} + \frac{\gamma}{\beta h} \boldsymbol{C}_T + \boldsymbol{K}_T & \boldsymbol{G}^T \\ \boldsymbol{G} & \boldsymbol{0} \end{bmatrix} \tag{56}$$

$$\boldsymbol{S}_T \begin{bmatrix} \Delta \boldsymbol{q} \\ \Delta \boldsymbol{\lambda} \end{bmatrix} = \begin{bmatrix} -\boldsymbol{R}^q + \boldsymbol{M}\boldsymbol{a}_t + \boldsymbol{C}_T \boldsymbol{d}_t \\ -\boldsymbol{R}^\lambda \end{bmatrix} \tag{57}$$

$$\begin{bmatrix} \Delta \boldsymbol{q} \\ \Delta \boldsymbol{\lambda} \end{bmatrix} = \boldsymbol{S}_T^{-1} \begin{bmatrix} -\boldsymbol{R}^q + \boldsymbol{M}\boldsymbol{a}_t + \boldsymbol{C}_T \boldsymbol{d}_t \\ -\boldsymbol{R}^\lambda \end{bmatrix} \tag{58}$$

The energy based convergence criterion [43], that must be satisfied before continuing to the next time step is:

$$\epsilon_R = \sqrt{\left| \begin{bmatrix} \boldsymbol{R}^q & \boldsymbol{R}^\lambda \end{bmatrix} \begin{bmatrix} \Delta \boldsymbol{q} \\ \Delta \boldsymbol{\lambda} \end{bmatrix} \right|} \tag{59}$$

An error criterion based on energy is quite often more stable for simulations where both rotations and translations are part of the generalized coordinates. Energy based convergence criteria is also considered more robust with respect to soft versus stiff systems as well as unit changes (meters to millimeters for instance).

3.4. Generalized-α for mechanical system

For further improvement of the Newmark-β integration, the G-α method [32] seeks to introduce high frequency dissipation. This is done by linear interpolation between the time steps, to improve stability. This means that if $\alpha = 0$, only the $t + 1$ time step is accounted for. The effect of the numerical damping decreases as the time step decreases. α_m is used for the inertia forces, and α_f is used for elastic, damping and external forces. The selection of the weight parameters α_m and α_f are done according to [32].

A proposal to implement the method for mechanical systems was suggested in [44]. The method handles non-constant mass, which is required for an accurate solution for ALE-ANCF cable elements. Instead of a weighted formulation of the residual equation, as the common G-α method, the dynamic equilibrium is, at every time step, enforced. This is done by rewriting the Newmark formulas in Eqs. (46) and (47). The acceleration, $\ddot{\boldsymbol{q}}$, is replaced with the auxiliary variable $\boldsymbol{a}$, which is an acceleration-like variable (not the true acceleration), and takes the form as in Eqs. (60) and (61). The weighting is done by Eq. (62).

$$\boldsymbol{q}_{t+1} = \boldsymbol{q}_t + h\dot{\boldsymbol{q}}_t + \left(\frac{1}{2} - \beta\right) h^2 \ddot{\boldsymbol{a}}_t + \beta h^2 \ddot{\boldsymbol{a}}_{t+1} \tag{60}$$

$$\dot{\boldsymbol{q}}_{t+1} = \dot{\boldsymbol{q}}_t + (1-\gamma) h\ddot{\boldsymbol{a}}_t + \gamma h \ddot{\boldsymbol{a}}_{t+1} \tag{61}$$

$$(1-\alpha_m)\boldsymbol{a}_{t+1} + \alpha_m \boldsymbol{a}_t = (1-\alpha_f)\ddot{\boldsymbol{q}}_{t+1} + \alpha_f \ddot{\boldsymbol{q}}_t \tag{62}$$

The solution procedure follows the algorithm in [44]. $\boldsymbol{S}_T$ takes the form as in Eq. (63), where β' and γ' are defined in Eq. (64) and (65). The mass $\boldsymbol{M}$, damping $\boldsymbol{C}_T$ and stiffness $\boldsymbol{K}_T$ follows the same derivation as in Eq. (42). The error criterion in the algorithm is modified and updated with Eq. (59), with a sufficiently small limit. For the first iteration each time step $\boldsymbol{a}_0 = \ddot{\boldsymbol{q}}_0$.

$$\boldsymbol{S}_T = \begin{bmatrix} \boldsymbol{M}\beta' + \boldsymbol{C}_T\gamma' + \boldsymbol{K}_T & \boldsymbol{G}^T \\ \boldsymbol{G} & \boldsymbol{0} \end{bmatrix} \tag{63}$$

$$\beta' = \frac{1-\alpha_m}{\beta h^2 (1-\alpha_f)} \tag{64}$$

$$\gamma' = \frac{\gamma}{\beta h} \tag{65}$$

The selection of the parameters are done according to Chung and Hulbert [32]. For second-order ODEs, the proposed algorithmic parameters are given in Eqs. (66), (67) and (68), where $\rho_\infty \epsilon [0, 1]$.

$$\alpha_m = \frac{2\rho_\infty - 1}{\rho_\infty + 1} \tag{66}$$

$$\alpha_f = \frac{\rho_\infty}{\rho_\infty + 1} \tag{67}$$

$$\beta = \frac{1}{4}\left(\gamma + \frac{1}{2}\right)^2 \tag{68}$$

γ is calculated according to Eq. (70), and the stability region is met for:

$$\alpha_m < \alpha_f < \frac{1}{2} \qquad \text{and} \qquad \gamma > \frac{1}{2} \tag{69}$$

The equations used to set the parameters are Eqs. (68) and (70), following the restrictions of Eq. (69).

$$\gamma = \frac{1}{2} - \alpha_m + \alpha_f \tag{70}$$

4. Case 1: Cable - cantilever bar and RK4 maximum time-step

The first case is a cable arranged and modeled as a cantilever. The model is relevant to investigate different attributes of the ALE-ANCF cable element:

- Firstly, to find the maximum stable time-step for an ALE-ANCF cable element model when using the RK4 time integrator.
- Secondly, to verify the axial frequencies for the 1 and 2nd axial vibration mode for the ALE-ANCF cable element.

The findings can further be applied to more advanced models.

The single degree of freedom problem, damped free vibration, shown in Fig. 3, takes the form as:

$$m\ddot{u} + c\dot{u} + ku = 0 \tag{71}$$

where m is the mass, k is the spring stiffness, c is the damping factor, and u is the displacement.

Assuming the solution on the form

$$u = u_0 e^{\lambda t}, \qquad \dot{u} = u_0 \lambda e^{\lambda t}, \qquad \ddot{u} = u_0 \lambda^2 e^{\lambda t} \tag{72}$$

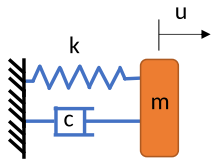

Fig. 3. A simple 1-D Mass–Spring–Damper system.

and inserting in the free vibration Eq. (71) gives us

$$\left(m\lambda^2 + c\lambda + k\right) u_0 e^{\lambda t} = 0 \tag{73}$$

where eigenvalue λ consists of a real and an imaginary part.

When introducing undamped eigenfrequency ω_0, critical damping c_c and relative damping ratio ξ, the eigenvalue can be written as:

$$\lambda = \omega_0 \left(-\xi \pm i\sqrt{1-\xi^2}\right) \quad \text{where} \quad \omega_0 = \sqrt{\frac{k}{m}}, \quad \xi = \frac{c}{c_c}, \quad c_c = 2\sqrt{km} = 2m\omega_0 \tag{74}$$

For the undamped system only the imaginary part remains, leading to:

$$m\lambda^2 + k = 0 \quad \Rightarrow \quad \lambda = i\sqrt{\frac{k}{m}} = i\omega_0 \tag{75}$$

The stability region for RK4 can be drawn from several sources, such as Figure 2.1 in [45, p. 17], and in this work presented in Fig. 4. For the undamped problem the, stable area for the solver is described by $\lambda h \leq 2.8i$. Combining the stable area with Eq. (75), the maximum stable time-step h is restricted by:

$$h \leq \frac{2.8}{\omega_0}, \quad \text{where} \quad \omega_0 = \sqrt{\frac{k}{m}} \tag{76}$$

4.1. Highest frequency of a meshed cable

For a discretized cable subjected to axial vibrations, which is modeled with linear bar elements, the highest frequency of the mesh is given by the vibration mode where every other node is moving in the same direction. All the nodes then have the same amplitude, as shown in Fig. 5.

Due to symmetry, as the nodes move opposite of each other, the system is simplified by a fixed spring with a mass m, stiffness k, and displacement u. The mass and stiffness for a half linear bar element is given in Eq. (77), and defines the highest frequency for a MSD.

$$m = \frac{1}{2}\rho A L_e, \qquad k = \frac{EA}{\frac{L_e}{2}} = \frac{2EA}{L_e} \tag{77}$$

When inserting the cable properties for half the linear bar element in Eq. (76), an alternative expression for eigenfrequency is achieved, Eq. (78). S is the speed of sound traveling through the given material.

$$\omega_0 = \sqrt{\frac{k}{m}} = \frac{2}{L_e}\sqrt{\frac{E}{\rho}} = \frac{2}{L_e}S \quad \text{where} \quad S = \sqrt{\frac{E}{\rho}} \tag{78}$$

This leads to an expression based on element length to be used as a criterion for maximum time-step for a stable RK4 solver:

$$h \leq \frac{2.8}{\omega_0} = 2.8\frac{L_e}{2S} \tag{79}$$

Note that this expression is based on a *linear* variation of the displacements along the element length L_e. We will later see that the ALE-ANCF cable element can represent a higher variation of the displacements along L_e, and the expression will then have to be modified.

The highest axial frequencies results from an undamped MSD and ALE-ANCF cable element are presented and compared in Fig. 6. The cable was modeled with $\rho A = 1$, $L = 1$ and $EA = 1000$, with a varying number of elements with evenly spaced nodes. The cable was pinned in one end, hanging in a gravity field working in the axial direction. It is clearly evident that MSD has significantly lower highest frequency than ANCF-ALE cable elements, thus MSD is not sufficient to predict the maximum time-step for RK4 directly. Another method to predict a general criterion for maximum time-step for a stable RK4 solver is therefore of interest. To establish such an expression for the highest frequency within a mesh based on the shortest ALE-ANCF cable element, a free 1-D axial element is investigated, Fig. 7(a). The DOFs for the model are $r_{1x}, r'_{1x}, r_{2x}, r'_{2x}$.

For an undamped system with multiple degrees of freedom, Eq. (80) can be used to find the eigenfrequencies. Here, $\boldsymbol{K}$ is the stiffness matrix for the element, $\boldsymbol{M}$ is the mass matrix for the element, ω is the eigenvalues given as angular velocity and $\boldsymbol{v}$ is the

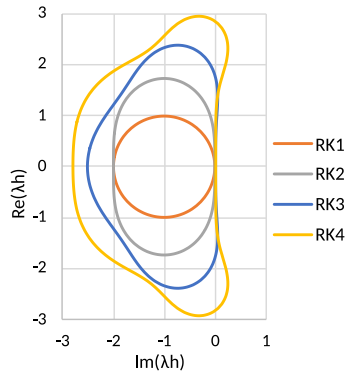

Fig. 4. Stability region for the Runge–Kutta orders RK1, RK2, RK3 and RK4 with imaginary and real λh on the axes.

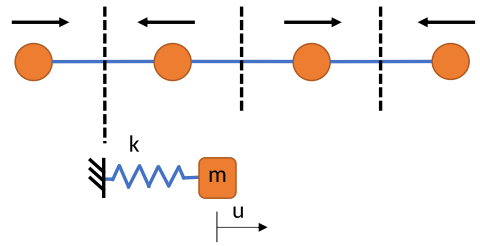

Fig. 5. A meshed cable where the smallest element is simplified to a Mass–Spring system due to symmetry. Vertical lines indicates zero displacement.

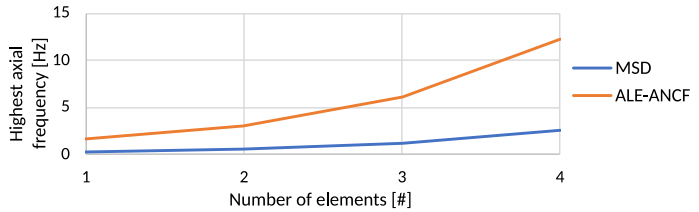

Fig. 6. The highest axial frequency for MSD and ALE-ANCF cable swinging freely with gravity in the axial direction. The number of elements are varying with constant cable length. The ratio between the highest frequencies verifies the effective length in Table 1.

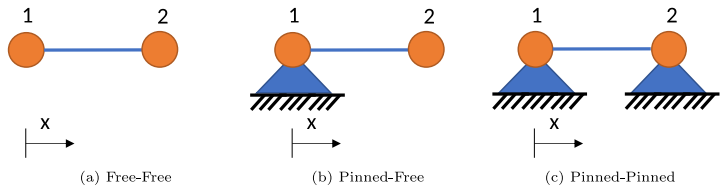

Fig. 7. Single element 1-D problem with different boundary conditions.

eigenvector. The element in Fig. 7(a) is not constrained in the x-direction, thus there will be one "0-frequency" Rigid Body Mode (RBM) and three "deformational" modes with positive eigenvalues.

$$\left(\boldsymbol{K} - \omega_i^2 \boldsymbol{M}\right) \boldsymbol{v}_i = \boldsymbol{0} \tag{80}$$

In Eq. (80) ω_i and $\boldsymbol{v}_i$ are corresponding eigenvalue and eigenvector. This eigenvector can be determined by an eigenvalue analysis, and will be the highest possible frequency in the system. The eigenvector can serve as a step towards getting a criterion to find the

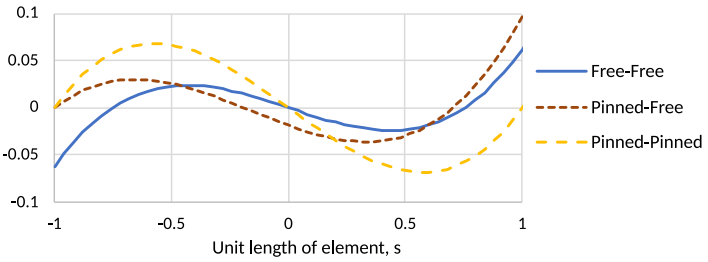

Fig. 8. The highest vibration modes for an element of length $L_e = 1$ with the three different boundary conditions presented in Fig. 7 introduced by Eqs. (82), (83), and (84).

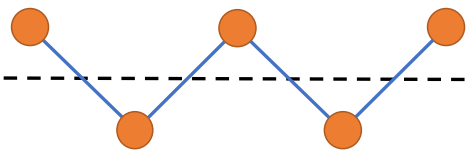

Fig. 9. The highest frequency for a propagatable mesh pattern in a bar.

maximum time-step, Eq. (82).

Free–Free Linear bar element:
$$\boldsymbol{v}_{max} = \begin{bmatrix} r_{1x} \\ r_{2x} \end{bmatrix} = \begin{bmatrix} 1.0L_e \\ -1.0L_e \end{bmatrix} \tag{81}$$

Free–Free ALE-ANCF element:
$$\boldsymbol{v}_{max} = \begin{bmatrix} r_{1x} \\ r'_{1x} \\ r_{2x} \\ r'_{2x} \end{bmatrix} = \begin{bmatrix} -0.06L_e \\ 0.71 \\ 0.06L_e \\ 0.71 \end{bmatrix} \tag{82}$$

Pinned–Free ALE-ANCF element:
$$\boldsymbol{v}_{max} = \begin{bmatrix} r'_{1x} \\ r_{2x} \\ r'_{2x} \end{bmatrix} = \begin{bmatrix} 0.38 \\ 0.10L_e \\ 0.92 \end{bmatrix} \tag{83}$$

Pinned–Pinned ALE-ANCF element:
$$\boldsymbol{v}_{max} = \begin{bmatrix} r'_{1x} \\ r'_{2x} \end{bmatrix} = \begin{bmatrix} 0.71 \\ 0.71 \end{bmatrix} \tag{84}$$

When rearranging and pre-multiplying Eq. (80) with $\boldsymbol{v}_{max}^T$, the familiar Rayleigh quotient for maximum squared eigenfrequency is established:

$$\frac{\boldsymbol{v}_{max}^T \boldsymbol{K} \boldsymbol{v}_{max}}{\boldsymbol{v}_{max}^T \boldsymbol{M} \boldsymbol{v}_{max}} = \omega_{max}^2 \tag{85}$$

In combination with the stable time-step region for RK4 in Eq. (76), a criterion for the maximum time-step is given in Eq. (86); where $\boldsymbol{v}_{max}$ is given by Eqs. (82) to (84).

$$h \leq \frac{2.8}{\omega_{max}} = \frac{2.8}{\sqrt{\frac{\boldsymbol{v}_{max}^T \boldsymbol{K} \boldsymbol{v}_{max}}{\boldsymbol{v}_{max}^T \boldsymbol{M} \boldsymbol{v}_{max}}}} \tag{86}$$

The element shape is found by $\boldsymbol{N}_e \boldsymbol{v}_{max}$, with the shape function from Eq. (2) and the eigenvectors from Eqs. (82) to (84). For an element with length $L_e = 1$ and configurations as in Fig. 7, the results are presented in Fig. 8.

For a cable modeled by several elements, a propagatable element displacement with a repeatable pattern has to be found. A requirement is then that the displacement and slope are continuous. This is not the case for the highest frequency in the Free–Free configuration, where there is discontinuity, see Fig. 8. None of the modes for the Free–Free configuration are found to be propagatable, see Table 1. Thus, this configuration is not directly relevant for a meshed cable.

When ALE-ANCF cable elements are connected, the shared nodes enforce equal displacement and slope. This is satisfied in the Pinned–Pinned configuration in Fig. 7(c). The highest frequency then has a mode shaped similar to a sine wave, see Fig. 8. For a cable pinned at both ends globally, this will be the highest frequency in the system.

The end element of the mesh does not have to be propagatable for a cable with a free end globally. Only the first node of the end element must be restrained to have a continuous displacement and slope. The Pinned–Free configuration in Fig. 8 is continuous

Table 1
Maximum time-steps h_{max} and equivalent effective element lengths L_{eff} for single element models of Fig. 7 (RBM: Rigid Body Mode).

Configuration	Prop mesh	ω_{max} [rad/s]	L_{eff}/L_e[–]	h_{max} [s]
$MSD_{f/f}$	Yes	63.3	1.00	44.3E−3
$\boldsymbol{v}_{f/f,1}$	No	412.5	0.15	6.8E−3
$\boldsymbol{v}_{f/f,2}$	RBM	0	0	0
$\boldsymbol{v}_{f/f,3}$	No	99.37	0.64	28.2E−3
$\boldsymbol{v}_{f/f,4}$	No	244.9	0.26	11.4E−3
$\boldsymbol{v}_{p/f,1}$	Yes, end	330.4	0.19	8.5E−3
$\boldsymbol{v}_{p/f,2}$	Yes, end	152.9	0.41	18.3E−3
$\boldsymbol{v}_{p/f,3}$	Yes, end	49.7	1.27	56.3E−3
$\boldsymbol{v}_{p/p,1}$	Yes	244.9	0.31	13.7E−3
$\boldsymbol{v}_{p/p,2}$	Yes	100.0	0.63	20.8E−3
$\boldsymbol{v}_{+/-,1}$	Yes	99.4	0.64	28.2E−3
$\boldsymbol{v}_{+/-,2}$	Yes	99.9	0.63	28.0E−3
$\boldsymbol{v}_{+/+,1}$	RBM	0	0	0
$\boldsymbol{v}_{+/+,2}$	Yes	204.9	0.31	13.7E−3

in one end and discontinuous in the other. The shape of this element has more than a sine wave over the element length, and thus has the highest frequency in an otherwise propagatable mesh. This will be the governing element if present in the cable model, provided that the elements are modeled with equal length.

Table 1 compares the highest eigenfrequencies, and thus the maximum stable time-step h_{max}, for the elements in Fig. 7 when they are modeled by MSD and ALE-ANCF cable elements respectively. The eigenvectors are given by Eqs. (81) to (84). The effective length in the table is independent of material data and element length.

The MSD cannot directly be used to predict the maximum time-step for RK4, but if Eq. (79) is updated with effective length to Eq. (87), the higher frequencies are accounted for. The effective length must be set according to the relevant boundary conditions, as suggested in Table 1. A strategy to predict the maximum time-step for RK4 with ALE-ANCF cable elements, according to a MSD, has thus been developed.

$$h \leq \frac{2.8}{\frac{2}{L_{eff}}\sqrt{\frac{E}{\rho}}} = 2.8\frac{L_{eff}}{2S} \tag{87}$$

For both the Free–Free and the Pinned–Free configuration in Fig. 8, the element is both in tension and compression internally.

For the Free–Free configuration, the element is in tension before $s = -0.77$ and after $s = 0.77$, and in compression between these. The points at $s = -0.77$, $s = 0$, and $s = 0.77$ can be considered pinned, as they are zero displacement points for the vibration mode

Applying the same procedure to the ALE-ANCF cable element as for the Mass–Spring in Fig. 5; by dividing the cable element into "sub-elements" introducing masses in $s = 0.5$ and $s = 1.0$ would lead to zero displacement at $s = 0.77$. The shortest element would then be $L_e = 0.23$, and the findings in Table 1 are supported, as it is reasonable to assume that the difference in effective length is due to the non-linear displacement.

An alternative method to enforce continuity in the mesh is to predetermine a mesh pattern. For a linear bar element, the highest frequency in a continuous mesh is given by a repeated pattern of +1, −1, as given in Eq. (81) and illustrated in Fig. 9.

A similar approach as for the bar element can be used for an ALE-ANCF cable element. To ensure a propagatable mesh, an enforced pattern can be introduced by repeatable eigenvectors, Eqs. (88) and (89). With a +/− pattern, both r_x and r'_x must have opposite sign at each end. $\boldsymbol{v}_{+/-}$ then takes the form as in Eq. (88). For the ALE-ANCF cable element, also an enforced +/+ pattern will provide a propagatable mode, Eq. (89).

$$\boldsymbol{v}_{+/-} = \begin{bmatrix} r_{1x} \\ r'_{1x} \\ r_{2x} \\ r'_{2x} \end{bmatrix} = \begin{bmatrix} r_{1x} \\ r'_{1x} \\ -r_{1x} \\ -r'_{1x} \end{bmatrix} = \begin{bmatrix} 1 & 0 \\ 0 & 1 \\ -1 & 0 \\ 0 & -1 \end{bmatrix} \begin{bmatrix} r_{1x} \\ r'_{1x} \end{bmatrix} = \boldsymbol{A}_{+/-} \begin{bmatrix} r_{1x} \\ r'_{1x} \end{bmatrix} \tag{88}$$

$$\boldsymbol{v}_{+/+} = \begin{bmatrix} r_{1x} \\ r'_{1x} \\ r_{2x} \\ r'_{2x} \end{bmatrix} = \begin{bmatrix} r_{1x} \\ r'_{1x} \\ r_{1x} \\ r'_{1x} \end{bmatrix} = \begin{bmatrix} 1 & 0 \\ 0 & 1 \\ 1 & 0 \\ 0 & 1 \end{bmatrix} \begin{bmatrix} r_{1x} \\ r'_{1x} \end{bmatrix} = \boldsymbol{A}_{+/+} \begin{bmatrix} r_{1x} \\ r'_{1x} \end{bmatrix} \tag{89}$$

The system can now be reduced from 4 to 2 DOFs by the use of $\boldsymbol{A}_{+/-}$ and $\boldsymbol{A}_{+/+}$, and the stiffness matrix and the mass matrix take the form $\widetilde{\boldsymbol{K}} = \boldsymbol{A}^T\boldsymbol{K}\boldsymbol{A}$ and $\widetilde{\boldsymbol{M}} = \boldsymbol{A}^T\boldsymbol{M}\boldsymbol{A}$. This is further used in the method presented for Eq. (85), to obtain the eigenfrequencies.

The four vibration modes for an element with predetermined patterns is presented in Fig. 10. The +/− pattern leads to a half sine wave over the element length, where one mode has zero displacement and the other has zero rotation. The +/+ pattern can have the same r_x at each node, which gives rigid body mode, while the other mode is equal to the Pinned–Pinned configuration in Fig. 8. The latter is given as Propagatable Free–Free in Table 1.

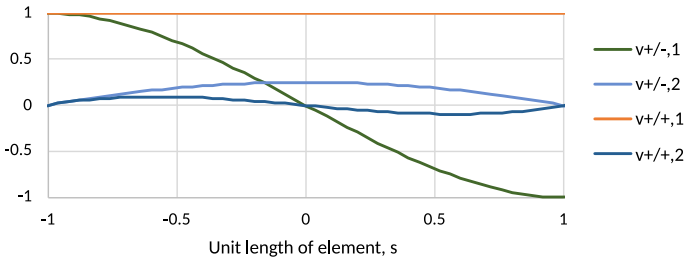

Fig. 10. The four vibration modes for an element of length $L_e = 1$ with predetermined pattern.

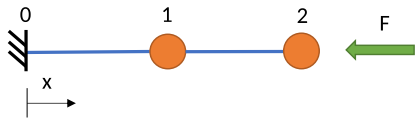

Fig. 11. Two-element cantilever bar undergoing the hammer test.

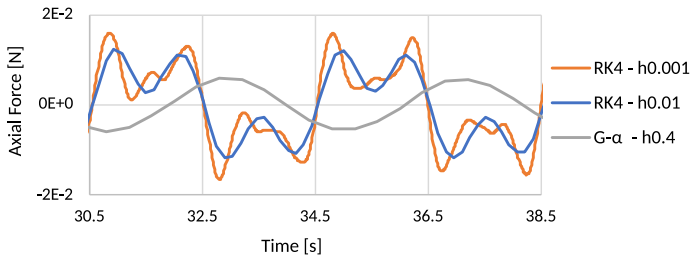

Fig. 12. The axial force from cable segment 2 from the two-element hammer test, for RK4 with time-step h=0.001 s, h=0.01 s, and G-α with time-step $h = 0.4$.

This method ensures a propagatable displacement. As the end element does not have to be repeatable, the method could fail to predict the maximum frequency, as it lacks a representation of the free end configuration. A weakness with this approach is that the Pinned–Free configuration is excluded by the predetermined pattern.

A hammer test was performed to find the frequencies in the ALE-ANCF cable element, as a verification to the maximum time-step criterion. The test procedure is to initially have an external force hit the end node, then allow the elements to swing freely, as if just hit by a hammer. This is presented for a two-element cable in Fig. 11, and has 5 DOFs, $r'_{0x}, r_{1x}, r'_{1x}, r_{2x}, r'_{2x}$. To detect the highest frequencies the results were analyzed by Fast Fourier Transform (FFT). To trigger the highest frequencies from a hammer test, the time-steps must be small enough to represent them. As an example, the procedure for a two-element hammer test is presented, with the material data $\rho A = 1m^2$, $L_e = 0.5m$ and $EA = 1N$, with an external force of $F = 0.01N$ for 1 s The response in the axial force is presented in Fig. 12, where it becomes evident that the smaller time-steps include higher frequencies. The force is plotted instead of displacement, as it is easier to observe the high frequency when the slope is part of the force expression. The FFT is presented in Fig. 13, and is based on 100 s series of the node displacement. Here, the 5 eigenfrequencies are visible for the smallest time-step, with the highest frequency at 3.1 Hz. The highest frequency is plugged into Eq. (76) to find the maximum time-step. The maximum time-step for a stable RK4 solver is congruent with the suggested criterion and verified by the FFT maximum time-step.

When using the maximum time-step, the number of time steps per highest frequency is just above 2, Fig. 12. For a decent representation of an oscillation it is recommended to have at least 10 time steps. This means that it is not required for RK4 to represent the highest frequencies accurately for it to be a stable solver. When running a FFT of a simulation with the maximum time-step, only the lower frequencies are captured, Fig. 13. If the time-step is larger than the criterion for maximum time-step, the simulation will diverge and fail as fictitious energy is added to the system.

As an alternative to RK4, G-α can be used as the numerical integration method. This method is not limited by the axial frequency. The time-steps can therefore be significantly larger than for RK4. For the two-element hammer test, the 1st vibration mode is 0.25 Hz, which equals a period of 4 s To have 10 time steps for each period, $h = 0.4s$. In Fig. 12 G-α represents the 1st axial vibration mode, which is confirmed in Fig. 13. This results in a relative error in the result and phase, which is further discussed in Section 7.

The hammer test was also carried out in a configuration of the elements where the node positions where fixed, and the flow variables were free. The slope DOFs were free, since they are associated with the strain. The 5 DOFs for the system were $r'_{0x}, p_1, r'_{1x}, p_2, r'_{2x}$. Instead of a force acting on the end node, a prescribed displacement was used on the fixed node to trigger the oscillations. Free flowing DOFs resulted in the same frequencies in the cable as with free position DOFs.

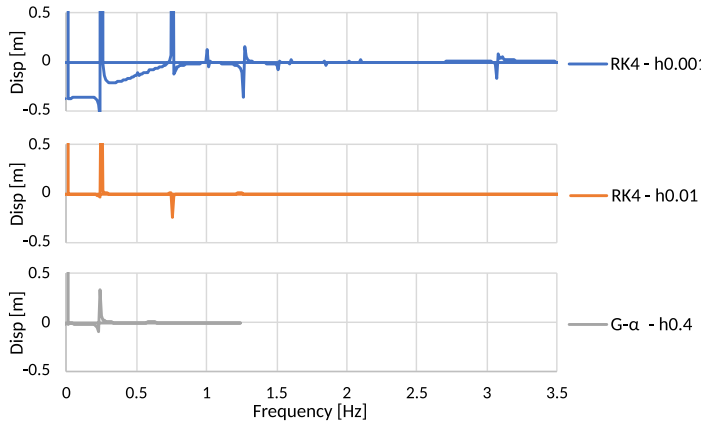

Fig. 13. Frequencies detected from FFT of displacement in node for RK4 with time-step h = 0.001 s, h = 0.01 s, and G-α with time-step h = 0.4.

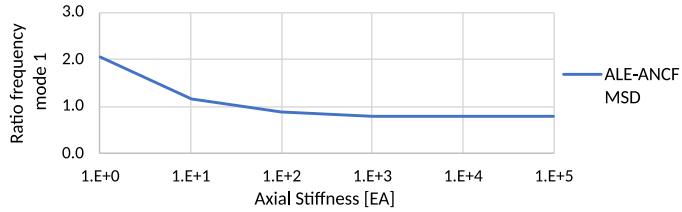

Fig. 14. Ratio between the 1st axial vibration mode for MSD and an ALE-ANCF cable, swinging freely with gravity in axial direction.

4.2. Nonlinear stiffness effects due to Green strain

To investigate how the axial stiffness influences the MSD and ALE-ANCF cable element, the cantilever bar was configured with a gravity field working in the axial direction, modeling a cable hanging in a gravity field. The cable was modeled with 1 element, $\rho A = 1$, $L = 1$, where different axial stiffnesses were tested, Fig. 14. The plot shows the ratio between the 1st vibration mode for MSD and an ALE-ANCF cable, based on FFT analysis. The trend in the plot is independent of the number of elements in the cable. It becomes evident that the axial frequency in MSD is only 79% of the ALE-ANCF cable for the stable area. To validate the results for axial frequency, the results were compared to an exact solution of axial vibration problems for elastic bars, [46]. The results for an ALE-ANCF cable matched perfectly. Thus, it can be concluded that a single element MSD is an insufficient simplification for an exact frequency representation. The MSD is a massless spring, only with a point mass at the end, while the cable is a continuous mass. The lumped mass instead of a distributed mass is believed to be one of the main issues.

Furthermore, from Fig. 14 a divergence in the frequency below an axial stiffness of $EA = 1000$ is observed. For a hanging cable in a gravity field with $EA = 1$, the frequency is over 2 times higher for the ALE-ANCF cable than the MSD. This was found to be due to the Green strain definition used in the ALE-ANCF cable element, Eq. (19). It became evident that the resulting nonlinear strain–displacement definition made the axial frequency too high. Therefore, the engineering strain definition, Eqs. (90) and (91), was tested instead of Green strain.

$$\epsilon_{eng} = \frac{\Delta \boldsymbol{r}}{\Delta \boldsymbol{p}} - 1 = \frac{\boldsymbol{r}_2 - \boldsymbol{r}_1}{p_2 - p_1} - 1 \tag{90}$$

$$\frac{\partial \epsilon_{eng}}{\partial \boldsymbol{q}} = \frac{\partial \left(\frac{\boldsymbol{r}_2 - \boldsymbol{r}_1}{p_2 - p_1} \right)}{\partial \boldsymbol{q}} \tag{91}$$

This resulted in a consistent relationship between frequencies of ALE-ANCF cable and the MSD, as the mass and stiffness changed.

A very large strain will affect the accuracy of the results. For a cable hanging in a gravity field using the Green strain definition, it is recommended to use the following relationship between mass and stiffness, Eq. (92). In the event of simulating a cable in a crane, this is far outside the maximum strain of 2%, [47]. In this strain range the difference between Green strain and engineering strain is negligible.

$$\rho A L < \frac{EA}{1000} \tag{92}$$

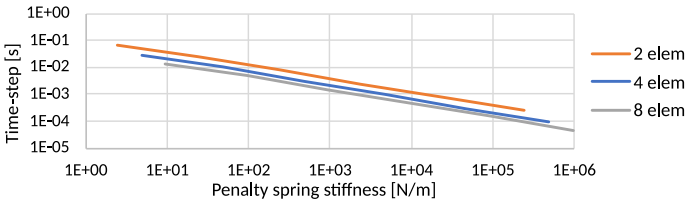

Fig. 15. Critical time-step plotted against penalty spring stiffness in cantilever beam.

5. Case 2: Constrained cable–cantilever beam

Different constraint methods are tested to connect the ALE-ANCF cable elements. In Case 1, the elements are connected by shared nodes, which is the simplest method as it reduces the number of DOFs in the system. This is equivalent to using the master–slave technique with linear coupling, to constrain the nodes. The constraint procedures tested in Case 2 are the penalty method and the Lagrange multiplier method. Constraints, $\boldsymbol{\phi}$, are used to connect the cable elements together. The constraint methods are applied to position DOFs, slope DOFs and flow DOFs from Eq. (1), as presented in Eq. (93), where the superscript e indicates the element number. This is done for two neighboring cable spans in x-, y- and z-direction, creating one constraint for each direction.

$$\boldsymbol{\phi} = \begin{bmatrix} \boldsymbol{r}_2^e - \boldsymbol{r}_1^{e+1} \\ \boldsymbol{r}'^e_2 - \boldsymbol{r}'^{e+1}_1 \\ p_2^e - p_1^{e+1} \end{bmatrix} = \mathbf{0} \tag{93}$$

In Case 2 the same cantilever beam model as in Case 1, Fig. 11, is used, where the elements have separate nodes connected by constraints instead of shared nodes.

For the penalty method, the penalty springs are user defined. To select an adequate stiffness the square root rule can be useful Eq. (94), [38, p. 9–5]. The largest stiffness in the system prior to adding the penalty springs is then found and given in the order of 10^k. b is the working machine precision. The unit of $\boldsymbol{k}_{pen}$ is defined by $\frac{EA}{L}$.

$$\lceil \boldsymbol{k}_{pen} \rfloor = 10^k \sqrt{10^b} \tag{94}$$

In this case the highest stiffness in the cable was found to be 4.8. For the set-up used, $b \approx 16$. According to the square root rule, the best penalty spring stiffness equals $\lceil \boldsymbol{k}_{pen} \rfloor = 10^9$. When solving the constrained system with the G-α method, the penalty method provides the same frequency as in Case 1. If a stiffer penalty spring is used, $\lceil \boldsymbol{k}_{pen} \rfloor = 10^{12}$, the results are the same but the number of iterations each time-step starts to increase. This is in accordance with the square root rule, Eq. (94).

The plot in Fig. 15 shows how the penalty spring stiffness impacts the maximum time-step for the of the cantilever beam. The penalty spring is a multiplication of the highest stiffness. With penalty springs added in the system, the stiffness increases, which also increases the frequencies. This results in a significant reduction in the maximum time-step for a stable RK4 solver. If the penalty spring stiffness is set with similar stiffness as the system stiffness, RK4 can run with a slightly reduced time-step, but the accuracy is poor as the constraints are too loose to properly connect the nodes. From the plot, a clear trend of how the penalty spring decrease the time-step can be observed. RK4 is a less than ideal method to use in combination with the penalty spring and will therefore not be used in combination with penalty constraints for the remainder of this paper.

When using the Lagrange Multiplier method to constrain the system, additional equations are introduced into the system matrix. For RK4, the method presented in Section 3.2 is used. The constraint method provides the same frequency and maximum time-step as found in Case 1.

The accuracy of the G-α is found to be unaffected by the choice of constraint method.

6. Case 3: Garden hose

To validate the accuracy of the constraint methods in combination with the numerical time integrators, a cantilevered garden hose with water flowing out at the free end is simulated. The garden hose makes a good case as it is an advanced model with several aspects of interest for benchmarking the solution procedure, such as large deformations and material flow. Water flows as the material, p, in the elements, causing frequency flutter in the hose. Two separate elements, placed on top of each other, represent the water and the hose. The overlaying elements share position DOFs and slope DOFs; and are connected with constraints. The flow nodes are fixed for the hose elements and prescribed for the water elements. The garden hose is held fixed at one end, and can thus be represented as a cantilever beam under gravity, Fig. 16. The case is based on work by [20], with the material parameters given in Table 2.

To test how the ALE-ANCF cable element behaves in bending with constraints, the model is first configured with flow speed below critical flutter speed. To find the statics solution, damping is added to the system to stabilize it. From the results in Fig. 17, the garden hose starts to straighten out as the water flow increases.

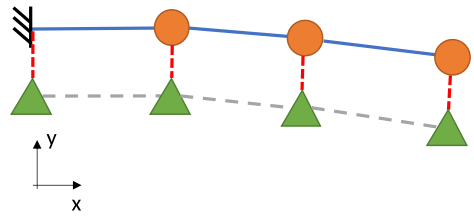

Fig. 16. A model of the garden hose; the red circular nodes indicate the hose, the green triangular nodes indicate the water with flow. The hose and the water is connected with constraints.

Table 2
The material parameters used in Case 3.

	Hose element	Water element
L_e [m]	0.05	0.5
Num elem [#]	10	10
EA [N]	10.0	0.0
EJ [N/m^2]	0.00108	0.0
ρA [kg/m]	0.0031316	0.0007854
cDamp [na]	0.0031316	0
Flow [m/s]	0	Prescribed

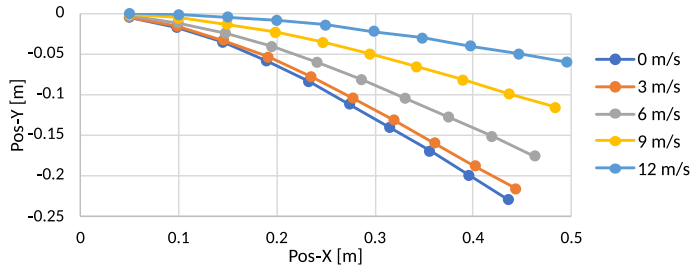

Fig. 17. Statics solution for garden hose with a water flow of 0 m/s, 3 m/s, 6 m/s, 9 m/s and 12 m/s.

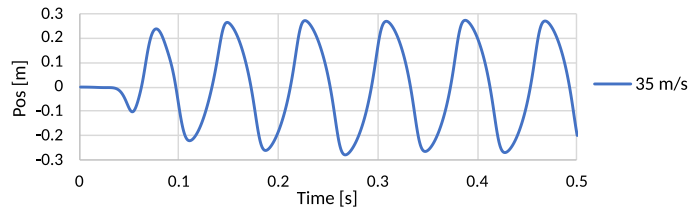

Fig. 18. Lateral displacement in the garden hose end plotted against time, with a water flow of 35 m/s.

The lateral displacement in the hose end is presented for a simulation with 35 m/s water flow in Fig. 18. The flutter is steady after initiation. In Fig. 19 the position and velocity for the hose end is plotted for water flows of 15 m/s, 25 m/s and 35 m/s. The results are in good agreement with [20].

To connect the water elements with the hose elements in the simulation linear coupling, penalty springs and the Lagrange multipliers were tested. For RK4, the maximum time-step for one hose element is found to be $h = 0.000245s$, according to the criterion described in Case 1. This agrees with simulation for the garden hose when using linear couplings or Lagrange multipliers, as this is the limit where the results starts to diverge.

The time-step requirement for the G-α method is to capture the movement of the garden hose. It is recommended to have 10 time-steps each oscillation. If the time-steps are too large to capture the behavior of the system the solver has difficulty converging and provides poor results.

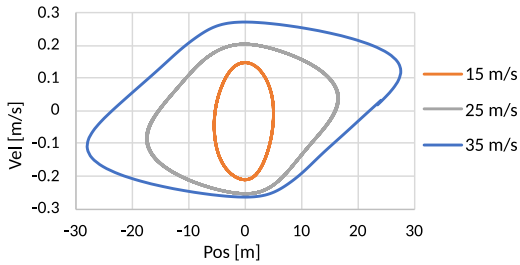

Fig. 19. Lateral position and lateral velocity of the hose end for water flows of 15 m/s, 25 m/s and 35 m/s.

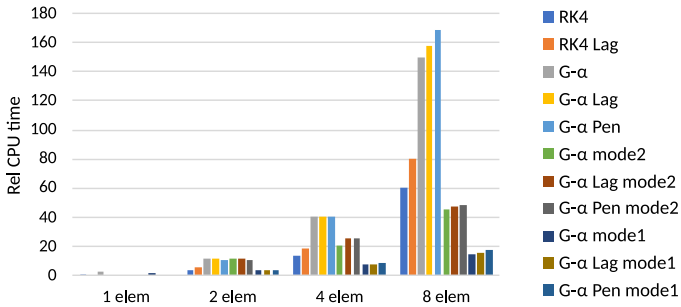

Fig. 20. Solution time comparison for RK4 and G-α with different constraint methods for Case 1 and 2.

7. Solution times

The various choices for constraint formulations and time integration algorithms will affect the overall solution time, both regarding accuracy and efficiency.

In general, the explicit RK4 algorithm has a maximum time-step based on the highest eigenfrequency in the system. If the actual loading and response has a significantly lower frequency, this often results in a very inefficient solution algorithm.

In general, the G-α algorithm does not have the same stability restriction, and the necessary time-step is guided more by accuracy considerations. The G-α thus allows a much more straight-forward tailoring of efficiency vs accuracy of the simulation.

Fig. 20 shows a comparison of relative solution time for RK4 and G-α for the cantilever beam in Case 1 and 2, with 1, 2, 4 and 8 elements. The relative solution time is found by normalizing the CPU time against the CPU time for 1 element RK4. RK4 is solved with the maximum time-step. RK4 is also solved with Lagrange multipliers connecting the nodes. The G-α method is solved with the same time-step size as the maximum for RK4, and for the required time-step to have 10 time steps each oscillation for 1st and 2nd vibration mode, (indicated as mode 2 and mode 1 in the plot). G-α is also solved with the Lagrange multiplier method and penalty method. For the 1 element configuration, no elements are connected, thus no constraints are used. This configuration only has the 1st axial vibration mode.

Calculating one time step for RK4 is faster than one time step for the G-α solver, as can be seen in Fig. 20. When solving the cantilever beam with 1 and 2 elements, RK4 is more efficient than G-α. With more than 2 elements, G-α becomes faster when only the 1st vibration mode is represented, and from 8 elements when also the 2nd vibration mode is represented. The constraint method chosen for G-α generally does not affect the solution time significantly; but there is a tendency for shared nodes to be slightly faster than the Lagrange multiplier method, which again is marginally faster than the penalty method.

From Case 3, the solution time for the garden hose with a 35 m/s water flow is compared for RK4 and G-α, Fig. 21. The total solution time for the G-α solver is almost 5 times faster than RK4. RK4 with Lagrange multipliers is slower than with linear couplings. RK4 is an inefficient solver due to the short elements. This is a simulation scenario where the advantage of G-α is evident.

The solution time for a simulation is affected by several factors, where the most apparent is the software/programming language used for implementation along with the computing power used to run the simulation. A useful tool to help select the best solution procedure for a real time simulation is a plot with accuracy plotted against relative CPU time. The relative CPU time is a relevant measure since the relation between the simulations is expected to be similar independent of software and computing power. Three different plots are made: error in position, error in axial force, and error in phase.

For a bar hanging in a gravity field, as presented in Case 1, the error in amplitude of the displacement, amplitude of the axial force, and phase of the displacement are plotted against the relative CPU time, Figs. 22, 23, and 24 respectively. The error is found

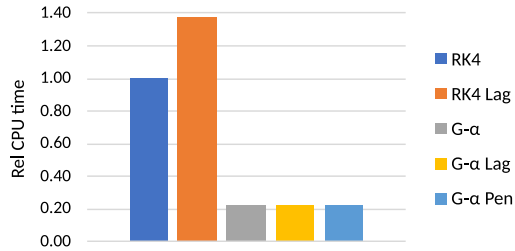

Fig. 21. Solution times comparison for RK4 and G-α with different constraint methods for Case 3, 35 m/s.

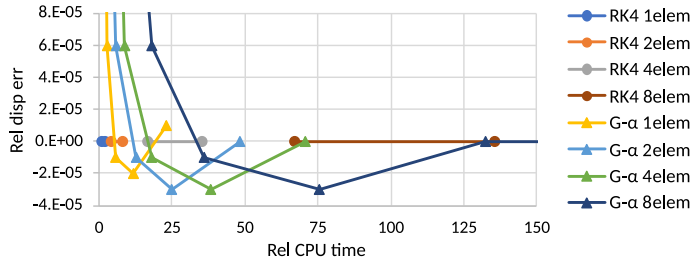

Fig. 22. Error plot for relative displacement plotted against relative computation time for RK4 and G-α with different constraint methods.

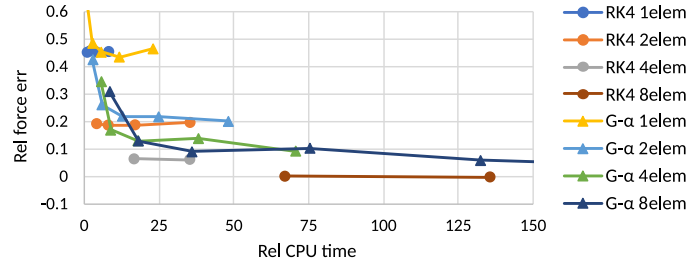

Fig. 23. Error plot for relative force plotted against relative computation time for RK4 and G-α with different constraint methods.

by normalizing against the RK4 run with 8 elements. The relative CPU time is found by normalizing against the RK4 run with 1 element.

In Fig. 22 the amplitude of the displacement is taken from the free end node of the cantilever bar. With a time-step capturing the oscillation in the bar, the error is very small also for G-α. RK4 is accurate for all the runs, while G-α overshoots a little before it stabilizes. G-α is faster than RK4 from 2 elements and onwards, and the advantage increases by reduction in the element length. For RK4, the maximum time-step is limited by the highest frequency in the mesh, and the accuracy is therefore mainly controlled by the number of elements in the mesh.

In Fig. 23 the amplitude of the axial force is taken from the pinned first node of the cantilever bar. The plot shows that the solution converges with increasing number of elements. It also shows that the convergence is slower than for displacement, which is expected as the force is a derived measure. For G-α both time-step size and the number of elements have an impact on the accuracy.

In Fig. 24, the phase of the displacement is taken from the free end node of the cantilever bar. The error is very small as the CPU time increases. The phase error for G-α is high at large time-steps. At lower time-steps G-α provides accurate results and is competitive against RK4.

To apply the insight from the plots, it is important for the user to know what the desired output from the simulation is, as there is a difference in accuracy between for example axial force and displacement.

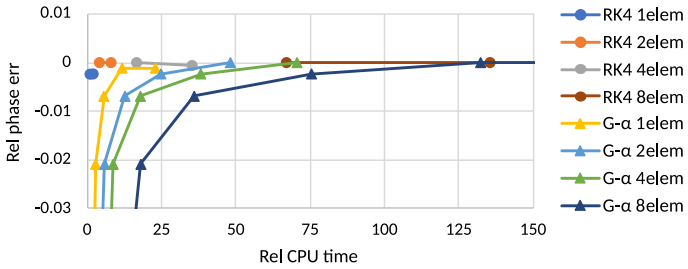

Fig. 24. Error plot for relative phase plotted against relative computation time for RK4 and G-α with different constraint methods.

8. Conclusion

The ALE-ANCF cable element has been investigated for cable simulation. With high demands on the solution time to obtain real time simulations, the selection of solver is important. The literature lacks a recommendation of which solver to choose for ALE-ANCF cable elements. Therefore, the present study presents a systematic approach to compare RK4 and G-α. RK4 is used in similar studies, and G-α is commonly used in classical structural mechanics software; making them good candidates for a numerical study with respect to explicit versus implicit time-integration. The systematic approach examines them with respect to the criteria *stability*, *accuracy*, and *efficiency*. It is found that RK4 is a good choice when simulating models with few elements and long cable spans. The stability limit for RK4 gets worse as the number of elements increase, despite the real frequency response in the system being the same. When performing simulations with equal time-steps, RK4 is about 3 times faster than G-α. For external loads requiring small time-steps, or where high frequencies in the system is of interest, RK4 is the most efficient solver. For loads with lower frequencies than the stability limit for RK4, G-α is better. G-α provides fast and accurate results as the high frequencies are dampened out and it is not hampered by requirements on the time-step size. The time-step size can be selected just by ensuring a sufficient number of time steps to capture the desired physical behavior of the model. Thus, G-α is found to often be the best alternative for most practical applications. Parts of the conclusions arrived in this paper is supported in [48], where the CPU time increase with element stiffness for an ANCF element with the explicit solver, while it has little effect on the implicit solver.

The axial frequencies obtained from the ALE-ANCF cable element for the 1st and 2nd vibration mode are in complete agreement with the frequency found in [46]. The frequency is the same whether it is the position DOF or the flow DOF that is free. A simplification of the cable to a single degree of freedom MSD does not provide an accurate axial frequency. Furthermore, the MSD element length cannot directly be used to predict the maximum time-step for RK4, as higher frequencies are present in the ALE-ANCF cable elements. A criterion to predict the maximum time-step for RK4 is created based on an easy to calculate *effective* (or *equivalent*) length as a fraction of the shortest element length in the mesh as well as the boundary conditions. The criterion is verified through eigenvalue analysis as well as numerical hammer test and FFT.

To achieve possibilities for advanced geometrical shapes, the ALE-ANCF cable element has to be connected with neighboring elements. In relation to the time integration methods, coupling methods are examined. The penalty method, Lagrange multiplier method and linear coupling are the methods used for connecting ALE-ANCF cable elements. For a system constrained by the penalty method, the penalty springs increase the stiffness in the system causing higher frequencies, which again reduces the maximum time-step for RK4. When using the Lagrange multiplier method with RK4, the solution is vulnerable to drifting as the constraints are differentiated as part of the solution procedure. To connect elements using constraints; the Lagrange multiplier method, penalty method or linear coupling are all valid methods providing similar results and solution times for the case with G-α.

There are several possibilities for further work for this research. To reduce the solution time, the ALE-ANCF cable element and the time integration solver could be written in a software with compiled code. This is believed to make a huge impact on the simulation speed, and thus the real time aspect. However, the relative performance between the algorithms are not expected to change.

Exploring the feasibility of a linear, lower order element, would be of interest. This would allow for an undemanding element formulation, where the material inertia forces probably can be derived from the angle between elements.

Moving towards a digital twin of an offshore crane, with an ALE-ANCF cable element used to model the wire, a laboratory knuckle boom crane should be simulated for benchmarking. The crane is to be instrumented, to enable sensor data input into the simulation. This will be a trial by fire for how the solver handles slack cables, and real time analysis with G-α. Furthermore, it will highlight the usefulness of this research for the industry.

A brief summary of findings are presented in Table 3.

Declaration of competing interest

The authors declare that they have no known competing financial interests or personal relationships that could have appeared to influence the work reported in this paper.

Table 3
Characteristic Pros and Cons of the G-α and RK4 algorithms.

G-α	
Pro	**Con**
• Allows large time-steps when loading and response is low-frequency • No step-size restriction, unconditionally stable. • Provides damping to modes that are high frequency relative to the time-step. • Time-step requirement unaffected by penalty method constraints.	• Each time-step is numerically expensive. • Require iterations for optimal accuracy for nonlinear problems, especially with large time-steps.
RK4	
Pro	**Con**
• Numerical low cost for each time-step. • Numerically efficient with high frequency loading. • Highly predictable computation times	• Has maximum time-step associated with smallest element in the model • Unnecessary number of time-steps for low frequency loading and response • Penalty method constraints affects maximum time-step negatively.

Acknowledgment

The research presented in this paper has received funding from the Research Council of Norway, SFI Offshore Mechatronics, project number 237896.

References

[1] G. Fotland, C. Haskins, T. Rølvåg, Trade study to select best alternative for cable and pulley simulation for cranes on offshore vessels, Syst. Eng. 23 (2) (2020) 177–188, http://dx.doi.org/10.1002/sys.21503.
[2] J.L. Escalona, An arbitrary Lagrangian–Eulerian discretization method for modeling and simulation of reeving systems in multibody dynamics, Mech. Mach. Theory 112 (2017) 1–21, http://dx.doi.org/10.1016/j.mechmachtheory.2017.01.014.
[3] F. Ju, Y.S. Choo, Super element approach to cable passing through multiple pulleys, Int. J. Solids Struct. 42 (11) (2005) 3533–3547, http://dx.doi.org/10.1016/j.ijsolstr.2004.10.014.
[4] A. Arena, A. Casalotti, W. Lacarbonara, M.P. Cartmell, Dynamics of container cranes: Three-dimensional modeling, full-scale experiments, and identification, Int. J. Mech. Sci. 93 (2015) 8–21, http://dx.doi.org/10.1016/j.ijmecsci.2014.11.024.
[5] B. Zhou, M.L. Accorsi, J.W. Leonard, Finite element formulation for modeling sliding cable elements, Comput. Struct. 82 (2) (2004) 271–280, http://dx.doi.org/10.1016/j.compstruc.2003.08.006.
[6] Y. Peng, Z. Zhao, M. Zhou, J. He, J. Yang, Y. Xiao, Flexible multibody model and the dynamics of the deployment of mesh antennas, J. Guid. Control Dyn. 40 (6) (2017) 1499–1510, http://dx.doi.org/10.2514/1.G000361.
[7] R. Xue, B. Ren, Z. Yan, Z. Du, A Cable-Pulley system modeling based position compensation control for a laparoscope surgical robot, Mech. Mach. Theory 118 (2017) 283–299, http://dx.doi.org/10.1016/j.mechmachtheory.2017.08.006.
[8] J.-H. Seo, H. Sugiyama, A.A. Shabana, Three-dimensional large deformation analysis of the multibody pantograph/catenary systems, Nonlinear Dyn. 42 (2) (2005) 199–215, http://dx.doi.org/10.1007/s11071-005-2789-9.
[9] S. Kulkarni, C.M. Pappalardo, A.A. Shabana, Pantograph/catenary contact formulations, J. Vib. Acoust. 139 (1) (2016) http://dx.doi.org/10.1115/1.4035132.
[10] B. Zemljarič, Analyses of the overhead-line cable stringing and sagging on hilly terrain with an absolute nodal coordinate formulation, Electr. Power Syst. Res. 140 (2016) 296–302, http://dx.doi.org/10.1016/j.epsr.2016.06.012.
[11] T.Z. Htun, H. Suzuki, D. García-Vallejo, Dynamic modeling of a radially multilayered tether cable for a remotely-operated underwater vehicle (ROV) based on the absolute nodal coordinate formulation (ANCF), Mech. Mach. Theory 153 (2020) 103961, http://dx.doi.org/10.1016/j.mechmachtheory.2020.103961.
[12] T. Wang, B. Tinsley, M.D. Patel, A.A. Shabana, Nonlinear dynamic analysis of parabolic leaf springs using ANCF geometry and data acquisition, Nonlinear Dyn. 93 (4) (2018) 2487–2515, http://dx.doi.org/10.1007/s11071-018-4338-3.
[13] D. Liu, S. Ai, L. Sun, J. Wei, N. He, Numerical modelling of offshore risers conveying slug flow under the ALE–ANCF framework, Ocean Eng. 235 (2021) 109415, http://dx.doi.org/10.1016/j.oceaneng.2021.109415.
[14] A.A. Shabana, Definition of the slopes and the finite element absolute nodal coordinate formulation, Multibody Syst. Dyn. 1 (3) (1997) 339–348, http://dx.doi.org/10.1023/A:1009740800463.
[15] K. Nachbagauer, State of the art of ANCF elements regarding geometric description, interpolation strategies, definition of elastic forces, validation and the locking phenomenon in comparison with proposed beam finite elements, Arch. Comput. Methods Eng. 21 (3) (2014) 293–319, http://dx.doi.org/10.1007/s11831-014-9117-9.
[16] J. Gerstmayr, H. Sugiyama, A. Mikkola, Review on the absolute nodal coordinate formulation for large deformation analysis of multibody systems, J. Comput. Nonlinear Dyn. 8 (3) (2013) 1–12, http://dx.doi.org/10.1115/1.4023487.
[17] J. Gerstmayr, A. Humer, P. Gruber, K. Nachbagauer, The absolute nodal coordinate formulation, in: Structure-Preserving Integrators in Nonlinear Structural Dynamics and Flexible Multibody Dynamics, in: CISM International Centre for Mechanical Sciences, Springer, Cham, 2016, pp. 159–200, http://dx.doi.org/10.1007/978-3-319-31879-0_4.
[18] A.M. Mikkola, A.A. Shabana, A non-incremental finite element procedure for the analysis of large deformation of plates and shells in mechanical system applications, Multibody Syst. Dyn. 9 (3) (2003) 283–309, http://dx.doi.org/10.1023/A:1022950912782.
[19] J. Sun, Q. Tian, H. Hu, N. Pedersen, Simultaneous topology and size optimization of a 3D variable-length structure described by the ALE–ANCF, Mech. Mach. Theory 129 (2018) 80–105, http://dx.doi.org/10.1016/j.mechmachtheory.2018.07.013.
[20] D. Hong, J. Tang, G. Ren, Dynamic modeling of mass-flowing linear medium with large amplitude displacement and rotation, J. Fluids Struct. 27 (8) (2011) 1137–1148, http://dx.doi.org/10.1016/j.jfluidstructs.2011.06.006.

[21] Q. Wang, Q. Tian, H. Hu, Dynamic simulation of frictional contacts of thin beams duing lage overall motions via absolute nodal coodinate fomulation, Nonlinear Dyn. 77 (4) (2014) 1411–1425, http://dx.doi.org/10.1007/s11071-014-1387-0.
[22] Q. Wang, Q. Tian, H. Hu, Dynamic simulation of frictional multi-zone contacts of thin beams, Nonlinear Dyn. 83 (4) (2016) 1919–1937, http://dx.doi.org/10.1007/s11071-015-2456-8.
[23] S. Takehara, M. Kawarada, K. Hase, Dynamic contact between a wire rope and a pulley using absolute nodal coordinate formulation, Machines 4 (1) (2016) 4, http://dx.doi.org/10.3390/machines4010004.
[24] R. Bulín, M. Hajžman, P. Polach, Nonlinear dynamics of a cable–pulley system using the absolute nodal coordinate formulation, SI: Advances/Dynamics, Mech. Res. Commun. 82 (2017) 21–28, http://dx.doi.org/10.1016/j.mechrescom.2017.01.001.
[25] Y. Peng, Y. Wei, M. Zhou, Efficient modeling of cable-pulley system with friction based on arbitrary-Lagrangian-Eulerian approach, Appl. Math. Mech. (English Ed.) 38 (12) (2017) 1785–1802, http://dx.doi.org/10.1007/s10483-017-2284-8.
[26] D. Hong, G. Ren, A modeling of sliding joint on one-dimensional flexible medium, Multibody Syst. Dyn. 26 (1) (2011) 91–106, http://dx.doi.org/10.1007/s11044-010-9242-7.
[27] N. Bel Hadj Ali, A.C. Sychterz, I.F.C. Smith, A dynamic-relaxation formulation for analysis of cable structures with sliding-induced friction, Int. J. Solids Struct. 126–127 (2017) 240–251, http://dx.doi.org/10.1016/j.ijsolstr.2017.08.008.
[28] Z. Kan, H. Peng, B. Chen, A simple linear complementarity approach for sliding cable modeling considering friction, Mech. Syst. Signal Process. 130 (2019) 293–314, http://dx.doi.org/10.1016/j.ymssp.2019.05.012.
[29] Z. Kan, F. Li, H. Peng, B. Chen, X. Song, Sliding cable modeling: A nonlinear complementarity function based framework, Mech. Syst. Signal Process. 146 (2021) 107021, http://dx.doi.org/10.1016/j.ymssp.2020.107021.
[30] C. Runge, Ueber die numerische Auflösung von Differentialgleichungen, Math. Ann. 46 (2) (1895) 167–178, http://dx.doi.org/10.1007/BF01446807.
[31] J.C. Butcher, A history of Runge-Kutta methods, Appl. Numer. Math. 20 (3) (1996) 247–260, http://dx.doi.org/10.1016/0168-9274(95)00108-5.
[32] J. Chung, G.M. Hulbert, A time integration algorithm for structural dynamics with improved numerical dissipation: The generalized-α method, J. Appl. Mech. 60 (2) (1993) 371–375, http://dx.doi.org/10.1115/1.2900803.
[33] H.M. Hilber, T.J.R. Hughes, R.L. Taylor, Improved numerical dissipation for time integration algorithms in structural dynamics, Earthq. Eng. Struct. Dyn. 5 (3) (1977) 283–292, http://dx.doi.org/10.1002/eqe.4290050306.
[34] W.L. Wood, M. Bossak, O.C. Zienkiewicz, An alpha modification of newmark's method, Int. J. Numer. Methods Eng. 15 (10) (1980) 1562–1566, http://dx.doi.org/10.1002/nme.1620151011.
[35] Y.-Q. Cui, Z.-Q. Yu, P. Lan, A novel method of thermo-mechanical coupled analysis based on the unified description, Mech. Mach. Theory 134 (2019) 376–392, http://dx.doi.org/10.1016/j.mechmachtheory.2019.01.001.
[36] E. Grossi, A.A. Shabana, Verification of a total Lagrangian ANCF solution procedure for fluid–structure interaction problems, J. Verif. Valid. Uncertain. Quant. 2 (4) (2018) http://dx.doi.org/10.1115/1.4038904.
[37] Y. Zhang, X. Jiang, Z.-f. Bai, J.-w. Guo, C. Wei, Dynamics and rebound behavior analysis of flexible tethered satellite system in deployment and station-keeping phases, Def. Technol. (2021) http://dx.doi.org/10.1016/j.dt.2021.04.007.
[38] C.A. Felippa, Introduction to Finite Element Methods - ASEN 5007, in: Lecture Notes, University of Colorado, pp. 1–791.
[39] D. Negrut, E.J. Haug, H.C. German, An implicit runge–Kutta Method for integration of differential algebraic equations of multibody dynamics, Multibody Syst. Dyn. 9 (2003) 121–142, http://dx.doi.org/10.1023/A:1022506312444.
[40] U.M. Ascher, H. Chin, S. Reich, Stabilization of DAEs and invariant manifolds, Numer. Math. 67 (2) (1994) 131–149, http://dx.doi.org/10.1007/s002110050020.
[41] U.M. Ascher, H. Chin, L.R. Petzold, S. Reich, Stabilization of constrained mechanical systems with DAEs and invariant manifolds, Mech. Struct. Mach. 23 (2) (1995) 135–157, http://dx.doi.org/10.1080/08905459508905232.
[42] N.M. Newmark, A method of computation for structural dynamics, J. Eng. Mech. Div. 85 (3) (1959) 67–94.
[43] T. Belytschko, D.F. Schoeberle, On the unconditional stability of an implicit algorithm for nonlinear structural dynamics, J. Appl. Mech. 42 (4) (1975) 865–869, http://dx.doi.org/10.1115/1.3423721.
[44] M. Arnold, O. Brüls, Convergence of the generalized-α scheme for constrained mechanical systems, Multibody Syst. Dyn. 85 (2007) 187–202, http://dx.doi.org/10.1007/s11044-007-9084-0.
[45] E. Hairer, G. Wanner, Solving Ordinary Differential Equations II. Stiff and Differential-Algebraic Problems, in: Springer Series in Computational Mathematics, Springer Berlin Heidelberg, 1996, http://dx.doi.org/10.1007/978-3-662-09947-6.
[46] H. Ma, Exact solutions of axial vibration problems of elastic bars, Int. J. Numer. Methods Eng. 75 (2) (2008) 241–252, http://dx.doi.org/10.1002/nme.2254.
[47] Certex Finland, Company Homepage, Technical description, 2020, (Accessed 22 October 2020).
[48] B. Hussein, D. Negrut, A.A. Shabana, Use of the implicit HHT-I3 and the explicit ADAMS methods with the absolute nodal coordinate formulation, 2007.

Paper 3

Modeling of Drill String Dynamics in Deviated Wells for Real-Time Simulation

This paper is awaiting publication and is therefore not included.

Appendices

Appendix A

Example of `YAML` Input File for the `Python` Program

```
##################################################
########   INPUT FILE FOR PYTHON PROGRAM   ########
##################################################

### The script is created to present relevant
### syntax for creation of a model in the program.

##################################################


CableModelMaterial:
    # Gravity field in X,Y,Z-direction
    Gravity: [0.0, 0, -9.81]


CableModel:
### NODES ###
    # BC = 1 -> hold, BC = 0 -> free, rx, ry, rz,
    # r'x, r'y, r'z, p, BC_function = 1 -> assigned
  - Node7Dof: { id: 0,  xyz: [0.0, 0.0, 0],
    xyz_d: [1.0, 0,  0], BC: [1, 1, 1, 0, 0, 0, 1]}
  - Node7Dof: { id: 1,  xyz: [0.5, 0.0, 0],
    xyz_d: [1.0, 0,  0], BC: [0, 0, 0, 0, 0, 0, 0]}
  - Node7Dof: { id: 2,  xyz: [1.0, 0.0, 0],
    xyz_d: [1.0, 0,  0], BC: [0, 0, 0, 0, 0, 0, 0]}
  - Node7Dof: { id: 3,  xyz: [1.0, 0.0, 0],
    xyz_d: [1.0, 0,  0], BC: [0, 0, 0, 0, 0, 0, 0]}
  - Node7Dof: { id: 4,  xyz: [1.5, 0.0, 0],
    xyz_d: [1.0, 0,  0], BC: [1, 1, 1, 0, 0, 0, 1],
    BC_functions: [0,0,0,0,0,0,1]}

### CABLE ELEMENTS ###
  - CableALEelement: { id: 0,  nodes7: [0, 1],
    EA: 1.0, EJ: 0.0, rhoA: 1.0, cDamp: 0.000}
  - CableALEelement: { id: 1,  nodes7: [1, 2],
    EA: 1.0, EJ: 0.0, rhoA: 1.0, cDamp: 0.000}
  - CableALEelement: { id: 2,  nodes7: [3, 4],
    EA: 1.0, EJ: 0.0, rhoA: 1.0, cDamp: 0.000}

### CONSTRAINTS ###
    # constr 0 -> r=r, 1 -> p=p, 2 -> rdp = rdp
    # Lagrange multipliers
  - LagMultipl7: { id: 1,  nodes7: [2, 3],  constr: 0}
  - LagMultipl7: { id: 2,  nodes7: [2, 3],  constr: 2}

    # Penalty springs
  - Penalty7: { id: 1,  nodes7: [2, 3],  constr: 0,  p_spring: 1000.0}
  - Penalty7: { id: 2,  nodes7: [2, 3],  constr: 2,  p_spring: 1000.0}

    # Linear coupling
    # slaveNode, slaveDOF, f0 = 0 -> Not prescripbed,
    # masterNode, masterDOF, factor.
    # Several masters possible.
  - LinearCoupl: {id: 1, sNode: 3, sDof: 1, f0: 0,
    masters: [{mNode: 2, mDof: 1, factor: 1}]}
  - LinearCoupl: {id: 2, sNode: 3, sDof: 2, f0: 0,
    masters: [{mNode: 2, mDof: 2, factor: 1}]}
  - LinearCoupl: {id: 3, sNode: 3, sDof: 3, f0: 0,
    masters: [{mNode: 2, mDof: 3, factor: 1}]}
  - LinearCoupl: {id: 4, sNode: 3, sDof: 4, f0: 0,
    masters: [{mNode: 2, mDof: 4, factor: 1}]}
  - LinearCoupl: {id: 5, sNode: 3, sDof: 5, f0: 0,
    masters: [{mNode: 2, mDof: 5, factor: 1}]}
  - LinearCoupl: {id: 6, sNode: 3, sDof: 6, f0: 0,
    masters: [{mNode: 2, mDof: 6, factor: 1}]}
  - LinearCoupl: {id: 7, sNode: 3, sDof: 7, f0: 0,
    masters: [{mNode: 2, mDof: 7, factor: 1}]}


```

```
####### ALTERNATIV FOR LINEAR ELEMENTS START #######

### NODES ###
    # BC = 1 -> hold, BC = 0 -> free, rx, ry, p,
    # BC_function = 1 -> assigned
  - Node4Dof: { id: 0,  xyz: [0.0, 0.0, 0],  BC: [1, 1, 1, 1]}
  - Node4Dof: { id: 1,  xyz: [0.5, 0.0, 0],  BC: [0, 0, 0, 0]}
  - Node4Dof: { id: 2,  xyz: [1.0, 0.0, 0],  BC: [0, 0, 0, 0]}
  - Node4Dof: { id: 3,  xyz: [1.0, 0.0, 0],  BC: [0, 0, 0, 0]}
  - Node4Dof: { id: 4,  xyz: [1.5, 0.0, 0],
    BC: [1, 1, 1, 1], BC_functions: [0,0,0,1]}

### CABLE ELEMENTS LINEAR###
  - CableALEelementLin: { id: 0,  nodes4: [0, 1],
    EA: 1.0, EJ: 0.0, rhoA: 1.0, cDamp: 0.000}
  - CableALEelementLin: { id: 1,  nodes4: [1, 2],
    EA: 1.0, EJ: 0.0, rhoA: 1.0, cDamp: 0.000}
  - CableALEelementLin: { id: 2,  nodes4: [3, 4],
    EA: 1.0, EJ: 0.0, rhoA: 1.0, cDamp: 0.000}

### CONSTRAINTS ###
    # constr 0 -> r=r, 1 -> p=p, 2 -> rdp = rdp
    # Lagrange multipliers
  - LagMultipl4: { id: 1,  nodes4: [2, 3],  constr: 0}
  - LagMultipl4: { id: 2,  nodes4: [2, 3],  constr: 2}

    # Penalty springs
  - Penalty4: { id: 1,  nodes4: [2, 3],  constr: 0,  p_spring: 1000.0}
  - Penalty4: { id: 2,  nodes4: [2, 3],  constr: 2,  p_spring: 1000.0}

    # Linear coupling
    # slaveNode, slaveDOF, f0 = 0 -> Not prescripbed,
    # masterNode, masterDOF, factor.
    # Several masters possible.
  - LinearCoupl: {id: 1, sNode: 3, sDof: 1, f0: 0,
    masters: [{mNode: 2, mDof: 1, factor: 1}]}
  - LinearCoupl: {id: 2, sNode: 3, sDof: 2, f0: 0,
    masters: [{mNode: 2, mDof: 2, factor: 1}]}
  - LinearCoupl: {id: 3, sNode: 3, sDof: 3, f0: 0,
    masters: [{mNode: 2, mDof: 3, factor: 1}]}
  - LinearCoupl: {id: 4, sNode: 3, sDof: 4, f0: 0,
    masters: [{mNode: 2, mDof: 4, factor: 1}]}

####### ALTERNATIV FOR LINEAR ELEMENTS END #######
```

```
### POINT FORCE ###
    # force in N, for number of seconds
  - PointForce: { id: 1, nodes7: [2], force: [0,8.5,0], timeInterval: [0,1.0]}

### ONE NODE SPRING ###
  - OneNodeSpring: { id: 1, nodes7: [3], stiffness: 1000.0, damping: 0.02}

### POINT MASS ###
    # mass in kg, gravity acting on the mass
  - PointMass: { id: 0, nodes7: [1], mass: 5.0}

### REELING FUNCTION ###
    # Assigned to BC_functions in NODES
  - Function_VelocityDefined:
        id: 1
        pos0: 0.0
        timeList:     [0, 0.5, 1, 1.5, 2, 100]
        velocityList: [0, 0.0, 0, 0.5, 1,   0]


### PLOTTING ###
Plots:
  - SubPlot: [{Cable:0, what:N, label: 'Axial Cable 0'},
              {Cable:1, what:N, label: 'Axial Cable 1'}]
  - SubPlot: [{Node:1, DOF:1, what:r, label: 'Node 1: x'},
              {Node:2, DOF:1, what:r, label: 'Node 2: x'}]


### NUMERICAL INTEGRATOR ###
GeneralizedAlpha:
  type: RK4 # Alternatives: G-alpha, RK4
  alpha_m: -0.05 # G-alpha parameter
  alpha_f: 0.10 # G-alpha parameter
  eps_energy: 1.0e-04 # error criterion limit
  time_step: 0.15 # time-step size
  massDamp: 0.00 # mass proportional damping

  maxIter:  20 # maximum iterations to quit
  time_end: 10.0 # total simulation time
  plotpoints: 0 # numer of plots points per sec
  skipVTK: True # write out vtk files

  plotpoints: 10 # Plot-points per second
```

```
########               END                 ########
```

ISBN 978-82-326-6332-3 (printed ver.)
ISBN 978-82-326-6878-6 (electronic ver.)
ISSN 1503-8181 (printed ver.)
ISSN 2703-8084 (online ver.)

NTNU

Norwegian University of
Science and Technology